UNIVERSITY OF LEEDS

DOCTORAL THESIS

Optimisation of Microfluidic Flow Systems

Author:
Foteini ZAGKLAVARA

Supervisors:
Prof. Peter K. JIMACK
Prof. Nikil KAPUR
Prof. Osvaldo QUERIN
Prof. Harvey M. THOMPSON

A thesis submitted in fulfillment of the requirements
for the degree of Doctor of Philosophy

in the

CDT of Fluid Dynamics
School of Computing

June 11, 2023

Declaration of Authorship

I, Foteini ZAGKLAVARA, declare that this thesis titled, “Optimisation of Microfluidic Flow Systems” and the work presented in it are my own. I confirm that:

- This work was done wholly or mainly while in candidature for a Doctor of Philosophy degree at this University.
- Where any part of this thesis has previously been submitted for a degree or any other qualification at this University or any other institution, this has been clearly stated.
- Where I have consulted the published work of others, this is always clearly attributed.
- Where I have quoted from the work of others, the source is always given. With the exception of such quotations, this thesis is entirely my own work.
- I have acknowledged all main sources of help.
- Where the thesis is based on work done by myself jointly with others, I have made clear exactly what was done by others and what I have contributed myself.

Signed: ***Foteini Zagklavara***

Date: *11 June 2023*

UNIVERSITY OF LEEDS

Abstract

Faculty of Engineering and Physical Sciences
School of Computing

Doctor of Philosophy

Optimisation of Microfluidic Flow Systems

by Foteini ZAGKLAVARA

This project investigates the fluid flow and heat transfer in microfluidic flow systems using Computational Fluid Dynamics (CFD) and experiments.

The first part of this work focuses on developing a CFD - enabled optimisation methodology of the geometrical features of i) a microfluidic heatsink design and ii) a single-phase (SP) continuous-flow (CF) Polymerase Chain Reaction (PCR) Device. This is achieved using COMSOL Multiphysics 5.4 ®to simulate the fluid flow, heat transfer (and PCR kinetics for the case of the microfluidic PCR device). Optimisation problems are then formed, selecting objective functions related to the performance of the devices. Design of Experiments is then used together with COMSOL Multiphysics 5.4 ®to collect the values of the objective functions over the design domain. Matlab© is then used to generate the response surfaces of the objective functions, using different techniques, locate the optimum design solutions (genetic algorithm, multi-level coordinate search method) and obtain the Pareto front for the cases of multi-objective optimisation problems.

Results of this work indicate the possibility of significantly enhancing the performance of SP-CF-PCR devices in terms of the DNA amplification, device volume, total operating time and total pressure drop by up to 16.4%, 43.2%, 17.8% and 80.5% respectively, after applying the appropriate design modifications for each objective. The increase in the DNA amplification is achieved by increasing the channel width and residence times while minimising the channel height. The reduction in the device volume, total operating time and total pressure drop are achieved when using the smallest residence times and higher channel width. According to this investigation, the DNA amplification appears to be linked to the temperature uniformity and to the residence time in the extension zone.

The second part of this work focuses on i) obtaining a better understanding of the role that the concentration and presence of droplets plays in conjugate heat transfer phenomena in droplet - laden flows, ii) creating and optimising a reusable, cheap and easy-to-fabricate device that can perform Melting Curve Analysis (MCA), in order to facilitate the work of a group of biologists at the University of Leeds. More specifically, this device aims to check for the presence of rare DNA species and possible contaminations in their collected samples in a fast, robust and cheap way, by testing if the DNA product has a unique melting temperature. The experimental setup is designed after performing a series of simulations using COMSOL Multiphysics 5.4 ®, considering different potential designs while at the same time simulating the energy requirements of the system. After finalising the design, a PID temperature controller is implemented on the Arduino Platform, achieving the required temperature difference between the two ends of the device. The results obtained during the experiments demonstrate a successful temperature control that is robust and does not require the adjustment of the PID parameters for the performance of similar experiments in the different temperature ranges tested.

Acknowledgements

I would like to express my deepest appreciation to Prof. Harvey M. Thompson, the lead supervisor of my PhD, for his continued support, excellent communication, patience and advice over the years. Together with my other supervisors, Prof. Peter K. Jimack, Prof. Nikil Kapur and Prof. Osvaldo Querin, they offered me important advice, guidance and excellent collaboration throughout my entire PhD, creating a very supportive and productive environment. I would also like to express my sincere appreciation to Joan Boyes and her group, Samuel Flint and William Davis Birch, for assisting me with their expertise on the development of the experimental rig. I am also grateful to the Engineering and Physical Sciences Research Council (EPSRC) Centre for Doctoral Training in Fluid Dynamics, Claire Savy, Emily Bryan–Kinns and my colleagues.

Furthermore, this journey would not have been possible without the sacrifices, continuous support and advice of my parents, Georgios Zagklavaras and Maria Mavromati. I am also extremely grateful to my sister, Despoina Zagklavara, who has always been there for me and to my partner, Triantafyllos Manios, for supporting and encouraging me during all these years. Special thanks goes to my friends, Markos Chasirtzoglou, Ioannis Gkioulekas and Khaled Al-Ghaithi, who helped me get through the difficulties I encountered and for the amazing moments we spent together. I would also like to thank my friends Andy and Richie for teaching and training with me in martial arts and making my time in Leeds much more interesting. Last but not least, I would like to thank my friends from the Chemical Engineering Department of the Aristotle University of Thessaloniki (AUTH), Charilaos, Lana, Poulios, Pilot, Lampas and Tsili, and my childhood friends, Mary, Christiana, Anastasia, Despoina, Despoina and Mariza for always making the times we spent together memorable.

Contents

List of Figures

List of Tables

List of Abbreviations

CFD	**C**omputational **F**luid **D**ynamics
CF	**C**ontinuous **F**low
CHT	**C**onjugate **H**eat **T**ransfer
CPU	**C**entral **P**rocessing **U**nit
CT	**C**rossing **P**oint
dTSA	**d**roplet-based **T**hermal **S**hift **A**ssay
DNA	**D**eoxyribo **N**ucleic **A**cid
DOE	**D**esign **O**f **E**xperiments
EDL	**E**lectric **D**ouble **L**ayer
EPSRC	**E**ngineering (and) **P**hysical **S**ciences**R**esearch **C**ouncil
HRM	**H**igh **R**esolution **M**elt
GA	**G**enetic **A**lgorithm
ID	**I**nternal **D**iameter
KRG	**K**riging
LED	**L**ight **E**mitted **D**iode
LHS	**L**eft **H**and **S**ide
LSM	**L**east **S**quare **M**ethod
MCA	**M**elting **C**urve **A**nalysis
MLSM	**M**oving **S**quare **M**ethod
NN	**N**eural **N**etwork
Nu	**Nu**sselt Number
OD	**O**uter **D**iameter
PCR	**P**olymerase **C**hain **R**eaction
PDE	**P**artial **D**ifferential **E**quation
PID	**P**roportional - **I**ntegral - **D**erivative
Pr	**Pr**andtl number
PS	**P**olyharmonic **S**pline
qPCR	**q**uantitative **P**olymerase **C**hain **R**eaction
RBF	**R**adial **B**asis **F**unction
RDA	**R**obust **D**esign **A**nalysis
RSA	**R**esponse **S**urface **A**pproximation
Re	**Re**ynolds Number
RHS	**R**ight **H**and **S**ide
SO	**S**imulation-based **O**ptimisation
SP	**S**ingle **P**hase

SSP	**S**ilica **S**uperparamagnetic **P**articles
SNP	**S**ingle **N**ucleotide **P**olymorphism
ULSM	**U**nweighted **L**east **S**quare **M**ethod
WLSM	**W**eighted **S**quare **M**ethod

Physical Constants

Speed of Light	$c_0 = 2.997\,924\,58 \times 10^8\,\mathrm{m\,s^{-1}}$ (exact)
Planck constant	$h = 6.626\,070\,15 \times 10^{-34}\,\mathrm{J \cdot s}$ (exact)
Gas constant	$R = 8.314\,462\,618\,153\,24\,\mathrm{J/(K \cdot mol)}$ (exact)
Stefan–Boltzmann constant	$\sigma = 5.6704 \times 10^{-8}\,\mathrm{W/(m^2{\cdot}K)}$ (exact)

List of Symbols

a	Distance	m
P	Power	W (J s^{-1})
c	Speed of light in a vacuum inertial frame	m/s
c_p	Heat capacity at constant pressure	J/K
c_v	Heat capacity at constant volume	J/K
C_i	Concentration of i^{th} species taking part in PCR	mol/m^3
$C_{i,o}$	Initial concentration of i^{th} species taking part in PCR	mol/m^3
D_i	Diffusion Coefficient of i^{th} species taking part in PCR	m^2/s
D_h	Hydraulic diameter	m
h	Heat transfer coefficient	$W/(m^2 \cdot K)$
H_c	Microchannel height	m
h_e	Specific enthalpy	J/kg
E	Electric field	V/m
e	Internal energy	J
$\mathbf{f}$	External forces applied in a volume of fluid	N
k_i^j	Reaction rate constant i, where i=D, A, E, j=+, -	$mol/(s \cdot m^3)$
k	Thermal conductivity	$W/(m \cdot K)$
M_g	The logarithm of $[Na^+]$	-
$[Na^+]$	Total concentration of Na^+	mol/L
$\bar{P}$	Pumping power	W
p	Pressure	Pa
Pr	Prandlt number	-
p_A	Absolute pressure	Pa
P_1	Single - stranded primer molecule	-
P_2	Single - stranded primer molecule	-
P_1S_2	Single-stranded template–primer complex	-
q''	Heat flux	W/m^2
Q	Heat source	W/m^3
Q_{vol}	Volumetric flowrate	m^3/s
R_{th}	Thermal resistance (absolute)	K/W
R	Thermal insulance (resistance)	$m^2 \cdot K/W$
Re	Reynolds number	-
R_i	Net reaction rate defined by PCR kinetics	$mol/(s \cdot m^3)$
S	Strain rate tensor	1/s

St	Stanton number	-
S_1S_2	Double - stranded DNA molecule	-
S_1	Single - stranded DNA molecule	-
S_2	Single - stranded DNA molecule	-
S_1P_2	Single-stranded template–primer complex	-
T	Temperature	K
T_w	Temperature at the wall interface	K
T_{in}	Inlet temperature	K
t	Time	s
T_f	Temperature of the fluid	K
T_m	Melting temperature	K
$\mathbf{u}$	Velocity vector	m/s
W_c	Microchannel width	m

α_P	Thermal expansion coefficient	1/K
δ_{ij}	Kronecker delta	-
δ_T	Thermal boundary layer region	m
δ_D	Concentration boundary layer region	m
Δp	Pressure Drop	Pa
θ	Microchannel width to depth ratio	-
ϵ	Surface Emissivity	-
Θ	Dimensionless thermal resistance	-
θ_{GC}	Fraction of GC pairs in DNA	%
λ	Second coefficient of viscosity	m^2/s
λ	Wavelength	nm
μ	Dynamic viscosity	Pa$\cdot$ s
ρ	Density	kg/m ^{3}
σ	Electrical conductivity	S/m
$\bar{\bar{\tau}}$	Viscous stress tensor	Pa
ϕ	Dissipation function	-
ϕ	Width of fin to depth	-

Chapter 1

Introduction

This project aims on using computational and experimental methods to study the thermal flow within two different systems utilising microfluidic channels, where Polymerase Chain Reaction (PCR) (Innis et al., 2012) or Melting Curve Analysis (MCA) (Farrar and Wittwer, 2017) are performed. Current designs of the vast array of microfluidic flow systems used throughout biology, chemistry and engineering are based on processing small volumes of liquid in arrays of simple fluidic channels formed from combinations of regular channel geometries (Kopp, Crabtree, and Manz, 1997; Ahrberg, Manz, and Chung, 2016). Wider adoption of microfluidic technologies will require much more flexible and robust channel geometry optimisation methods which can deliver a step-change in functional performance whilst accounting for variations in manufacturing tolerances and operating conditions.

The first part of this work involves the development of a Computational Fluid Dynamics (CFD) model using COMSOL Multiphysics ®5.4, that simulates the fluid flow, heat transfer and reaction kinetics for a single phase (SP) continuous flow (CF) microfluidic PCR device. A CFD-enabled optimisation methodology is also developed, leading to the improvement of the function of such devices under different objectives. Considering the small number of reaction optimisation studies on the microscale where the effects of flow rates, stoichiometry, concentrations, mixing design, residence time distribution, and temperature are considered (Radadia, 2008), this work is expected to provide a good understanding on the importance of the geometrical parameters in heat transfer and PCR performance. Use is made of NAG and MATLAB® optimisation routines to access a variety of problems. These methods are developed and applied first to liquid-cooled serpentine channel heat sinks for electronics cooling and then to the effective design of microfluidic channels for the use of PCR to replicate DNA, requiring precise temperature control of the liquids being manipulated (Hsieh et al., 2008).

As far as the performance of PCR is concerned, it highly depends on the temperature control over the different stages of the reaction (Papadopoulos et al., 2015). In particular, for the cases where the reaction is performed in microfluidic channels, a lot of interest exists in optimising its performance while reducing the cost and volume of the commercially produced final product. These objectives are often found to compete against each other, as improving one might result in deteriorating the other, hence requiring a multi-objective optimisation approach. However, little work has been published on the optimisation of PCR microfluidic devices. On the contrary, a lot of work exists in the optimisation of heat sinks, another type of microfluidic technology, where temperature control and Conjugate Heat Transfer (CHT) problems have been studied extensively. As a result, work on the optimisation of heat sinks is studied and validated for the purposes of this research work, in order to become familiar with the use of different optimisation techniques.

The second aspect of this work involves developing an experimental device that will facilitate the understanding of heat transfer in microfluidic droplet-based devices, together with the impact that droplet packing can have on heat transfer. This device is built while at the same time facilitating the work of a group of biologists in the University of Leeds, allowing them to quantify and differentiate between different DNA molecules, present in one sample by performing MCA. Computational work is also performed prior to experimental work, in order to assist and optimise the design prior to development.

Chapter 2

Literature Review

2.1 Polymerase Chain Reaction (PCR)

The biomedical industry is currently developing and using microfabricated fluidic devices for patient diagnosis, patient monitoring, and drug delivery. Examples of microfluidic devices for biomedical research include microscale flow cytometers for cancer cell detection, micromachined electrophoretic channels for DNA fractionation, and PCR chambers for DNA amplification. The details of the fluid motion through these small channels, coupled with nonlinear interactions between macromolecules, cells, and the surface-dominated physics of the channels, create very complicated phenomena, which can be difficult to simulate numerically (Nguyen, Wereley, and Shaegh, 2019).

PCR consists of a molecular technique that aims to amplify a single or a few DNA segments to thousands or millions. The discovery of PCR (Mullis and Faloona, 1989; Saiki et al., 1985) and the development in PCR technology has revolutionized molecular diagnostics since PCR offers the ability of exponentially amplifying the target sequence of interest, allowing the identification of mutations within a day (Patrinos and Ansorge, 2010) or even a few minutes (Dinca et al., 2009).

The main applications of PCR are in molecular identification (DNA fingerprinting, mutation screening, prenatal diagnosis, detection of pathogen, genotyping, Genetic matching etc.), sequencing (bioinformatics, human genome cloning) and genetic engineering (ex. gene expression studies). According to Chen and Li (2018), PCR has become one of the most widely used techniques in gene analysis, identification of infectious diseases, clinical diagnosis etc..

The main steps of PCR are the following (Figure 2.1):

- **Denaturation** (strand separation): the double-stranded DNA molecules, comprising of two hydrogen-bonded complementary chains of DNA, separate into a pair of single-stranded polynucleotide molecules when the sample is heated (94 °C to 96 °C).
- **Annealing** (primer binding): the temperature is lowered (45-60 °C) so the primers can attach themselves to the single-stranded DNA strands.
- **Extension** (synthesis of new DNA): it starts at the end of the annealed primer and works its way along the DNA strand, generating new DNA molecules (72 °C).

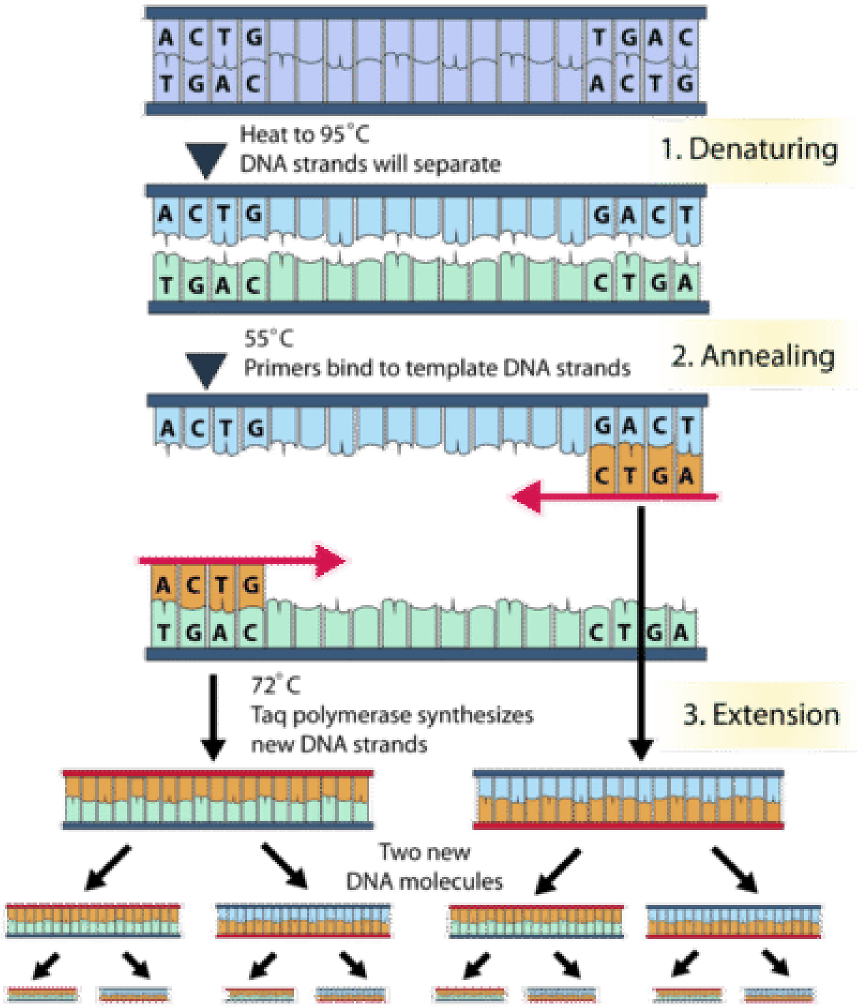

FIGURE 2.1: PCR process (Figure obtained from Wilkin, 2018)

2.1.1 PCR kinetics

Several studies regarding the kinetics of PCR can be found in literature, developing mathematical models to investigate the mechanisms of PCR and calculate the DNA concentrations during reactions (Hunicke-Smith, 1998; Aach and Church, 2004; Wang and Wang, 2010; Chen and Li, 2018).

Athavale et al. (2001) performed a numerical simulation for PCR chemistry to evaluate the sample temperature and the concentrations of some chemical species in an oscillatory PCR reactor. Mehra and Hu (2005) developed a detailed kinetic model for PCR, while examining the effect different factors can have on the performance of PCR. According to their results, the amplification efficiency was found to be constant at first while gradually decreasing when the primer concentration becomes rate-limiting. For optimum efficiency conditions, all single-stranded DNA molecules should be converted to single-stranded–primer complexes in each annealing step, which requires maintaining a high ratio of primer-to-substrate and a high primer concentration.

Papadopoulos et al. (2015) included a model of the kinetics of PCR (similar to the one of Athavale et al. (2001)) into their simulations with COMSOL Multiphysics, in order to compare the DNA amplification in the two typed of microfluidic PCR devices; a continuous flow and a static chamber PCR device. Priye, Hassan, and Ugaz (2013) presented the PCR process in a Rayleigh–Bénard convection cell. According to Priye, Hassan, and Ugaz (2013), increasing the complexity of the kinetics model by introducing more chemical reactions was not found to significantly change the DNA amplification efficiency (comparison between a 3-, 5- and 7- reaction models). As a result, the model to be used for the purposes of this work (Equations 1 - 5) is the one presented in the publication of Papadopoulos et al. (2015).

As far as the kinetics of the first stage of the PCR (denaturation) are concerned, the double-stranded DNA molecules, S_1S_2, dissociate into two single strands, S_1 and S_2 in denaturation zone according to Reaction 1.

$$\mathrm{S_1S_2} \xleftrightarrow[{\mathrm{k_D}}^{-}]{{\mathrm{k_D}}^{+}} \mathrm{S_1} + \mathrm{S_2} \qquad \{1\}$$

where k_D is the denaturation constant for melting of D at melting temperature; k_{-D} is the denaturation constant for binding of S at melting temperature.The arrow symbols “ ← ” and “ →" are used to denote net forward and backward reactions. The high melting temperature causes thermal denaturation of the enzyme responsible for DNA amplification.

In the annealing zone, the single-stranded primer molecules, P_1 and P_2, bind to S_2 and S_1 respectively, and form the single-stranded template–primer complexes, P_1S_2 and S_1P_2 (Reactions 2 and 3).

$$\mathrm{S_1} + \mathrm{P_2} \xleftrightarrow[{\mathrm{k_A}}^{-}]{{\mathrm{k_A}}^{+}} \mathrm{S_1P_2} \qquad \{2\}$$

$$\mathrm{S_2} + \mathrm{P_1} \xleftrightarrow[{\mathrm{k_A}}^{-}]{{\mathrm{k_A}}^{+}} \mathrm{P_1S_2} \qquad \{3\}$$

where k_A^+ is the annealing coefficient of P_1 and P_2 to S_2 and S_1 respectively; k_A^- is the dissociation coefficient of P_1S_2 and S_1P_2.

In the extension zone, the polymerase enzyme binds to P_1S_2 and S_1P_2 to form the single-stranded template–primer–enzyme complexes. Then these complexes dissociate into the enzyme and the DNA molecules at the beginning of the subsequent denaturation step (Reactions 4 and 5).

$$\mathrm{S_1P_2} \xrightarrow{\mathrm{k_E}} \mathrm{S_1S_2} \qquad \{4\}$$

$$\mathrm{P_1S_2} \xrightarrow{\mathrm{k_E}} \mathrm{S_1S_2} \qquad \{5\}$$

where k_E is the addition constant of the enzyme to P_1S_2 and S_1P_2.

The temperature dependence of the various rate constants mentioned earlier,

k_D^+, k_D^-, k_E, k_A^+ and k_A^-, are given by Equations E.1 - E.5 of Appendix E, as demonstrated also in the work of Papadopoulos et al. (2015). The reaction rates are given by Equations E.6 - E.12 presented in Appendix E, while the temperature dependence of the rate constants is presented in Figure 2.2.

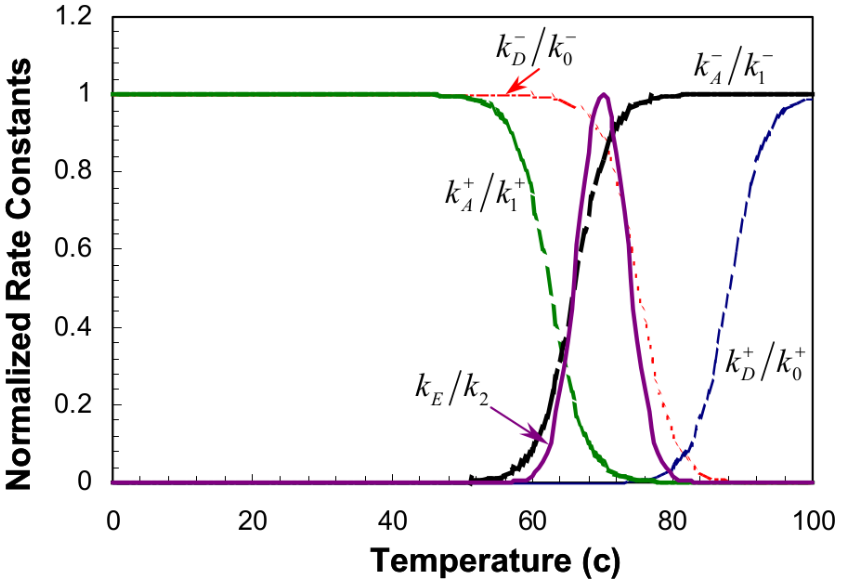

FIGURE 2.2: Temperature dependence of rate constants (Figure obtained from Wang et al., 2007).

These steps complete one PCR cycle, and ideally, each piece of DNA in the mixture is duplicated. By carrying out the three steps, the DNA concentration can be increased dramatically and then the DNA mixture can be analysed through a commercial detector (Chen and Li, 2018). Apart from the number of PCR cycles performed, the temperature uniformity of the sample is another key parameter for PCR efficiency (Kang et al., 2006; Papadopoulos et al., 2015; Moschou et al., 2014).

2.1.2 Residence time PCR protocols

There is a number of publications describing different PCR protocols used for the reaction. Cao, Kim, and Klapperich (2011) mention in their work that the residence times required for a DNA molecule to successfully complete the denaturation, annealing and extension stages are 1, 1 and 1.5 seconds (Wittwer and Garling, 1991) respectively from the moment the molecule reaches the required respective temperature (for the amplification case of a 150 bp). In practice, these values should be considered as the minimum residence time values, since the PCR environment on a chip is different than the one of a tube (Cao, Kim, and Klapperich, 2011). For example, Papadopoulos et al. (2015) utilised a different PCR protocol, where a total number of 30 cycles is performed, with 3s:4.2s:6.2s spent in denaturation, annealing, and extension per cycle respectively.

The values of some typical cycling parameters for PCR (for Taq Polymerase) are presented in Table 2.1, as suggested by Biolabs (2019) and Sigma-Aldrich (2019).

TABLE 2.1: Typical PCR Protocols and Cycling conditions (for Taq Polymerase)

Reference	Stage	No of Cycles	Temperature (C^o)	Time (s)
Biolabs (2019)	Prior Treatment	1	95	120
	Denaturation	25	95	15
	Annealing	25	55	15
	Extension	25	68	45
	Final treatment*	1	68	300
	Storage	1	4-10	Infinite period
Sigma-Aldrich (2019)	Denaturation	25	95	60
	Annealing	25	55	120
	Extension	25	68	180

* To finish replication on all templates

2.1.3 PCR efficiency

PCR enzymatically extends single-stranded DNA molecules over a specific region surrounded by a set of primers. Theoretically, the number of templates is expected to double after each PCR cycle. In reality, the DNA instead increases by a factor of (1+η), where η is the cycle efficiency. In this case, an efficiency of η = 1 would imply a doubling of the DNA concentration (theoretical efficiency) (Booth et al., 2010). Although the efficiency can change from cycle to cycle, the overall efficiency (η) for n cycles (Booth et al., 2010) is often reported. Saiki et al. (1985) related the overall efficiency (η) and yield (X) by Equation 2.1.

$$X = (1+\eta)^n \tag{2.1}$$

Equation 2.1 is considered the standard way to express the overall efficiency of PCR processes (Keohavong and Thilly, 1989; Li et al., 1988). A small variation in this relation has been proposed by Newton, Graham, and Ellison (1997) if the original DNA is genomic DNA with a length greater than the target DNA length. Experiments have shown that reaction yields can vary from cycle to cycle, while the yield tends to decrease as the number of cycles increases (Kainz, 2000; Schnell and Mendoza, 1997; Schnell and Mendoza, 1997; Stolovitzky and Cecchi, 1996). More references can be found in Waterfall, Eisenthal, and Cobb (2002). The use of Equation 2.1 has been implemented in a variety of applications like gene expression studies, mutation detection, forensic analysis and pathogen detection with the aim at both clinical diagnostics and food safety (Harvey, Ferrier, et al., 2011; Logan et al., 2009; Pfaffl et al., 2004).

Although the value of an overall efficiency is often used to quantify experiments, it provides no insight into any changes that might occur from cycle to cycle in terms of efficiency (Booth et al., 2010). More advanced models have been developed to account for the variation of the efficiency between cycles (Liu and Saint, 2002; Platts et al., 2008), reporting a single efficiency value per cycle and but do not give an extra insight on the different processes that take place in the overall PCR process. According to Booth et al. (2010), the overall efficiency depends linearly on the denaturing efficiency and changes from cycle to cycle, while various mechanisms may take place over the course of 30 or 40 cycles.

2.1.4 Scales of the system

In the literature review that took place, most of the simulations regarding PCR microfluidic devices simulated the flow of water or other carrier fluids commonly used in the PCR process, without taking into account the presence of DNA molecules (Moschou et al., 2014; Papadopoulos et al., 2015; Chen and Li, 2018; Perwez et al., 2019).

In order to understand the effect that the presence of DNA molecules has on the fluidynamic behaviour of its carrier fluid, the different scales/dimensions of the system are studied. Table 2.2 presents the Kuhn, the DNA base pair, and some indicative DNA fragments and PCR device characteristic lengths (Hatch et al., 2014). Figures 2.3 and 2.4 present the characteristic lengths of different microfluidic devices and the concentrations of typical diagnostic analytes in human blood or other samples respectively.

Considering the fact that the dimensions of both SP-CF and DR-CF PCR devices, as well as the droplets of the carrier fluid are about 10 - 100 times larger than the size of the DNA fragments, the DNA molecules can be omitted from the simulations, as they are not expected to significantly affect the fluid dynamic behaviour of the fluid they are contained in.

TABLE 2.2: Scales of PCR systems

Dimensions	Scales of the system (m)	Description
$b_k\|_{DNA}$	10^{-10}	Kuhn length (Monjezi et al., 2017)
base pair$\|_{DNA}$	10^{-10}	Length of 1 base pair of DNA molecule
DNA fragments$\|_{length}$	10^{-6}-10^{-5}	Length of DNA fragment (Cheng et al., 1994)
SP-CF-PCR device	10^{-4}	Length of PCR device (Park and Park, 2017)
DR-CF-PCR device	10^{-4}	Length of PCR device (Zhang and Jiang, 2016)
Carrier droplet $\|_{diametre}$	10^{-4}	Carrier droplet's diametre (Zhang and Jiang, 2016)

*Kuhn length: shortest polymer segment length which is not bent or stretched by thermal fluctuation

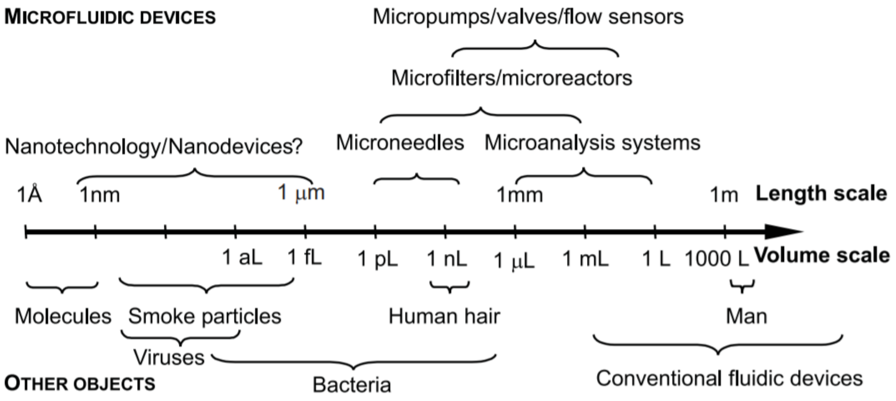

FIGURE 2.3: Size characteristics of microfluidic devices (Figure obtained from Nguyen, Wereley, and Shaegh, 2019)

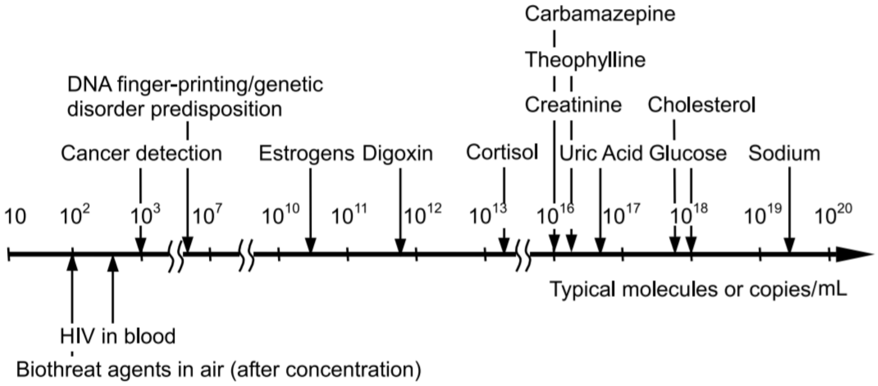

FIGURE 2.4: Concentrations of typical diagnostic analytes in human blood or other samples (Figure obtained from Nguyen, Wereley, and Shaegh, 2019)

2.1.5 PCR devices and Techniques

In the last two decades, significant progress has been achieved in the development of PCR devices (Zhang and Jiang, 2016), with one of the first microfluidic devices being reported in 1993, where a continuous single phase flow PCR device was used to perform the thermal cycles of the process (Northrup et al., 1993). According to Radadia (2008), a conventional PCR device performs a single PCR cycle approximately in 5-10 min, therefore requiring a total of 150 - 300 min approximately for 30 cycles. When using a microfluidic device, the total reaction time required for 20 PCR cycles ranges between 90 s to 18.7 min, depending on the flowrate applied in the microchannel (Kopp, De Mello, and Manz, 1998). As a result, the time required per cycle when using a commercial PCR device compared to a microfluidic PCR device appears to be ∼5 - ∼133 times greater.

Recent research appears to also focus on the development of a different type of continuous flow PCR device, the droplet-based microfluidic PCR devices. This type of devices appears to present some advantages over the single-phase technologies and they are also suitable for single-cell and single-molecule analysis (Zhang and

Jiang, 2016). However, it is more expensive compared to single-phase continuous-flow PCR devices.

2.1.5.1 Single-phase Continuous Flow PCR

In single-phase microfluidic PCR devices, the small thermal mass leads to a negligible thermal inertial effect. Moreover, the large surface-to-volume ratio of the device enables fast heat transfer. As a result, the time required for the samples to achieve equilibrium temperatures in denaturation and annealing steps is reduced. Because of the rapid thermal response to the environment, PCR mixtures are able to achieve a more uniform temperature distribution that leads to higher yield. Mixing can be fast even purely by diffusion, reducing the need to use expensive reagents (Zhang and Jiang, 2016). According to Kopp, De Mello, and Manz (1998), the time required for a sample to arrive at a new temperature is only affected by the time needed to transport the sample into the new temperature zone. More specifically, for the case of a flat rectangular channel (and under the assumption that the heat capacity of the heating elements and the chip is infinite compared to the one of the heated fluid), the time required for the heat to dissipate is proportional to the square of the channel's depth.

In single-phase microfluidic PCR devices however, the PCR mixture experiences adsorption phenomena at the flow channel surfaces, which leads to PCR inhibition and carryover contamination. Moreover, the adsorption of biological/chemical particles is enhanced by the large surface/volume ratio between the channel surface area and the sample volume. Another drawback that this type of technology presents is the yield reduction and the increase in the total residence time in the device, given to the fact that the dwell times of PCR mixture in each thermal cycle are very different (PCR mixture moves faster in the channel centre than it does close to the surface). Furthermore, this type of PCR microfluidic device has the preference of amplifying short fragments and producing chimerical molecules (Zhang and Jiang, 2016).

Because of these disadvantages and the complicated pre-treatment requirement of the reactor, there is limited use of continuous-flow PCR systems in recent commercial applications (Dong et al., 2021). However, there remains significant research interest in CFPCR flows, as evidenced by several studies appearing recently (Papadopoulos et al., 2015; Moschou et al., 2014; Kaprou et al., 2019; Kulkarni et al., 2021; Kulkarni, Salve, and Goel, 2021).

An example of a combined experimental and computational study on the performance of single-phase microfluidic PCR devices is the work of Cao, Kim, and Klapperich (2011). Cao, Kim, and Klapperich (2011) studied the performances of three different designs with different PCR cycle times. All three designs were found to perform better for longer cycle times, while one design (enlarged tube in the extension and denaturation zones) was found to perform best in all case studies. Also, the effect of the template size on the PCR yield was also studied, with the smaller template presenting a better PCR yield than the larger one under the same experimental conditions.

A Single-Phase Continuous-Flow (SP-CF-PCR) PCR device is presented in Figure 2.5. Figures 2.6, 2.7 and 2.8 present the experimental setup of a 3D printed single-phase PCR device, the thermographic images captured for two different volumetric flowrates (5 and 10 μL/min) and the measured temperature distributions along the different positions of the device respectively.

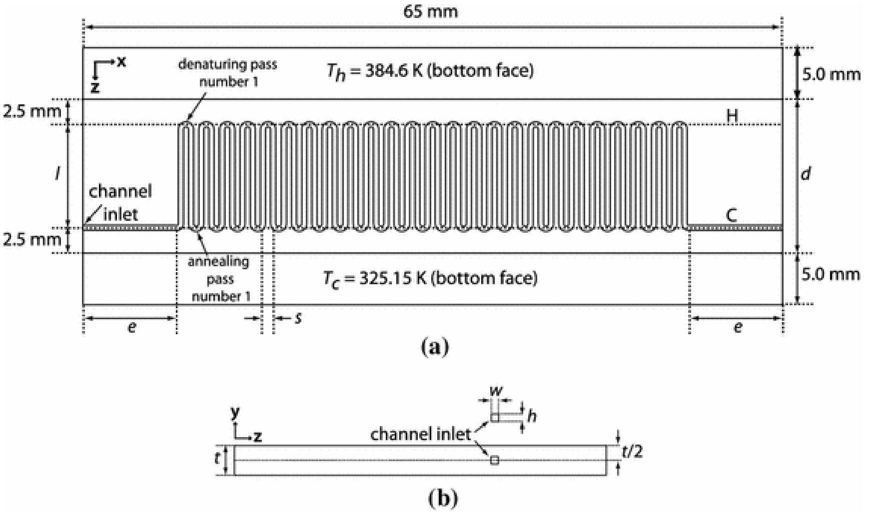

FIGURE 2.5: An example of a schematic Graph of SP-CF-PCR devices (Figures obtained from Thomas, Orozco, and Ameel, 2014)

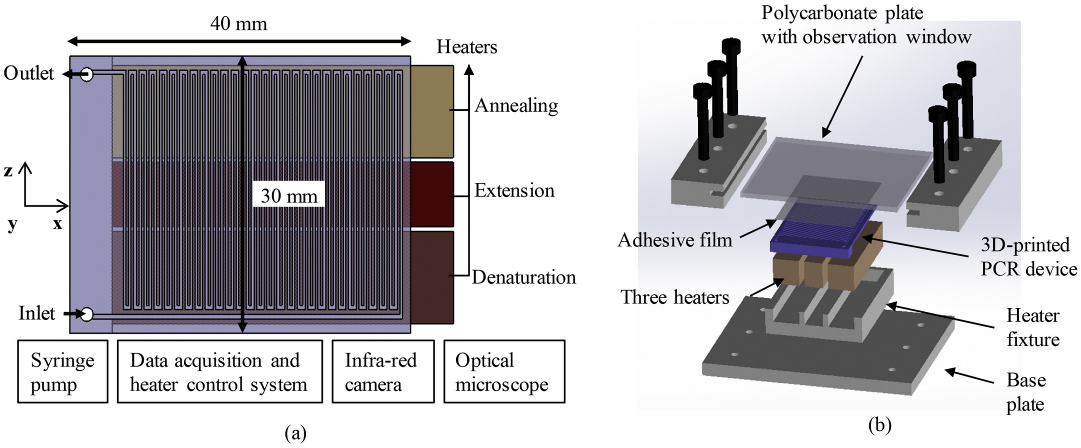

FIGURE 2.6: (a) A 3D printed PCR device with three heaters integrated for controlling the temperatures in the annealing, extension and denaturation zones; (b) An exploded view of the PCR device with the fixture assembly (Figures obtained from Park and Park, 2017).

2.1.5.2 Real-Time PCR

Real-Time PCR (RTPCR) or quantitative PCR (qPCR) is a precise, efficient and fast method for detecting nucleic acids. qPCR is based on traditional PCR technology,

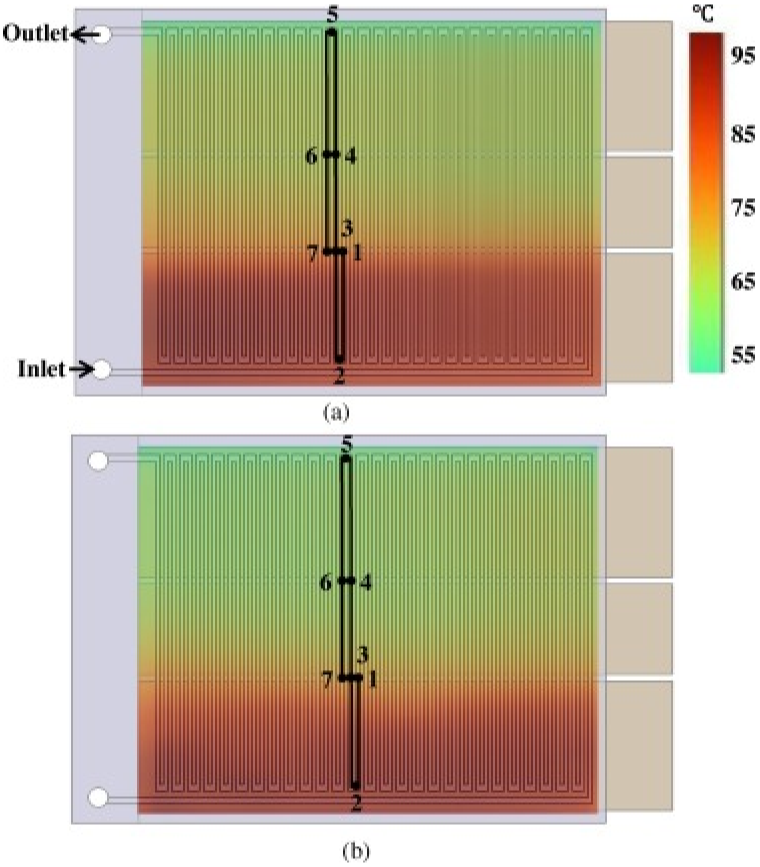

FIGURE 2.7: Thermographic images captured by infra-red camera for 5(a) and 10(b) μL/min (Figure obtained from Park and Park, 2017).

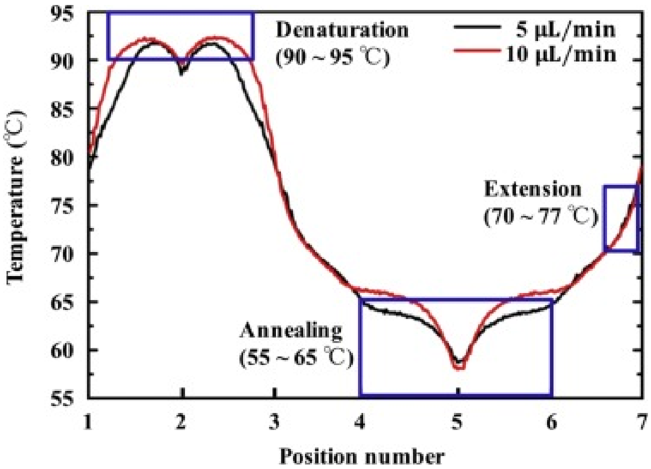

FIGURE 2.8: The measured temperature distributions for the two different flowrates of 5 and 10 μL/min (Figure obtained from Park and Park, 2017).

and it performs nucleic acid amplification and detection at the same time. This technique utilises less sample material than the traditional PCR techniques, and enables the real-time quantification of the product by using fluorescent dyes. More specifically, qPCR allows the continuous collection of fluorescent signals from one or more PCRs over a range of cycles (Heid et al., 1996). According to Dorak (2007), when the

DNA undergoes the log-linear phase of amplification, fluorescence becomes measurable (crossing point, CT) since it increases above the background. A standard curve can be developed, through the use of multiple dilutions of a known amount of standard DNA. This curve presents the log DNA concentration against CT, and can be used to obtain the amount of DNA in an unknown sample when its CT value is known (Dorak, 2007).

qPCR is also used to determine relative quantities of DNA molecules. More specifically, PCR can be performed using unique primers for amplifying specific target regions, while tagging them with different fluorescent dyes. Furthermore, several commercially available quantitative thermal cyclers offer the ability of multiple detections (multiplex) (Dorak, 2007).

Two types of detection chemistry are used for real-time PCR analysis. The first uses an intercalating dye that incorporates into double-stranded DNA. Of these fluorescent dyes, SYBR Green I dye is used most commonly. This detection method is suitable when a single amplicon is being studied, as the dye will intercalate into any double-stranded DNA generated (Dorak, 2007). The second detection method uses a primer or oligonucleotide specific to the target of interest, as in TaqMan probes, Molecular Beacons, or Scorpion primers. The oligonucleotide is labelled with a fluorescent dye and quencher. The oligonucleotide itself has no significant fluorescence, but fluoresces either when annealed to the template (as in Molecular Beacons) or when the dye is clipped from the oligo during extension (as in TaqMan probes). Multiplex PCR is possible by using dyes with different fluorescent emissions for each primer (Dorak, 2007).

2.1.5.3 Digital PCR (dPCR)

The concept behind digital PCR was first described in the work of Sykes et al. (1992). The basic idea behind digital PCR (dPCR) is the following: the sample is diluted and partitioned, so that one (positive) or no (negative) copies remain in each one of the separate reaction chambers that are created. The number of partitions might range from hundreds to millions. By detecting the exact amount of positive partitions, a determination of the number of DNA molecules present in the original sample can be made. Over the years, digital PCR has been used for a number of applications, such as the quantification of cancer genes in patients, the detection of fetal DNA in circulating blood and others (Baker, 2012).

Even though both digital PCR and qPCR utilise the same primers and probes, the former presents higher sensitivity and precision than the latter. More specifically, in most standard cases, qPCR cannot distinguish gene expression differences or small copy number variants. Identifying alleles with frequencies (incidence of a gene variant in a population) of less than about 1% is difficult because such tests would also detect highly abundant common alleles with similar sequences. In contrast, dPCR can measure a 30% or smaller difference in gene expression, distinguish whether a variant occurs in five versus six copies and identify alleles occurring at a frequency of one in thousands. It can also be used to standardize qPCR assays (Baker, 2012).

dPCR has many potential advantages over real-time PCR, including the capability to obtain absolute quantification without external references and robustness to variations in PCR efficiency (Bustin and Nolan, 2004). Recently, technology has become commercially available that permits reactions to be partitioned into nanoliter-sized, aqueous droplets in oil rather than multi-well plates. Rapid microfluidic analysis of thousands of droplets per sample makes droplet-digital (dd) PCR practical for routine use (Hindson et al., 2011; Pinheiro et al., 2012). In addition, the practical dynamic range of the system is substantially improved by using highly uniform droplets, which (with Poisson correction for multiple target molecules per droplet) enable the precise calculation of concentrations even above conditions of limiting dilution (Hindson et al., 2011; Pinheiro et al., 2012).

2.1.5.4 Droplet-based PCR

The droplet-based PCR (DR-PCR) device is a type of PCR device that use small volumes of droplets, where PCR takes place, that act as individual chemical reactors. These droplets offer high reproducible reaction conditions, while their volume is reduced to the size of picolitre or even femptolitre. With this type of technology, scientists are able to perform single-cell and single-molecule analyses (Zhang and Jiang, 2016).

The DR-PCR technology presents several advantages over the SP-CF-PCR devices described earlier:

- the droplets provide an isolated environment, avoiding contamination from the direct contact with the surface of the channels.

  Even though no adsorption of the biological/chemical particles on the surface takes place other phenomena of contamination are still likely to occur (such as during the injection of PCR mixture into the droplets, which can be prevented by using some specific techniques, like pico-injection method, where reagents are added to the droplets in sequential order) (Zhang and Jiang, 2016).

- the synthesis of short, chimeric products can be avoided.

  More specifically, in DR-PCR devices, the template fragments are located in the droplets, which encapsulate the target genes and are immersed in an immiscible oil carrier phase. Since droplets can reach the size of femtoliter, they generally contain small or even any amounts of template DNA molecules, and therefore recombination between homologous or partially homologous gene fragments during PCR process is prevented. As a result, the nucleic acids of from one cell can be successfully amplified inside one single droplet (Zhang and Jiang, 2016).

- multiplex assay can be more conveniently acquired in droplets, which makes the use of DR-PCR microfluidic devices more suitable for such a process.
- the thermal mass and thermal cycles in droplet PCR technologies are reduced compared to the one in SP-CF-PCR devices.
- uniform temperature change in the droplets, due to their very small size (up to femtolitre).
- all droplets are characterised by similar dwell times.

  This fact allows the droplets to be detected and then sorted in chip. Furthermore, the strict order in which the droplets move through the channel results in reproducible chemical and thermal conditions for the droplets, leading to reaction stability and high reproducibility of the method, and hence homogeneous processes and products (Zhang and Jiang, 2016).

Two main technological approaches exist in the DR-PCR microfluidic devices; the (i) digital (d) and the (ii) continuous flow (CF) DR-PCR. In digital DR-PCR devices, the biochemical processes take place in stationary or semi-stationary droplets, while on the other hand, in CF-DR-PCR devices the droplets are in motion (Zhang and Jiang, 2016). In the case of CF-DR-PCR technologies, the precise flow control, the droplet manipulation and the rapid detection appear to be of high technological interest.

As far as the thermocycling technology is concerned in the continuous flow droplet-based PCR devices, there are two main types used: the off-chip and on-chip thermocycling. For the first case, the thermocycling takes place off-chip, which enables the simultaneous processing of a large number of droplets. However, two main concerns exist about this method, the difficulties in automation of the process and the labelling of the individual droplets during and after this off-chip process (Zhang and Jiang, 2016).

Given these two main difficulties that off-chip technology presents, more emphasis will be given to on-chip technologies. Such an example of on-chip PCR technology is the work of Mohr et al., (2006), where a two-temperature CF-DR-PCR polymer chip was constructed, in order to avoid sample contamination and adsorption at the surface. Thirty-two thermal cycles were performed while the generated aqueous droplets of $\sim$51 nL uniform volume were created through a T junction. The droplets were continuously moved by an oil carrier-fluid, introducing the possibility of real-time qPCR. This paper investigated some of the factors affecting droplet-based PCR chip design, such as specific heat capacity, density, flow rate, and thermal resistance. The study focused particularly on the fluid and substrate temperature distribution within the PCR chip and the droplet residence times in critical temperature zones. The results of Mohr et al. (2006) showed that, in general, the carrier-fluid should have a low thermal mass to ensure minimal heating and cooling times. The simulations demonstrated that the flow rate is strongly affected by the carrier-fluid's temperature field. Moreover, the thermal resistance of the different layers was shown to have a major impact on the temperature profile in the channel.

Several more authors have worked on developing DR-PCR devices, as described in detail in the publications of Zhang and Ozdemir (2009) and Zhang and Jiang (2016). Wang et al. (2005) developed a droplet-based micro oscillating-flow PCR chip by using the silicon microfabrication technique. PCR mixture was injected in a single droplet in a straight channel that oscillated between the three different temperature zones created for denaturation, extension and annealing stages, performing a PCR cycle. After numerically studying the thermal performance of the chip, the time required for such a droplet's temperature to reach the target one was found to be below than 1 s. Wang et al. (2005) then injected a 1 μl droplet containing PCR mixture into the micro oscillating-flow PCR chip, and managed to amplify the HPV-DNA in 15 min. Brouzes et al. (2009) developed a droplet-based microfluidic technology that enables high-throughput screening of single mammalian cells. Their device used aqueous microdroplets (1 pL to 10 nL volumes) dispersed in an immiscible carrier oil, containing single cells and reagents. They performed a droplet-based cytotoxicity screen, by screening a drug library for its cytotoxic effect against U937 cells.

2.2 Heat Sinks & microchannels

This Chapter consists of a literature review on experimental and computational studies related to phenomena taking place on the microscale and in heat sinks; a type of heat exchangers that are used to dissipate the heat generated by electronic devices, heat engines, and refrigeration to gas, liquid or ambient air (Kumar et al., 2018). Some of the same phenomena can also be found in the PCR microfluidic devices described in Chapter 2.1.5, since both of CHT and fluid flow take place.

The idea of liquid-cooled heat sinks was first introduced by Tuckerman and Pease (1981), as a means to obtain better heat rejection by lowering the area-to-volume ratio of a thermal device. According to Mohammed Adham, Mohd-Ghazali, and Ahmad (2013), most studies on microchannel heat sinks before 2000 use mainly experimental or analytical approaches, while the ones after 2000 utilise numerical simulations and evolutionary algorithms. Furthermore, laminar flow conditions appear to be mostly studied.

The more heat sinks develop towards miniaturisation and integration in electronic equipment, the difficulty to handle high heat fluxes increases, since they are often characterised by non-uniform temperature distributions, that can cause the reduction of the life span and reliability of electronic devices (He, Yan, and Zhang, 2021). Temperature control and distribution have been studied a lot in literature for this type of CHT problems (Kim, 2004; Ahmed et al., 2018; He, Yan, and Zhang, 2020; Hajmohammadi, Alipour, and Parsa, 2018), including topology optimisation cases

(Yan et al., 2019; Dede, Joshi, and Zhou, 2015; Joo, Lee, and Kim, 2017; Haertel et al., 2015; Li et al., 2019; Srinivas and Ananthasuresh, 2006).

A metal device composed of a series of fins is an example of a simple heat sink device in microscale. Many studies have focused on improving the heat transfer rate of such types of heat sinks, enhancing the thermal conductivity of fins, the heat transfer coefficient, or the surface area of fins (Kumar et al., 2018). Li and Chao (2009) and Li et al. (2010) investigated experimentally the effect that the height, thickness and number of fins can have on the thermal resistance of a plate-fin heat sink, demonstrating that by increasing the fin height (and hence the heat transfer area) the thermal resistance is reduced. Yang et al. (2010) studied the effect that the location of triangular vortex generators have on the thermal resistance and pressure drop on a plain-fin heat sink. Others studied the improvement that can be achieved in heat transfer, when flow disruption, channel curvature, secondary flow, surface treatment and surface roughness phenomena are present/implemented (Steinke and Kandlikar, 2004; Tullius, Vajtai, and Bayazitoglu, 2011). Abouali and Baghernezhad (2010) performed a numerical investigation on the effects that arc grooves and rectangular microchannel heat sink geometries may have on heat transfer and pressure drop for a single-phase flow and laminar flow. Their results indicate that using grooved surfaces increases the heat removal rate from the microchannel. When compared to the rectangular grooves, the arc grooves appear to offer higher heat removal flux but lower coefficient of performance, when grooves are made on the floor and side walls. Abouali and Baghernezhad (2010) also demonstrated that by using a grooved microchannel with higher wall thickness and lower mass flow rate of cooling water, greater heat removal rate and coefficient of performance can be achieved, compared to a microchannel with the minimum wall thickness.

Further publications concerning the effect that different types of nanofluids and geometries of microfluidic channels have on the heat transfer rate and coefficient can be found in the work of Kumar et al. (2018). According to Alkasmoul et al. (2018), when comparing the results obtained related to the actual heat transfer coefficient or tube temperature versus flow rate or pressure drop, the presence of nanoparticles in the water appears to deteriorate heat transfer for the nanofluids considered.

As mentioned earlier in this chapter, a strong correlation appears between microscale heat sinks and PCR microfluidic systems, considering that both require the understanding and study of CHT and fluid flow in microchannels. As a result, considering the similarities in the phenomena that take place, studying the physics and optimisation of heat sink technology can lead to a better understanding of the techniques and design of the PCR microfluidic devices.

2.2.1 Significant phenomena in microscale

The study of heat transfer phenomena in large channels has been extensive over the years, combining both experimental and computational work. In a large scale, several assumptions are usually made: i) steady fully developed flow field, ii) independence of the fluid thermophysical properties with the temperature, iii) consideration of the fluid as a continuum medium, iv) incompressible flow, v) simplification of the boundary conditions, vi) negligible heating due to viscous dissipation, vii) negligible surface roughness (Rosa, Karayiannis, and Collins, 2009). These assumptions, depending on the phase of the fluid, are often not valid when it comes to describing microfluidic channels (hydraulic diameter, D_h, ranging from 1 μm to 1mm (Celata et al., 2004)) (Rosa, Karayiannis, and Collins, 2009).

Rosa, Karayiannis, and Collins (2009) investigated the importance of scaling effects in microscale. More specifically, according to Rosa, Karayiannis, and Collins (2009), the entrance effects and the dependence of the fluid properties on the temperature are expected to become significant when it comes to microscale. When gases are considered: i) the fluid might not be best described as a continuum and ii) the pressure drop can often be quite large, leading to compressibility effects. Furthermore, heat conduction in the fluid and walls may play an important role in heat transfer in microchannels, contrary to large-scale flows. As a result, CHT needs to be taken into account (Rosa, Karayiannis, and Collins, 2009). Also, due to the increased surface-to-volume ratio in microchannels, phenomena taking place between the fluid and the wall need to also be examined (viscous heating and surface roughness). In addition, for liquid aqueous flows, the electric double layer (EDL) effects might also become important, because of the interaction between the electrostatic charges on the wall and the ions in the fluid. As a result, when it comes to heat transfer, effects that are usually neglected in macro-scale (scaling effects), become significant in micro-scale.

Similarly, Herwig and Hausner (2003) examined the significance of the various phenomena at different scales. For devices/geometries with a characteristic dimension greater than 5 μm, Navier-Stokes Equations can be used to describe Newtonian fluids for both micro- (characteristic dimensions of less than 1 mm) and macro-scale. Furthermore, they pointed out that several problems are often described in their nondimensional form, where the physical dimensions are removed from the equations. However, some phenomena can be of different significance in micro- compared to macro-systems. For microscale flows, the following effects were pointed as important: a) axial heat conduction (small Peclet numbers), b) conjugate heat transfer, c) temperature and pressure-dependent properties (large axial temperature and pressure gradients respectively), and d) wall roughness (specific wall roughness distribution).

When it comes to viscous dissipation in microscale and in particular in microconduits, Koo and Kleinstreuer (2004) demonstrated that it depends on the hydraulic diameter, the geometrical features of the microchannels, the Reynolds, Re, and Prandtl, Pr, dimensionless numbers. The Reynolds and Prandtl dimensionless numbers are presented in Equations 2.2 and 2.3 respectively:

$$Re = Lu\rho/\mu \tag{2.2}$$

$$Pr = C_p\mu/k \tag{2.3}$$

,where ρ: the density of the fluid, u: the flow velocity, L: a characteristic linear dimension, μ: the dynamic viscosity of the fluid, C_p: the specific heat and k: the thermal conductivity of the solid.

Xu et al. (2002) concluded that its effect becomes important because of the higher velocity gradients in microchannels with smaller hydraulic diameters, for constant Reynolds number. Furthermore, they presented a criterion of the significance of the viscous dissipation for water flow in microtubes with an adiabatic thermal boundary condition (Equation 2.4):

$$Vi \cdot Pr^{-0.1} = \begin{cases} \leq 0.056, & \text{no viscous dissipation effects.} \\ \geq 0.056, & \text{viscous dissipation effects.} \end{cases} \tag{2.4}$$

,where Vi: the viscous number that it measures the viscous dissipation energy relative to fluid energy rise and Pr: Prandtl number (Xu et al., 2002).

2.2.2 Thermal Resistance & Optimisation Problems

A lot of work in heat sink technology has focused on the reduction of the thermal resistance, R_{th}. R_{th} describes the temperature difference (ΔT) by which a material resists a heat flow, q (Mishra, Militky, and Venkataraman, 2019). R_{th} depends on thermal conductivity ($k, W/mK$) and thickness (L, m) of the material, and is given by Equation 2.5).

$$R_{th} = \frac{\Delta T}{q} = \frac{L}{k} \tag{2.5}$$

Fisher and Torrance (2001) studied the effects of wall thickness, channel width and shape of the channel boundary on the overall R_{th}. Their results showed that increasing the boundary curvature could reduce the optimal distance between the channels. Furthermore, they concluded that elliptical or nearly elliptical shapes generated an equivalent optimal thermal performance compared to rounded rectangular shapes. Curved boundary shapes were found to decrease the optimal fin thickness in comparison to rectangular channel shapes, allowing a bigger number of channels to fit in the same substrate volume. That was achieved with only a 5 %

increase in the total thermal resistance value, as the boundary shape changed from a rounded rectangle to an ellipse (Fisher and Torrance, 2001).

Knight, Goodling, and Hall (1991) completed an analytical study on developing an optimal thermal design of forced heat convection in a heat sink, so that thermal resistance is minimised. The equations for calculating the thermal resistance for laminar flow for the cases of constant temperature and constant heat flux thermal boundary conditions were derived (Equations 2.6 and 2.7 respectively). They considered that the true thermal boundary condition lies somewhere in between the two. The minimum values of thermal resistance obtained from Equations 2.6 and 2.7 were given by Equations 2.8 and 2.9 respectively. The two models generated values of minimum thermal resistance that differed only by 6 %, and therefore the choice of the model (constant temperature or constant flux) appeared not to affect the results significantly. As a result, Equation 2.12 was considered to give the value of the optimum number of channels required to achieve the minimum value of thermal resistance, Θ_{lam}.

$$\Theta_{lam} = \frac{12n^2}{N_{\Delta p}Pr(D/W)}[1 - exp(-12St_{lam}n^4)]^{-1} \tag{2.6}$$

$$\Theta_{lam} = \frac{12n^2}{N_{\Delta p}Pr(D/W)}[1 + 1/(12St_{lam}n^4)]^{-1} \tag{2.7}$$

$$12St_{lam}n^4 = 1.256 \tag{2.8}$$

$$12St_{lam}n^4 = 1.000 \tag{2.9}$$

$$St_{lam} = \frac{Nu}{N_{\Delta p}Pr}\frac{L}{W} \tag{2.10}$$

$$N_{\Delta p} = \frac{(\Delta p/L)W^3}{\rho v^2} \tag{2.11}$$

$$n = (12St_{lam})^{-1/4} \tag{2.12}$$

,where Θ: dimensionless thermal resistance, St: Stanton number (Equation 2.10),

$N_{\Delta p}$: pressure difference number (Equation 2.11), Δp: pressure drop, n: number of channels, Pr: Prandtl number, ρ: density, ν: kinematic viscosity, W: width of heat sink and L: length of heat sink in the direction of fluid flow.

Similarly for turbulent flow, Equations 2.13 and 2.14 produced the values of thermal resistance for the thermal boundary conditions of constant temperature and constant flux respectively. The minimum values of thermal resistance obtained from Equations 2.13 and 2.14 are given by Equations 2.15 and 2.16 respectively.

$$\Theta_{turb} = \frac{0.21n^{5/7}}{{N_{\Delta p}}^{4/7} Pr(D/W)}[1 - exp(-0.045St_{turb}n^{10/7})]^{-1} \tag{2.13}$$

$$\Theta_{turb} = \frac{0.21n^{5/7}}{{N_{\Delta p}}^{4/7} Pr(D/W)}[1 + 1/(0.045St_{turb}n^{10/7})] \tag{2.14}$$

$$0.045St_{lam}n^{10/7} = 1.256 \tag{2.15}$$

$$0.045St_{lam}n^{10/7} = 1.000 \tag{2.16}$$

The results of this work were then compared with the work of Goldberg (1984), where selecting a ratio of fin/channel dimensions different than 1 lead to a reduction of the thermal resistance for the case of an air-cooled narrow channel heat sink. Another comparison was made with the work of Tuckerman and Pease (1981), who studied the laminar flow of water (coolant) in a setup of narrow channels. When turbulent flow was studied by Knight, Goodling, and Hall (1991), thermal resistance's value was reduced by 34 % from the one Tuckerman and Pease's design predicted (for laminar flow). Knight et al. (1992) found that for small values of pressure drop through the channels, thermal resistance appears to be lower for laminar flow compared to turbulent. For large values of pressure drop, thermal resistance was lower for turbulent flows.

Wei and Joshi (2003) developed a thermal resistance network model that predicted the overall thermal performance of a stacked microchannel heat sink (Figure 2.9). An optimisation problem was then solved with the use of Genetic Algorithm, with the overall thermal resistance selected as the objective function and the aspect ratio, fin thickness and the ratio of channel width to fin thickness as the design variables of the problem. The results of this work indicated that thermal resistance can be reduced by optimising the channel configuration, while the effects of the number of layers in the stack, pumping power per unit area, and the channel length were also investigated.

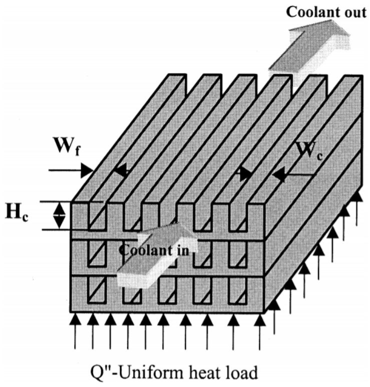

FIGURE 2.9: Three-dimensional stack of micro-channels (Figure obtained by Wei and Joshi, 2003)

Husain and Kim (2007) performed a numerical optimisation study on a rectangular microchannel geometry, for laminar flow, using the surrogate method. The design variables selected were the ratios of micro-channel width to depth (θ) and the width of the fin to the depth (ϕ), with their values varying as follows: $\theta \in [0.10, 0.25]$ and $\phi \in [0.04, 0.10]$. A four-level Full Factorial Design was used in order to generate the DoE Points. Thermal resistance was selected as the objective function, while Kriging was used to construct the surrogate surface. The optimum solution was found by sequencing quadratic programming. Their results were validated with the experimental work of Kawano et al. (1998).

An extension of their work to a multi-objective optimisation problem was published by Husain and Kim (2008). Figure 2.10 presents the computational domain and the schematic graph of the heat sink simulated. The design variables selected (θ and ϕ) were defined in the same way as in the work of Husain and Kim (2007). The overall thermal resistance, R_{th} (Equation 2.17), and the pumping power required for the fluid to pass through the microchannel, P (Equation 2.18), were selected as the two objective functions of the problem. Due to the high number of objective functions' evaluations required for the evolutionary algorithm, a surrogate was constructed to reduce the computational expense. The Response Surface Approximation (RSA) was used to evaluate the objective function values, by fitting a second-order polynomial function (Equation 2.19). The forms of the two objective functions obtained by RSA are presented in Equations 2.20 and 2.21.

$$R_{th} = \frac{\Delta T_{max}}{q A_s} \tag{2.17}$$

$$\overline{\mathrm{P}} = Q \cdot \Delta p \tag{2.18}$$

$$y(x) = \beta_o + \sum_{j=1}^{N} \beta_j x_j + \sum_{j=1}^{N} \beta_{jj} {x_j}^2 + \sum \sum_{i \neq j}^{N} \beta_{jj} x_i x_j \tag{2.19}$$

$$R_{th} = 0.0964 + 0.31240\theta - 0.7005\phi - 1.1122\theta\phi + 0.6044\theta^2 + 4.8528\phi^2 \tag{2.20}$$

$$\overline{\mathrm{P}} = 0.9925 - 9.39555\theta + 3.5575\phi - 14.9250\theta\phi + 22.90240^2 - 0.0706\phi^2 \tag{2.21}$$

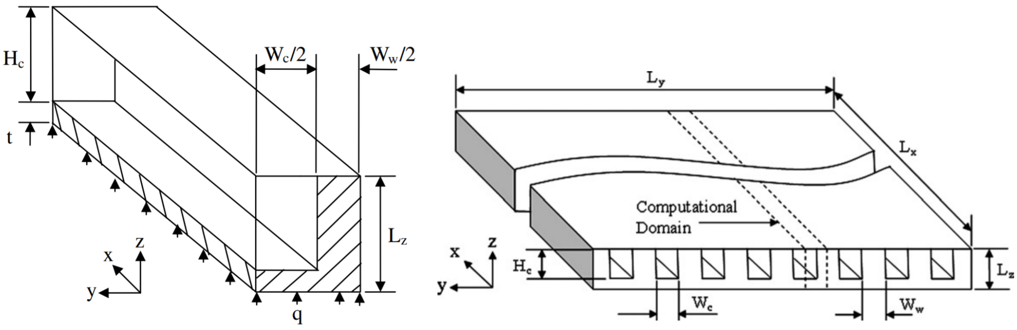

(A) (B)

FIGURE 2.10: (a) Computational domain and (b) schematic graph of microchannel heat sink (Figures obtained by Husain and Kim, 2008)

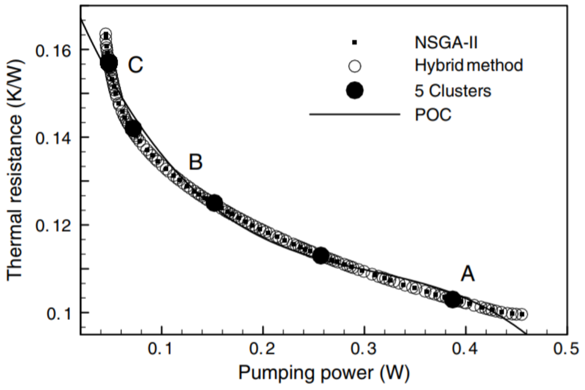

FIGURE 2.11: Pareto optimal solutions using NSGA-II, hybrid multi-objective evolutionary approach, five clusters, and global Pareto optimal curve (POC) (Figure obtained by Husain and Kim, 2008)

Husain and Kim (2008) generated the approximate Pareto optimal solutions using real coded NSGA-II, as part of a Hybrid Multi-objective Evolutionary Approach (HMEA). Pareto optimal solutions are generally used where several conflicting objectives need to be considered during an optimisation process, and it permits more than one objectives to be optimised at the same time (Brisset and Gillon, 2015). These solutions were then refined with the search of local optimal solutions for the two objective functions, using sequential quadratic programming (SQP), while the NSGA-II solutions were used as initial guesses. K-mean clustering was then performed to find a representative solution for a group of solutions. Five representative clusters were created and three of them were reproduced numerically. Figure 2.11 presents the Pareto Optimal solutions using NSGA-II, HMEA, five clusters and Global Pareto Optimal curve (POC) (Husain and Kim, 2008).

A further extension of the previous work to a 3-design variable optimisation problem was performed by Husain and Kim (2008), who used surrogate analysis and the evolutionary algorithm to solve a multiobjective optimisation problem in a heat sink. The three design variables selected were related to the microchannel width bottom and top (W_b and W_c respectively), depth (H_c) and fin width (W_w); θ ($= \frac{W_c}{H_c}$), ϕ ($= \frac{W_w}{H_c}$) and η ($= \frac{W_b}{W_c}$) (Figure 2.12). The DoE points were generated through a three-level full factorial design, with the design space as follows: $\theta \in [0.1, 0.25]$, $\phi \in [0.02, 0.1]$ and $\eta \in [0.5, 1.0]$. The two objective functions selected were the thermal resistance (Equation 2.17) and the pumping power required to drive the fluid through the microchannel (Equation 2.18). Global Pareto optimal solutions were obtained using NSGA-II in combination with a local search strategy, and the same process was repeated as presented in the work of Husain and Kim (2008). K-mean clustering was also performed; seven representative clusters were created and three of them were reproduced numerically. The results are presented in Figure 2.13.

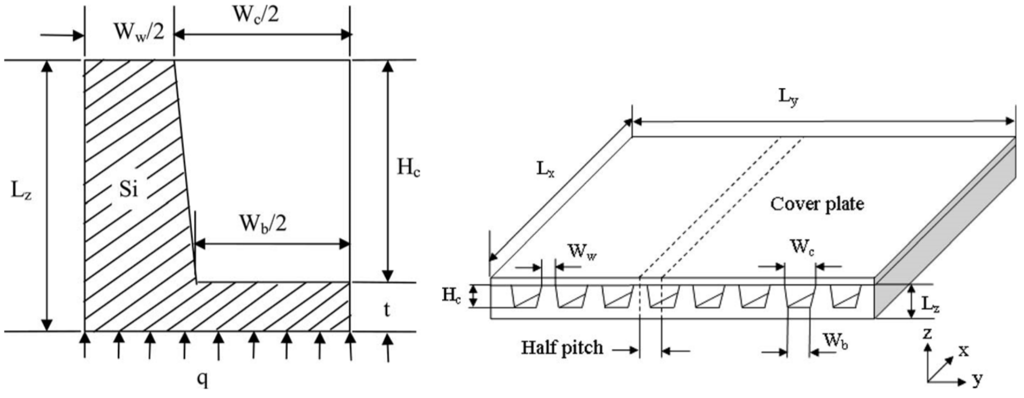

(A) (B)

FIGURE 2.12: (a) Computational domain and (b) schematic graph of microchannel heat sink (Husain and Kim, 2008)

Another study performed by the same authors (Husain and Kim, 2008) focused on a shape optimisation problem of a heat sink design. The same design variables as before, θ and ϕ, were selected and three different surrogate methods were studied. Thermal resistance was used as the single objective function of the problem, while the pumping power was used as a constraint. The DoE points were created by adjusting the mass flowrate while keeping the pumping power constant. The

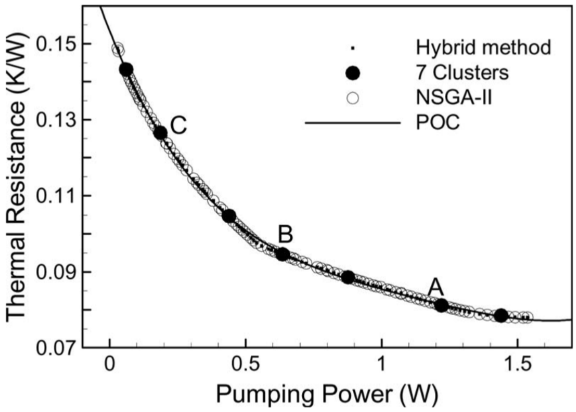

FIGURE 2.13: Pareto optimal solutions using hybrid multiobjective evolutionary approach, NSGA-II, seven clusters, and global Pareto Optimal Curve (POC) (Husain and Kim, 2008)

surrogates were formed by the RSA, Kriging (KRG), and Radial Basis Neural Network (RBNN) methods, while the optimum design was obtained using sequential quadratic programming.

The three surrogate models were found to predict very similar optimum values for different design variables. When CFD simulations were performed, the calculated optimum values of thermal resistance were found to be very similar to the ones predicted by the three surrogate models. A sensitivity analysis of the objective function was also performed by varying the design variables around the values of ϕ and θ at the optimum points.

A later publication of the same authors (Husain and Kim, 2010) was built upon two of their previous works; the multiobjective optimisation study (Husain and Kim, 2008) and the three surrogate models single optimisation study (Husain and Kim, 2008) of a heat sink. The design variables were the same as the ones selected in the work of (Husain and Kim, 2008); θ $(= \frac{W_c}{H_c})$, ϕ $(= \frac{W_w}{H_c})$ and η $(= \frac{W_b}{W_c})$. The DoE points were generated through a three-level Full Factorial Design, with the design space as follows: $\theta \in [0.10, 0.25]$, $\phi \in [0.02, 0.10]$ and $\eta \in [0.50, 1.00]$. In order to reduce the computational cost, multiple surrogates (RSA, KRG and RBNN) were used to evaluate the objective function values required at a number of locations by hybrid Multi-objective Evolutionary Algorithm. The two objective functions selected were similar to the ones described in the work of Husain and Kim (2008); the thermal resistance and the required pumping power. K-means clustering was applied as described previously, so that representative solutions from the Pareto optimal front to be generated. Figure 2.14 presents the global Pareto optimal solutions obtained using RSA, KRG and RBNN surrogate models, including the numerical data calculated.

When comparing the different surrogate models, the KRG model's predictions were found to be in better agreement with the numerical data. RSA and RBNN models were found to underpredict the values of the two objective functions at the

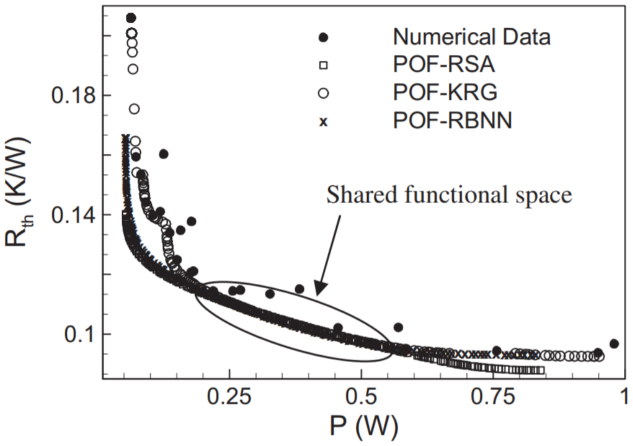

FIGURE 2.14: Pareto-optimal solutions using the RSA, KRG and RBNN surrogate models (Figure obtained from Husain and Kim, 2010)

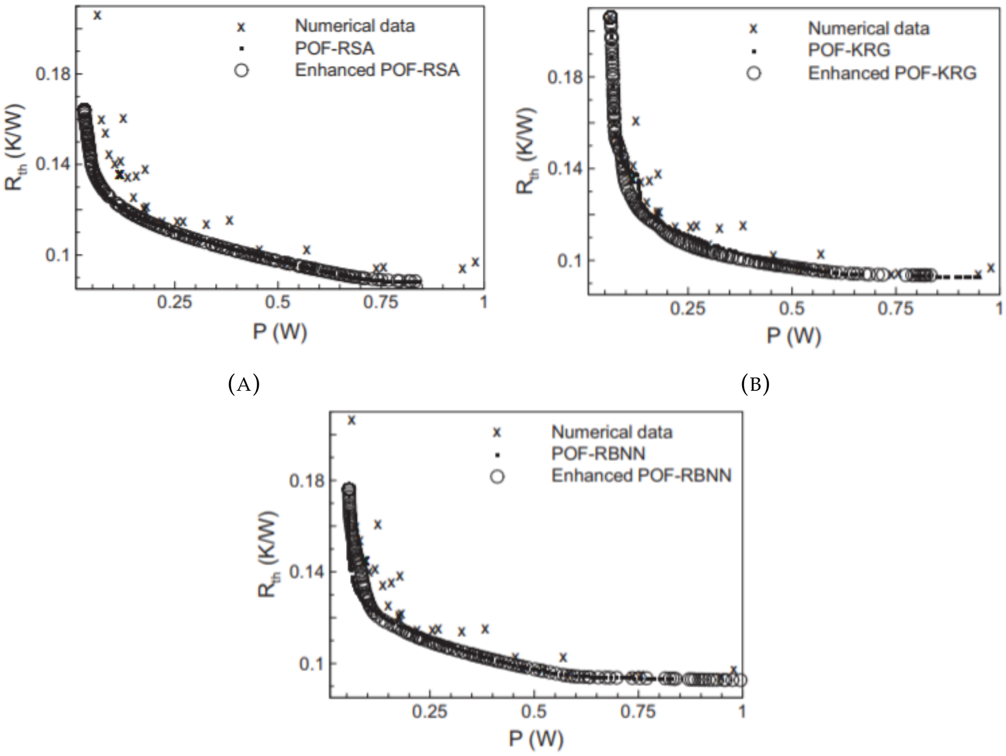

(A)

(B)

(C)

FIGURE 2.15: Enhanced Pareto-optimal fronts using: (a) RSA, (b) KRG and (c) RBNN (Figures obtained from Husain and Kim, 2010)

"end" solutions of their Pareto fronts. In order to increase the performance of the surrogate models, the respective numerically derived solutions for the representative solutions of the Pareto optimal front were added to the initial DoE points. The surrogate models were then recreated for the increased number of DoE points and a new Pareto-optimal front was obtained for each surrogate model (Figure 2.15).

2.2.3 Experimental work

As far as the experimental work is concerned, several reviews have been published during the last two decades on heat transfer in microchannels. More specifically, Palm (2001), Palm and Peng (2004), Obot (2002), Hetsroni et al. (2005) and Morini (2004) are some examples of such work published in the area of single-phase liquid heat transfer in microchannels (Celata et al. (2006)).

In the work of Palm (2001), channels with hydraulic diameters less than 1 mm were considered for single-phase flow experiments. For two-phase flow, a larger diameter range was considered. Equations for predicting the values of the Nusselt numbers for single-phase flow are presented for laminar and turbulent flows in Equations 2.22 and 2.23 respectively.

$$Nu_{lam} = 0.1165 \cdot (\frac{D_h}{W_c})^{0.81} \cdot (\frac{H}{W})^{-0.79} \cdot Re^{0.62} \cdot Pr^{1/3} \tag{2.22}$$

$$Nu_{turb} = 0.00222 \cdot Re^{1.09} \cdot Pr^{0.4} \tag{2.23}$$

,where Nu: Nusselt number, Pr: Prandtl number, W: width of heat sink, Re: Reynolds Number, W_c the centre to centre distance between channels, D_h the hydraulic diameter of the rectangular microchannel and H the channel's height. The dimensionless numbers Nu, Pr and Re numbers describe the ratios of convective to conductive heat transfer at a boundary in a fluid, momentum diffusivity to thermal diffusivity and inertial forces to viscous forces within a fluid respectively.

According to Palm (2001), some authors concluded that the transition from laminar to transitional and turbulent flow in microchannels begins at smaller Reynolds numbers than expected for larger hydraulic diameters. As far as the friction coefficients are concerned, they were found to depend on the Reynolds number and their experimental values to deviate from the classical-laminar-theory predicted ones by ± 30 %. For the cases of turbulent flow, higher values of Nusselt numbers were calculated compared to the ones theoretically predicted, while both higher and lower values were reported for the laminar flow cases. The surface roughness effects, entrance effects, electric double-layer effects, non-constant fluid properties, two- and three-dimensional transport effects and slip flow (for gases) were mentioned as possible reasons behind the deviations reported.

As far as the work of Obot (2002) is concerned, their review focused on the microchannel transport phenomena present in microchannel flows. More specifically, they concluded that for smooth microchannels, the transition from the laminar to the turbulent regime starts for Re > 1000. Moreover, the Nusselt number was found to be proportional to the square root of the Reynolds number ($Nu \propto Re^{1/2}$) for laminar flows.

The review of Hetsroni et al. (2005) focused on small Knudsen numbers, and heat transfer was studied for circular, triangular, rectangular, and trapezoidal microchannel cross-sections, with hydraulic diameters of 60 -2000 μm. They compared the various experimental data published by several investigators to the conventional theory of heat transfer. According to their results, axial conduction and wall effects were found to be important for heat transfer in microchannels. Two heat transfer regimes were defined for laminar flow; the first one for $Re > 150$ and $M < 0.01$ and the second one for $Re < 150$ and $M > 0.01$, where M is the conductive to convective heat flux ratio ($M = \frac{|F_{cond}|}{|F_{conv}|}$). In this first regime, heat transferred through the solid substrate can be neglected while in the second one it should be taken into account. Another important conclusion they made about the evaluation of the experimental results in general was about the possibility of predicting wrong values of Nusselt numbers when temperature measurements are taken only at the inlet and outlet of the fluid (Hetsroni et al., 2005).

Bucci et al. (2003) reported the results of an experimental review of water flow and heat transfer in stainless steel capillary tubes. They examined three different diameters; 172 μm, 290 μm and 520 μm for Re $\in[200, 6000]$. The results of their work showed that in the laminar regime, the friction factor was predicted well by the Hagen-Poiseuille theory for Re $\in[800, 1000]$. The critical transition from laminar to turbulent flow regime took place at Re $\in[1800, 3000]$, and for higher Re values, Hagen-Poiseuille law should not be used. From the heat transfer experiments studied, the values of the heat transfer coefficient were higher than the theoretical ones. In the turbulent regime, the experimental results were not found to differ significantly from the theoretical ones.

An investigation of the thermal behaviour in a capillary tube with an internal diameter of 0.130 mm was carried out by Celata et al. (2002). Reynolds number of 100 to 8,000 were achieved, and the transition from laminar to turbulent regime was monitored. According to their experiments, the transition from laminar to turbulent flow took place for Reynolds numbers: Re $\in[1, 880, 2, 480]$. When comparing conventional tubes to microtubes, the heat transfer correlations developed for the first ones were found not to be able to describe accurately the heat transfer coefficients in microchannels.

Lelea, Nishio, and Takano (2004) performed a combined experimental and numerical work in the same area. Microchannels of 0.1, 0.3 and 0.5 mm diameter were used, while the maximum Reynolds number achieved was 800. Distilled Water was used for the experiments, while the tubes were made of stainless steel. The experimental measurements were compared with theoretically predicted values and numerical results. For the microchannels with the diameter sizes mentioned earlier, the experimental results appeared to be in agreement with the classical theories.

In their experimental work, Celata et al. (2006) validated the single-phase heat transfer scaling effects that are important in microscale laminar flow. Four circular channels of different inner diameters were examined; 528 μm, 325 μm, 259 μm and

120 μm. Their results showed that i) for smaller diameters, the Nu decreases, ii) the Nu depends on the axial position and is related to the thermal entrance effects and iii) the dependence of Nu on Re.

Morini (2004) performed a detailed review for convective heat transfer in microchannels, with their main experimental results focusing on the friction factor, laminar-to-turbulent transition and Nusselt number in channels with hydraulic diameter less than 1 mm. The data obtained from the experiments in microchannels related to the friction factor and Nu were found to be inconsistent with the theoretical ones but also disagree with one another. In order to account for this deviation, Morini (2004) suggested a number of possible explanations; compressibility effects, viscous dissipation effects, electro-osmotic effects (EDL), property variation effects, channel surface conditions and experimental uncertainties.

2.3 Heat transfer modes

There are three main ways that heat can be transferred; radiation, convection and conduction (Bejan and Kraus,2003). The basic principles of radiation, heat convection, conduction and conjugate heat transfer are described in the following sections, while all of these heat transfer modes can be considered relevant (each one at a different extent) in microfluidic systems.

2.3.1 Heat transfer through radiation

Thermal radiation is emitted by all matter when it is at non-zero temperature. Depending on the temperature of the material, the transmitted radiation ranges from ultraviolet to far-field infrared (wavelength range from 0.1 μm to 100 μm). Contrary to other heat transfer modes, the transfer of energy by radiation does not require the presence of a material medium (Zhang et al., 2019; Balayssac and Garnier, 2017; Meseguer, Pérez-Grande, and Sanz-Andrés, 2012). On the macroscopic level, the calculation of thermal radiation is based on the Stefan-Boltzmann law, which relates the energy flux emitted by an ideal radiator (or black body) to the fourth power of the absolute temperature (Equation 2.24):

$$e = \epsilon \sigma T^4 \tag{2.24}$$

,where ϵ is the surface emissivity and σ Stefan–Boltzmann constant and T is the temperature.

2.3.2 Heat transfer through convection

Convection describes the transfer of heat from an object/surface to a fluid in motion (Sheng, 2013). There are two main types of convection heat transfer; the *forced convection* and *natural convection*. In forced convection, the fluid motion is usually created by a pump, blower, a fan etc., while in natural convection, the motion is created as a result of the density difference that is itself generated by the temperature difference (Agrawal and Tiwari, 2010).

When heat convection takes place, both heat transfer and fluid flow happen simultaneously. As a result, due to the interaction of the two fields, the equations of motion and energy conservation are combined (Bejan and Kraus, 2003). For example, the contribution of the fluid motion can be observed in the energy conservation equation for ideal gases given by Equation 2.25 (COMSOL, 2018):

$$\rho C_p \frac{\partial T}{\partial t} + \rho C_p \mathbf{u} \cdot \nabla T = \nabla \cdot (k \nabla T) + (\frac{\partial p}{\partial t} + \mathbf{u} \cdot \nabla p) + \tau\mathbf{:}\nabla \mathbf{u} + Q \tag{2.25}$$

,in the i) convective term responsible for transporting the heat through the fluid motion, ii) the term used to describe the viscous effects responsible for fluid heating (this term might be neglected in a number of cases, but becomes important for viscous fluids and high velocities), and the iii) pressure-dependent term that accounts for the heat produced when fluid is compressed, for the cases of fluids with temperature-dependent densities (Bejan and Kraus, 2003). In Equation 2.25, the term k is the thermal conductivity ($W/m/K$), ρ the density (kg/m^3), Q the heat source (W/m^3) and C_p the heat capacity at constant pressure ($J/kg/K$), p is the pressure (Pa), $\mathbf{u}$ the velocity flow field (m/s), and τ the viscous stress tensor (N/m^2).

In convective heat transfer, the (convective) heat transfer coefficient, h, is introduced, defined by Equation 2.26, which is known as *Newton's law* of cooling:

$$\mathbf{q}'' = h(T_w - T_f) \tag{2.26}$$

$$R_{th} = 1/hA \tag{2.27}$$

,where T_w and T_f are the temperatures at the surface/wall and the fluid respectively (D'Auria, 2017).

The thermal resistance, R_{th}, is given by Equation 2.27, and it expresses the resistance at a surface-to-fluid interface (Bejan and Kraus, 2003). At the wall, heat transfer is considered to take place by conduction, and therefore by $Fourier'sLaw$, at y=0 (where y: normal to the flow direction) we obtain Equation 2.28. From equations 2.26 and 2.28, we obtain Equation 2.29:

$$\mathbf{q}''|_{y=0} = -k \frac{\partial T}{\partial y}|_{y=0} \tag{2.28}$$

$$h = \frac{\mathbf{q''}|_{y=0}}{T_w - T_f} = -\frac{k\frac{\partial T}{\partial y}|_{y=0}}{T_w - T_f} \tag{2.29}$$

According to Prandtl, viscosity's effect is significant to a very thin region very close to the body, while the rest of the flow field can be considered as inviscid. This thin region is known as the *boundary layer*. The viscous forces within the boundary layer region, δ, are described in terms of the shear stress, τ, between the fluid layers. This stress is proportional to the normal velocity gradient, and is defined by Equation 2.30 (Bejan and Kraus, 2003).

$$\tau = \mu\frac{\partial u}{\partial y} \tag{2.30}$$

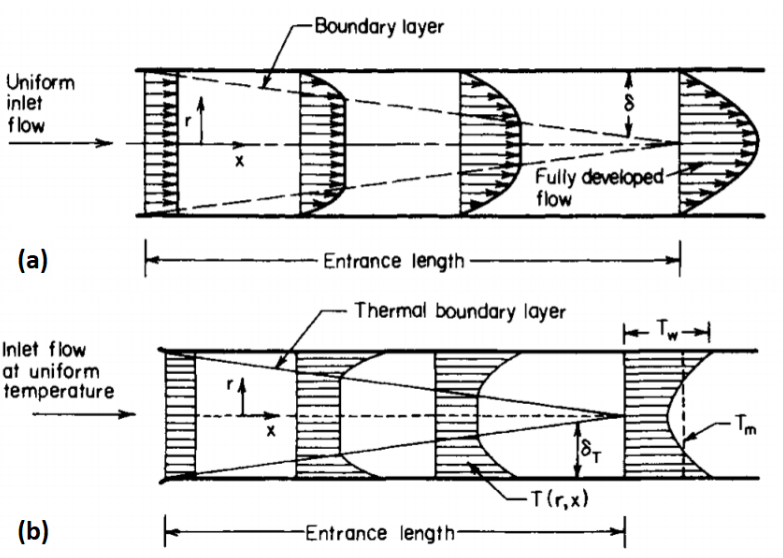

FIGURE 2.16: (a) Velocity profile for laminar flow in a tube and (b) development of temperature profile in the entrance region of a tube (Figures obtained from Bejan and Kraus, 2003).

When heat transfer takes place between the fluid and the solid surface, the thermal (δ_T) boundary layer is observed. The effect of thermal conductivity is confined within this region, while outside the boundary layer region the flow is essentially non-conducting. The thermal boundary layer can be seen in Figure 2.16 (b) (Bejan and Kraus, 2003).

The dimensionless Nusselt number (Equation 2.31), Nu, is often used to measure heat convection:

$$Nu = hL/k \tag{2.31}$$

,where h, L and k are the convective heat transfer coefficient, characteristic length and thermal conductivity of the fluid respectively (Faghri, Zhang, and Howell,2010).

2.3.3 Heat transfer by conduction

Conduction describes the heat transfer due to a temperature gradient, and it takes place at the molecular level, involving the energy transfer from the more energetic molecules to those with a lower energy level (Eckert and Drake Jr, 1987). Thermal conductivity (k) can be considered as a measure of the heat conduction that takes place. The conductive heat flux ($q\prime\prime$) is expressed by *Fourier's Law*, as presented in Equation 2.32 (Bejan and Kraus, 2003). For time-dependent heat transfer, the heat equation takes the form presented in Equation 2.33:

$$\mathbf{q}\prime\prime = -k\nabla T \tag{2.32}$$

$$\rho C_p \frac{\partial T}{\partial t} = \nabla \cdot (k\nabla T) + Q \tag{2.33}$$

,where k is the thermal conductivity ($W/m/K$), ρ the density (kg/m^3), Q the heat source (W/m^3) and C_p the heat capacity at constant pressure ($J/kg/K$).

2.3.4 Conjugate Heat Transfer

Conjugate heat transfer describes the combination of heat transfer in solids and fluids. In solids, conduction dominates whereas in fluids, convection usually dominates. Considering the different contributions to the heat equation described earlier, the heat equation becomes:

$$\rho C_p(\frac{\partial T}{\partial t} + \mathbf{u} \cdot \nabla T) = \alpha_p T(\frac{\partial p_A}{\partial t} + \mathbf{u} \cdot \nabla p_A) + \tau : S + \nabla \cdot (k\nabla T) + Q \tag{2.34}$$

,where S is the strain rate tensor ($1/s$), α_p the thermal expansion coefficient ($1/K$), p_A the absolute pressure (Pa) and τ the viscous stress tensor (N/m^2) (COMSOL,2014).

Conjugate heat transfer is observed in many engineering problems. For example, heat sinks are optimised to combine heat transfer by conduction in the heat sink with the convection in the surrounding fluid. In such applications, substrate materials work as heat conductors, creating a heat path from the heat source to the fluid flow (Ortega, Wirth, and Kim,1994). Another type of devices where conjugate heat transfer takes place are the PCR devices described in Chapter 2.1.5. In these cases, the dimensions of the microchannel are of the same order of magnitude to the thickness of the substrate and therefore both heat convection in the fluid and axial heat conduction in the solid become important (Duryodhan et al.,2016).

2.4 Fluid Flow

The movement of fluids can be described by a variety of mathematical models and engineering correlations that have been generated through time. The mass, momentum and total energy balances are described by the following three Partial Differential Equations (PDEs); Continuity Equation (Equation 2.35), Navier Stokes (Equation 2.36) and Total Energy Equation (Equation 2.37):

$$\frac{\partial \rho}{\partial t} + \nabla \cdot (\rho \mathbf{u}) = 0 \tag{2.35}$$

$$\frac{\partial \rho \mathbf{u}}{\partial t} + \nabla \cdot (\rho \mathbf{u}\mathbf{u}) = -\nabla p + \nabla \cdot \tau + \mathbf{f} \tag{2.36}$$

$$\frac{\partial}{\partial t}[\rho(e + \frac{1}{2}u^2)] + \nabla \cdot [\rho \mathbf{u}(e + \frac{1}{2}u^2)] = \nabla \cdot (k\nabla T) + \nabla \cdot (-p\mathbf{u} + \tau \cdot \mathbf{u}) + \mathbf{u} \cdot \mathbf{f} + Q \tag{2.37}$$

Equations 2.35 - 2.37 can describe a variety of flows; from the creeping flow in a microfluidic device to the turbulent flow in a heat exchanger and even the supersonic flow around a jet fighter. However, solving Equation 2.35 for the purposes of a jet plane is not feasible. However, even for the problems where it is feasible to solve Equations 2.35 - 2.37, such as for a microfluidic device, it still requires a lot of calculations. As a result, computational fluid dynamics (CFD) is focused on developing appropriate approximations to Equations 2.35 - 2.37 in order to obtain accurate results with a reasonable computational cost (COMSOL, 2018).

Equation 2.35 - 2.37) rely on the continuum hypothesis, and the fluid is hence regarded as a continuum and not as a collection of molecules. A fluid in liquid form is considered in most cases as a continuum, and is defined by its viscosity (described by the viscous stress tensor, τ). For Newtonian fluids, τ is proportional to the deviatoric stress tensor and is given by Equation 2.38. For incompressible Newtonian fluids, where heating due to viscous dissipation can be neglected, Equations 2.35 - 2.37 take the form of Equations 2.39 - 2.41. Equation 2.40 can be non-dimensionalised by replacing the variables with the ones appearing in Table 2.3 into Equations 2.42 (for low Re) and 2.43 (for high Re) depending on the parameterization of the pressure. For low *Re* values (creeping flow), the viscous forces dominate the flow while for high *Re* values the flow is inviscid. The flow where Re $\rightarrow$ 0 is known as Stokes Flow, and is expressed by Equation 2.44.

$$\tau = \mu(\nabla \mathbf{u} + \nabla \mathbf{u}^T) - \frac{2}{3}\mu \mathbf{I}(\nabla \cdot \mathbf{u}) \tag{2.38}$$

$$\nabla \cdot (\mathbf{u}) = 0 \tag{2.39}$$

$$\rho \frac{\partial \mathbf{u}}{\partial t} + \rho \mathbf{u} \nabla \cdot (\mathbf{u}) = -\nabla p + \nabla \cdot (\nabla \mathbf{u} + \nabla \mathbf{u}^T) + \mathbf{f} \tag{2.40}$$

$$\rho C_p (\frac{\partial T}{\partial t} + \mathbf{u} \cdot \nabla T) = \nabla \cdot (k \nabla T) + Q \tag{2.41}$$

$$\frac{Re}{St} \frac{\partial \mathbf{u}^*}{\partial t^*} + Re \mathbf{u}^* \cdot \nabla \mathbf{u}^* = -\nabla p^* + \nabla^2 \mathbf{u}^* \tag{2.42}$$

$$\frac{1}{St} \frac{\partial \mathbf{u}^*}{\partial t^*} + \mathbf{u}^* \cdot \nabla \mathbf{u}^* = -\nabla p^* + \frac{1}{Re} \nabla^2 \mathbf{u}^* \tag{2.43}$$

$$-\nabla^* p^* + \nabla^{2*} \mathbf{u}^* = 0 \tag{2.44}$$

TABLE 2.3: Dimensionless Variables.

Parameters	Values
Length (L)	$\mathbf{r}^* = \frac{\mathbf{r}}{L}$, $\nabla^* = L\nabla$ and $\nabla^* 2 = L^2 \nabla^2$
Flow velocity (U)	$\mathbf{u}^* = \frac{\mathbf{u}}{U}$
Time (L/U)	$t^* = \frac{t}{L/U}$
Pressure	$p^* = \begin{cases} (p - p_o)/(\rho U^2), & \text{high Re.} \\ (p - p_o)L/(U\mu), & \text{low Re.} \end{cases}$

2.4.1 Flow in ducts

Fluid flow in microchannels has been studied by several authors (Mour, Das, and Mullick, 2010; Hetsroni et al., 2005; Sharp et al., 2019; Liu and Garimella, 2004; Duan and Yovanovich, 2009). According to the work of Sharp et al. (2019), the general continuum description of the flow of an incompressible, Newtonian fluid with variable properties and no body forces other than gravity consists of the incompressible continuity equation (Equation 2.39), the momentum equation (Equation 2.40) and energy equation (Equation 2.45):

$$\rho C_p (\frac{\partial T}{\partial t} + \mathbf{u} \cdot \nabla T) = \nabla \cdot (k \nabla T) + \Phi \tag{2.45}$$

,where **u** is the velocity vector, ρ (kg/m^3) is the mass density and Φ is the rate of conversion of mechanical energy into heat due to internal viscous heating.

As far as the velocity profiles are concerned, their analytical expressions have been studied extensively in the literature for ducts with a variety of different cross-sectional geometries (Firouzi and Hashemabadi, 2009; Tamayol and Bahrami, 2009; Ding and Manglik, 1996; Spiga and Morino, 1994).

The analytical solution that describes the velocity profile of a fluid flowing in a rectangular duct is presented in the works of Shah and London (1978) (Equation 2.46, Figure 2.17). The velocity profile described by Equation 2.46 is in agreement with the experimental work of Holmes and Vermeulen (1968), while it can be simplified in the dimensionless form of Equation 2.47, for $\alpha^* = b/a \leq 0.5$. The parameters a and b are the constants describing the rectangular cross-sectional area (see Figure 2.17), while m and k are given by Equations 2.48 and 2.49 respectively.

As far as rectangular microchannels are concerned, they are used in many technological applications. The description of the fluid flow and heat transfer in rectangular microchannels requires an analysis in 2D, since it lacks the symmetry and the ability to make the appropriate assumptions that characterise circular ducts or the flow between parallel plates (Shah and London, 1978). The work of Nguyen, Wereley, and Shaegh (2019) presents the comparison of the different velocity profiles for various Reynolds numbers (laminar and turbulent) for a rectangular cross-section of a hydraulic diameter $D_h = 327mm$ (Figure 2.18).

$$u(y,z) = -\frac{16\alpha^2}{\mu\pi^3}(\frac{\partial p}{\partial x}) \sum_{n=1,3,...}^{\infty} \{\frac{1}{n^3}(-1)^{(n-1)/2}[1 - \frac{cosh(n\pi y/2\alpha)}{cosh(n\pi b/2\alpha)}]cos(\frac{n\pi z}{2\alpha})\} \tag{2.46}$$

$$\frac{u(y,z)}{u_{max}} = [1 - (\frac{y}{b})^k][1 - (\frac{z}{a})^m], \qquad for \;\; \alpha* = b/a \leq 0.5 \tag{2.47}$$

$$m = 1.7 + 0.5(\alpha^*)^{-1.4} \tag{2.48}$$

$$k = \begin{cases} 2, & \text{for} \quad \alpha^* \leq 1/3. \\ 2 + 0.3(\alpha^* - 1/3), & \text{for} \quad \alpha^* \geq 1/3. \end{cases} \tag{2.49}$$

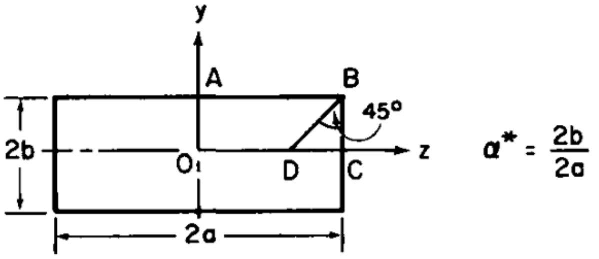

FIGURE 2.17: Rectangular duct (Figure obtained from Shah and London,1978)

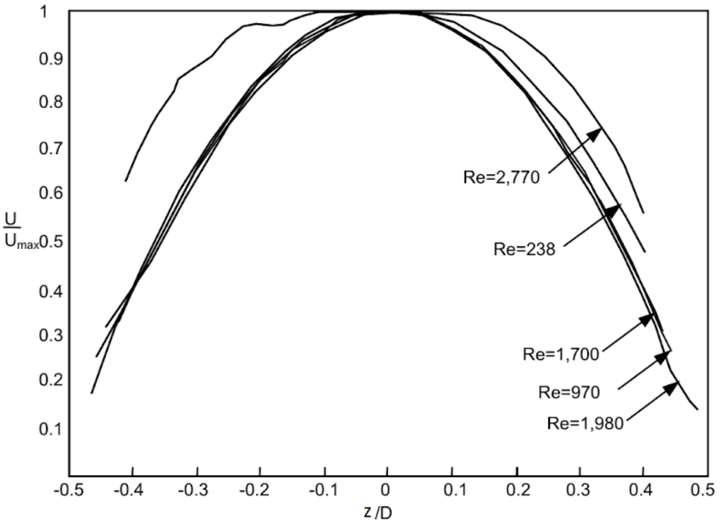

FIGURE 2.18: Velocity profiles for different Reynolds numbers in a Rectangular duct of $D_h = 327mm$ (Figure obtained from Nguyen, Wereley, and Shaegh, 2019)

2.5 Optimisation Theory

According to Cavazzuti (2013), optimisation is generally defined as the process of seeking values for the variables of a problem that lead to the best value of a function. This function is known as the *objective function*, and measures the performance of a system. The set of the possible values of the objective function defines the *solution space*. The variables that have an impact on the objective function are known as the *input* or *design variables* of the problem, and their values are often constrained by equality or inequality conditions. The different combinations of the design variables define the *design space/domain*, with each point in the design space corresponding to a chosen design (Cavazzuti, 2013).

After defining the design variables and the optimisation problem, the next step requires a way of evaluating its performance while varying the design variables. This step can be either an experimental or a numerical process, while the results generated constitute the *output parameters*. The objective function can be either one of the output parameters, a function of them or even of the design variables. Moreover, in the optimisation process, one can often come across problems where considering more than one objective functions simultaneously is required. Such problems are known as *multiobjective optimisation* problems (Cavazzuti, 2013).

As far as industries are concerned, they often deal with nonlinear terms and uncertainties, making the systems highly complicated. One typical example is that of the multiobjective optimisation of the production, distribution and capacity planning of global supply chains in the process industry (Liu and Papageorgiou, 2013).

In order to address the complexity of these systems, several modelling methods have been proposed. Some of them include analytical methods, that require a great amount of work when a change occurs in any parameter of the system. In more complicated systems, developing an analytical model is no longer an option, and hence simulation models are used instead (Syberfeldt, Grimm, and Ng, 2008). Although simulation runs provide insight to the user about how the system works, such evaluations have sometimes proven not to be enough to obtain information about the optimal operating conditions of the system. Instead, simulation-based optimisation (SO) techniques can be applied, using simulation models to evaluate the performance of the system and obtain the optimum values of the design variables (Syberfeldt, Grimm, and Ng, 2008).

However, due to the large number of simulation evaluations required and the minutes to hours of computing time that one single evaluation can take, SO methods cannot be used daily for operational optimisation purposes. This problem can be addressed with the use of computationally efficient meta-models. Meta-models can be therefore considered as models with computational efficiency that provide an approximation to the relation between the input of the simulations and output parameters (Syberfeldt, Grimm, and Ng, 2008).

2.5.1 Design of experiments

According to Cavazzuti (2013), the area of optimisation can be divided into three main subjects: i) Design of Experiments, ii) optimisation Algorithms and iii) Robust Design Analysis (RDA).

Design of Experiments (DOE) describes the methods of selecting the necessary samples with the appropriate arrangement in the design space, in order to obtain the maximum amount of information with a small number of resources (CPU requirements or laboratory work). There is a number of available techniques regarding the selection of the most suitable samples arrangement, in order to obtain the data needed to reach accurate conclusions about the behaviour of the system of interest. At the same time, reducing the number of samples lowers the quality of the information obtained (Cavazzuti, 2013).

2.5.1.1 Formulating DOE

Computer models are used to explore different designs and reduce significantly the expenses of prototypes. A great number of engineering problems are investigated using computer simulators that describe the phenomena of interest instead of lab experiments or field observations when these become hard or very expensive to perform (Levy and Steinberg, 2010; Garud, Karimi, and Kraft, 2017).

The main goal of DoE in such cases is to provide the points or designs where the system's behaviour is to be simulated. Despite the fact that many studies appear in the literature related to physical DoE methods, applying DoE to computer experiments comes with some difficulties related to the significant differences between physical and computer experiments (Garud, Karimi, and Kraft, 2017). As far as the laboratory experiments are concerned, most of them are considered to be stochastic due to unpredictable and uncontrolled errors/parameters, while a linear/ quadratic approximation is commonly used to describe the behaviour of these systems (Garud, Karimi, and Kraft, 2017). The measured response, y(x), of a physical experiment can be modelled as y(x) = $y_t(t) + \epsilon$, where $y_t(t)$ is the true response of the system, and ϵ is the random error. According to Giunta, Wojtkiewicz, and Eldred (2003) and Myers, Montgomery, and Anderson-Cook (2016), for the cases of physical experiments where a linear/quadratic response model is considered, the DoE points located at the faces of the design domain are thought to be the best for sampling and providing the best possible approximation, $\hat{y}$(x). Contrary to physical experiments, computer experiments deal with deterministic simulations, while a linear/ quadratic response is not used. The best sampling points are considered to be the ones within the design domain (Garud, Karimi, and Kraft, 2017). As far as the selection of the total number of DoE points is concerned, the "10k" rule can be applied, where the initial sampling size can be defined at least 10 times the number of design variables (Jones, Schonlau, and Welch, 1998; Li et al., 2019).

The setup of computer experiments resembles that of factorial experiments, with each run of the simulator requiring the input values of design variable(s) and parameters, generating one or more output values that are characteristic of the process. In order to identify the input factors that are important for the output values of interest, careful design of the study and data analysis is required. Considering that many of the computer simulators are deterministic (every run with the same input values produces the same output), repetition that is usually required in lab experiments can be omitted (Levy and Steinberg, 2010).

Their use however often requires significant computational power and long running times of the computer code/models. The development of optimisation algorithms that utilise such functions often appears challenging and commonly includes the fitting of response surfaces to the data collected through the evaluation of the objective and the constraint functions only at the selected points. The response surfaces are then used to visualise the connection between input variables and objectives and obtain the local or global optimum designs (Jones, Schonlau, and Welch, 1998). The response surface methodology used by Jones, Schonlau, and Welch (1998) for instance is based on modelling the objective function and constraints by fitting stochastic processes to data, calibrating the model.

A lot of work has been conducted in optimising the selection of sample size of computer experiments. Loeppky, Sacks, and Welch (2009) published a study related to the empirical $n = 10d$ rule described in Chapman et al. (1994) and Jones, Schonlau, and Welch (1998), with d (the number of design variables) ranging from 4 to 20 in their examples and simulations.

2.5.1.2 Basic terms in DOE

One of the basic terms used in Design of Experiments is the term *factor*, which describes the design variables of the problem (x_{ij}, for $i : 1, 2, .., p$ and $j : 1, 2, .., n$, where p : No of design variables or dimensional coordinates and n : No of data points). The values of the factors chosen by the DOE, ($\vec{x}_j$, where $j : 1, 2, .., n$), are known as *training data*. A specific set of training data values is called *design*, X (Equation 2.50) (Cavazzuti, 2013).

$$X = (\vec{x}_1, ..., \vec{x}_n) = \begin{pmatrix} x_{11} & ... & x_{1n} \\ : & : & : \\ x_{p1} & ... & x_{pn} \end{pmatrix} \tag{2.50}$$

The terms used to describe the design space and the number of different values a variable can take in DOE are *region of interest* and *levels* respectively. As far as the experimental design is concerned, the objective function is called *response variable*, the output variables *responses* and the set of experiments selected to be performed *sample space* (Cavazzuti, 2013).

In DOE, the number of levels used is usually small, and qualitative or quantitative discrete variables are usually selected. When quantitative continuous variables are used, they are discretised within their range (Cavazzuti, 2013).

Moreover, considering the fact that at the beginning there is no information about the response of the system, the region of interest might not include the optimum solution. In this case, the region of interest can be readjusted once the problem is evaluated. In addition, the type of DOE technique as well as the specific number of levels are selected depending on the number of experiments/ simulations that can be performed (Cavazzuti, 2013).

2.5.1.3 DOE Sampling Technique

There is a variety of DOE techniques that are used to define the training data. Some of the most important DOE techniques are: 1) Latin Square, 2) Randomised Complete Block Design, 3) Full Factorial, 4) Fractional Factorial, 5) Central Composite, 6) Box-Behnken, 7) Latin Hypercube (Cavazzuti, 2013).

The Latin Hypercube (LH) technique is used in this work. According to Kleijnen (2017), LH is one of the most popular sampling techniques. This technique is considered to offer great advantages over others, such as i) the ability to vary the

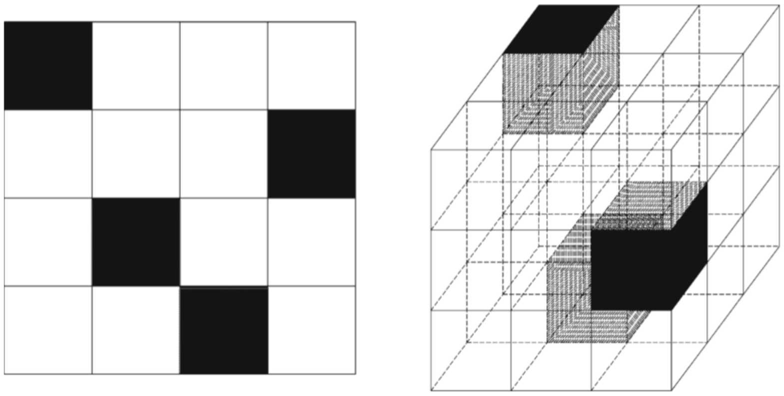

(a) $p = 2,\ n = 4$ **(b)** $p = 3,\ n = 3$

FIGURE 2.19: Example of Latin Hypercube experimental designs (Figure obtained from Cavazzuti, 2013)

number of sampling points, ii) the orthogonality of the sampling points and iii) the independence of the sampling points on the surrogate model selected (Viana, Venter, and Balabanov, 2010).

More specifically, in Latin Hypercube designs (LHD), the design space is divided into an orthogonal grid. This grid can exist in multiple dimensions and is divided into n^p sub-volumes (n: number of samples, p: number of design variables) or *hypercubes* of equal probability, where each variable is discretised into n levels. The sampling is performed to ensure that there exist no two data points that lie in the same hypercube (Keane and Nair, 2005). For cases with two or three design variables, the volumes - elements selected in each case are presented in Figure 2.19 in black.

However, this condition does not necessarily guarantee a good distribution of the samples over the design space. More specifically, the LHD configuration and the sample placement within the hypercubes remains random; as a result optimisation is needed in order to guarantee adequate space-filling for all designs (Garud, Karimi, and Kraft, 2017). An example that illustrates an LHD case of poorly distributed samples is the one where the samples are distributed along the diagonal of a two-design variable problem. In such a problem, most of the design space is not explored (Simpson, Lin, and Chen, 2001). There are several techniques that are used to reduce the correlations in LHD and produce a uniform DOE design, such as the Audze-Eglais Latin Hypercube (AELH) (Audze, 1977), the Morris Mitchell Latin Hypercube (MMLH) (Morris and Mitchell, 1995) and others presented in Tables 2.4 and 2.5. The MMLH technique is used in this work, as the space-filling criterion introduced by Morris and Mitchell in 1995 is considered a widely-used and accepted one (Garud, Karimi, and Kraft, 2017).

As far as the case of MMLH is concerned, they defined a random function, Y (stationary Gaussian process), over T ($T = [0,1]^p$, where p is the number of variables, that are scaled between 0-1) as an initial expression of the uncertainty over y

TABLE 2.4: Overview of LHD optimisation literature based on space-filling criteria and optimisation algorithms (Garud, Karimi, and Kraft, 2017). Optimisation Algorithms (OA): 1: SA, 2: RCE, 3: QNS, 4: CP, 5: TA-GS, 6: PerGA, 7: ESE, 8: BB, 9: ILS, 10: TP, 11: QLHD, 12: ESE, 13: SLE, 14: PSO, 15: TP-SLE, 16:AMPSO, 17:SOBSA, 18:S-SLE.

Author(s)*	OA	PE	MST	Mm	ϕ_p	D_2*	C_2	IMSE	ME
A	1				x				
B	2,3							x	x
C	4				x				x
D	5						x		
E	6	x							
F	7				x	x			x
G	4	x		x					
H	8			x					
I	9			x	x				
J	10				x				
K	11			x					
L	12	x		x					
M	13				x				
N	14				x				
O	12, 1		x						
P	15	x		x	x		x		
Q	16	x							
R	17				x				
S	18			x					

*Details for the authors are presented in Table 2.5.

TABLE 2.5: Details of the authors appearing in Table 2.4 (Garud, Karimi, and Kraft, 2017).

Author/s	Symbols
Morris and Mitchell (1995)	A
Park (1994)	B
Kenny, Li, and Sudjianto (2000)	C
Fang, Ma, and Winker (2002)	D
Bates, Sienz, and Toropov (2004)	E
Jin, Chen, and Sudjianto (2003)	F
Liefvendahl and Stocki (2006)	G
Van Dam et al. (2007)	H
Grosso, Jamali, and Locatelli (2009)	I
Viana, Venter, and Balabanov (2010)	J
Xiong et al. (2009)	K
Husslage et al. (2011)	L
Zhu et al. (2012)	M
Chen et al. (2013)	N
Damblin, Couplet, and Iooss (2013)	O
Pan, Ye, and Wang (2014)	P
Aziz and Tayarani-N (2014)	Q
Pholdee and Bureerat (2015)	R
Long et al. (2016)	S

(a computer model that can be considered as a scalar). For Y, the correlation between the responses ($Y(x_s)$, $Y(x_t)$) at two inputs (x_s, x_t), is given by a function of distance, d, between the two inputs (Equation 2.51). As far as the distance is concerned, the *rectangular* and *Euclidean* were considered (Equations 2.52 and 2.53 respectively).

$$corr[Y(x_s), Y(x_t)] = R[d(x_s, x_t)] \tag{2.51}$$

$$d(x_s, x_t) = \sum_{l=1}^{k} |x_s^{(l)} - x_t^{(l)}| \tag{2.52}$$

$$d(x_s, x_t) = \sum_{l=1}^{k} [(x_s^{(l)} - x_t^{(l)})^2]^{0.5} \tag{2.53}$$

The next steps involved: 1) performing n runs and evaluations of y, 2) using the $Bayes' theorem$ and obtaining the posterior process (Gaussian). The posterior mean function was used as the prediction, $\hat{y}$. The standard deviation or the variance can be used to present the "predictive uncertainty" (Morris and Mitchell, 1995). Further details on the Gaussian process can be found in the work of Williams and Rasmussen (2006). In order to rank the different designs, a scalar-valued criterion was used (Equation 2.54):

$$\phi_p(D) = [\sum_{j=1}^{m} J_j d_j^{-p}]^{1/p} \tag{2.54}$$

where for a given design D, d_j is the distance between input values (j=[1,2,...,m]), J_j is the number of pairs of inputs separated by distance d_j, $\phi_p(D)$ is a family of functions, p is a positive integer and $m \in [1, \binom{n}{2}]$ (Morris and Mitchell, 1995). The code used in this work is developed in MATLAB® and generates DoE points using Morris Mitchell Latin Hypercube method (Mathworks, 2019).

2.5.2 Optimisation Algorithms

Optimisation algorithms are used in order to find the set of inputs that can result in the maximum or minimum value of an objective function. An example where optimisation algorithms are used is in the generation of new samples in the design space. There is a variety of optimisation algorithms, such as deterministic, gradient-based, stochastic, evolutionary, genetic, unconstrained, constrained, single-objective, multi-objective, local, global, convex, discrete and others. A brief description of these optimisation algorithms is presented according to the work of Cavazzuti (2013):

Deterministic optimisation: Deterministic optimisation algorithms do not generate or use any random values, while the effect of uncertainty on the optimisation process is not explored.

Gradient-based optimisation: In gradient-based algorithms, the computation of the gradient (or the Hessian) of the objective function is required.

Stochastic optimisation: Stochastic optimisation algorithms are optimisation algorithms that include the generation and use of random numbers.

One stochastic optimisation algorithm that is examined in this work is the Particle swarm optimisation (PSO); a population-based algorithm inspired by the behaviour and interaction of some animals (ex. insects, birds, fish, herds) when found in groups. The idea behind this type of algorithm is based on the cooperation observed amongst swarms in order to find food, where the behaviour of each member of the group changes according to its own or other members' experience (Wang, Tan, and Liu, 2018).

According to Van Den Bergh (2001), five basic criteria are presented as a guide for the establishment of the swarm artificial life systems: (1) proximity, (2) quality, (3) diverse response, (4) stability and (5) adaptability. More specifically, each member of the swarm can update their position and speed based on the environmental change (proximity, quality). At the same time, the movement of the swarm is not restricted and is constantly trying to achieve the optimal solution in space. While in search of the optimum solution, the members of the swarm maintain stable movement, while at the same time changing their movement in order to adapt to the environmental change (Wang, Tan, and Liu, 2018).

Evolutionary optimisation: This algorithm belongs to the stochastic optimisation algorithms. The method of defining the samples is based on the evolutionary theory of Darwin. The basic steps of the Evolutionary Algorithm are the following: 1) Generation of an initial population of designs, 2) Mutation with a difference of vectors to generate a donor design vector, 3) Crossover to generate a design vector and 4) Selection (accept/reject) the trial design vector using the fitness function.

Genetic optimisation: The Genetic Algorithm (GA) is a type of stochastic algorithm which simulates natural inheritance and Darwin's survival of the fittest concept. GA method performs a multi-directional search by keeping a population of solutions and exchanging information between the different directions, while the design variables are stored in binary strings. In GA, during the simulated evolution step, the relatively good solutions are reproduced while the bad ones die. The basic steps of the genetic algorithm are the following: 1) Evaluation, 2) Selection, 3) Reproduction (Cross-over), 4) Mutation, 5) Elitism and 6) Extermination.

Unconstrained and Constrained optimisation: In the unconstrained optimisation algorithms, the factors are not subjected to any constraints. In the case of constrained optimisation, the design variables of the optimisation problem are subjected to constraints.

Single and multi-objective optimisation: In single and multi-objective algorithms, there are one and more than one objective functions respectively. Deterministic optimisation is by definition single objective. Stochastic optimisation can be both single-objective and multi-objective.

Local and Global optimisation: The local optimisation algorithms are the algorithms where the solution can be "trapped" into a local optimum. This is usually the case for the gradient-based algorithms, that search for a stationary point in the objective function, that is not necessarily the global optimum. The global optimisation algorithms however are able to locate the global optimum, while overcoming the local optimum points. Non-gradient-based methods are usually able to locate the global optimum point.

Convex optimisation: In the case of convex objective functions, convex optimisation algorithms are expected to converge very fast. This type of algorithm is considered to be a subset of gradient-based algorithms.

Discrete optimisation: Discrete optimisation algorithms are algorithms that include non-continuous variables.

2.5.3 Meta-modelling Techniques

Response surface modelling or Meta-modelling includes a variety of different techniques that are used to process the results of DOE, in order to create an approximation of the response variable (output) over the design space. This approximation is known as *Response Surface* or *Meta-model*. Building the meta-model provides the opportunity to find the optimal response of the system very fast and without extra experiments or simulations, since it is an analytical function. As a result, even in cases where very little information is known about the problem, the meta-model can still be useful. However, if the design space is poorly explored through the DOE or an unsuitable meta-modelling technique is used and the response variable is irregular, the meta-model assisted optimisation might not present correctly the behaviour of the response variable (Cavazzuti, 2013).

The mathematical representation of the relation between the response surface, $\hat{y}$ (approximation of y), and the objective function, y (unknown), is given by the following equation:

$$y = f(\mathbf{x}) = \hat{f}(x) + \epsilon(\mathbf{x}) \Rightarrow \hat{y} = \hat{f}(x) \tag{2.55}$$

where $\epsilon(\mathbf{x})$: the error in the estimated response and $\mathbf{x}$: design variables (Cavazzuti, 2013).

Some of the meta-modelling techniques described in this chapter are: 1) Least Squares Method, 2) Shepard and K-Nearest, 3) Kringing, 4) Radial Basis Functions and 5) Neural Networks (Cavazzuti, 2013).

2.5.3.1 Least Squares Method

The Least Squares Method (LSM) is a regression technique that helps to minimise the contribution from random measurement errors to the surrogate surface. More specifically, the coefficients of the response surface are adjusted so that they best fit the results of the DOE run.

In the most basic form of LSM, the Unweighted Least Square Method (ULSM), all the data points are weighted equally. In the Weighted Least Squares Method (WLSM), the points with greater weight will contribute more to the overall surrogate surface. The Moving Least Squares Method (MLSM) is a form of WLSM, with varying values of the weights. More specifically, the weights are biased around a point x_*, where the objective function has been evaluated. The weight of a training point decays as it moves away from the point x_* (Choi, Youn, and Yang, 2001, Toropov et al., 2005).

The response surface is a function of $\hat{f}(x,\beta)$, where $\beta = [\beta_1, ..., \beta_m]^T$ is the vector of the m coefficients to be tuned and $x = [x_1, ..., x_p]^T$ is the vector of the p design variables. The data set consists of (x_i, y_i) pairs, $i = 1, ..., n$, where x_i is the vector of the input parameters of the i^{th} experiment, whose response variable is y_i. In LSM, in order for the response surface to best fit the data, the right choice of coefficient β_j, j=1,...,m, should be made, so that they give the minimum value of the squared residuals, S (Equations 2.56 and 2.57) (Cavazzuti, 2013):

$$S = \sum_{i=1}^{n} \epsilon_i^2 \tag{2.56}$$

$$\epsilon_i = y_i - \hat{f}(x_i, \beta), i = 1, ..., n \tag{2.57}$$

Different model functions can be used to derive the response surface. Some of the most important ones are presented in Table 2.6, together with the m number of β coefficients.

2.5.3.2 Shepard and K-Nearest

The Shepard and K-nearest methods are interpolating techniques that are suitable for large data sets. For the DOE results, (x_i, y_i), where i=1,...,n, the value of the response surface at any point **x**, is given by the weighted average presented in Equation 2.58, where λ_i coefficients are inversely proportional to the p^{th} power of the Euclidean distance d_i.

$$\hat{f}(\mathbf{x}) = \sum_{i=1}^{n} \lambda_i(\mathbf{x}) f(x_i) = \sum_{i=1}^{n} \lambda_i(\mathbf{x})(y_i) \tag{2.58}$$

TABLE 2.6: Polynomial model functions (Cavazzuti, 2013)

Model Function	Number of Coefficients for p design variables	Expression $\hat{f}(x,\beta)$
Linear	$m = p+1$	$\hat{f}_{lin}(x,\beta) = \beta_o + \sum_{i=1}^{p} \beta_i x_i$
Quadratic	$m = \frac{(p+1)(p+2)}{2}$	$\hat{f}_{quad}(x,\beta) = \hat{f}_{lin} + \sum_{i=1}^{p} \sum_{j=1}^{i} \beta_{i,j} x_i x_j$
Cubic	$m = \frac{(p+1)(p+2)(p+3)}{2}$	$\hat{f}_{cub}(x,\beta) = \hat{f}_{quad}$+$3^{rd}$ order terms
n^{th} degree polynomial	$m = \frac{(p+n)!}{p!n!}$	$\hat{f}_{nth}(x,\beta) = \hat{f}_{(n-1)th}$+$n^{th}$ order terms
Bilinear	$m = 2^p$	for p=3: $\hat{f}_{lin}(x,\beta) = \beta_4 x_1 x_2 + \beta_5 x_1 x_3$ $+\beta_6 x_2 x_3 + \beta_o + \sum_{i=1}^{3} \beta_i x_i$
Biquadratic	$m = 3^p$	for p=2: $\hat{f}_{biq}(x,\beta) = \beta_5 x_1 x_2 + \beta_8 {x_1}^2 {x_2}^2$ $+\beta_6 {x_1}^2 x_2 + \beta_7 x_1 {x_2}^2 + \sum_{i=1}^{2} \beta_i x_i + \beta_o$ $+ \sum_{i=1}^{2} \beta_{i+2} {x_i}^2$

The Shepard and K-Nearest methods, unlike other methods, computes the response surface as the weighted average of only the *q-nearest* experimental results, and not of all the experimental results, as the Shepard method does.

2.5.3.3 Kriging

This method is often used in geostatistics to interpolate spatial data, and it belongs to the linear least squares algorithms. It is usually applied in nonlinear responses and is considered to be computationally intensive. Moreover, the method is considered to be either an interpolating or a regression technique, depending on the nature of the noise parameter, *nugget*; if it is equal to zero or not respectively (Cavazzuti, 2013). There are different types of Kriging methods; the *Simple*, the *Ordinary*, the *Universal*, the *IRF-k*, the *indicator*, the *disjunctive* and the *lognormal Kriging*.

The response variable's estimate at a point $\boldsymbol{x}$ is given by the linear combination of the results from the DOE run (Equation 2.59). The weights, λ_i, are derived by solving a system of linear equations obtained by making the assumption that *f(x)* is a sample-path of a random process whose error of prediction is to be minimized (Cavazzuti, 2013).

$$\hat{f}(\mathbf{x}) = \sum_{i=1}^{n} \lambda_i(\mathbf{x}) f(x_i) = \sum_{i=1}^{n} \lambda_i(\mathbf{x})(y_i) \tag{2.59}$$

2.5.3.4 Radial Basis Functions

The Radial Basis Function (RBF) is an interpolation technique, where the values of the response surface are calculated based on their distance (usually the Euclidean (see Equation 2.53)) from certain points called the centres (Cavazzuti, 2013):

$$\phi(\mathbf{x}, \mathbf{c}) = \phi(||\mathbf{x} - \mathbf{c}||) \tag{2.60}$$

For n DOE runs (x_i, y_i), the response surface gets the following form:

$$\hat{f}(\mathbf{x}) = \sum_{i=1}^{n} \lambda_i \phi(\mathbf{x}) f(x_i) \tag{2.61}$$

where the weights, λ_i, are calculated according to Equation 2.62:

$$\boldsymbol{\Phi\lambda} = \mathbf{y} \tag{2.62}$$

$\boldsymbol{\Phi}$ is defined by Equation 2.63, where $\mathbf{y}$ and $\boldsymbol{\lambda}$ are the vectors of the DOE outputs and weights respectively. Classical choices for radial basis functions ϕ are shown in Table 2.7.

$$\Phi_{i,j} = \phi(||x_i - x_j||) = \phi(r) \tag{2.63}$$

TABLE 2.7: Commonly used RBF (Cavazzuti, 2013)

Model of RBF Function	Expression of $\phi(r^*)$	Parameters
Gaussian	$exp(-\beta^2 r^2)$	β
Multiquadric	$(r^2 + \beta^2)^{0.5}$	β
Inverse Multiquadric	$(r^2 + \beta^2)^{-0.5}$	β
Polyharmonic Splines	r^{ν}	$\nu > 0, \nu \notin 2N$
	$r^{2\nu} log(r)$	$\nu \in N$

$^*r = ||x_i - x_j||$, β=constant

2.5.3.5 Neural Networks

A lot of research exists in the application of neural networks (NN) to the development of simulation meta-models, that allow predicting the output values (of simulation models) for any given input values, without having to simulate the behaviour of the system (Pierreval, 1996).

The Artificial Neural Networks (ANN) mimic the function of the central nervous system, where the information processing occurs at elements called *neurons*. Figure 2.20 presents an example of a simple NN, consisting of five *units* or *neurons* (represented by the circles) and six *connections* (represented by the arrows). The weight (w) of each connection appears next to it, and it is a measurement of the strength of the connection. When the weights take positive and negative values, the connections are called *excitatory* and *inhibitory* respectively (Koehn, 1994).

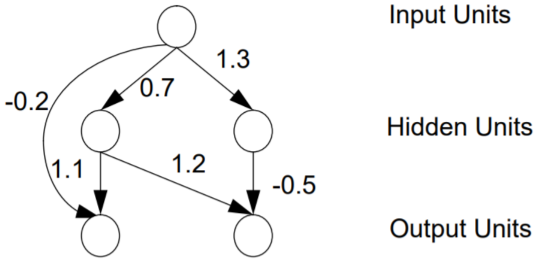

FIGURE 2.20: Simple neural network (Figure obtained from Koehn, 1994).

Figure 2.21 demonstrates the steps of processing the information in a single node. The first stage includes the *summation* of the input connections (Σ) to the node, the result of which is then introduced to an $activation function$ (σ). For each output connection, the activation value is then multiplied with the appropriate weight and then exits this node, entering the next (Koehn, 1994).

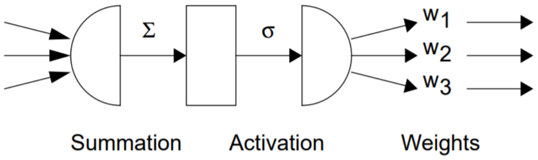

FIGURE 2.21: Processing of information in a node (Figure obtained from Koehn, 1994).

A great number of different NN models have been developed by researchers for different applications over the years (feedforward, deep feedforward etc.), with some of the most important types presented in the work of Leijnen and Veen (2020) (see Appendix A.1). However, all of them are based on the principles of biological neural systems, and therefore have some common characteristics, such as the *training*, *validation* and *test* datasets used. The training dataset includes the data used to fit the NN model. The validation dataset includes data used to evaluate how a model fits the training dataset, while at the same time tuning the hyperparameters of the model. The test dataset includes the data used to evaluate the latest version of the model fit on the training dataset (Wu, 1994).

As far as the type of feedforward networks are concerned, they consist of several layers. The first and last layers are connected to the input and output of the node respectively. Every layer in between is connected to the previous one. The information is transferred in only one direction (forward), from the input, through the hidden layers (if they exist) to the output (MathWorks, 2020), without the presence of any loops in the network (Emmert-Streib et al., 2020). The design of NN can be improved with the use of genetic algorithms, by optimising and updating its weights (parameters) (Gad, Gad, and John, 2018).

Chapter 3

CFD-enabled optimisation of diverging channels and μPCR chips

The governing equations that describe the behaviour of a fluid (mass, energy and momentum conservation) are given by a set of coupled, nonlinear partial differential equations, that are unsolvable for most engineering problems. In Computational Fluid Dynamics (CFD), these governing equations are transformed into algebraic equations that are solved numerically, providing the user with an approximate computer-based solution for a great variety of applications. More specifically, the continuous domain is replaced with a discrete one using a grid, where the variables are defined only at the grid points and not on every point of the domain (Bhaskaran and Collins, 2002).

The CFD software used in this work is COMSOL Multiphysics®, due to its fully coupled multiphysics and single-physics modelling capabilities (COMSOL, 2022).

3.1 COMSOL Multiphysics ®

The finite element analysis, solver, and simulation software package, COMSOL Multiphysics ®, is used to solve the governing equations of the problems along with their boundary conditions in this Chapter. Several studies on conjugate heat transfer have been conducted using COMSOL Multiphysics ® (Al-Farhany and Abdulkadhim, 2018; Bodey, Arimilli, and Freels, 2011; Caccavale, De Bonis, and Ruocco, 2016; Hadzhiev, Yatchev, and Mechkov, 2018), while the same CFD software has been used by authors conducting similar studies where PCR takes place in microfluidic channels (Papadopoulos et al., 2015; Moschou et al., 2014; Mollajan, Mehrizi, and Bazaz, 2016; Hamad et al., 2021; Hamad et al., 2021).

Chapters 3.2 and 3.3 present studies where COMSOL Multiphysics ® is used to simulate different cases of conjugate heat transfer in microchannels, similar to the ones presented in the works of Toh, Chen, and Chai (2002) and Duryodhan et al. (2016). The simulations are performed in order to become familiar with the software while at the same time validating the models with other well-examined problems that study similar physics and take place in the same scale as the ones appearing in microfluidic PCR devices. Moreover, three optimisation problems are performed on a diverging microchannel geometry, with the use of RBF and MMLH (Chapter 3.3.4).

In Chapter 3.4, COMSOL Multiphysics ® is used to simulate and optimise the performance of a SP CF PCR device, consisting of three copper wire heaters and microchannels with sigmoid shape. Several optimisation problems examining different design variables and objective functions are considered, and can be found in the following publications; Zagklavara et al. (2021); Zagklavara et al. (2021); Zagklavara et al. (2022); Zagklavara et al. (2022). More specifically, the objective functions considered describe different potential design objectives, when developing these microfluidic devices. The DNA amplification metric expresses a measurement of the efficiency of the PCR reaction. The pressure drop is linked to the pumping requirements and potential cost of the microfluidic device, while the total substrate volume can be linked to the latter. The total residence time presents a metric of the total operating time of the device. As it is presented in the following chapters, some of these objectives are often found to compete against each other; in other words, improving the one deteriorates the other. As a result, through multi-objective optimisation, design compromises can be achieved, depending on the designer's approach. A summary of the optimisation studies presented in this chapter are presented in Table 3.1.

TABLE 3.1: Summary of the single- (SO) and multi- (MO) optimisation studies on PCR systems, examining the following objectives; DNA amplification (DA), Pressure Drop (ΔP), Residence time ($t_{R,tot}$) and Substrate volume ($V_{S,tot}$).

Vars/Obj	DA	ΔP	$t_{R,tot}$	$V_{S,tot}$	SO	MO	Ref.
Channel width	x	x			x		2
Channel height	x	x			x		2
Heaters' spacings	x	x			x		4
Heaters' spacing & channel width	x	x			x		1
Residence time in denaturation	x	x	x	x	x	x	3
Residence time in annealing	x	x	x	x	x	x	3
Residence time in extension	x	x	x	x	x	x	3
Relative increase in channel extension width	x	x	x	x	x	x	3

1: Zagklavara et al. (2021), 2: Zagklavara et al. (2021), 3: Zagklavara et al. (2022)
4: Zagklavara et al. (2022)

3.2 Modelling the fluid flow and heat transfer inside heated microchannels

This Chapter presents the development of the first models using COMSOL Multiphysics ® and their validation with the computational work of Toh, Chen, and Chai (2002) and the experimental work of Tuckerman (1984).

3.2.1 Setting up the simulations

At the early stages of using COMSOL Multiphysics ® 5.4, the software is used to validate the work of Toh, Chen, and Chai (2002), simulating the 3D fluid flow and heat transfer phenomena inside heated microchannels. The schematic drawing of the test configuration and the dimensions of the microchannels are presented in Figure 3.1. Figure 3.2 presents the computational domain, where half of a 0.9 mm long microchannel is chosen to be simulated (due to the computational intensity of simulating 150-200 microchannels, and the y-axis symmetry of the microchannel). Table 3.2 presents the different designs studied by Toh, Chen, and Chai (2002).

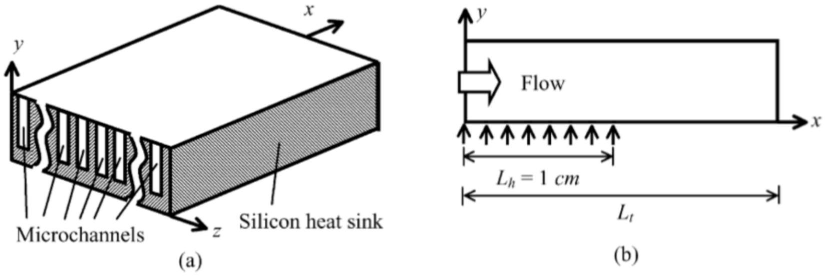

FIGURE 3.1: Schematic of the (a) microchannels and of their (b) dimensions (Toh, Chen, and Chai, 2002)

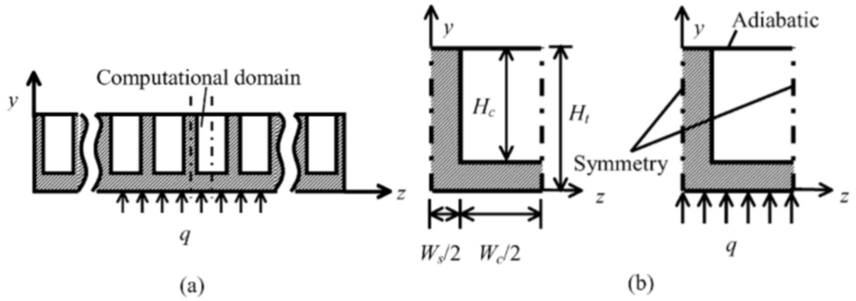

FIGURE 3.2: Computational domain: (a) normal view, (b) enlarged view (Toh, Chen, and Chai, 2002)

TABLE 3.2: Parameters for the different sets of microchannels used by Toh, Chen, and Chai (2002).

Parameters	No of Case Study				
	0	1	2	3	4
$L_t(cm)$	2	2	1.4	1.4	1.4
$L_h(cm)$	1	1	1	1	1
$W_t(cm)$	1.5	1.5	2	2	2
$W_c(\mu m)$	64	64	56	55	50
$W_s(\mu m)$	36	36	44	45	50
$H_t(\mu m)$	489	489	533	430	458
$H_c(\mu m)$	280	280	320	287	302
$Q_{tot}(cm^3/s)$	1.277	1.860	4.700	6.500	8.600
$Q_{ch}(cm^3/s)$	$8.513 \cdot 10^{-3}$	$12.4 \cdot 10^{-3}$	$23.5 \cdot 10^{-3}$	$32.5 \cdot 10^{-3}$	$43 \cdot 10^{-3}$
$q(W/cm^2)$	34.6	34.6	181	277	790
$T_{in}(°C)$	20	20	20	20	20
No of channels (N_{ch})	150	150	200	200	200

3.2.1.1 Model in COMSOL Multiphysics ®

3.2.1.1.1 Fluid Flow The inlet velocity of the microchannel is equal to $U_{in} = 475.07 mm/s$ (Equation 3.1). The flow is laminar for the indicative inlet temperature of $T_{in} = 20°C$, since the Reynolds number is found to be ~ 50 (Equation 3.2). The Navier Stokes Equations for i) incompressible and ii) steady-state flow are given by Equations 3.3 and 3.4. The hydraulic diameter, D_h, is calculated by Equation 3.5.

$$U_{in} = \frac{Q_{tot}}{N_{ch} H_c W_c} = \frac{Q_{ch}}{H_c W_c} = 475.07 mm/s \tag{3.1}$$

$$Re = \frac{D_h U_{in} \rho_{20}}{\mu_{20}} = \frac{1.0419 \cdot 10^{-4} \cdot 0.47507 \cdot 998.21}{1.02 \cdot 10^{-3}} = 49.309 \tag{3.2}$$

$$\rho(\mathbf{u} \cdot \nabla)\mathbf{u} = \nabla \cdot [-p\mathbf{I} + \mu(\nabla \mathbf{u} + (\nabla \mathbf{u})^T)] + \mathbf{f} \tag{3.3}$$

$$\rho \nabla \cdot (\mathbf{u}) = 0 \tag{3.4}$$

$$D_h = \frac{2H_c \cdot W_c}{H_c + W_c} \tag{3.5}$$

3.2.1.1.2 Heat Transfer The heat transfer model used to describe both fluid and solids includes multiple heat transfer phenomena that take place in the system (conjugate heat transfer). The model is implemented in steady-state (Equation 3.6), with the velocity **u** set to zero for all domains except for the fluid one. The terms on the LHS and RHS of Equation (3.6) express the heat transfer due to convection and conduction respectively.

$$\rho C_p(\mathbf{u} \cdot \nabla T) = \nabla \cdot (k \nabla T) \tag{3.6}$$

3.2.1.2 Boundary Conditions

The boundary conditions implemented are in accordance with the work of Toh, Chen, and Chai (2002) (Figure 3.2b). More specifically:
i) a symmetry boundary condition is implemented at the sides of the computational domain on both fluid ($z = W_c + W_s$, face CLNF of Figure 3.3) and silicone ($z = 0$, face AKMD of Figure 3.3), in order to a) account for a channel placed in the middle of a chip and b) reduce the computational time by simulating half the channel and taking advantage of the channel symmetry
ii) an adiabatic boundary condition (zero heat flux, thermally insulated) is implemented at the top plane of the computational domain ($y = H_t$, face ACFD of Figure 3.3), and at the bottom plane ($y = 0$) for $x > L_h$,
iii) a constant heat flux, q, is implemented at the bottom plane ($y = 0$) for $x \leq L_h$ (Figure 3.1b),
iv) a no-slip boundary condition is implemented at the fluid-wall interface (faces BGIE and GHJI, Figure 3.3), assuming that at a solid boundary, the fluid has zero velocity relative to the boundary.

At the inlet (face BCHG, Figure 3.3), the water uniform velocity at the computational domain is set as U_{in} (Equation 3.1), while the inlet temperature is set at $T_{in} = 20°C$.

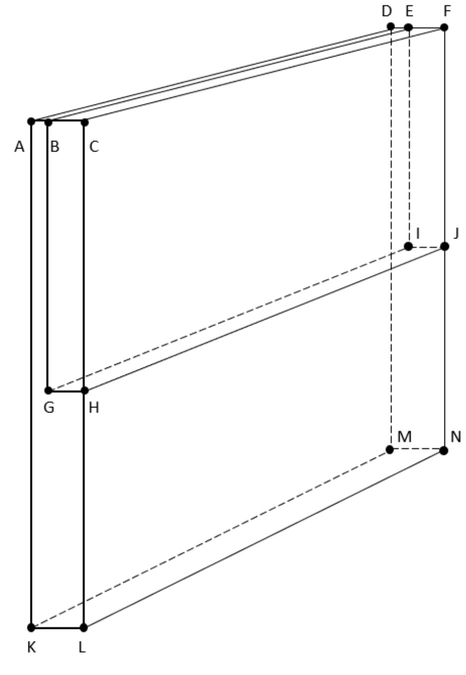

FIGURE 3.3: Schematic graph of the geometry introduced in COMSOL Multiphysics ® to validate the work of Toh, Chen, and Chai (2002).

3.2.2 Mesh Independence study

A mesh independence study is performed in order to obtain a model that both converges and is independent of the mesh resolution (Table 3.3). The results indicate that mesh No 4 is to be selected, presenting a <1 % variation from the finest mesh tried (mesh No 6). Figure 3.4 presents the comparison of the different values of thermal resistance, R_{th}, for the meshes tested and the values presented by Toh, Chen, and Chai,(2002) and Tuckerman (1984). Meshes No 4 and 5 are presented in Figure 3.5.

TABLE 3.3: Mesh independence study for Case 0 (Toh, Chen, and Chai, 2002)

Mesh	No of Elements	R (cm^2K/W) Toh, Chen, and Chai, (2002)	Current Simulation	deviation of R_{th} (%) from mesh No 6
1	189,452	0.331	0.325	1.56
2	305,627		0.323	0.94
3	850,476		0.314	-1.88
4	2,932,170		0.318	-0.62
5	13,920,185		0.319	-0.31
6	15,802,562		0.320	

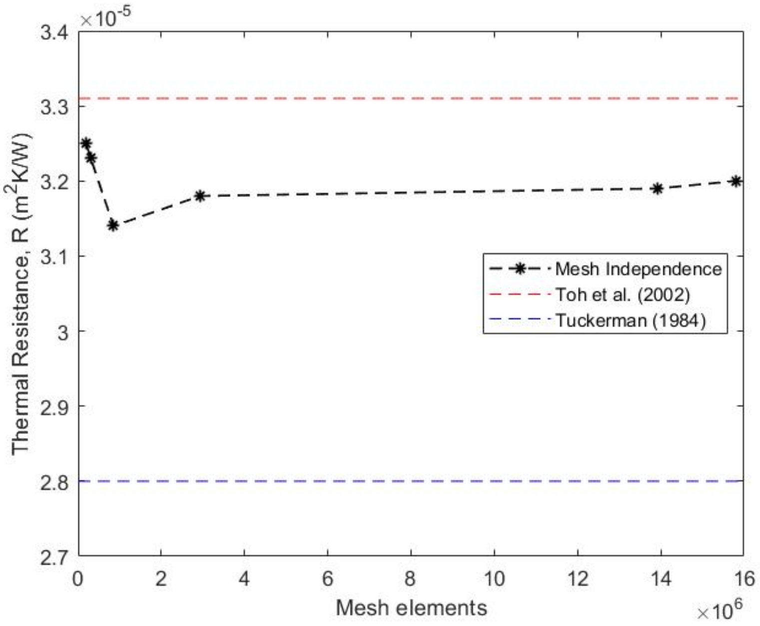

FIGURE 3.4: Mesh independence study for Case 0 as presented in Toh, Chen, and Chai, (2002). The star points present the results obtained from the six meshes, using COMSOL Multiphysics ®.

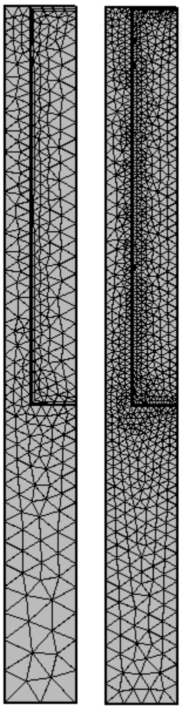

FIGURE 3.5: Meshes No 4 and 5 (see Table 3.3), obtained using COMSOL Multiphysics ®.

3.2.3 Validation with the work of Toh, Chen, and Chai (2002)

The heat flux (q) and the volumetric flow rate (Q) applied in the simulations executed in COMSOL Multiphysics ® 5.4, together with the thermal resistances calculated for each case, are presented in Table 3.4. Good agreement is observed between the current work and the publications of Toh, Chen, and Chai (2002) and Tuckerman (1984) (Figure 3.6). Additionally, the temperature distributions (Figure 3.7) at four different cross-sections ($x = 1, 3, 6$ and $9mm$) of the microchannel for Case Study 0 of Toh, Chen, and Chai (2002) are compared to the ones produced in the work of Toh, Chen, and Chai (2002) (Figure 3.8). The temperature profiles in Figures 3.7 and 3.8 appear to be in agreement.

TABLE 3.4: Comparison of thermal resistances at x=0.9mm

No Case	q (W/cm^2)	Q (cm^3/s)	R_{th} (cm^{2}K/W) Toh, Chen, and Chai, (2002)	Current Simulation
0	34.6	1.277	0.331	0.318
1	34.6	1.860	0.253	0.237
2	181	4.700	0.157	0.144
3	277	6.500	0.128	0.112
4	790	8.600	0.105	0.091

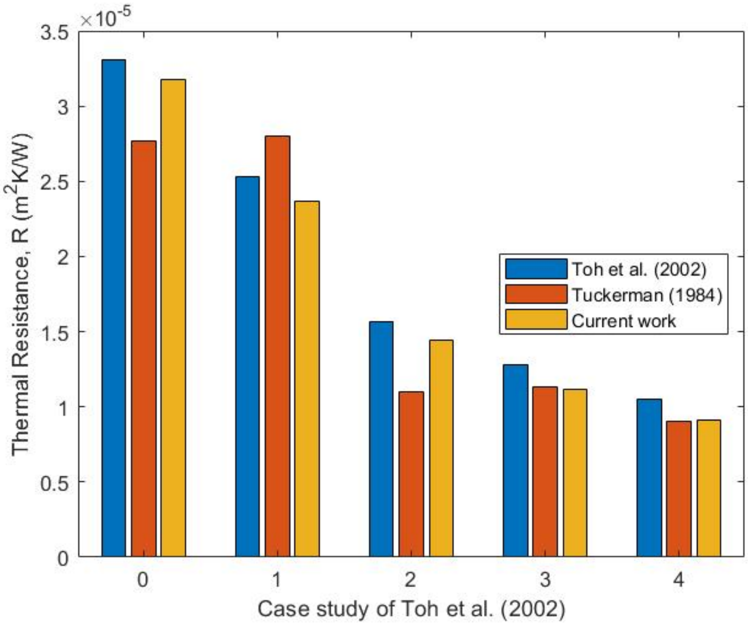

FIGURE 3.6: Thermal resistance for the different cases of Toh, Chen, and Chai, (2002), validated with the experimental work of Tuckerman, (1984).

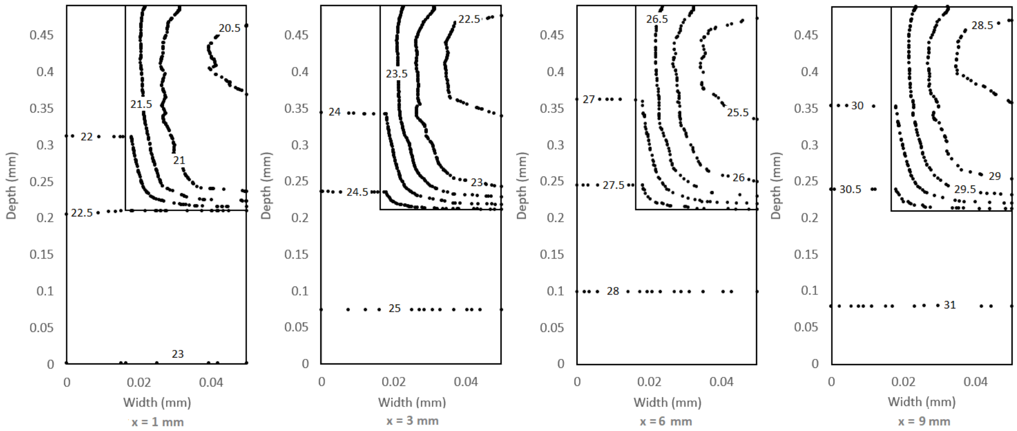

FIGURE 3.7: Temperature distribution profiles produced in COMSOL Multiphysics ® 5.4 at four different cross-sections along the microchannel for Case 0 of Toh, Chen, and Chai (2002).

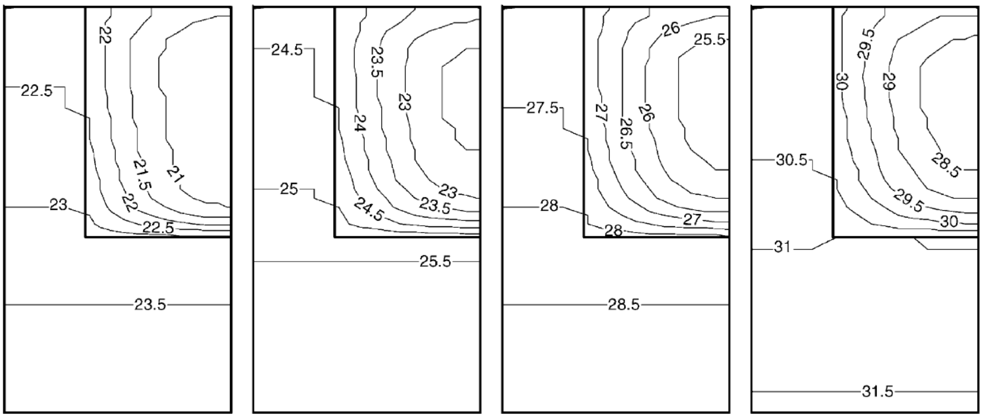

x=1 mm *x=3 mm* *x=6 mm* *x=9 mm*

FIGURE 3.8: Temperature distribution profiles at four different cross-sections along the channel for Case 0 (Toh, Chen, and Chai, 2002).

3.3 Modelling and optimising the flow and conjugate heat transfer of diverging microchannel.

In devices where PCR is performed, there is the need to operate under the three specific temperature regimes described in Chapter 2.1. In order to supply the necessary heat in the system, separate heaters are used (Papadopoulos et al., 2015; Moschou et al., 2014), applying uniform heat flux at the bottom of the solid substrate material. Due to the complexity of the CHT phenomena in such devices, the understanding of the heat flux and its uniformity at the solid-fluid interface is required. This Chapter focuses on improving the understanding of how optimising diverging microchannels can lead to a better a more uniform temperature distribution at the solid-fluid interface.

Heat flux profiles at the solid - fluid interfaces are studied in the publications of Duryodhan et al., (2016) and Moharana, Singh, and Khandekar, (2012), while the peripheral averaged local wall temperature and bulk fluid temperature at the fluid – solid interface are presented in detail in the work of Moharana, Singh, and Khandekar, (2012), for different Reynolds numbers and substrate conductivity values.

More specifically, the work of Duryodhan et al.(2016) focuses on developing a way to apply constant wall temperature on microfluidic devices at the solid-fluid interface in order to achieve a more uniform distribution and a better temperature control; two features that are quite useful in lab-on-chip technologies. This type of boundary condition is preferred, since the temperature of the fluid can never exceed the temperature of the solid (T_s) at the solid - fluid interface (Figure 3.9 (b)), ensuring a good temperature control. On the contrary, when a constant heat flux boundary condition is applied at the solid - fluid interface, the temperature of the fluid is constantly increasing with the length (Figure 3.9 (a)), including the danger of overheating. Therefore, applying a constant wall temperature at the solid - fluid interface throughout a temperature regime lead to a more controlled heating of the

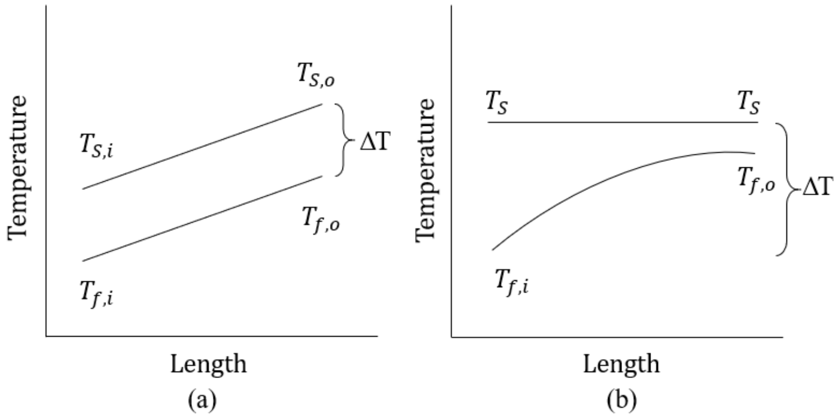

FIGURE 3.9: Thermal profile at the fully-thermally developed regime with (a) constant heat flux at the boundaries, (b) constant temperature at the boundaries (Knight, Goodling, and Hall, 1991).

fluid, and a higher yield of the reaction.

3.3.1 Setting up the simulations

Duryodhan et al.(2016) proposed a design of a diverging microchannel, in order to achieve a constant wall temperature at the solid - fluid interface. A schematic graph of the conjugate heat transfer problem studied is presented in Figure 3.10. The diverging microchannel design is compared to the one of a straight microchannel, where the temperature distribution is visualized for the mass flowrate and heat flux of 8.33 $\cdot 10^{-5}$kg/s and 4.8 W/cm^2 respectively. The surface temperature difference between inlet and outlet is compared for both the straight and diverging silicon microchannels, and it is found to be 11 and 1 °C respectively. As mentioned by Farnaghi (2017), temperature uniformity plays a very important role in duplicating DNA samples with a high quality and precision.

Moreover, four mass flowrates (4.16$\cdot 10^{-5}$ kg/s, 5.83$\cdot 10^{-5}$ kg/s, 7.50$\cdot 10^{-5}$ kg/s and 9.16$\cdot 10^{-5}$ kg/s) are implemented in a silicon diverging microchannel, and the surface temperature from the simulations is compared to the experimental values produced. A uniform heat flux of $\dot{q} = 4W$ is implemented at the bottom of the microchannel, while the thermal conductivity is modeled according to Equation 3.7. A parameter study is also performed in order to investigate the effect of divergence angle (1 - 8°), the length of the channel (10 - 30 mm), the depth (86 - 200 μm), the solid-to-fluid thickness ratio (1.5 - 4), the solid-to-fluid thermal conductivity ratio (27 - 247), the mass flow rate (4.16 - 9.16 $\cdot 10^{-5}$kg/s) and the heat flux ($\dot{q}$ = 2.4-9.6 W/cm^2) on the homogeneity in the wall temperature.

$$k = 0.0033 + 0.0019 \cdot T, \qquad 300K < T < 373K \quad (3.7)$$

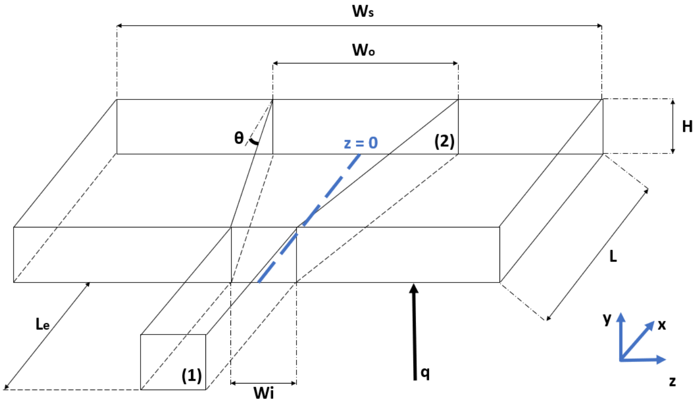

FIGURE 3.10: Schematic graph of the diverging microchannel studied in the work of Duryodhan et al. (2016)

3.3.2 Mesh Independence Study

Figure 3.11 presents the mesh independence study performed for the mass flowrate of 9.16 $\cdot 10^{-5}$ kg/s. It is observed that the 659,889 elements mesh produces similar results to the 1,182,381 elements one, and it is therefore used to obtain the results presented in Figure 3.12. As far as Figure 3.11 is concerned, it is observed that the current simulations describe well the experimental and numerical data presented in the work of Duryodhan et al. (2016). The deviation from the data in the entering and exiting parts of the channel can be explained by the missing values of some important parameters used by Duryodhan et al. (2016), such as the inlet temperature. Duryodhan et al. (2016) mention that they select: i) DI water as the working fluid, ii) a uniform heat flux of $\dot{q} = 4W$ is implemented at the bottom of the microchannel, iii) a channel depth = 86μm, iv) a diverging angle of 8^o, v) a channel length of 20 mm.

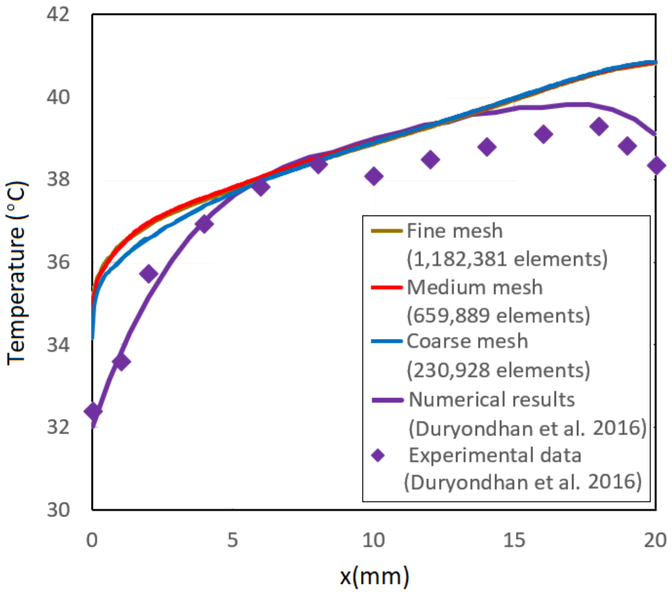

FIGURE 3.11: Mesh independence study (fine, medium, coarse) validated with the experimental (diamonds) and numerical results presented in the work of Duryodhan et al. (2016) for $\dot{m}$=9.16 $\cdot 10^{-5} kg/s$.

3.3.3 Validation with the work of Duryodhan et al.(2016)

Figure 3.12 presents the comparison between the simulations and the experiments of Duryodhan et al. (2016) and the ones produced in this work using COMSOL Multiphysics ® 5.4. The geometry simulated is half of the microchannel presented in Figure 3.10, while a symmetry plane is placed at z=0. Table 3.5 presents the values of the parameters implemented in the simulations, with silicon and water selected as the substrate and fluid materials respectively. Water enters and exits the microchannel at positions (1) and (2) respectively (Figure 3.10). An entry part of L_e length is added in the simulations, in order to ensure a fully developed flow when entering the microchannel.

As far as the boundary conditions are concerned, the top, side, inlet and outlet walls are thermally insulated, while the bottom wall is subjected to a constant uniform heat flux $\dot{q}$.

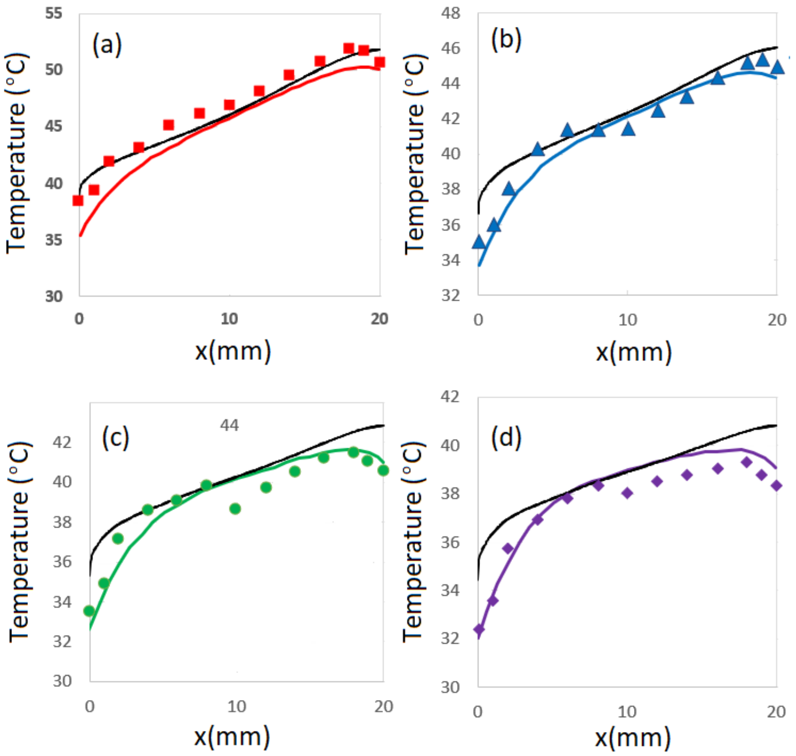

FIGURE 3.12: Comparison of the results obtained to the work of Duryodhan et al. (2016) for $\dot{m}$ = 4.16 (a), 5.83 (b), 7.5 (c) and 9.16 $\cdot 10^{-5} kg/s$ (d) for the medium mesh (659,889 elements). The black lines present the simulations in COMSOL Multiphysics, the coloured lines the numerical results of Duryodhan et al. (2016) and the different markers the experimental work of Duryodhan et al. (2016).

TABLE 3.5: Parameters implemented on the current numerical study

Parameters	Values	Parameters	Values	Parameters	Values
H (μm)	86	$\dot{q}$(W)	4	$L_e(mm)$	5
L (mm)	20	t_s/t_f(-)	2.86	$\theta(^\circ)$	8
$W_o(\mu m)$	3052	$\dot{m}_{in}(kg/s)$	9.16, 7.5, 5.83, 4.16 $\cdot 10^{-5}$	$W_s(mm)$	5
$W_i(\mu m)$	270	$T_{in}(K)$	300		

3.3.4 Optimisation Problems for diverging microchannels

Having modelled the fluid flow through a diverging microchannel and the heat transfer while implementing a constant heat flux (as described in Chapter 3.3.3), this chapter now focuses on formulating and addressing two optimisation problems. The optimisation problems consider two objective functions when varying two design variables, in order to control the temperature at the solid-fluid interface (measurement of temperature uniformity), while at the same time minimising the total pressure drop. The importance of temperature uniformity becomes more significant when it comes to devices such as heatsinks, since as mentioned earlier, the non-uniform temperature distributions in heatsinks can cause the reduction of the life span and reliability of electronic devices (He, Yan, and Zhang, 2021). At the same time, different meta-modelling techniques are used and compared.

The motivation for studying these optimisation problems is driven by the need to examine further the physics and performance of such microfluidic setups. More specifically, due to the heat conduction that takes place in the walls, when a constant heat flux is provided at the bottom solid surface of PCR devices, the heat flux is redistributed at the fluid-solid interface and it becomes no longer constant (Duryodhan et al., 2016). According to the work of Duryodhan et al. (2016), modifying the geometry of the channel could result in a more uniform temperature at the fluid-solid interface. This can be seen in Figure 3.13, where a diverging microchannel geometry is applied, and the heat flux is modified at the fluid-solid interface.

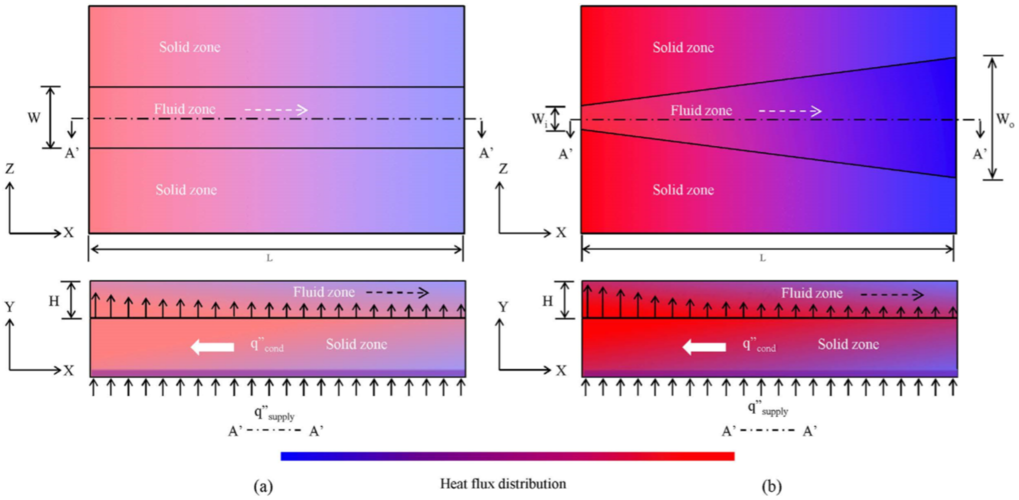

FIGURE 3.13: Schematic representation of proposed method to bring constant wall temperature wall condition (a) Uniform cross section microchannel, (b) Diverging microchannel (Duryodhan et al.,2016)

3.3.4.1 First Optimisation Problem

3.3.4.1.1 Methodology The selected design variables, their lower and upper limits as well as the two objective functions are presented in Table 3.6. The values of the limits of the design variables are chosen to be close to the ones considered in the work of Duryodhan et al. (2016). More specifically, during the parametric study performed in their work, the values of the diverging angles studied are between 0 and 8°, while the value of W_i selected for the simulations is set to 270 μm.

As far as the objective functions are concerned, the first one (Obj_1, Table 3.6) provides a measurement of the uniformity in wall temperature at the bottom of the diverging microchannel, while the second one (Obj_2, Table 3.6) is the pressure drop along the channel (between (1)-(2)). The first objective function is formed as the sum of the squares of the temperature differences between the centre line and the corner of the diverging microchannel, at locations $x = L/4, L/3, 3L/4$ and L. The four pairs of points where the temperature differences are calculated are presented in Figure 3.14 as star points.

TABLE 3.6: Design Variables and Objective Functions of the optimisation problem

	Design Variables	Lower Limit	Upper Limit	Objective Functions
1	$W_i(\mu m)$	210	330	$Obj_1 = \sum_{i=1}^{4}(T_{centre,i} - T_{corner,i})^2$
2	$\theta(°)$	2	10	$Obj_2 = \Delta P_{(1)-(2)}$

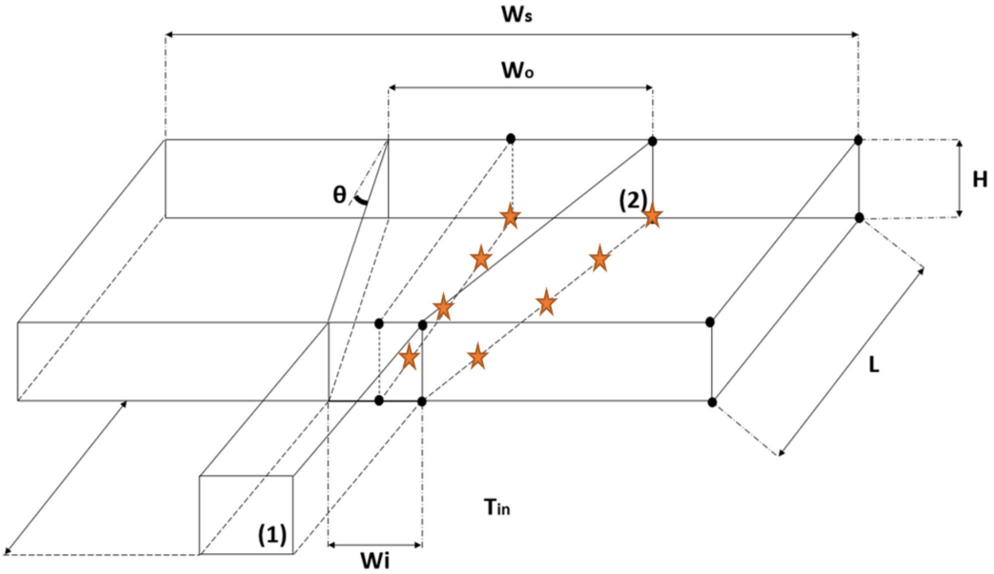

FIGURE 3.14: Schematic representation of the points where the temperature differences are calculated for Obj_1.

3.3.4.1.2 Design of Experiments In this step, the formulation of the DoE points takes place using the Morris Mitchell Latin Hypercube method (Chapter 2.5.1.3). The number of the DoE points, design variables, populations and iterations used to create them are set at 30, 2, 50 and 50 respectively. The second and third columns of Table B.1 (Chapter B of Appendix) present the produced DoE points.

After completing this step, the model designed in COMSOL ® 5.4 is run for all the DoE points and the values of the two objective functions are collected/calculated (Table B.1, Chapter B of Appendix). The data are introduced to MATLAB® for the generation of the response surfaces and the optimisation of the device.

3.3.4.1.3 Results

Response Surfaces Three types of Radial Basis Functions (RBF) (Chapter 2.5.3.4) are used and compared; inverse multi-quadric, the multi-quadric and the gaussian (see Table 2.7). The response surfaces of the two objective functions, Obj_1 and Obj_2 (Table 3.6), are presented in Figures 3.15 and 3.16 and appear to have similarities.

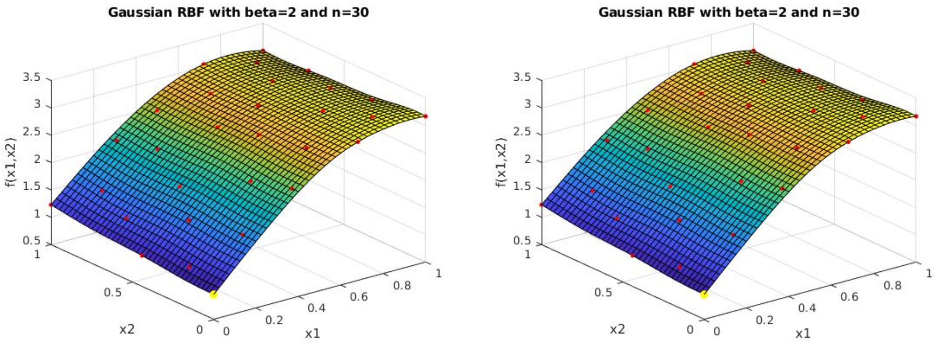

(A) RBF: Gaussian, GA

(B) RBF: Gaussian, PSO

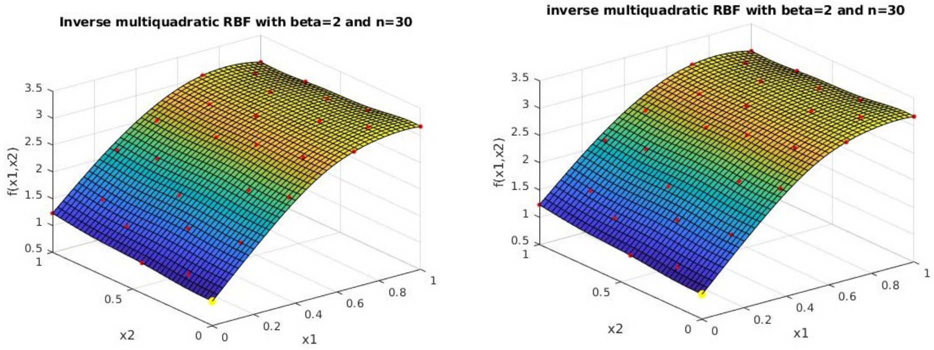

(C) RBF: Inverse Multiquadratic, GA

(D) RBF: Inverse Multiquadratic, PSO

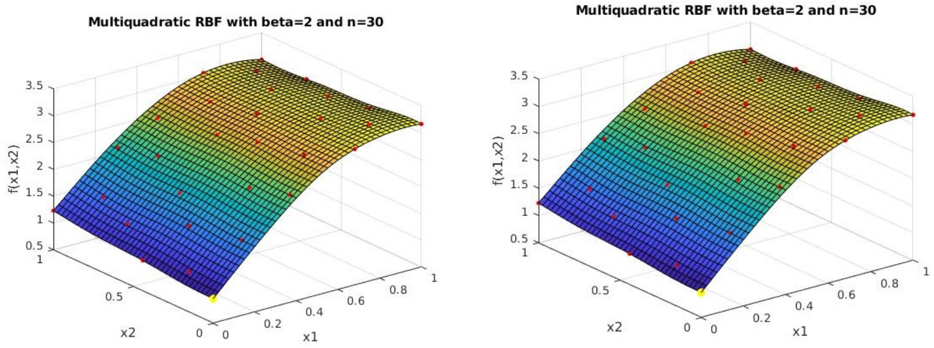

(E) RBF: Multiquadratic, GA

(F) RBF: Multiquadratic, PSO

FIGURE 3.15: Response surfaces for Obj_1: Gaussian with (a) GA and (b) PSO, Inverse Multi-quadratic with (c) GA and (d) PSO, Multiquadratic with (e) GA and (f) PSO.

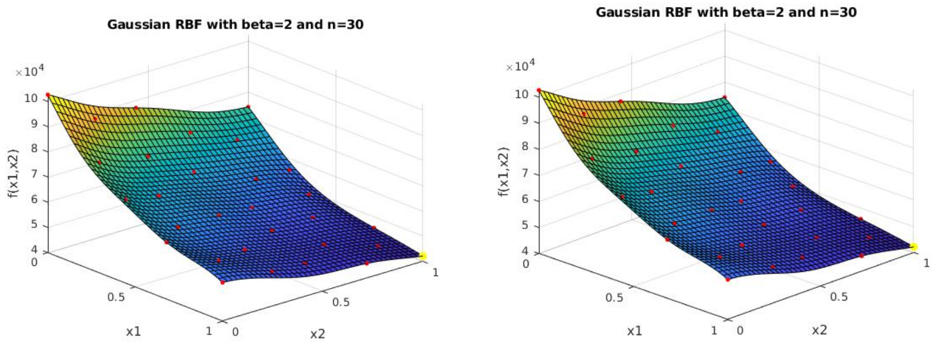

(A) RBF: Gaussian, GA (B) RBF: Gaussian, PSO

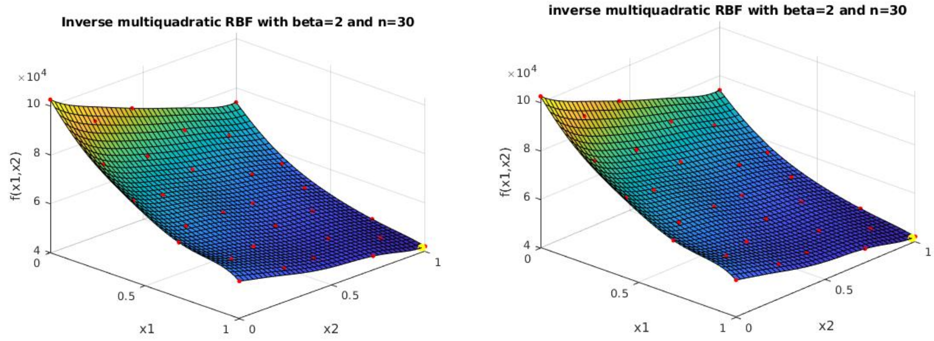

(C) RBF: Inverse Multiquadratic, GA (D) RBF: Inverse Multiquadratic, PSO

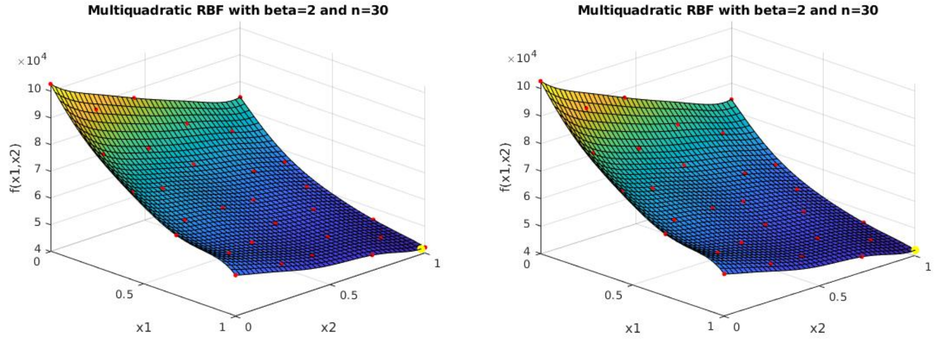

(E) RBF: Multiquadratic, GA (F) RBF: Multiquadratic, PSO

FIGURE 3.16: Response surfaces for Obj_2: Gaussian with (a) GA and (b) PSO, Inverse Multi-quadratic with (c) GA and (d) PSO, Multi-quadratic with (e) GA and (f) PSO.

Optimisation As far as the optimisation techniques are concerned, the i) Genetic Algorithm (GA) and ii) the Particle Swarm Optimisation (PSO) techniques are used to find the optimum designs for the two objective functions, after the response surfaces are created. The optimum points are presented in Tables 3.7 and 3.8, and all methods appear to be in agreement with each other. Both GA and PSO appear to obtain the optimum designs at the corners of the design domain for both objective functions. More specifically, the best temperature uniformity (minimum values of Obj_1) is obtained for the smallest θ and W_i values, while the minimum pressure drop (minimum values of Obj_2) is obtained for the greatest θ and W_i values. However it can be observed that the optimum design for one objective results in high values for the other objective. As a result, no single design optimises both objectives at the same time. As part of a multi-objective study, the pareto front curve is generated, in order to obtain the available compromises between the two competing objectives.

TABLE 3.7: RBF-assisted optimisation using Genetic Algorithm for Obj_1 and Obj_2

Optimum Points	θ (°)	$W_i(\mu m)$	Obj_1	θ (°)	$W_i(\mu m)$	Obj_2	RBF Method
1	2	210.03	0.964	10	329.97	42,119.80	IMQ
2	2	210.07	0.963	10	329.83	42,119.85	MQ
3	2	210.00	0.962	10	330.00	42,119.73	G

G: Gaussian, MQ: Multi-quadric, IMQ: Inverse Multi-quadric

TABLE 3.8: RBF-assisted optimisation using Particle Swarm Optimisation for Obj_1 and Obj_2

Opt. Points	θ (°)	$W_i(\mu m)$	Obj_1	θ (°)	$W_i(\mu m)$	Obj_2	RBF Method
1	2	210.04	0.963	10	329.95	42,119.90	IMQ
2	2	210.06	0.964	10	329.84	42,119.88	MQ
3	2	210.00	0.962	10	330.00	42,119.73	G

G: Gaussian, MQ: Multi-quadric, IMQ: Inverse Multi-quadric

More specifically, for the Multi-Objective Genetic Algorithm-based optimisation, the RBF (Chapter 2.5.3.4) and the Moving Least Squared method (MLSM) (Chapter 2.5.3.1) are used to create the response surfaces for the two objective functions. The MLSM method is examined in order to compare the results obtained by the two techniques. The Genetic Algorithm is used to produce the optimum points for the two objective functions, for both the RBF- and MLSM-based methods. Then, the Pareto front curves are created for both the RBF- and MLSM-based methods, and they are compared (Figure 3.17). The values used to generate the Pareto fronts are dimensionless and scaled between 0 and 1.

The two Pareto fronts present great similarities. Three points of the RBF-based Pareto front are selected to be validated, as presented in Figure 3.17 (blue squares).

TABLE 3.9: Evaluation of the three selected points

Selected	Pareto Front		Response Surface		COMSOL ®	
Points	Obj_1	Obj_2	$\theta(^\circ)$	$W_i(\mu m)$	Obj_1	Obj_2
Point 1	2.476	55,851.34	5.20	309	2.511	55,850.4
Point 2	2.757	50,038.86	6.22	324	2.772	50,161.4
Point 3	2.960	47,275.62	7.26	324	2.965	47,558.9

For the same values of design variables, simulations are performed using the model developed in COMSOL Multiphysics ®, obtaining the points marked with red circular shapes in Figure 3.17. These points appear to be very close to the selected-for-validation points.

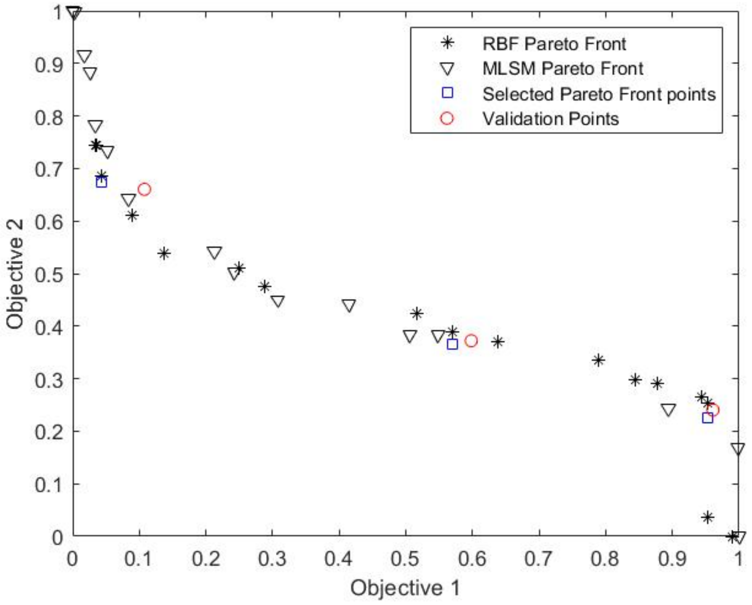

FIGURE 3.17: Pareto Fronts for RBF and MLSM assisted optimisation, including the points to be validated.

Figure 3.18 presents the geometry of the microfluidic channel for the Points appearing in Table 3.9. Point 1 of the Pareto front curve (Figure 3.17) describes a microchannel with a smaller inlet hydraulic diameter and a smaller diverging angle. This geometry is indeed expected to produce higher values of pressure drop and temperature distribution in the z-axis. Points 2 and 3 present geometries with higher diverging angles, and are therefore expected to produce higher pressure drop compared to Point 1. They both have similar inlet hydraulic diameters, but the diverging angle of Point 3 is higher than Point 2; it is therefore expected that Point 3 has greater temperature variation in z-axis and smaller pressure drop compared to Point 2.

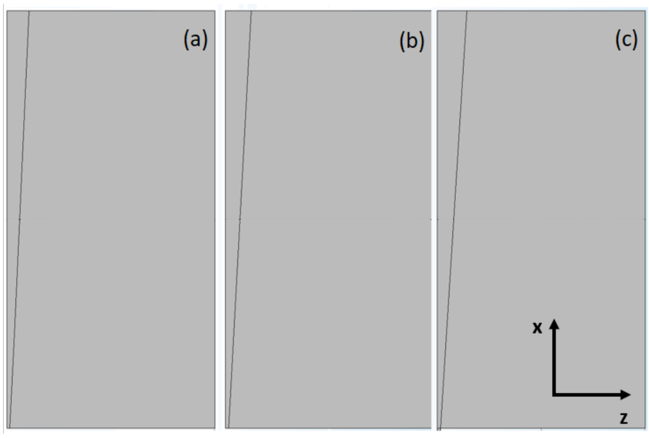

FIGURE 3.18: Geometry setup for (a) Point 1 (Wi (μm): 309, $\theta(^{\circ})$: 5.20), (b) Point 2 (Wi (μm): 324, $\theta(^{\circ})$: 6.22) and (c) Point 3 (Wi (μm): 324, $\theta(^{\circ})$: 7.26) presented in Table 3.9.

3.3.4.2 Second Optimisation Problem

3.3.4.2.1 Methodology In the second optimisation problem, the effect of varying two different design variables is explored. This problem is formulated in order to obtain the design that offers the best temperature uniformity and minimum pressure drop, for a constant volume of fluid. The design variables, their lower and upper limits as well as the two objective functions are presented in Table 3.10. The upper and lower limits of the design variables are at 0 and 5° respectively, in order to include the design of the straight channel as well. As far as the objective functions are concerned, Obj_2 is used to describe the pressure drop across the channel (see Chapter 3.3.4.1). Obj_1 is used to examine the temperature variation between the corner of the bottom solid-fluid interface to the volumetric average temperature.

TABLE 3.10: Design Variables and Objective Functions of the 3^{rd} optimisation problem

	Design Variables	Lower Limit	Upper Limit	Objective Functions
1	$\theta_1(^{\circ})$	0	5	$Obj_1 = (T_{ABC} - T_{Vol_{Ave}})^2$
2	$\theta_2(^{\circ})$	0	5	$Obj_2 = \Delta P_{(1)-(2)}$

The simulations are performed using COMSOL Multiphysics ® while: a) keeping the volume and volumetric inlet flow of the fluid constant in all cases and b) varying the inlet width of the microchannel (W_{AD}) and the two diverging angles, θ_1 and θ_2 (Figure 3.19). Equations 3.8-3.13 are used to calculate W_{AD} for the values of θ_1 and θ_2 of Table B.2 (Appendix Chapter B.2), considering a constant fluid volume or in this case fluid-solid interface area for simplicity ($4 \cdot 10^{-5}$ m^2). Table 3.11 presents the values of the parameters and variables of this optimisation problem. After running the simulations, the values of the two objective functions are calculated and added in Table B.2 of Chapter B.2 of Appendix. The data are then introduced to MATLAB®.

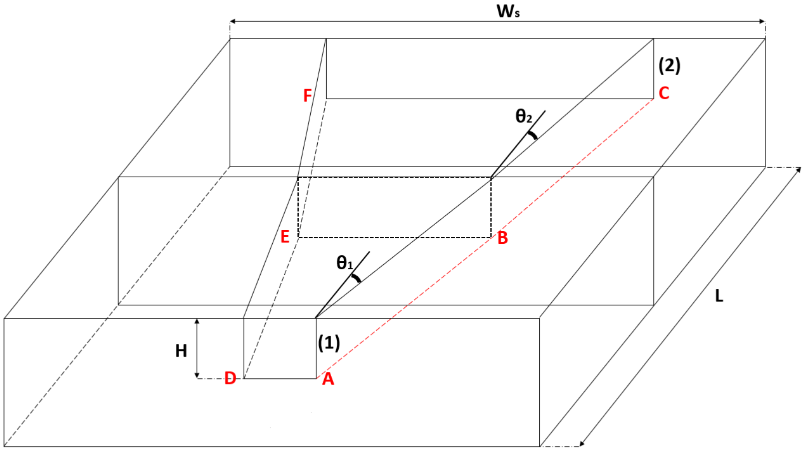

FIGURE 3.19: Schematic graph of the diverging microchannel for the third optimisation problem

$$E_{tot} = E_{ABED} + E_{BCFE} \tag{3.8}$$

$$E_{ABED} = \frac{L}{4}(W_{AD} + W_{BE}) \tag{3.9}$$

$$E_{BCFE} = \frac{L}{4}(W_{BE} + W_{CF}) \tag{3.10}$$

$$W_{BE} = 2tan(\theta_1)\frac{L}{2} + W_{AD} \tag{3.11}$$

$$W_{CF} = 2tan(\theta_2)\frac{L}{2} + W_{BE} \tag{3.12}$$

$$(3.8) - (3.12) : W_{AD} = \frac{1}{L}[E_{tot} - \frac{L^2}{4}(3tan(\theta_1) + tan(\theta_2))] \tag{3.13}$$

TABLE 3.11: Parameters and variables implemented on the current numerical studies

Parameters	Values	Parameters	Values	Parameters	Values
H (μm)	86	$\dot{q}$(W)	2	$T_{in}(K)$	305
L (mm)	20	$W_s(mm)$	5	$\dot{m}_{in}(kg/s)$	$8.33 \cdot 10^{-5}$
$W_{AD}(\mu m)$	Eq.(3.13)	$W_{BE}(\mu m)$	Eq.(3.11)	$W_{CF}(\mu m)$	Eq.(3.12)

3.3.4.2.2 Design of Experiments The DoE points are generated using the MMLH method (Chapter 2.5.1.3), and they are presented in Chapter B.2 of Appendix (Table

B.2). The number of DoE points, design variables, populations and iterations used to create them are 50, 2, 50 and 50 respectively.

3.3.4.2.3 Results

Response surfaces The methods examined are similar to the ones presented in Chapter 3.3.4.1. The response surfaces are presented in Figures 3.20 and 3.21.

Optimisation For the Single-Objective RBF-assisted optimisation, the optimum points produced by the GA and PSO are presented in Table 3.12.

A significant drop can be observed in the response surfaces of Obj_2 (Figure 3.21) for values of X_1 and X_2 approach 1. Even though, the smallest values of pressure drop are expected for the highest values of X_1, X_2, the steep slope can be explained by the low number of data points in this area of the design domain.

It can be observed that the optimum values presented in Table 3.12 are similar for both GA and PSO for Obj_1 and Obj_2. Furthermore, both the smallest pressure drop and variation of the temperature from the volumetric average value are observed for the largest diverging angle of 5^o. As a result, no multiobjective optimisation problems will be studied in this case.

TABLE 3.12: RBF-assisted optimisation - Genetic Algorithm and Particle Swarm Optimisation

Opt. Method	Points	$\theta_1(^\circ)$	$\theta_2(^\circ)$	Obj_1	$\theta_1(^\circ)$	$\theta_2(^\circ)$	Obj_2	RBF Method
GA	1	5.000	5.000	$41.363 \cdot 10^{-2}$	5.000	5.000	8,716.00	G
	2	5.000	4.925	$41.339 \cdot 10^{-2}$	5.000	5.000	8,716.00	MQ
	3	5.000	4.950	$41.356 \cdot 10^{-2}$	5.000	5.000	8,716.00	IMQ
PSO	1	5.000	5.000	$41.363 \cdot 10^{-2}$	5.000	5.000	8,716.00	G
	2	5.000	4.925	$41.339 \cdot 10^{-2}$	5.000	5.000	8,715.88	MQ
	3	5.000	5.000	$41.363 \cdot 10^{-2}$	5.000	5.000	8,716.00	IMQ

G: Gaussian, MQ: Multi-quadric, IMQ: Inverse Multi-quadric

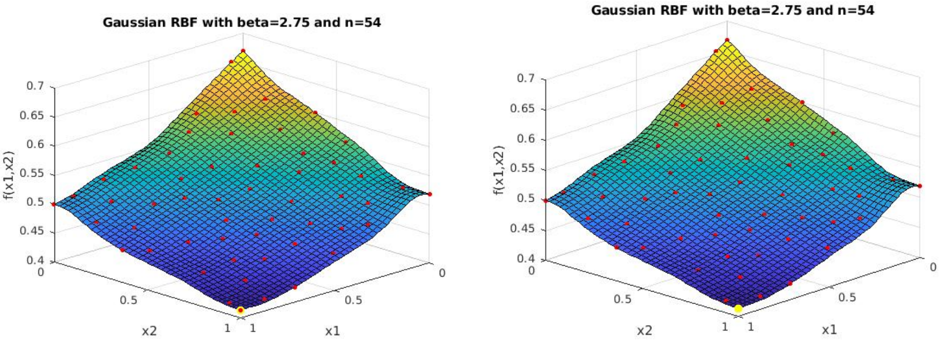

(A) RBF: Gaussian, GA

(B) RBF: Gaussian, PSO

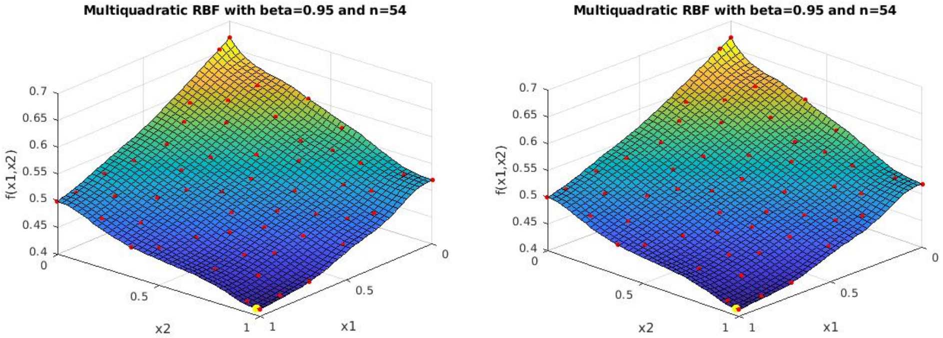

(C) RBF: Multiquadratic, GA

(D) RBF: Multiquadratic, PSO

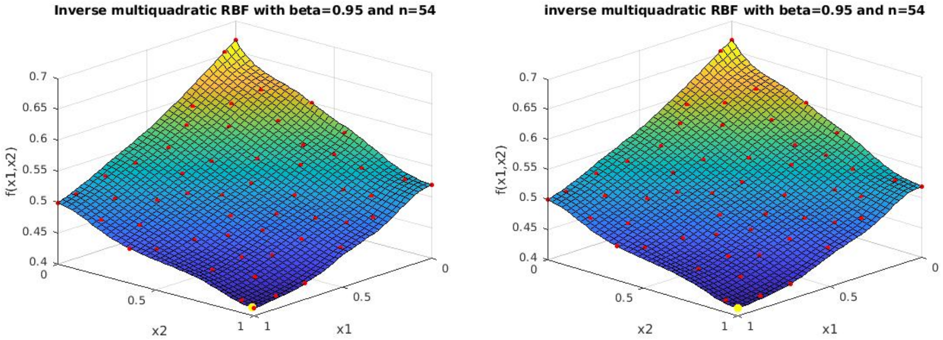

(E) RBF: Inverse Multiquadratic, GA

(F) RBF: Inverse Multiquadratic, PSO

FIGURE 3.20: Response surfaces for Obj_1: Gaussian with (a) GA and (b) PSO, Multi-quadratic with (c) GA and (d) PSO, Inverse Multi-quadratic with (e) GA and (f) PSO.

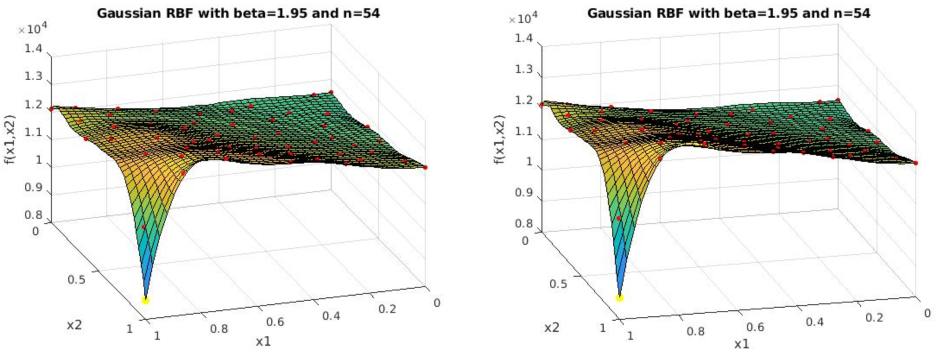

(A) RBF: Gaussian, GA (B) RBF: Gaussian, PSO

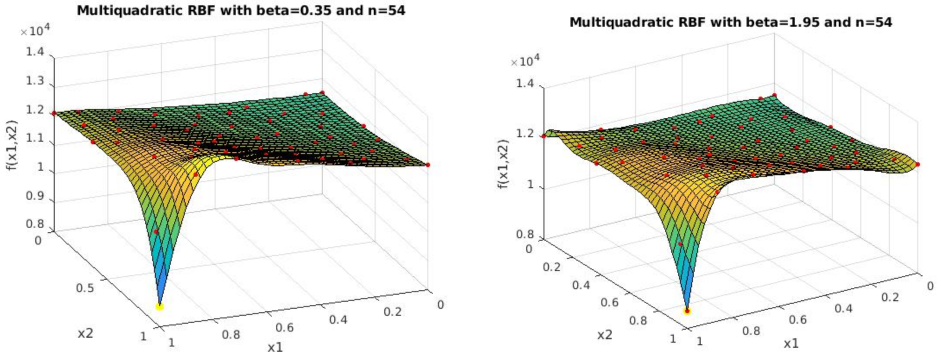

(C) RBF: Multiquadratic, GA (D) RBF: Multiquadratic, PSO

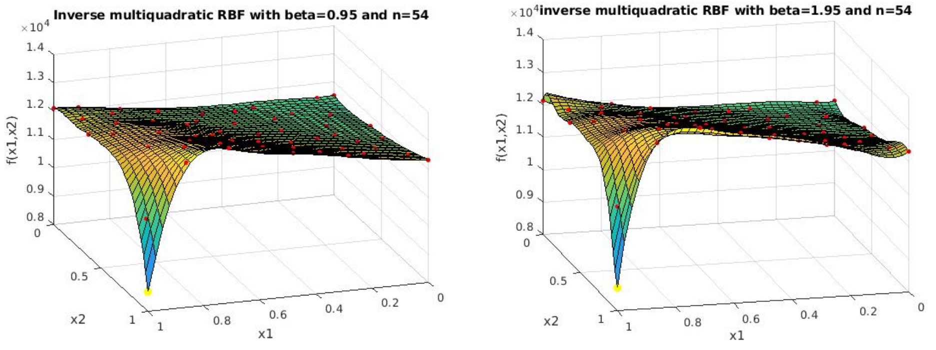

(E) RBF: Inverse Multiquadratic, GA (F) RBF: Inverse Multiquadratic, PSO

FIGURE 3.21: Response surfaces for Obj_2: Gaussian with (a) GA and (b) PSO, Multi-quadratic with (c) GA and (d) PSO, Inverse Multi-quadratic with (e) GA and (f) PSO.

3.3.5 Summary

According to the results obtained in this Chapter, increasing the diverging angle and the hydraulic diameter reduces the temperature uniformity (across the axis perpendicular to the axis of the channel) at the solid-fluid interface (in agreement with the results of Duryodhan et al. (2016)). At the same time, the increase of the diverging angle and the hydraulic diameter are found to lead to a decrease in the pressure drop, which is in agreement with the findings of Duryodhan, Singh, and Agrawal (2013). Hence, when developing/testing such channel geometries, developing the Pareto Front is expected to be beneficial in the designing process.

Furthermore, when maintaining a constant volume of fluid in such channel geometries while varying the diverging angles (and at the same time adjusting the hydraulic diameter), the higher the diverging angles, the better the temperature uniformity (between the volumetric average and the temperature along the channel corner edge at the solid-fluid interface) and smaller pressure drop. The results obtained with regards to the temperature uniformity appear to be in agreement with the work of Duryodhan et al. (2016)). The behaviour of the pressure drop profile along the design domain appears to have similarities with the results presented in the work of Duryodhan, Singh, and Agrawal (2013).

As part of all these studies, different algorithms/methods have been used and compared to develop the response surfaces and generate the optimum designs. The inverse multi-quadric, the multi-quadric and the Gaussian Radial Basis Functions (RBF) successfully managed to generate the response surfaces for all optimisation studies considered. Both genetic algorithm (*ga* MATLAB® function) and Particle Swarm Optimisation (PSO) method (*particleswarm* MATLAB® function) successfully managed to obtain the global optimum solutions.

3.4 Modelling and optimising PCR in a unitcell.

This Chapter describes the simulations conducted on a unitcell of a CF-PCR device (Figure 3.23), that works as the basic unit of a CF-PCR device (Figure 3.22). The mathematical model described in Section 3.4.2 is introduced in COMSOL Multiphysics ® 5.4. A template of the code used in Matlab to run the DOE is presented in Appendix J (the inputs and outputs of the functions present in the code are modified depending on each optimisation problem).

3.4.1 Setting up the simulations

The design of the microchannel is based on the one presented in the work of Papadopoulos et al. (2015). The dimensions of the design parameters and the material properties of the serpentine channel are presented in Tables 3.13 and 3.14 respectively. Three temperature regimes are created along the microchannel for the denaturation, annealing and extension zones. The properties of the fluid simulated are

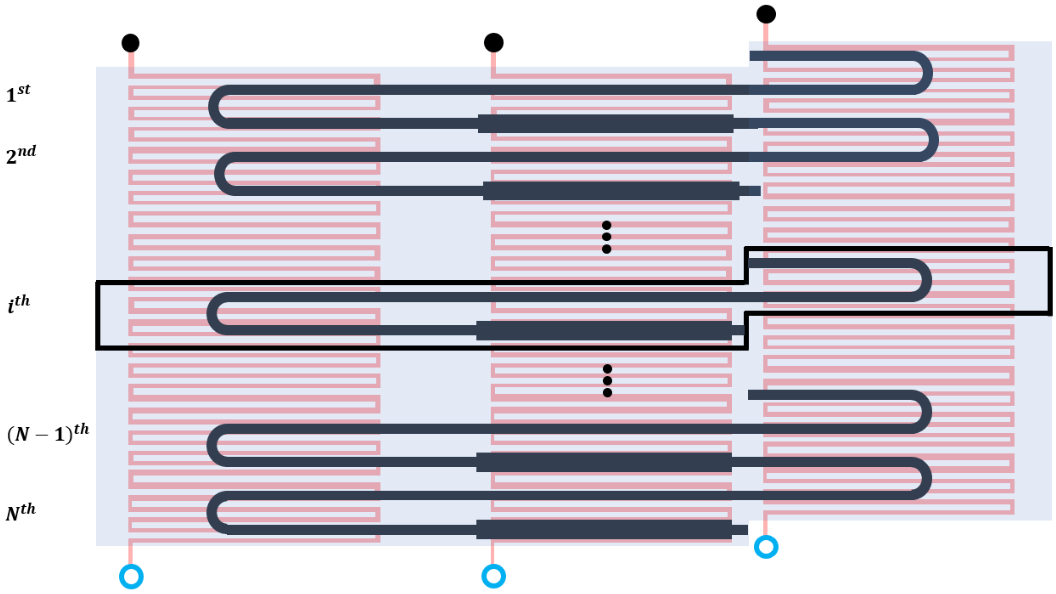

FIGURE 3.22: Schematic graph of the μPCR device, consisting of N cycles (top view).

the ones of water, while the kinetics of PCR are described in detail in Chapter E of the Appendix. The values of the volumetric flowrate at the inlet (Q_{vol}), the ambient temperature (T_{amb}), the heat transfer coefficient (h) and the heights of Kapton, PDMS and PE (H_{Kapton}, H_{PDMS}, H_{PE}) are set equal to the ones appearing in the work of Papadopoulos et al. (2015) (Table 3.13). The length of the serpentine channel in each temperature regime (denaturation, annealing, extension) varies in each simulation, and is calculated by Equation 3.16 (for the different values of W_2 and H_{Fluid}). Natural heat convection occurs at the walls of the channel, as illustrated in Figure 3.23. The ambient temperature and heat transfer coefficient are set to $T_{amb} = 25^oC$ and $h = 5W/(m^2 \cdot K)$ respectively. As far as the surface-to-ambient radiation is concerned, the surface emissivity of all materials is presented in Table 3.14.

Several optimisation problems are studied with different design variables and objective functions, as presented in Tables 3.15 and 3.16. The minimum number of sampling DoE points for these studies is selected according to the "10k" rule described in Chapter 2.5.1.1, with am extra factor of 4 added in order to allow a good exploration of the design domain (Jones, Schonlau, and Welch, 1998; Li et al., 2019). In the optimisation problem described in Chapter 3.4.5, the variable W_2 (width of the channel in denaturation and annealing) varies in the simulations, while the width of the channel in the extension zone is always kept double that value. The average velocity in each regime is calculated by Equations 3.14 and 3.15, for the different cases of W_2 and H_{Fluid}. While varying W_2, the length of the channel in each temperature zone varies according to Equation 3.16 in order to achieve the PCR protocol used in the work of Papadopoulos et al. (2015); 3s:4.2s:6.2s. By varying the three lengths, all simulations have the same values of residence time in each temperature regime, allowing the effect of geometry on the objectives to be studied. In the optimisation

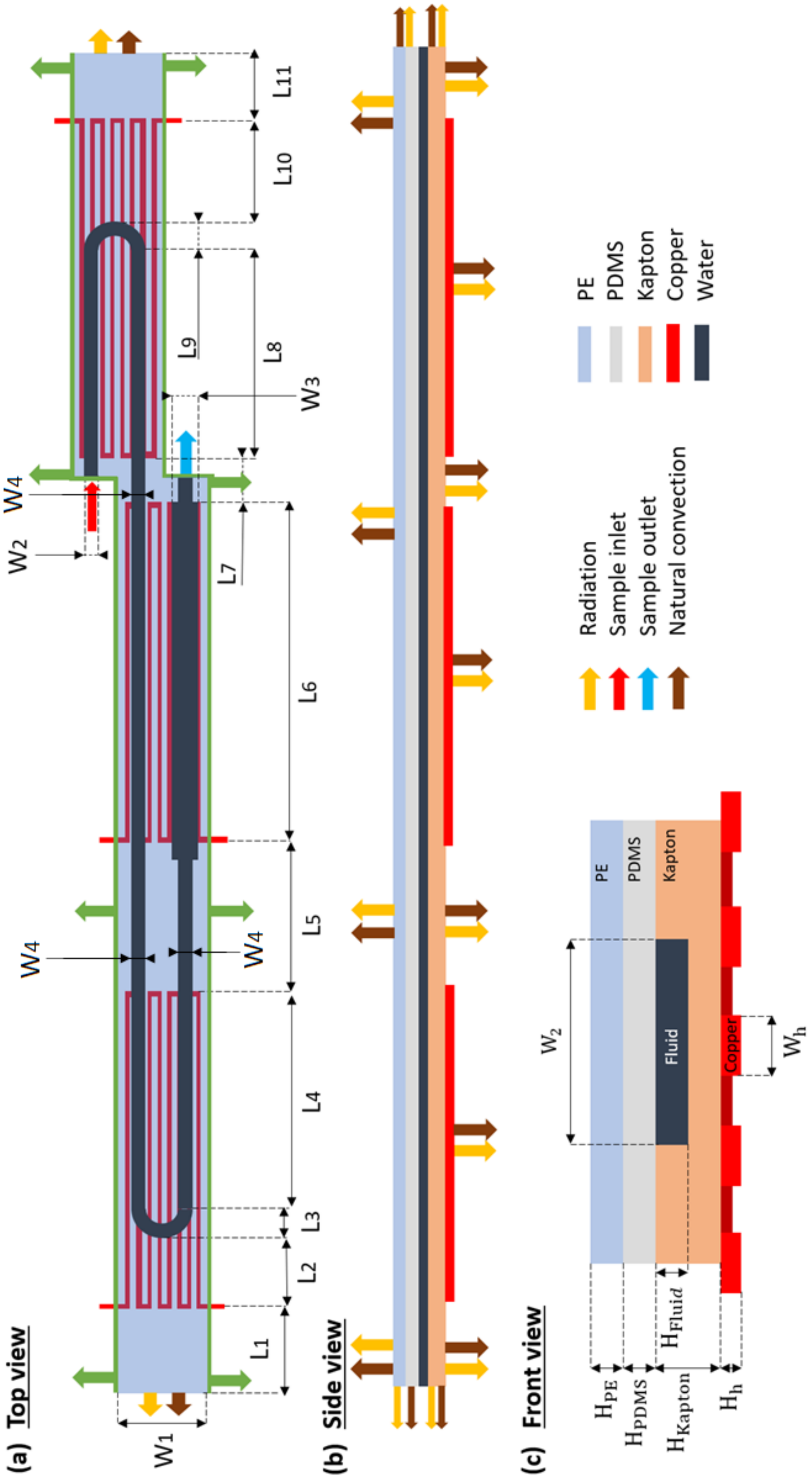

FIGURE 3.23: Unitcell of a CF-PCR device: a) top view, b) side view, c) front view.

TABLE 3.13: Design Parameters of the Microchannel

Parameter	Values	Description
U_{in} $[mm/s]$	Equation 3.14	Average inlet velocity (fully developed)
Q_{vol} $[\mu L/min]$	1.800*	Volumetric flowrate
$T_{amb}[K]$	298.15*	Ambient temperature
$h[W/(m^2 \cdot K)]$	5*	Heat transfer coefficient
L_1 $[mm]$	4.190*	See Figure 3.23
L_2 $[mm]$	0.714*	See Figure 3.23
L_3 $[mm]$	0.500*	See Figure 3.23
L_4 $[mm]$	Equation 3.16	See Figure 3.23
L_6 $[mm]$	Equation 3.16	See Figure 3.23
L_8 $[mm]$	Equation 3.16	See Figure 3.23
L_9 $[mm]$	0.500*	See Figure 3.23
L_{10} $[mm]$	3.114*	See Figure 3.23
L_{11} $[mm]$	2.000*	See Figure 3.23
W_1 $[mm]$	2	See Figure 3.23
H_{Kapton} $[\mu m]$	100*	See Figure 3.23
H_{PDMS} $[\mu m]$	50*	See Figure 3.23
H_{PE} $[\mu m]$	50*	See Figure 3.23

* Values obtained by Papadopoulos et al. (2015)

TABLE 3.14: Material properties

Material	Heat Capacity [J/(kg K)]	Density [kg/m^3]	Thermal conductivity coefficient [W/(mK)]	Surface emissivity [-]
Copper	$358 + 0.09623384 \cdot T$	8960	401	0.6[2]
Kapton	1090	1420	0.1200	0.78[1]
PDMS	1430	983	0.1511	0.96[1]
PE	2400	950	0.4450	0.92[1]

[1] Papadopoulos et al. (2015), [2] Moschou et al. (2014)

TABLE 3.15: Design variables and objectives of the four optimisation problems.

Optimisation Problem	Chapter	Design Variables (see Figure 3.23)	Objective Functions
OP1	3.4.5	W_2, H_{Fluid}	$log_2 \frac{[DNA]}{[DNA]_o}$, ΔP
OP2	3.4.6	L_5, L_7	$log_2 \frac{[DNA]}{[DNA]_o}$, ΔP
OP3	3.4.7	L_{gap} (L_5=L_7=L_{gap}), W_{gap} (W_4 = W_{gap})	$log_2 \frac{[DNA]}{[DNA]_o}$, ΔP
OP4	3.4.8	$t_{R,den}$,$t_{R,ext}$,$t_{R,ann}$, W_3	$log_2 \frac{[DNA]}{[DNA]_o}$, ΔP, $t_{R,total}$ and $V_{s,total}$

problems described in Chapter 3.4.6-3.4.7, W_2 and H_{Fluid} are kept constant at 200 μm and 50 μm, adopting the design of Papadopoulos et al. (2015). Chapter 3.4.6 presents the optimisation of the spacing between the heaters, while Chapter 3.4.7 presents the optimisation of the channel width and length in the regions between the heaters. Chapter 3.4.8 describes a more complex optimisation problem, that investigates the effect that the PCR protocol can have on four objective functions, together with the

TABLE 3.16: Additional details of the four optimisation problems.

Variables/ Parameters	OP1	OP2	OP3	OP4
$t_{R,den}$ (s)	3*	3*	3*	**DV**
$t_{R,ext}$ (s)	6.2*	6.2*	6.2*	**DV**
$t_{R,ann}$ (s)	4.2*	4.2*	4.2*	**DV**
H_{Fluid} (μm)	**DV**	50*	50*	50
W_2 (μm)	**DV**	200*	200*	400
W_3 (μm)	$2W_2^*$	400*	400*	**DV**
W_4 (μm)	W_2^*	200*	**DV**	400
L_5 (μm)	1670*	**DV**	**DV**	1670*
L_7 (μm)	1110*	**DV**	L_5	1110*

* Values obtained from Papadopoulos et al. (2015),
DV: Design Variable.

TABLE 3.17: Nomenclature of the objectives.

Description of objective	Objective	Symbols Real values/ dimensions	 Dimensionless and scaled (0-1)
DNA amplification	$log_2 \frac{[DNA]}{[DNA]_o}$ $(-)$	O1	obj_1^*
Pressure Drop	ΔP (Pa)	O2	obj_2
Total residence time	$t_{R,total}$ (s)	O3	obj_3
Total substrate volume	$V_{s,total}$ (m^3)	O4	obj_4

* The dimensionless and scaled (0-1) values of $log_2 \frac{[DNA]}{[DNA]_o}$ $(-)$, obj_1, are calculated using the negative of $log_2 \frac{[DNA]}{[DNA]_o}$, in order to switch to a minimisation study.

width of the channel in the extension zone.

Four objective functions are considered in these four optimisation problems; i) $log_2(\frac{[DNA]}{[DNA]_o})$ (O1), where $[DNA]$ is the DNA concentration at the end of the channel and $[DNA]_o$ the initial DNA concentration, ii) the pressure drop along the microchannel (O2), the total residence time (O3) and iv) and the total substrate volume (O4). The nomenclature of the objectives that is adapted from hereon is presented in Table 3.17. The reduction of the total substrate volume and total residence time can lead to cost and performance time reduction of the device respectively. The pressure drop is selected as one of the objectives of interest in order to facilitate the development of microfuidic pumps for lab-on-chip devices, that are often sophisticated and expensive (Ahn et al., 2004; Fajrial et al., 2021; Zagklavara et al., 2022).

$$U_{in} = Q_{vol}/A \tag{3.14}$$

$$A = W_2 \cdot H_{Fluid} \tag{3.15}$$

$$L_{zone} = \begin{cases} \frac{(u_{zone} \cdot t_{R,zone} - \pi R_{zone})}{2} = \frac{Q_{vol} \cdot t_{R,zone}/(W_2 \cdot H_{Fluid}) - \pi R_{zone}}{2}, & \text{zone:DEN, ANN.} \\ u_{zone} \cdot t_{R,zone} = Q_{vol} \cdot t_{R,zone}/(W_3 \cdot H_{Fluid}) & \text{zone: EXT.} \end{cases} \quad (3.16)$$

3.4.2 Model in COMSOL Multiphysics ®

This Chapter describes the model implemented in COMSOL Multiphysics ®. The boundary conditions implemented are presented in Figure 3.23, and together with the initial conditions are explained in detail in Chapters 3.4.2.1-3.4.2.4.

3.4.2.1 Fluid Flow

The fluid flow in this type of devices is laminar since an indicative value of $Re = 0.35$ (Equation 3.17) can be calculated for a temperature of 72 ^{o}C with $Q_{vol} = 3 \cdot 10^{-11} m^3/s$, H_{Fluid} = 50 μm, W_2 = 100 μm and the fluid properties of water. As a result, the Laminar Flow model of COMSOL Multiphysics ® 5.4 is selected to describe the laminar flow field. For i) a steady-state problem and ii) an incompressible fluid, the Navier-Stokes Equations take the form of Equations 3.18 and 3.19.

$$Re = D_h \cdot U_{in} \cdot \rho/\mu = (\frac{2H_{Fluid}W_2}{H_{Fluid} + W_2})\frac{U_{in} \cdot \rho}{\mu} = 0.35 \quad (3.17)$$

$$\rho(\mathbf{u} \cdot \nabla)\mathbf{u} = \nabla \cdot [-p\mathbf{I} + \mu(\nabla\mathbf{u} + (\nabla\mathbf{u})^T)] + \mathbf{f} \quad (3.18)$$

$$\rho\nabla \cdot (\mathbf{u}) = 0 \quad (3.19)$$

As far as the boundary conditions implemented are concerned:

i) the no-slip boundary condition is applied at the walls of the microchannel, assuming that at a solid boundary, the fluid has zero velocity relative to the boundary,

ii) a fully developed flow, and a value of the average inlet velocity, U_{in}, are applied at the inlet of the serpentine channel, given by Equations 3.14 and 3.15.

iii) a zero (relative) pressure boundary condition is applied at the exit of the microchannel (equal to 1 atm in absolute pressure).

As far as the initial conditions are concerned:

i) the initial average velocity is set to $\mathbf{u}$ = (U_{in}, 0,0), as it is derived by Equations 3.14 and 3.15.

ii) the initial relative pressure is set to its default value, 0 (equal to 1 atm in absolute pressure).

Furthermore, the presence of gravity has been ignored in all simulations ($\mathbf{f}$=$\mathbf{0}$), assuming no effect on the gravity on the vertical components of the velocity vector.

3.4.2.2 Heat Transfer

The heat transfer model used to describe both fluid and solids includes multiple heat transfer phenomena that take place in the system (conjugate heat transfer, thermal radiation etc). The model is implemented in steady-state in all problems studied (Equation 3.20), with the velocity **u** in Equation 3.20 set to zero for all domains except for the fluid one.

$$\rho C_p(\mathbf{u} \cdot \nabla T) = \nabla \cdot (k \nabla T) + Q_{heater,j} + Q_{rad,i} + Q_{nat.conv} \tag{3.20}$$

The first term on the LHS and the first term on the RHS of Equation (3.20) express the heat transfer due to convection and conduction respectively. $Q_{heater,j}$ is the heater generation rate of the j^{th} (j = {1, 2, 3}) heater, and is only non-zero at the j^{th} heater-kapton interface. A different heat generation rate is required at each heater to achieve the desired set point (95, 55, and 72^{o}C at denaturation, annealing and extension respectively). $Q_{rad,i}$ is the heat flux due to thermal radiation (Equation 3.21 (Stefan-Boltzmann law)) of the i^{th} solid substrate (i = {Copper, PDMS, PE, Kapton}), and is only non zero at the outer surfaces of the substrate materials. $Q_{nat.conv}$ is the heat flux due to the heat losses to the ambient, and is given by Equation 3.22:

$$Q_{rad,i} = \epsilon_i \sigma (T_{amb}^4 - T^4) \tag{3.21}$$

$$Q_{nat.conv} = h(T_{amb} - T) \tag{3.22}$$

where T_{amb}: the ambient temperature, ϵ: surface emissivity, σ: the Stefan–Boltzmann constant and h: heat transfer coefficient.

As far as the boundary conditions implemented are concerned:

i) a periodic boundary condition is implemented at the inlet and outlet temperature of the channel, setting a zero temperature offset. This boundary condition takes into account that the inlet of the i^{th} unitcell is the outlet of the $(i-1)^{th}$ one (Figure 3.22).

ii) the heater temperatures at the copper-solid interface are set to T_{den} = 95 ^{o}C, T_{ext} =72 ^{o}C and T_{ann} = 55 ^{o}C. This boundary condition is used instead of the Joule Heating model (Chapter 3.4.2.3), in order to avoid the trial and error process required to obtain the values of the currents for the three copper wire heaters.

iii) a periodic boundary condition is implemented between the two sides of the microchannel, setting a zero temperature offset. With this boundary condition, the unitcell simulated is not placed at a corner location of the PCR device (Figure 3.22).

iv) a heat flux of $Q_{nat.conv}$ is set at the top, bottom, front and back sides of the microchannel (Figure 3.23), due to natural convection (Equation 3.22).

v) a heat flux of $Q_{rad,i}$ is considered at the front, back, top and bottom surfaces of the unitcell (Figure 3.23), where i accounts for the different materials (Equation 3.21).

As far as the initial conditions are concerned, the initial temperature of all domains is set to T_{amb}.

3.4.2.3 Electric Current

This model is used to describe the Joule heating phenomenon that takes place in the copper wire microheaters used in the simulations. The energy of the electric current in this type of heaters is converted into heat as it flows through a resistance. More specifically, this is achieved by converting electric energy to heat through the resistive losses in a material, as electric current flows through (Hauser et al., 2016). The power dissipated in a piece of wire will be related to the voltage across the ends of the wire, V, and the current flowing through it, I (Equation 3.23) (Balakrishnan et al., 2018).

$$P = V \cdot I = I^2 \cdot R \tag{3.23}$$

The steady-state form of the partial differential equation for electric currents is given by Equation 3.24, where **J** is the electric current (Equation 3.25). σ is the electric conductivity and is usually considered as an isotropic (scalar) value but in the most general case can be an anisotropic tensor. Equation 3.26 describes the relation between the electric field (**E**) and the potential (V). The Joule Heating effect introduces a heat load of the form presented in Equations 3.27 and 3.28, where ρ is the electric resistivity. According to Equation 3.27, the generated resistive heat Q is proportional to the square of the magnitude of the electric current density, J (Bansal et al. (2011), Sujatha et al. (2012)).

$$\nabla \cdot \mathbf{J} = 0 \tag{3.24}$$

$$\mathbf{J} = \sigma \mathbf{E} \tag{3.25}$$

$$\mathbf{E} = -\nabla V \tag{3.26}$$

$$Q_e = \mathbf{J} \cdot \mathbf{E} \overset{(Eq.3.25)}{=} \frac{1}{\sigma} \mid J^2 \mid = \rho \mid J^2 \mid, \tag{3.27}$$

$$Q_e \overset{(Eq.3.25,3.27)}{=} \sigma \mathbf{E} \cdot \mathbf{E} = \sigma_{isotropic} \begin{pmatrix} E_x \\ E_y \\ E_z \end{pmatrix} \cdot \begin{pmatrix} E_x \\ E_y \\ E_z \end{pmatrix} = \left(\begin{bmatrix} \sigma_{xx} & \sigma_{xy} & \sigma_{xz} \\ \sigma_{yx} & \sigma_{yy} & \sigma_{yz} \\ \sigma_{zx} & \sigma_{zy} & \sigma_{zz} \end{bmatrix} \begin{pmatrix} E_x \\ E_y \\ E_z \end{pmatrix} \right) \cdot \begin{pmatrix} E_x \\ E_y \\ E_z \end{pmatrix} \tag{3.28}$$

As described earlier in Chapter 2.3.3, the heat flux due to heat conduction in the solids is described by the term $\nabla \cdot (k \nabla T)$ appearing in Equation 2.33. As a result, through the Electromagnetic Heating feature available within the Multiphysics branch, the coupling of Equations 2.33 and 3.27 takes place as presented in Equation 3.29, where Q_e is given by Equation 3.27.

$$\rho C_p \frac{\partial T}{\partial t} = \nabla \cdot (k \nabla T) + Q_e \tag{3.29}$$

As far as the boundary conditions are concerned:

i) the outlet cross-sectional area of the three copper heaters is set as *ground* boundary condition, where the electric potential is set to 0 V.

ii) the inward (normal) current densities of the three copper heaters are set to the values appearing in Table 3.18.

iii) electric insulation boundary condition is applied in all the walls of the copper heaters, as presented in Equation 3.30.

$$\mathbf{n} \cdot \mathbf{J} = 0 \tag{3.30}$$

TABLE 3.18: Parameters of the copper microheaters (Papadopoulos et al., 2015)

Heating zone	Parameter	Values	Description
Denaturation	J_1 (A/m^2)	$1.0600 \cdot 10^8$	Normal current density
	L_{h1} (mm)	7.1	Length of the wire
Extension	J_2 (A/m^2)	$7.6325 \cdot 10^7$	Normal current density
	L_{h2} (mm)	9.4	Length of the wire
Annealing	J_3 (A/m^2)	$6.2750 \cdot 10^7$	Normal current density
	L_{h3} (mm)	6.5	Length of the wire
General	H_h (μm)	20	Height of the copper wires
	W_h (μm)	100	Width of the copper wires

As far as the initial conditions are concerned, the initial electric potential is set to 0 V.

3.4.2.4 Transport of diluted species

The general equation for the mass conservation of the species in steady-state is presented in Equations 3.31 and 3.32. The diffusion coefficients of the species appearing in the set of Equations 3.32 are presented in Table 3.19 (Athavale et al., 2001). The net reaction rates, the reaction rate constants and the parameters appearing in these equations are presented in Equations E.6 - E.12, E.1 - E.5 and Table 3.19 respectively (Athavale et al., 2001). The initial conditions are presented in Table 3.20.

$$\nabla \cdot \mathbf{J}_i + \mathbf{u} \cdot \nabla C_i = R_i \tag{3.31}$$

$$\mathbf{J}_i = -D_i \nabla c_i \tag{3.32}$$

TABLE 3.19: Kinetics parameter Values (Papadopoulos et al., 2015; Athavale et al., 2001)

Parameter	Values	Description
D_1	$10^{-10}\ (m^2/s)$	Diffusion Coefficient of S_1S_2 (c_1)
D_2	$10^{-10}\ (m^2/s)$	Diffusion Coefficient of S_1 (c_2)
D_3	$10^{-10}\ (m^2/s)$	Diffusion Coefficient of S_2 (c_3)
D_4	$10^{-9}\ (m^2/s)$	Diffusion Coefficient of P_1 (c_4)
D_5	$10^{-9}\ (m^2/s)$	Diffusion Coefficient of P_2 (c_5)
D_6	$10^{-10}\ (m^2/s)$	Diffusion Coefficient of P_1S_2 (c_6)
D_7	$10^{-10}\ (m^2/s)$	Diffusion Coefficient of S_1P_2 (c_7)
k_o^+	$12.5(1/s)$	Constant in reaction rate constant k_D^+
k_o^-	$10^3(m^3/(mol \cdot s))$	Constant in reaction rate constant k_D^-
k_1^+	$5 \cdot 10^3(m^3/(mol \cdot s))$	Constant in reaction rate constant k_A^+
k_1^-	$10^{-4}(1/s)$	Constant in reaction rate constant k_A^-
k_2	$0.32(1/s)$	Constant in reaction rate constant k_E

TABLE 3.20: Initial Conditions (Papadopoulos et al., 2015)

Initial concentration	Values (mol/m^3)	Description of the species
C_1	$5.71 \cdot 10^{-12}$	Double-stranded DNA (S_1S_2)
C_2	0	Single-stranded DNA (S_1)
C_3	0	Single-stranded DNA (S_2)
C_4	$3 \cdot 10^{-7}$	Single-stranded primer molecule (P_1)
C_5	$3 \cdot 10^{-7}$	Single-stranded primer molecule (P_2)
C_6	0	Single-stranded template–primer complex (P_1S_2)
C_7	0	Single-stranded template–primer complex (S_1P_2)

As far as the boundary conditions implemented are concerned:

i) no flux boundary condition is applied to all sides of the microchannel, excluding the inlet and outlet.

ii) the concentrations of the various species at the inlet are set to values of the initial concentrations (Table 3.20).

iii) a zero inward species flux boundary condition is applied at the exit of the microchannel ($\mathbf{n} \cdot D_i \nabla C_i$).

3.4.3 Mesh Independence Study

The effect of mesh density is considered for the case with $W_2 = 200\mu m$ and $H_{Fluid} = 50\mu m$, with five different mesh densities with 163,517, 321,151, 865,781, 4,035,872 and 6,133,359 elements. The Joule Heating model is implemented to describe the function of the copper wire heaters (Appendix D), as performed by Papadopoulos et al. (2015).

The effect of mesh density on DNA amplification (log_2 of the ratio of the average concentration of double-stranded DNA at the end of the first cycle to the initial one), pressure drop (ΔP(Pa)) and power consumption of the heaters (P_h(W)) is given in Table 3.21. Table 3.22 presents the values of the residual errors for the temperature (T), [DNA] and velocity (U) together with the computation times for the five meshes. This shows that the solutions on the mesh with 321,151 elements are effectively mesh-independent and all results presented below are obtained on this mesh.

A comparison of the DNA amplification ($log_2 \frac{[DNA]}{[DNA]_o}$), the pressure drop ($\Delta P$(Pa)) and the power consumption of the heaters (P_h(W)) (Table 3.21) is made. Given the variation in the values of $log_2 \frac{[DNA]}{[DNA]_o}$, ΔP and P_h observed in Table 3.21, the 321,151 element - mesh is selected to generate the DoE points ($\leq$1 % deviation for all objectives from the 6,133,359 elements-mesh). Furthermore, a comparison of the temperature profiles at the centreline of the middle plane along the length of the entire microchannel is presented in Figure 3.24.

TABLE 3.21: Comparison of the $log_2 \frac{[DNA]}{[DNA]_o}$, P_h and ΔP for different number of mesh elements.

Mesh Elements	$log_2 \frac{[DNA]}{[DNA]_o}$ (-)	Deviation (%)	ΔP (Pa)	Deviation (%)	P_h (W)	Deviation (%)
163,517	0.67	0	288.59	0.91	0.071	0
321,151	0.67	0	284.29	-0.59	0.071	0
865,781	0.67	0	283.05	-1.02	0.071	0
4,035,872	0.67	0	286.01	0.01	0.071	0
6,133,359	0.67	0	285.98*	0	0.071	0
Reference**	0.67*		NG		0.071*	

* Reference values for calculating the deviation (%), ** Papadopoulos et al. (2015)

TABLE 3.22: Residual Errors and computation times of the temperature, [DNA] and velocity.

No	Mesh Elements	Computing time (s)	Residual Error T(K)	Residual Error [DNA] (mol/m^3)	Residual Error U (m/s)
1	163,517	200	$2.545 \cdot 10^{-12}$	$4.174 \cdot 10^{-37}$	$2.9513 \cdot 10^{-15}$
2	321,151	585	$9.6719 \cdot 10^{-13}$	$1.8469 \cdot 10^{-37}$	$1.1491 \cdot 10^{-15}$
3	865,781	1,557	$9.4439 \cdot 10^{-13}$	$1.4754 \cdot 10^{-37}$	$9.3432 \cdot 10^{-16}$
4	4,035,872	15,096	$2.3523 \cdot 10^{-13}$	$-1.0762 \cdot 10^{-34}$	$3.3608 \cdot 10^{-16}$
5	6,133,359	16,915	$1.9196 \cdot 10^{-13}$	$-1.1391 \cdot 10^{-34}$	$2.8907 \cdot 10^{-16}$

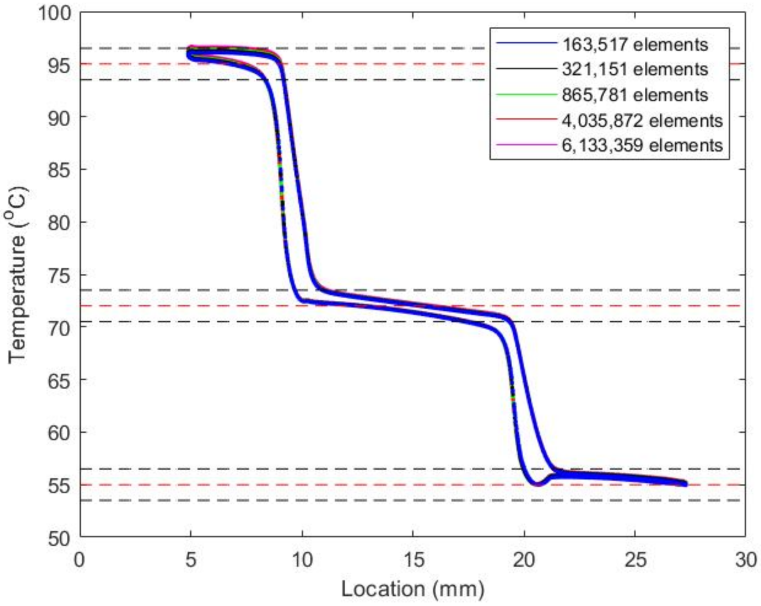

FIGURE 3.24: Comparison of the temperature (^oC) profiles of the five meshes at the cetreline of the middle plane along the microchannel. The three different temperature regimes of interest are observed (±1.5 ^oC (black dotted lines) from the set points (red dotted lines)).

3.4.4 Validation with the work of Papadopoulos et al. (2015)

The model implemented in COMSOL Multiphysics ® is validated with the works of Papadopoulos et al. (2015) and Wang et al. (2007) as follows:

- The kinetics are implemented and the temperature dependence of the rate constants (k_D^+, k_D^-, k_E, k_A^+ and k_A^-) is compared to the one presented in the work of Wang et al. (2007). Papadopoulos et al. (2015) used the same kinetics model with a 2 ^oC variation in the target temperature of extension (72 and 70 ^oC in the work of Papadopoulos et al. (2015) and Wang et al. (2007) respectively), which explains the deviation between the two k_E/k_2 curves.

- The temperature uniformity in each temperature regime while varying the inlet velocity is also compared to the one of Papadopoulos et al. (2015) (Figure 3.25). The temperature uniformity values are calculated via Equation 3.33.

$$T.U.(\%) = \frac{\iiint(|T - T_{stp}| < 1.5)}{\iiint(T > 273.15)}, \qquad T_{stp}[K] = \{T_{den}, T_{ext}, T_{ann}\}, \tag{3.33}$$

- The log_2 of the ratio of the average concentration of double-stranded DNA at the end of the first cycle to the initial one is found to be equal to 0.67, equal to the one presented in the work of Papadopoulos et al. (2015).

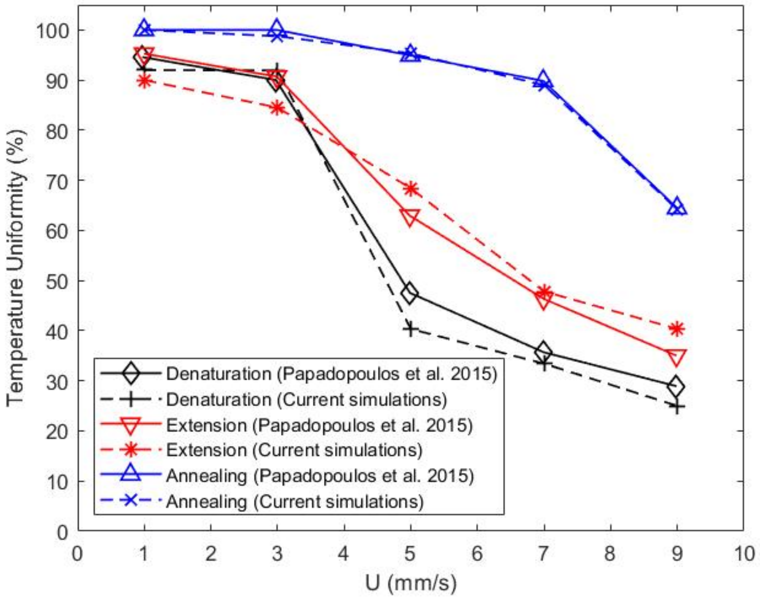

FIGURE 3.25: Comparison of the temperature uniformity (% of the zone with fluid temperature within a range of ±1.5 ^{o}C from the set point) of the three zones versus inlet velocity with the work of Papadopoulos et al. (2015).

- The power requirements of the unit cell for performing 1 PCR cycle are found to be equal to 0.071 W, the same value as the one predicted by Papadopoulos et al. (2015).

  The indicative power consumption for the denaturation copper-wire heater with a rectangular cross-section is calculated as presented in Equations D.1-D.6 in Appendix D.

3.4.5 Optimisation of the cross-section of the unitcell

The rectangular cross-sectional area (W_2, H_{Fluid}) of the microchannel is optimised, in order to maximise and minimise the DNA amplification and pressure drop respectively. While varying the two design variables, the channel length in each regime is adjusted (Equation 3.16) in order to achieve the required residence times in the three temperature regimes, in all the simulations. The PCR protocol followed is the one presented in Papadopoulos et al. (2015); 3s:4.2s:6.2s for $t_{R,den}$:$t_{R,ann}$:$t_{R,ext}$ respectively.

Two objective functions of interest are studied in this work; a dimensionless measurement of the DNA amplification, $log_2(\frac{[DNA]}{[DNA]_o})$ (see O1, Table 3.17) and the pressure drop along the microchannel, ΔP (see O2, Table 3.17). The power consumption is not considered an objective function, since the temperatures at the surface of the copper wire heaters are set at the $T_{target,zone}$, where zone= $\{den, ext, ann\}$. This assumption is made in order to avoid the trial and error process required for defining the variable values of the electric currents (I_{den}, I_{ext}, I_{ann}) for all the DoE points. As a result, the Electric Current model is not used in the simulations that are part of the optimisation, but only for validation purposes. Part of this Chapter is presented in the publication of Zagklavara et al. (2021).

3.4.5.1 Design of Experiments

The design of experiments is performed by varying the values of these two design variables within their upper and lower boundaries (100 - 400 μm and 50 - 80 μm for W_2 and H_{Fluid} respectively). Considering that the values of H_{Fluid} and H_{Kapton} (see Figure 3.23) are set equal to 50 μm and 100 μm respectively in the work of Papadopoulos et al. (2015), the design parameter of H_{Fluid} is allowed to vary between 50 and 80 μm, considering a minimum of 20 μm distance of the channel from the heaters as a physical constraint. The second design variable, W_2, is allowed to vary between 100 - 400 μm. The upper limit of 800 μm (for the width of the extension zone) is set to be lower than the width of the substrate, W_1, allowing for a 100 μm gap at each side of the microchannel (physical constraint). The other dimensions of the design parameters and the material properties of the channel are presented in Tables 3.13 and 3.14 respectively, and are based on the design proposed by Papadopoulos et al. (2015).

The Morris Mitchel Latin Hypercube method is used to generate 80 DoE points. The code used (Chapter B.3 of Appendix) is based on the work of Julie (2012), after modifying it to include the four corner points of the design domain.

3.4.5.2 Response surfaces

In order to study the behaviour of these objective functions throughout the selected design domain, the response surfaces or meta-models need to be created. The original model implemented in COMSOL Multiphysics ® is evaluated at 80 sample points (see Appendix B.3). After obtaining all the data, the dimensionless and scaled (0-1) (see Table 3.17) response surfaces of obj_1 and obj_2 are generated using:

- a polyharmonic spline (PS) (Chapter 2.5.3.4) function in MATLAB® (Wiens, 2014). The polyharmonic radial basis function, ϕ, is given by Equation 3.34, while r is given by Equation 3.35:

$$\phi(r) = \begin{cases} r^k & \text{if k=1,3,5,...,} \\ r^k ln(r) & \text{if k=2,4,6,...} \end{cases} \tag{3.34}$$

$$r = |\mathbf{x} - \mathbf{c}_i| = \sqrt{(\mathbf{x} - \mathbf{c}_i)^T(\mathbf{x} - \mathbf{c}_i)} \tag{3.35}$$

  where $\mathbf{c}_i$: centres or in this case the DOE points (Barnett, Flyer, and Wicker, 2015; Beatson, Powell, and Tan, 2007). The PS order, k, is set to 3 (see Table 2.7).

- a feedforward type Neural Network (NN) (Leijnen and Veen, 2020). MATLAB® function *fitnet* (MathWorks, 2020) is used to develop the response surfaces, using Levenberg-Marquardt backpropagation. The Mean Squared Error (MSE) performing function is selected together with k-fold evaluation (Manriquez-Sandoval, 2021), in order to test and improve the quality of the neural network. For the resulting NNs, 8 folds are selected for the $log_2(\frac{[DNA]}{[DNA]_o})$ and ΔP, resulting to $MSE_{log_2(\frac{[DNA]}{[DNA]_o})} = O(10^{-5})$ and $MSE_{\Delta P}$=$O(10^{-5})$. The number of hidden layers selected is [4, 4] and [4, 4] for $log_2(\frac{[DNA]}{[DNA]_o})$ and ΔP respectively.

3.4.5.3 Optimisation Algorithms

Two optimisation algorithms are used to find the optimum values of the generated meta-models for the two objective functions of interest (obj_1 and obj_2); the *genetic algorithm* (*ga* MATLAB® function (MathWorks, 2021)) and the *e05jbc* of the NAG optimisation library (NAG, 2020).

As far as the genetic algorithm (GA) is concerned, the *ga* (MathWorks, 2021) MATLAB® function is used to obtain the minimum values of the produced response surfaces. Some of the default parameters of the *ga* function selected are presented in Table 3.23 (MathWorks, 2021), for all response surfaces produced.

The genetic algorithms are based on the principles of natural selection and genetics. More specifically, GA performs a multi-directional search by maintaining a population of potential solutions. The design variables are represented as a binary string, called chromosome (or individual). Each chromosome holds all of the design variables and needs to be optimised. Since the design variables are all embedded inside the chromosome, then all of the segments which make up each individual design variable are the genes. At each generation, the population undergoes an "evolution", where the best solutions "reproduce" and the worst ones "die". The six functions that take place in the algorithm are evaluation, selection, reproduction, mutation, elitism and extermination (Aggarwal and Singh, 2005).

TABLE 3.23: Default parameters of *ga*

No	Parameter of *ga*	Value or function name
1	FunctionTolerance	10^{-6}
2	MaxGenerations	200
3	PopulationSize	50
4	MutationFcn	mutationgaussian
5	SelectionFcn	selectionstochunif
6	ConstraintTolerance	10^{-3}

As far as the e05jbc (NAG, 2020) NAG routine is concerned, it is designed to locate the global minimum or maximum of an arbitrary function, and is based on the Multi-level Coordinate Search method described in Huyer and Neumaier (1999). Derivatives are not required, but convergence is only guaranteed if the objective function is continuous in a neighbourhood of a global optimum (NAG, 2020).

Due to the fact that two objective functions are studied in this work, ways to approach a multiobjective optimisation problem are considered. In this type of problem, there exists more than one objective function to be optimised at the same time. However, it is often the case that the two objectives might conflict, where improving the solution of one results in deteriorating the solution of the other. Therefore, there is no single optimal solution with respect to all the objective functions, but a set of optimal solutions instead (Pareto optimal solutions or Pareto front) (Amanifard et al., 2008; Shojaeefard et al., 2013).

3.4.5.4 Results

3.4.5.4.1 Response surfaces The polyharmonic spline and the neural network generate response surfaces of the two objective functions, providing the ability to compare the two different methods and their results. The polyharmonic spline described in subsection 3.4.5.2 generates the response surfaces appearing in Figures 3.26a, 3.27a and 3.28a, 3.29a for obj_1 and obj_2 respectively. The *fitnet* MATLAB® function is used to generate the response surfaces appearing in Figures 3.26b, 3.27b and 3.28b, 3.29b for the obj_1 and obj_2 respectively. The same function is also used to generate the response surfaces of the temperature uniformity of the fluid, at the three temperature regimes of interest; denaturation, extension and annealing (Figure 3.30).

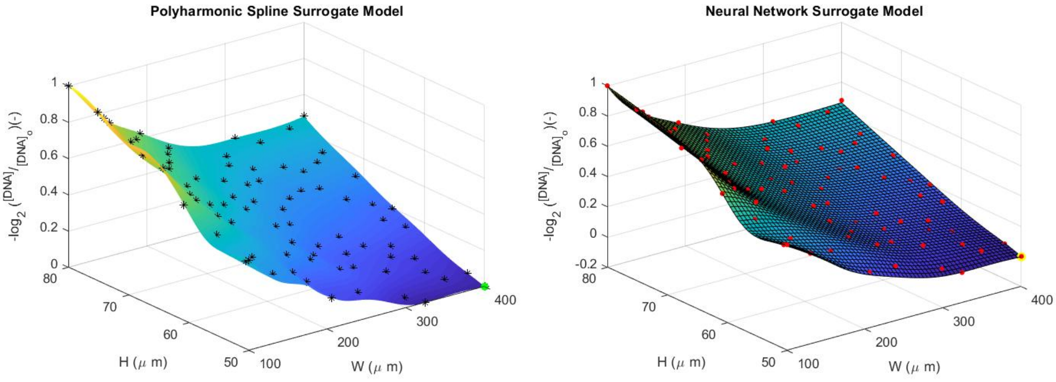

(A) Polyharmonic Spline

(B) Neural Network.

FIGURE 3.26: Response surfaces of obj_1, generated with (a) PS and (b) NN. Genetic algorithm (*ga*) is used to obtain the optimum values, presented in green and yellow in (a) and (b) respectively.

The dimensionless and scaled values of the negatives of the response surfaces of the temperature uniformity and the $log_2(\frac{[DNA]}{[DNA]_o})$ are generated, so that the minimum values of these plots would correspond to the maximum values of the actual objective function. The exact DoE points are presented in Table B.3 of Appendix B.3, including the temperature uniformity values in all three temperature regimes.

3.4.5.4.2 Optimisation The minima of the response surfaces of obj_1 and obj_2 are found at $[W_2\ (\mu m),\ H_{Fluid}\ (\mu m)]_{obj_1}$ = [400, 50] and $[W_2\ (\mu m),\ H_{Fluid}\ (\mu m)]_{obj_2}$ = [400,

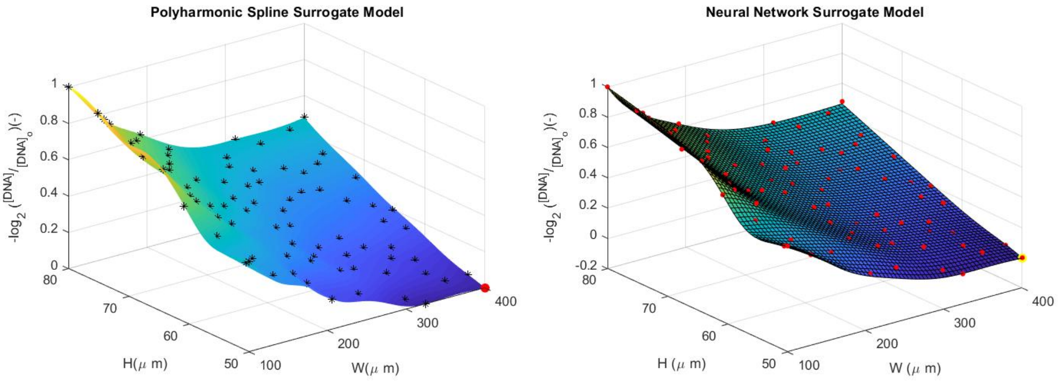

(A) Polyharmonic Spline

(B) Neural Network.

FIGURE 3.27: Response surfaces of the obj_1, generated with (a) PS and (b) NN. The *e05jbc* NAG routine is used to obtain the optimum values, that are presented in red and green respectively.

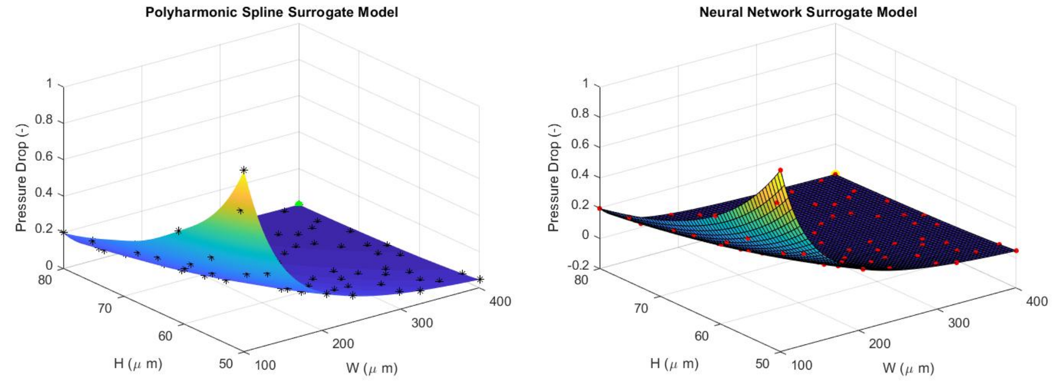

(A) Polyharmonic Spline

(B) Neural Network.

FIGURE 3.28: Response surfaces of obj_2, generated with (a) PS and (b) NN. Genetic algorithm (*ga*) is used to obtain the optimum values, which are presented in green and yellow respectively.

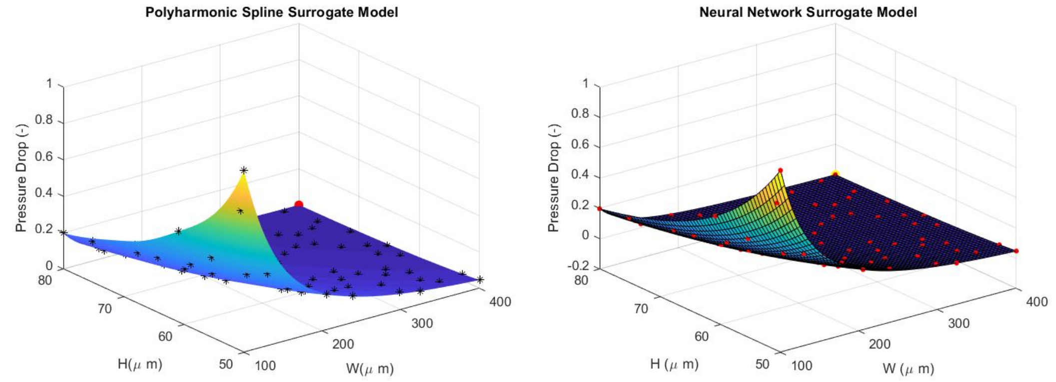

(A) Polyharmonic Spline

(B) Neural Network.

FIGURE 3.29: Response surfaces of obj_2, generated with (a) PS and (b) NN. The *e05jbc* NAG routine is used to obtain the optimum values, presented in red and green respectively.

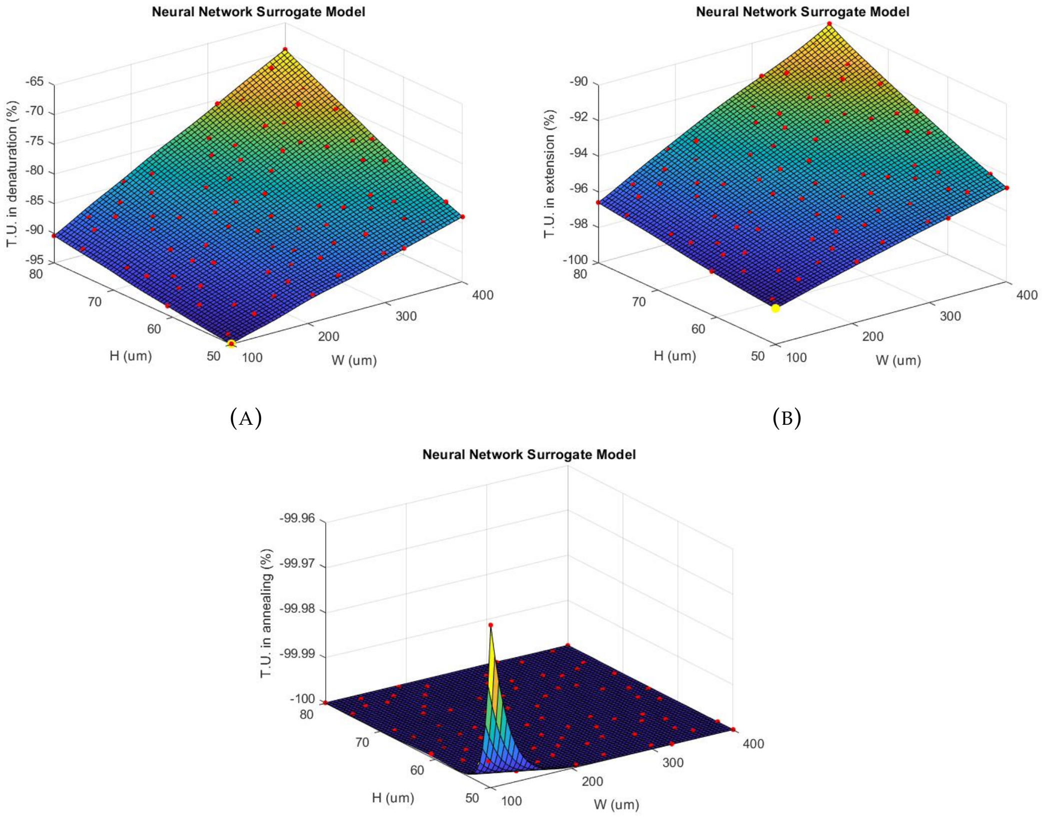

(A)

(B)

(C)

FIGURE 3.30: Temperature uniformity (T.U.) at the (a) denaturation, (b) extension and (c) annealing temperature, zones scaled accordingly. The minimum points are presented in yellow.

80] respectively. The [W_2 (μm), H_{Fluid} (μm)]$_{obj_1}$=[400, 50] design is then tested including the Joule Heating model (Tables 3.24 and 3.26), resulting to a 4.48% increase and a 73.7% decrease in the values of $log_2\frac{[DNA]}{[DNA]_o}$ and pressure drop respectively, from the values obtained from the [W_2 (μm), H_{Fluid} (μm)]=[200, 50] design (Papadopoulos et al., 2015). The [W_2 (μm), H_{Fluid} (μm)]$_{obj_1}$ = [400, 50] design leads to a $\sim$ 33.5 % unitcell volume reduction compared to the [W_2 (μm), H_{Fluid} (μm)] = [200, 50] design (Papadopoulos et al., 2015). The response surface for obj_1, shows that doubling the width of the microchannel to 400 μm while maintaining the height at the value of the original design (Papadopoulos et al., 2015) can lead to a $\sim$ 2.1% increase in [DNA] (or $\sim$ 4.48% increase in the $log_2\frac{[DNA]}{[DNA]_o}$). This optimal design can therefore significantly reduce the required pressure drop while increasing the DNA amplification.

Tables 3.25 and 3.27 present the design solution that generates the minimum pressure drop ([W_2 (μm), H_{Fluid} (μm)]$_{obj_2}$ = [400, 80]). The [W_2 (μm), H_{Fluid} (μm)]$_{obj_2}$ = [400, 80] design leads to a 37.5 % unitcell volume reduction and a 95.17 % decrease in the value of unitcell pressure drop compared to the from the [W_2 (μm), H_{Fluid} (μm)] = [200, 50]. One can observe that no single solution exists that simultaneously optimises both objectives since they are conflicting with each other (green points in Figure 3.31). Therefore, the Pareto front is obtained using the *gamultiobj* function (MathWorks, 2020) and is presented in Figure 3.32 to demonstrate the available compromises between the two objectives.

TABLE 3.24: Optimum solutions obtained with genetic algorithm for $log_2\frac{[DNA]}{[DNA]_o}$

Polyharmonic			Neural Network		
W (μm)	H (μm)	$log_2\frac{[DNA]}{[DNA]_o}$ (-)	W (μm)	H (μm)	$log_2\frac{[DNA]}{[DNA]_o}$ (-)
399.98	50	0.70438	400	50	0.70438

TABLE 3.25: Optimum solutions obtained with genetic algorithm for the pressure drop

Polyharmonic			Neural Network		
W (μm)	H (μm)	ΔP (Pa)	W (μm)	H (μm)	ΔP (Pa)
400	79.98	13.742	400	80	13.742

TABLE 3.26: Optimum solutions obtained with e05jbc NAG routine for $log_2\frac{[DNA]}{[DNA]_o}$

Polyharmonic			Neural Network		
W (μm)	H (μm)	$log_2\frac{[DNA]}{[DNA]_o}$ (-)	W (μm)	H (μm)	$log_2\frac{[DNA]}{[DNA]_o}$ (-)
400	50	0.70438	400	50	0.70438

TABLE 3.27: Optimum solutions obtained with e05jbc NAG routine for the pressure drop

Polyharmonic			Neural Network		
W (μm)	H (μm)	ΔP (Pa)	W (μm)	H (μm)	ΔP (Pa)
400	80	13.742	400	80	13.742

The values of obj_1 and obj_2 in Figures 3.31 and 3.32 are scaled between 0 and 1, to aid the visualisation of the multi-objective problem, while at the same time ensuring that both objective functions will be weighted the same when using the gamultiobj optimisation function (MathWorks, 2020). Three of the optimal solutions presented in the Pareto front plot are validated using the simulation model (Table 3.28), deviating less than 3.38 % for all three cases.

Ten consecutive PCR cycles are simulated for $[W_2(\mu m), H_{Fluid}(\mu m)]$ = [200, 50] (Papadopoulos et al., 2015) and $[W_2(\mu m), H_{Fluid}(\mu m)]_{obj_1}$=[400, 50] using the Joule Heating model for the function of the copper wire heaters. The results are presented in Figure 3.33. According to the data obtained for the $[W_2(\mu m), H_{Fluid}(\mu m)]_{obj_1}$=[400,

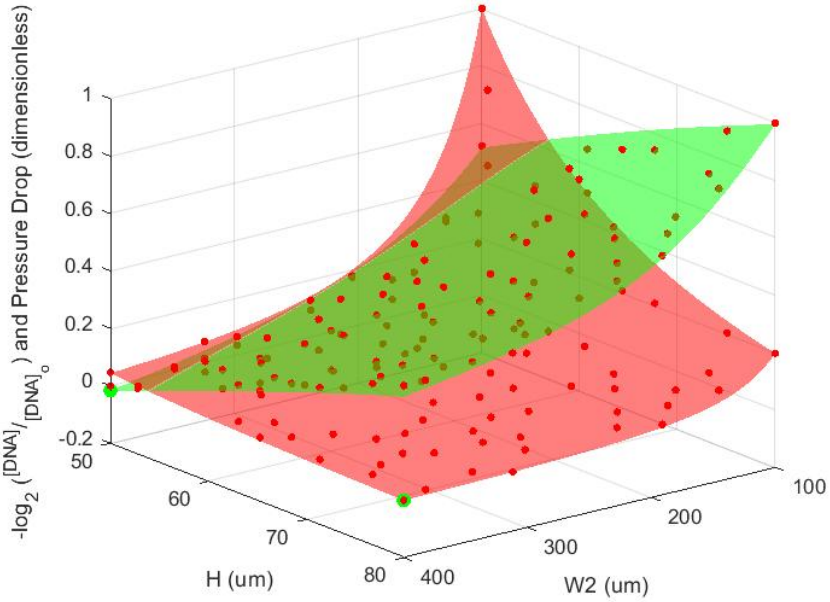

FIGURE 3.31: Response surfaces of obj_1 (green) and obj_2 (red) (see Table 3.17). The optimum values are presented in green.

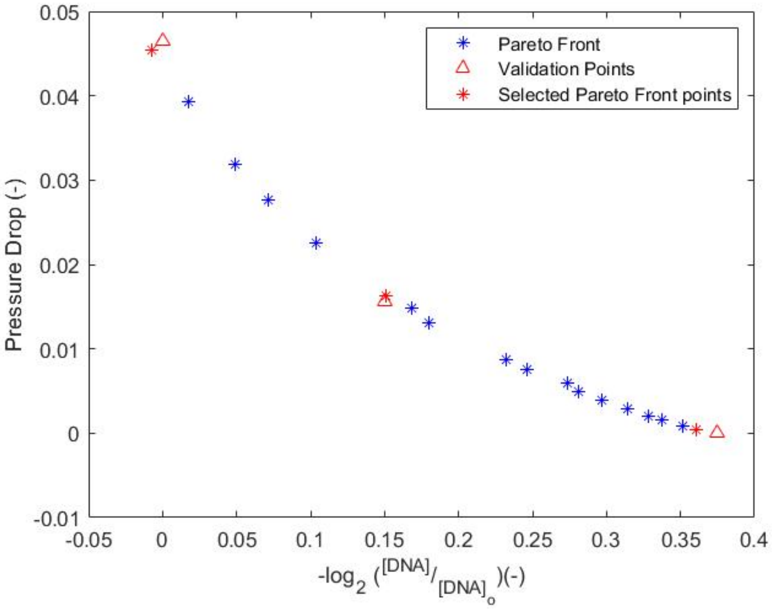

FIGURE 3.32: Pareto front (star points) generated with *gamultiobj* (MathWorks, 2020) of MATLAB®, for the scaled (0-1) and dimensionless expressions of $log_2 \frac{[DNA]}{[DNA]_o}$ (obj_1) and pressure drop (obj_2). Three points (red star) are validated (red triangle).

50], this $\sim$ 2.1% increase in [DNA] in the first PCR cycle, is expected to increase the concentration of DNA approximately by $\sim$ 3.2% in ten cycles. As presented in Appendix I, this increase leads to a reduction of the estimated required number of cycles from 36 to 35 for the case studied (Biosystems, 2004). Combined together with

TABLE 3.28: Validation of three points appearing in the Pareto-front plot (Figure 3.32).

		Model		Pareto Optimum		Deviation	
W (μm)	H (μm)	$log_2\frac{[DNA]}{[DNA]_o}$ (-)	ΔP (Pa)	$log_2\frac{[DNA]}{[DNA]_o}$ (-)	ΔP (Pa)	$log_2\frac{[DNA]}{[DNA]_o}$ (%)	ΔP (%)
1.0000	0.0500	-0.7065	73.2066	-0.7062	74.7342	-0.0405	2.0866
0.9834	0.4168	-0.7005	34.2000	-0.7005	35.1694	-0.0049	2.8346
1.0000	1.0000	-0.6867	13.7420	-0.6925	14.2070	0.8446	3.3838

the 33.5% unitcell volume substrate reduction of the design $[W_2(\mu m), H_{Fluid}(\mu m)]_{obj_1}$ = [400, 50], the total estimated material cost reduction is expected to reach at 35.3 % compared to the design $[W_2(\mu m), H_{Fluid}(\mu m)]$ = [200, 50]. As far as the operating cost is concerned, design $[W_2(\mu m), H_{Fluid}(\mu m)]_{obj_1}$ = [400, 50] is expected to be reduced significantly due to the 73.7 % reduction in the unitcell pressure drop.

As far as the temperature uniformity (T.U.) is concerned, the optimum solution of the DNA amplification ($log_2\frac{[DNA]}{[DNA]_o}$) is observed for T.U. values of above 84%, in all three temperature regimes. Figures 3.34a and 3.34b present the response surfaces of $T.U._{den}$ and $T.U._{ext}$ combined with obj_1 respectively. The significance of T.U. needs to be studied further, since according to Figures 3.34a and 3.34b, one can observe that the highest DNA amplification is not achieved at the greatest values of T.U. in denaturation and extension zones. However, it is important to point out that the presented values of T.U. are obtained without the use of the Joule Heating model, as described in the second boundary condition presented in Chapter 3.4.2.2. It is therefore important to perform simulations including the Joule Heating model before finalising any conclusions related to the relation between the DNA amplification and T.U..

Furthermore, a correlation coefficient of 0.88 is observed between the width-to-height channel ratio and the value of $log_2\frac{[DNA]}{[DNA]_o}$, which is justified due to the better temperature uniformity in all three temperature regimes (Figure 3.35). For cross-sectional areas with high W_2 and low H_{Fluid} values, the heat transfer and the DNA amplification ($log_2\frac{[DNA]}{[DNA]_o}$) are facilitated by the i) relatively low Re and ii) the small dimension of the z-axis, leading to values of high temperature uniformity.

3.4.6 Optimisation of the heater spacing of the unitcell

This study aims on obtaining a better understanding on the significance of the heater spacing in the performance of the unitcell. More specifically, the spacing (L_5, L_7 of Figure 3.23) between the three copper wire heaters of the unitcell is optimised, in order to maximise and minimise the DNA amplification and pressure drop respectively. While varying the two design variables, the width and height of the microchannel are set to 200 and 50 μm respectively. The two types of objective functions studied in this Chapter are the same as the ones studied in Chapter 3.4.5; the $log_2(\frac{[DNA]}{[DNA]_o})$ and the pressure drop along the microchannel (see O1 and O2 of Table

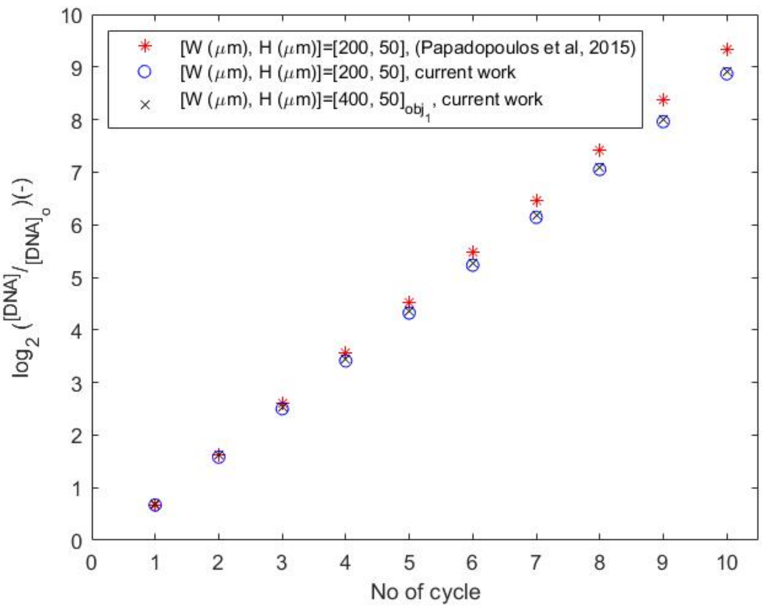

FIGURE 3.33: Values of $log_2(\frac{[DNA]}{[DNA]_o})(-)$ for 10 PCR cycles.

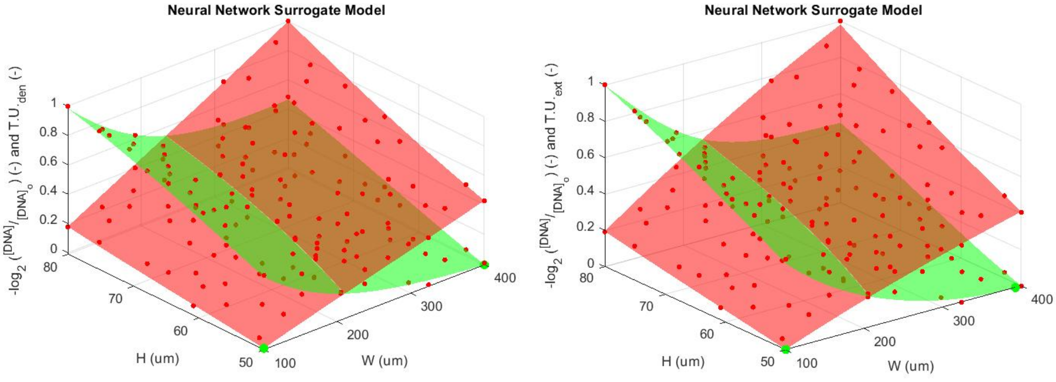

(A)

(B)

FIGURE 3.34: Response surfaces of $-log_2(\frac{[DNA]}{[DNA]_o})$ (green) and the temperature uniformity (red) at (A) denaturation and (B) extension zone, obtained using NN. The *e05jbc* routine is used to obtain the optimum values, presented in green. The values are scaled between 0 and 1.

3.17). The content of this Chapter is also presented in the publication of Zagklavara et al. (2022).

3.4.6.1 Design of Experiments

The design of experiments is performed by varying the values of these two design variables within their upper and lower boundaries of 500 - 2500 μm for both L_5 and L_7. The other dimensions of the design parameters and the material properties of the channel are based on the design proposed by Papadopoulos et al. (2015) (see Tables

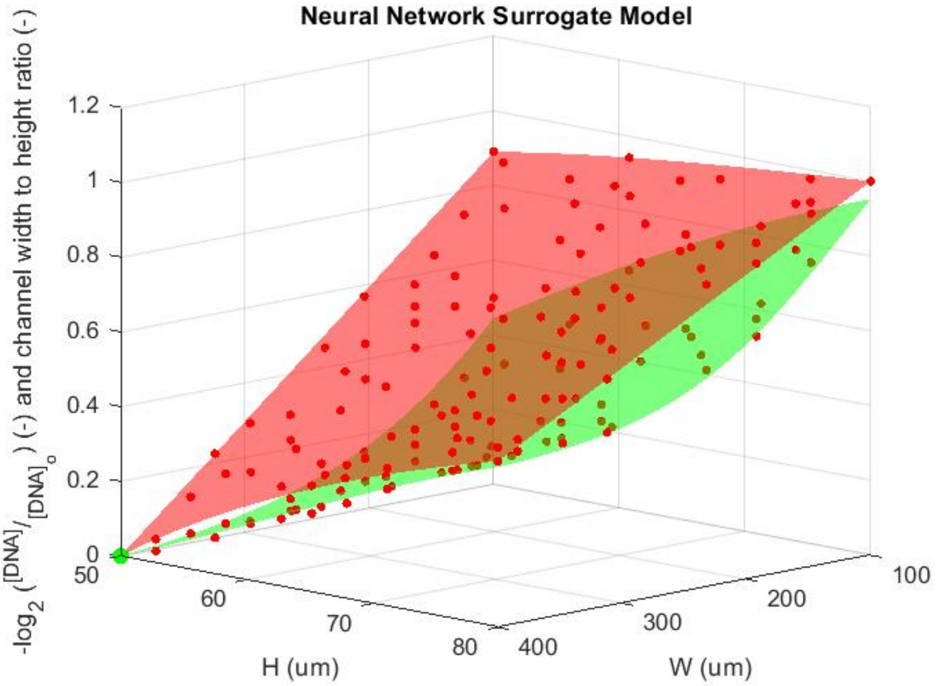

FIGURE 3.35: Response surfaces of $-log_2(\frac{[DNA]}{[DNA]_o})(-)$ (green) and channel width to height ratio (-) (red). The greatest value of channel width to height ratio appears to present the greatest DNA amplification. All values are scaled between 0 and 1.

3.15, 3.16, 3.13 and 3.14). The Morris Mitchel Latin Hypercube method is used to generate the DoE points. The code used to generate 80 DoE points (Chapter B.4 of Appendix) is based on the work of Julie (2012), after modifying it to include the four corner points of the design domain.

3.4.6.2 Response surfaces

In order to study the behaviour of these objective functions throughout the selected design domain, the response surfaces or meta-models need to be created. The original model implemented in COMSOL Multiphysics ® is evaluated at 80 sample points (see Appendix B.4). The obj_1 and obj_2 response surfaces are generated with a polyharmonic spline (PS) (see Chapter 3.4.5.2 for more details).

3.4.6.3 Optimisation Algorithms

Two optimisation algorithms are used to find the optimum values of the generated meta-models for the two objective functions of interest (obj_1 and obj_2, see Table 3.17); the *genetic algorithm* (*ga* MATLAB® function (MathWorks, 2021)) and the *e05jbc* of the NAG optimisation library (NAG, 2020). For more details, see Chapter 3.4.5.3.

Similarly to the optimisation problem presented earlier in Chapter 3.4.5, there exists more than one objective function to be optimised at the same time. Considering that improving the solution of one objective might result in deteriorating the solution of the other, no single optimal solution with respect to all the objective functions exists. Instead, a set of optimal solutions is generated using the Pareto optimal solutions or Pareto front (Amanifard et al., 2008; Shojaeefard et al., 2013).

3.4.6.4 Results

3.4.6.4.1 Response surfaces The PS generates response surfaces of the two objective functions, presented in Figures 3.36 and 3.37 for obj_1 and obj_2 respectively. The exact DoE points are presented in Table B.4 of Appendix B.4, including the temperature uniformity values in all three temperature regimes.

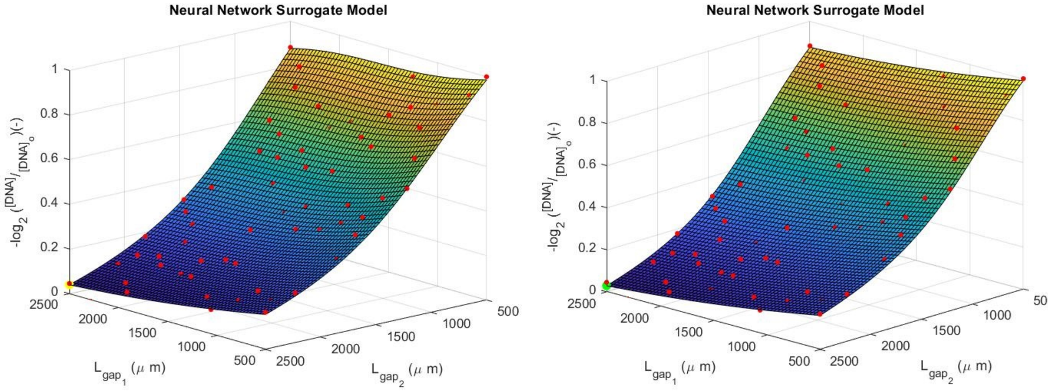

(A) GA

(B) *e05jbc* NAG routine

FIGURE 3.36: Response surfaces of the $-log_2(\frac{[DNA]}{[DNA]_o})$, generated with Polyharmonic Spline. The (a) Genetic algorithm (*ga*) and (b) *e05jbc* NAG routine are used to obtain the optimum values, presented in yellow and green respectively.

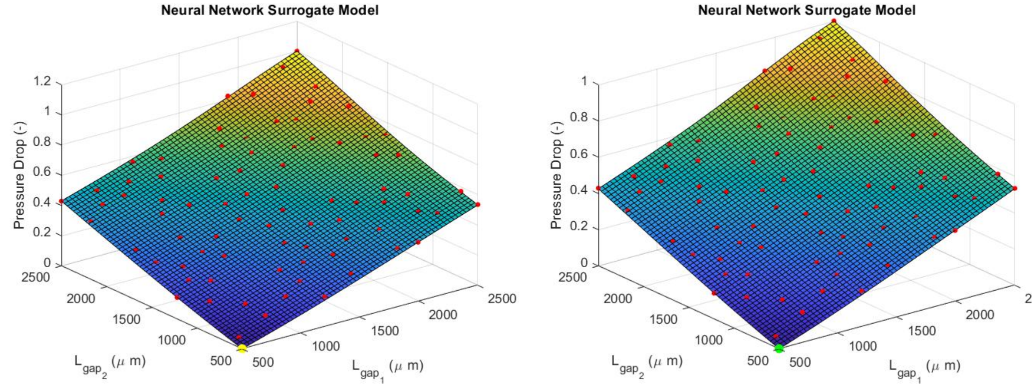

(A) GA

(B) *e05jbc* NAG routine

FIGURE 3.37: Response surfaces of the total pressure drop, generated with PS. The (a) Genetic algorithm (*ga*) and (b) *e05jbc* NAG routine are used to obtain the optimum values, presented in yellow and green respectively.

3.4.6.4.2 Optimisation The optimum values of the response surfaces of obj_1 and obj_2 produced by PS are presented in Tables 3.29 and 3.30. Table 3.31 presents the optimum values obtained (for the same designs) using the Joule Heating model with GA. One can observe that no single solution exists that simultaneously optimises both objectives since they are conflicting with each other (green and yellow points in Figure 3.38). Therefore, a pareto-front plot (star points in Figure 3.39) is generated in order to obtain the optimum design of this multi-objective optimisation problem, providing a number of equally-good Pareto optimal solutions with the *gamultiobj* function (MathWorks, 2020). The Pareto front plot is presented in Figure 3.39.

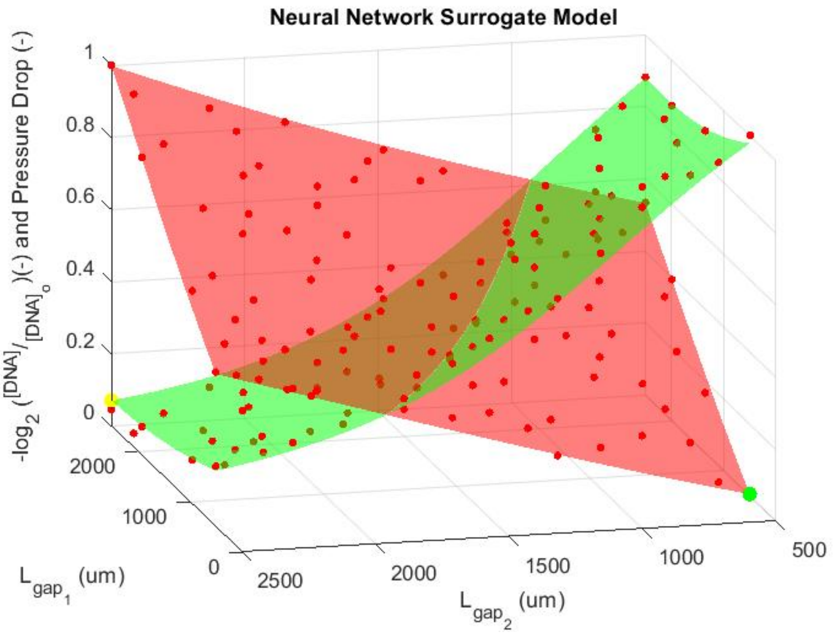

FIGURE 3.38: Response surfaces of $-log_2(\frac{[DNA]}{[DNA]_o})(-)$ (green) and pressure drop (-) (red). The optimum values are presented in yellow and green respectively, while both objective functions are dimensionless and scaled between 0 and 1.

TABLE 3.29: Optimum solutions obtained with genetic algorithm for $log_2\frac{[DNA]}{[DNA]_o}$ and pressure drop.

GA					
L_{gap_1} (μm)	L_{gap_2} (μm)	$log_2\frac{[DNA]}{[DNA]_o}$ (-)	L_{gap_1} (μm)	L_{gap_2} (μm)	ΔP (Pa)
2500	2500	0.71323	500	500	260.25

For the different optimisation methods (genetic algorithm, e05jbc NAG routine) used, the optimum solutions appear to be in very good agreement with each other i.e. when using different optimisation method, the values of each of the objectives are found to differ by less than 5.75 % for all cases (Tables 3.29 and 3.30).

One can observe in Figures 3.38 and 3.39 that the values of pressure drop and -$log_2\frac{[DNA]}{[DNA]_o}$ are dimensionless and scaled between 0 and 1. This is done in order to

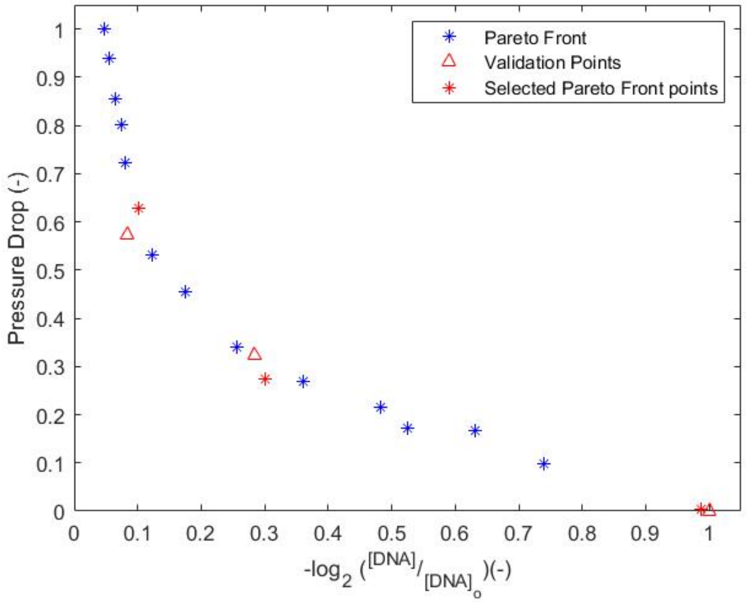

FIGURE 3.39: Pareto front (star points) generated with *gamultiobj* (MathWorks, 2020) of MATLAB®, for the $-log_2(\frac{[DNA]}{[DNA]_o})$ (Objective 1) and the pressure drop (Objective 2). Three points (red star) are validated (red triangle).

TABLE 3.30: Optimum solutions obtained with e05jbc NAG routine for $log_2\frac{[DNA]}{[DNA]_o}$ and pressure drop.

e05jbc NAG routine					
L_{gap_1} (μm)	L_{gap_2} (μm)	$log_2\frac{[DNA]}{[DNA]_o}$ (-)	L_{gap_1} (μm)	L_{gap_2} (μm)	ΔP (Pa)
2500	2500	0.71282	500	500	260.25

TABLE 3.31: Optimum solutions obtained for $log_2\frac{[DNA]}{[DNA]_o}$ and pressure drop, using the Joule Heating Model (Zagklavara et al., 2022).

GA using the Joule Heating Model					
L_{gap_1} (μm)	L_{gap_2} (μm)	$log_2\frac{[DNA]}{[DNA]_o}$ (-)	L_{gap_1} (μm)	L_{gap_2} (μm)	ΔP (Pa)
2500	2500	0.678	500	500	259.86

TABLE 3.32: Validation of three points appearing in the Pareto-front plot (Figure 3.32).

Point	Model				Pareto Optimum	
	L_{gap_1} (μm)	L_{gap_2} (μm)	$log_2\frac{[DNA]}{[DNA]_o}$ (-)	ΔP (-)	$log_2\frac{[DNA]}{[DNA]_o}$ (-)	ΔP (-)
1	0.002608	0	1	0	0.986277	0.002765
2	0.106555	0.658109	0.283815	0.323647	0.300688	0.274467
3	0.319249	0.963341	0.083207	0.573801	0.101101	0.627400

visualise better the multi-objective nature of the optimisation problem, while at the same time ensuring that both objective functions will be weighted the same when using the gamultiobj optimisation function (MathWorks, 2020). Three of the optimal solutions presented in the pareto-front plot are validated using the simulation model (Table 3.32).

After considering the results obtained from the response surfaces of the $log_2 \frac{[DNA]}{[DNA]_o}$, the joule heating model is run for the optimum solution (L_{gap_1} and L_{gap_2} equal to 2500 μm). The results indicate that for these design parameters, a $\sim$ 1.8% increase in the $log_2 \frac{[DNA]}{[DNA]_o}$) and $\sim$ 8.6% increase in the pressure drop are observed in one PCR cycle, compared to the values of the original design of Papadopoulos et al. (2015). This optimum design provides an indication of the importance of selecting the appropriate heater spacing when designing such devices, since the overall performance and DNA amplification can be affected (especially when more than one PCR cycles are considered). As a result, even if the increase in the DNA amplification is small for one PCR cycle, it is important to consider the optimisation of the distance between the heaters, in order to achieve the optimum design solution of the unitcell performance.

3.4.7 Further optimisation on the spacing between heaters of the unitcell

The distance between the three copper wire heaters, L_{gap}, (L_5=L_7=L_{gap}, Figure 3.23) and the width of the microchannel in the same areas, W_{gap}, (W_4 = W_{gap}, Figure 3.23) are optimised, in order to maximise and minimise the DNA amplification and pressure drop respectively. The motivation behind this study is to investigate how varying the geometrical characteristics of the microfluidic channel in between the heaters affects the two objectives of interest. While varying the two design variables (in the area between the heaters), the width and height of the microchannel are set to 200 and 50 μm respectively at all other areas.

The two objective functions studied in this Chapter are the same as the ones studied in Chapter 3.4.5; the $log_2(\frac{[DNA]}{[DNA]_o})$ and the pressure drop along the microchannel (see O1 and O2 of Table 3.17). Part of the work appearing in this Chapter is presented and published in the proceedings at the 6^{th} World Congress on Momentum, Heat and Mass Transfer (Zagklavara et al., 2021).

3.4.7.1 Design of Experiments

The design of experiments is performed by varying the values of these two design variables within their upper and lower boundaries of 500 - 2500 μm and 100 - 200 μm for L_5 (= L_7) and W_4 respectively. The other dimensions of the design parameters and the material properties of the channel are based on the design proposed by Papadopoulos et al. (2015) (see Tables 3.15, 3.16, 3.13 and 3.14). The MMLH method is used to generate the 80 DoE points. The code used to generate 80 DoE points

(Chapter B.5 of Appendix) is based on the work of Julie (2012), after modifying it to include the four corner points of the design domain.

3.4.7.2 Response surfaces

In order to study the behaviour of the two objective functions throughout the design domain, the response surfaces need to be created. The original model implemented in COMSOL Multiphysics ® is evaluated at 80 sample points (see Appendix B.5). The dimensionless and scaled (0-1) response surfaces of $-log_2(\frac{[DNA]}{[DNA]_o})$ (obj_1) and pressure drop (obj_2) are generated using a polyharmonic spline (PS) and a feedforward Neural Network (NN) (see Chapter 3.4.5.2 for more details).

3.4.7.3 Optimisation Algorithms

Two optimisation algorithms are used to find the optimum values of the generated meta-models for the two objective functions of interest (obj_1 and obj_2); the *genetic algorithm* (*ga* MATLAB® function (MathWorks, 2021)) and the *e05jbc* of the NAG optimisation library (NAG, 2020). For more details, see Chapter 3.4.5.3.

Similarly to the optimisation problems presented earlier in Chapters 3.4.5 and 3.4.6, there exists more than one objective functions to be optimised at the same time. Considering that improving the solution of one objective results in deteriorating the solution of the other, no single optimal solution with respect to all the objective functions exists. Instead, a set of optimal solutions is generated using the Pareto optimal solutions or Pareto front (Amanifard et al., 2008; Shojaeefard et al., 2013).

3.4.7.4 Results

3.4.7.4.1 Response surfaces The PS and NN are used to generate response surfaces of the two objective functions, providing the ability to compare the two different methods and their results. The PS generates the response surfaces appearing in Figures 3.40a, 3.41a and 3.42a, 3.43a for obj_1 and obj_2 respectively. An alternative version of Figure 3.40a is published in Zagklavara et al. (2021) for $log_2(\frac{[DNA]}{[DNA]_o})$. The *fitnet* MATLAB® function is used to generate the response surfaces appearing in Figures 3.40b, 3.41b and 3.42b, 3.43b for obj_1 and obj_2 respectively. The DoE points are presented in Table B.5 of Appendix B.5.

3.4.7.4.2 Optimisation The optimum values of the response surfaces of the DNA amplification and pressure drop, produced by PS and NN, are presented in Tables 3.33, 3.35 and 3.34, 3.36 respectively. The values presented in these tables are obtained from simulations that include the Joule Heating model, hence describing a non-ideal function of the copper wire heaters. As pointed out earlier, the response surfaces generated and the simulations of the DoE points are completed without the Joule Heating model, in order to avoid the trial and error process required the three values of current at the copper wire heaters (changes in each DoE point).

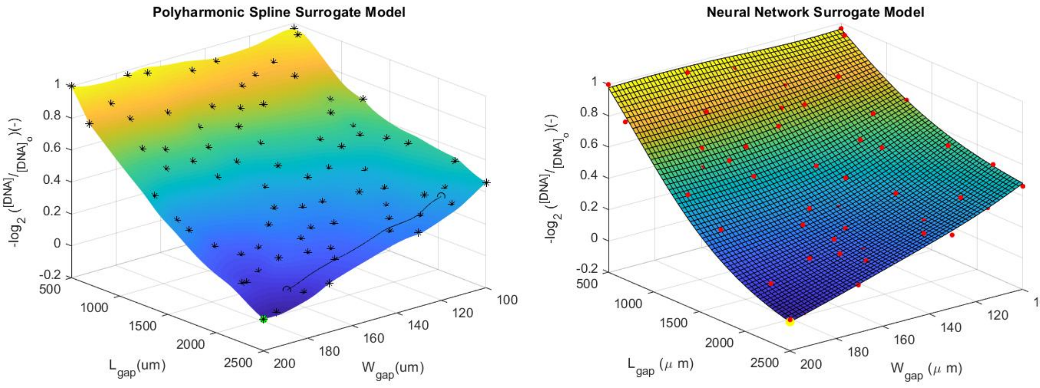

(A) Polyharmonic Spline (B) Neural Network

FIGURE 3.40: Response surfaces of the $-log_2(\frac{[DNA]}{[DNA]_o})$, generated with (a) PS and (b) NN. Genetic algorithm (*ga*) is used to obtain the optimum values, presented in green and yellow in graphs (a) and (b) respectively.

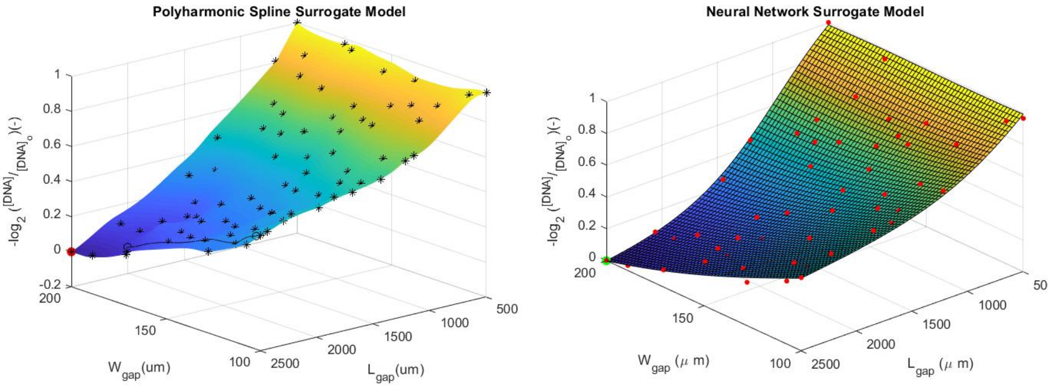

(A) Polyharmonic Spline (B) Neural Network

FIGURE 3.41: Response surfaces of the $-log_2(\frac{[DNA]}{[DNA]_o})$, generated with (a) PS and (b) NN. The *e05jbc* NAG routine is used to obtain the optimum values, that are presented in red and green respectively.

One can observe that no single solution exists that simultaneously optimises both objectives since they are conflicting with each other (green points in Figure 3.44). Therefore, a pareto-front plot (star points in Figure 3.45) is generated in order to obtain the optimum design of this multi-objective optimisation problem, providing a number of equally-good Pareto optimal solutions with the *gamultiobj* function (MathWorks, 2020). The Pareto front plot is presented in Figure 3.45.

TABLE 3.33: Optimum solutions obtained with genetic algorithm for $log_2\frac{[DNA]}{[DNA]_o}$

Polyharmonic			Neural Network			Deviation
W_{gap} (μm)	L_{gap} (μm)	$log_2\frac{[DNA]}{[DNA]_o}$ (-)	W_{gap} (μm)	L_{gap} (μm)	$log_2\frac{[DNA]}{[DNA]_o}$ (-)	$log_2\frac{[DNA]}{[DNA]_o}$ (%)
200	2500	0.68627	200	2500	0.68627	0.00

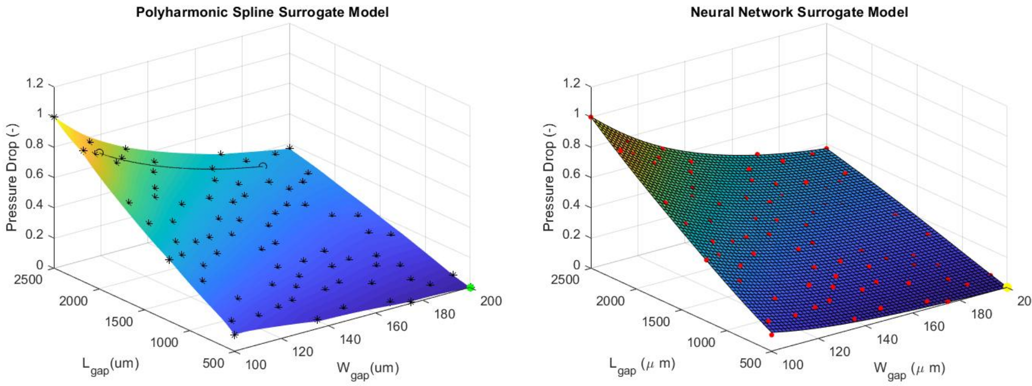

(A) Polyharmonic Spline (B) Neural Network

FIGURE 3.42: Response surfaces of the total pressure drop, generated with (a) PS and (b) NN. Genetic algorithm (*ga*) is used to obtain the optimum values, which are presented in green and yellow respectively.

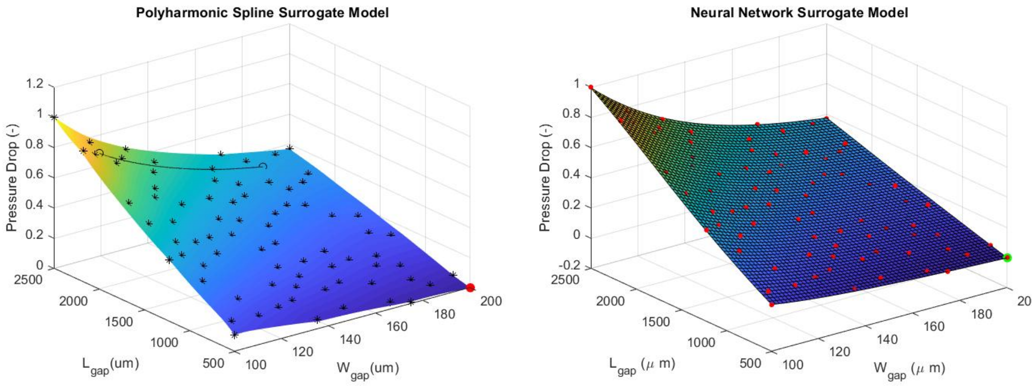

(A) Polyharmonic Spline (B) Neural Network

FIGURE 3.43: Response surfaces of the total pressure drop, generated with (a) PS and (b) NN. The *e05jbc* NAG routine is used to obtain the optimum values, presented in red and green respectively.

TABLE 3.34: Optimum solutions obtained with genetic algorithm for the pressure drop

Polyharmonic			Neural Network			Deviation
W_{gap} (μm)	L_{gap} (μm)	ΔP (Pa)	W_{gap} (μm)	L_{gap} (μm)	ΔP (Pa)	ΔP (%)
200	500	260.25	200	500.118	260.33	0.03

For all the different meta-modelling (polyharmonic spline, neural network) and optimisation methods (genetic algorithm, e05jbc NAG routine) used, the optimum solutions appear to be in very good agreement with each other i.e. when using the same optimisation method but different meta-modelling technique, the values of the two objectives are found to differ by less than 0.05 % for all cases (Tables 3.33 - 3.36).

After considering the results obtained from the response surfaces of the $log_2 \frac{[DNA]}{[DNA]_o}$, the joule heating model is run for the optimum solution (W_{gap} and L_{gap} equal to 200

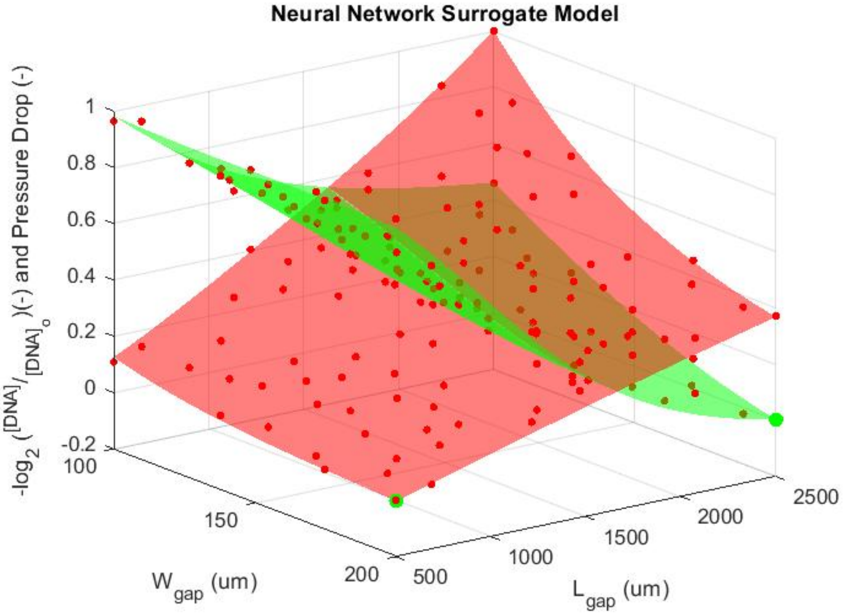

FIGURE 3.44: Response surfaces of the $-log_2(\frac{[DNA]}{[DNA]_o})(-)$ (green) and the pressure drop (-) (red). The optimum values are presented in green, while both objective functions are dimensionless and scaled between 0 and 1.OK

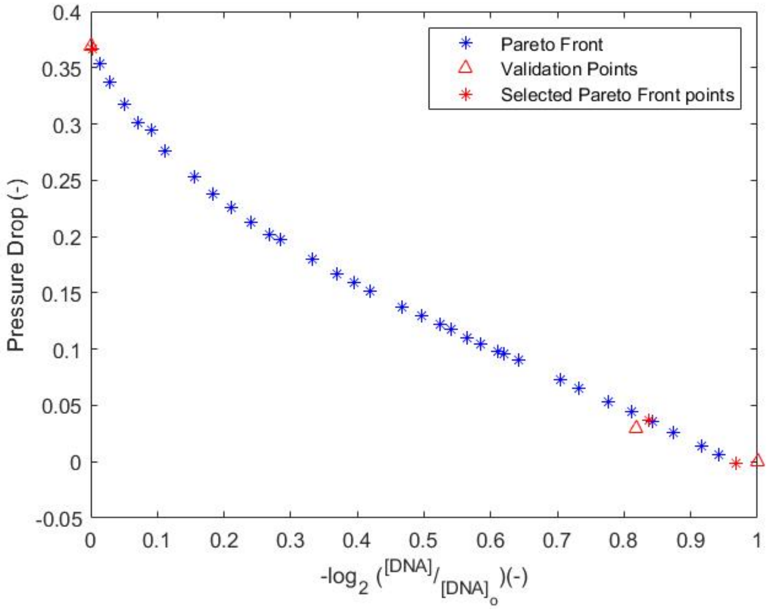

FIGURE 3.45: Pareto front (star points) generated with *gamultiobj* (MathWorks, 2020) of MATLAB®, for the $-log_2(\frac{[DNA]}{[DNA]_o})$ (obj_1) and the pressure drop (obj_2). Three points (red star) are validated (red triangle).

μm and 2500 μm respectively). The results indicate that for these design parameters, a $\sim$ 3% increase in the $log_2\frac{[DNA]}{[DNA]_o}$ and $\sim$ 13.3% increase in the pressure drop

TABLE 3.35: Optimum solutions obtained with e05jbc NAG routine for $log_2\frac{[DNA]}{[DNA]_o}$

Polyharmonic			Neural Network			Deviation
W_{gap} (μm)	L_{gap} (μm)	$log_2\frac{[DNA]}{[DNA]_o}$ (-)	W_{gap} (μm)	L_{gap} (μm)	$log_2\frac{[DNA]}{[DNA]_o}$ (-)	$log_2\frac{[DNA]}{[DNA]_o}$ (%)
200	2500	0.68627	200	2500	0.68627	0.00

TABLE 3.36: Optimum solutions obtained with e05jbc NAG routine for the pressure drop

Polyharmonic			Neural Network			Deviation
W_{gap} (μm)	L_{gap} (μm)	ΔP (Pa)	W_{gap} (μm)	L_{gap} (μm)	ΔP (Pa)	ΔP (%)
200	500	260.25	200	500	260.382	0.05

TABLE 3.37: Validation of three points appearing in the Pareto-front plot (Figure 3.32).

	Model				Pareto Optimum	
Point	W_{gap} (μm)	L_{gap} (μm)	$log_2\frac{[DNA]}{[DNA]_o}$ (-)	ΔP (-)	$log_2\frac{[DNA]}{[DNA]_o}$ (-)	ΔP (-)
1	1	1	0	0.3696	0.0027	0.3672
2	1	0	1	0	0.9677	-0.0016
3	1	0.093	0.8177	0.0294	0.8362	0.03718

are observed in one PCR cycle, compared to the values of the original design of Papadopoulos et al. (2015). Furthermore, for W_{gap} and L_{gap} equal to 200 μm and 500 μm respectively, a 10.7% reduction in the pressure drop can be observed, accompanied by a 2.1% decrease in the $log_2\frac{[DNA]}{[DNA]_o}$.

One can observe in Figures 3.44 and 3.45 that the values of pressure drop and -$log_2\frac{[DNA]}{[DNA]_o}$ are scaled appropriately between 0 and 1. This is done in order to visualise better the multi-objective nature of the optimisation problem, while at the same time ensuring that both objective functions will be weighted the same when using the gamultiobj optimisation function (MathWorks, 2020). Three of the optimal solutions presented in the pareto-front plot are successfully validated using the simulation model (Table 3.37). As mentioned previously, no single solution exists that can optimise both objectives at the same time.

Varying the spacing between the heaters appears to have a bigger impact on both objectives compared to W_{gap}, especially for the lower values of L_{gap} (for the ranges of values of the design variables considered). The effect of varying W_{gap} appears to become more significant for the higher values of L_{gap} for both objectives. In terms of DNA amplification, this is to be expected, since the higher values of L_{gap}, the higher the amount of time the fluid spends outside the temperature zones of interest, a residence time that is increased even further by higher values of W_{gap}.

3.4.8 Optimisation of the PCR protocol and channel width in the extension zone of the unitcell

After completing the 2-design variable optimisation studies presented in Chapters 3.4.5 - 3.4.7, a four design variable problem is formulated to study the effect that the implemented PCR protocol and doubling the width of the microchannel in the extension zone can have on the objectives of interest. The content of this Chapter is presented in the publication of Zagklavara et al. (2022).

More specifically, the design variables selected for this problem are the following (Figure 3.23): i) the residence time in denaturation zone, $t_{R,den}$, ii) the residence time in extension zone, $t_{R,ext}$, iii) the residence time in annealing zone, $t_{R,ann}$ and iv) the width (W_3) of the microchannel in the (second part of) extension zone. The values of the residence times ($t_{R,den}$, $t_{R,ext}$ and $t_{R,ann}$) and the three channel lengths in the denaturation, extension and annealing zones vary in each simulation, in order to observe the effect that the PCR protocol has on the objectives of interest. More specifically, L_4, L_8, and L_6 are calculated by Equation 3.16 for the different values of $t_{R,den}$, $t_{R,ext}$ and $t_{R,ann}$. Furthermore, W_3 is selected as the fourth variable and is defined according to Equation 3.36, where z_{w3} is a parameter $\in [0, 1]$. The selection of the fourth variable, W_3, is made in order to study the benefit of doubling the width of the microfluidic channel in the extension zone (as originally used by Papadopoulos et al. (2015)).

As far as the objective functions are concerned, the $log_2(\frac{[DNA]}{[DNA]_o})$ and the pressure drop along the microchannel (ΔP (Pa)) are selected for this study as well. Furthermore, the total processing time together with the total substrate volume are also considered objective functions, since reducing the total substrate volume and total residence time can lead to significant reductions in cost and processing times of the device (Zagklavara et al., 2022).

$$W_3 = (z_{w3} + 1)W_2, \qquad z_{w3} \in [0, 1], \tag{3.36}$$

3.4.8.1 Design of Experiments

The design of experiments is performed by varying the values of the four design variables within their upper and lower boundaries appearing in Table 3.38. The ranges of the residence times are created by $t_{R,zone(\text{Papadopoulos et al., 2015})} \pm 1.5s$, where zone = {denaturation, extension, annealing}. The range of the fourth design variable, W_3, is set at 400 - 800 μm in order to examine the benefits of increasing (up to twice the width of the microchannel in the other zones, W_2) the width in the extension zone in particular, as performed by Papadopoulos et al. (2015). The upper limit of 800 μm is set to be lower than width of the substrate, W_1, allowing for at least 100 μm gap at each side of the microchannel. The other dimensions of the design parameters and the material properties of the channel are presented in Tables 3.13

and 3.14 respectively, and are based on the design proposed by Papadopoulos et al. (2015).

The Morris Mitchel Latin Hypercube method is used to generate the DoE points. The code used to generate 160 DoE points (Chapter B.6 of Appendix) is based on the work of Julie (2012), after modifying it to include the sixteen corner points of the design domain.

TABLE 3.38: Upper and lower boundaries of the four design variables (Figure 3.23)

Design Variables	Lower Limit	Upper Limit
$t_{R,den}$ (s)	1.5	4.5
$t_{R,ext}$ (s)	4.7	7.7
$t_{R,ann}$(s)	2.7	5.7
W_3 (μm)	400	800

3.4.8.2 Response surfaces

In order to study the behaviour of the four objective functions throughout the selected design domain, meta-models need to be created. The original model implemented in COMSOL Multiphysics ® is evaluated at 160 sample points (see Appendix B.6).

The *fitnet* MATLAB® function is used to generate the NNs for $-log_2\frac{[DNA]}{[DNA]_o}$, Δp, $t_{R,tot}$ and $V_{S,tot}$. The values of the objectives are scaled appropriately between 0-1 (see Appendix G). The 3D response surfaces (for constant values of z_{w3}) are developed using the libraries presented by Zhivomirov (2021), and are presented in Figures 3.46, 3.47, 3.48 and 3.49 for $log_2\frac{[DNA]}{[DNA]_o}$, Δp, $t_{R,tot}$ and $V_{S,tot}$ respectively. The colour bar is used to present the values of the objectives, while a 3D response surface is printed for a different value of the fourth design variable, z_{w3}. The sampling data points used to create the response surfaces are provided in Table B.6 of Appendix B.6. Appendix F presents the response surfaces for all four objectives for more values of z_{w3}.

The correlation coefficients between the DNA amplification - total residence time and the DNA amplification - individual residence times are given in Table 3.39. $log_2\frac{[DNA]}{[DNA]_o}$ and $t_{R,ext}$ appear to be strongly related, while there appears to be very little correlation between $log_2\frac{[DNA]}{[DNA]_o}$ - $t_{R,den}$ and $log_2\frac{[DNA]}{[DNA]_o}$ - $t_{R,ann}$. The $log_2\frac{[DNA]}{[DNA]_o}$ also appears to not be significantly related to the width of the channel in the extension zone.

3.4.8.3 Optimisation

The *e05jbc* function of the NAG optimisation library (NAG, 2020), which is based on the Multi-level Coordinate Search method described in Huyer and Neumaier (1999), uses the meta-models of the objectives to solve the optimisation problems. Subsection 3.4.8.4.1 presents the meta-models for obj_1, obj_2, obj_3 and obj_4. Subsection 3.4.8.4.2 then describes the optimisation method used to locate the optimum values for the four objectives, which is based on the *e05jbc* NAG routine (NAG, 2020). Furthermore, the results of a multi-objective optimisation study are also presented in the form of a Pareto front, showing the available compromises between competing objectives.

3.4.8.4 Results

3.4.8.4.1 Response surfaces The *fitnet* MATLAB® function is used to generate the NNs for $-log_2(\frac{[DNA]}{[DNA]_o})$, Δp, $t_{R,tot}$ and $V_{S,tot}$. The values of the objectives are scaled between 0-1 (see Appendix G). The 3D response surfaces are developed using the libraries presented by Zhivomirov (2021), and are presented in Figures 3.46, 3.47, 3.48 and 3.49 for $log_2(\frac{[DNA]}{[DNA]_o})$, Δp, $t_{R,tot}$ and $V_{S,tot}$ respectively. The colour bar is used to present the values of the objectives, while a 3D response surface is printed for a different value of the fourth design variable, z_{w3}. The sampling data points used to create the response surfaces are provided in Table B.6 of Appendix B.6. Appendix F presents the response surfaces for all four objectives for more values of z_{w3}.

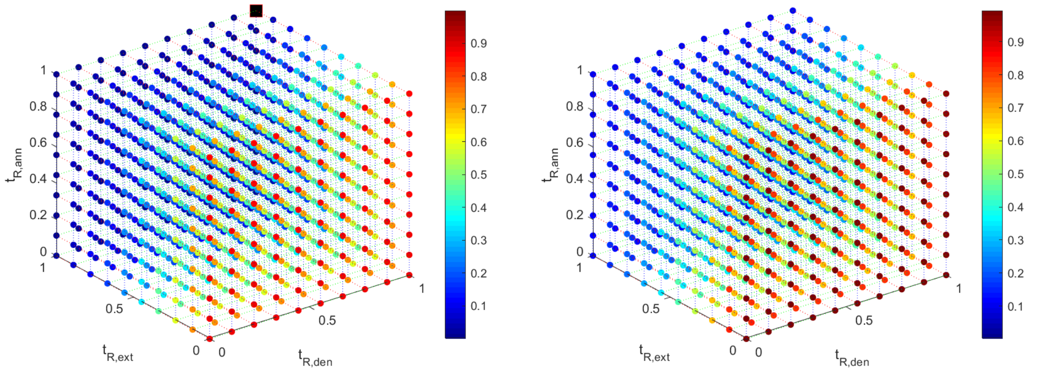

(A) (B)

FIGURE 3.46: Visual representation of the $log_2(\frac{[DNA]}{[DNA]_o})$(-) data (colorbar) for (a) z_{w3} = 0 and (b) z_{w3} = 1. The optimum solution is presented in a black square in Figure 3.46a.

TABLE 3.39: Correlation Coefficients.

Function	$t_{R,den}$	$t_{R,ext}$	$t_{R,ann}$	$t_{R,tot}$	z_{w3}
$log_2\frac{[DNA]}{[DNA]_o}$	-0.08	0.98	-0.01	0.72	-0.16

The correlation coefficients between the DNA amplification - total residence time and the DNA amplification - residence times are given in Table 3.39. $log_2\frac{[DNA]}{[DNA]_o}$ and $t_{R,ext}$ appear to be strongly related, while there appears to be very little correlation

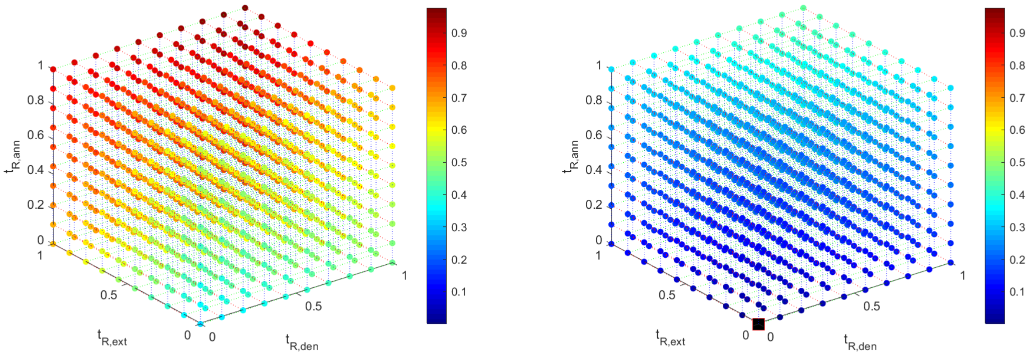

(A) (B)

FIGURE 3.47: Visual representation of the Δp(-) data (colorbar) for (a) z_{w3} = 0 and (b) z_{w3} = 1. The optimum solution is presented in a black square in Figure 3.47b.

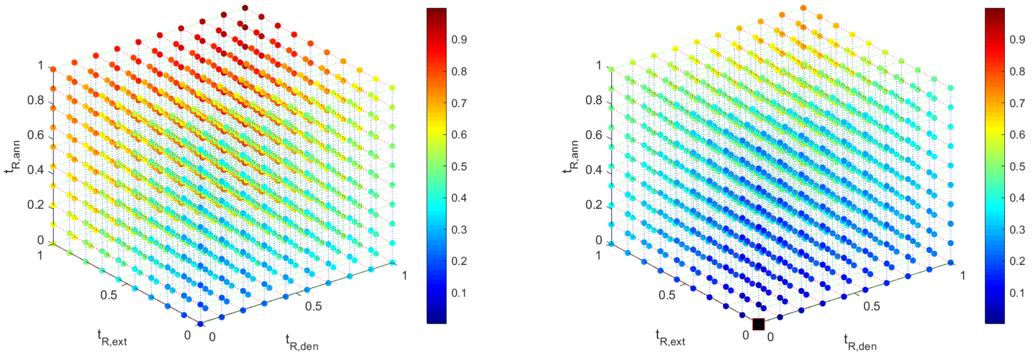

(A) (B)

FIGURE 3.48: Visual representation of the $t_{R,tot}$(-) data (colorbar) for (a) z_{w3} = 0 and (b) z_{w3} = 1. The optimum solution is presented in a black square in Figure 3.48b.

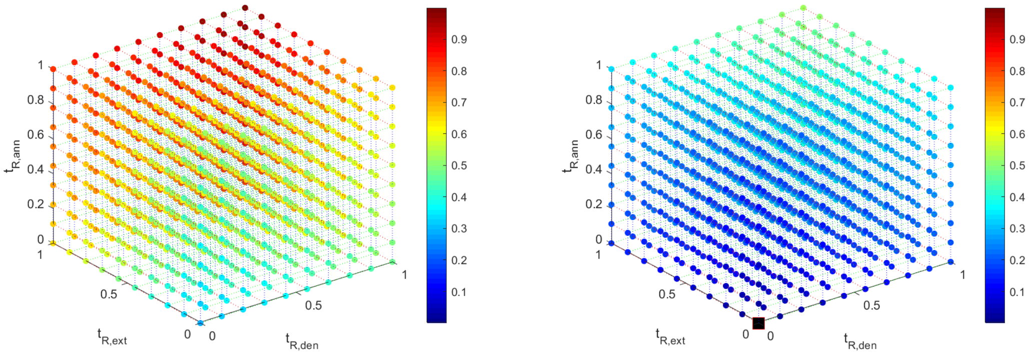

(A) (B)

FIGURE 3.49: Visual representation of the $V_{S,tot}$(-) data (colour bar) for (a) z_{w3} = 0 and (b) z_{w3} = 1. The optimum solution is presented in a black square in Figure 3.49b.

between $log_2\frac{[DNA]}{[DNA]_o}$ - $t_{R,den}$ and $log_2\frac{[DNA]}{[DNA]_o}$ - $t_{R,ann}$. The $log_2\frac{[DNA]}{[DNA]_o}$ also appears to not be significantly related to the width of the channel in the extension zone.

3.4.8.4.2 Optimisation

Single-Objective studies As part of the single-objective studies, the minima of the meta-models of obj_1, obj_2, obj_3 and obj_4 are found at $[t_{R,den}$ (s), $t_{R,ext}$ (s), $t_{R,ann}$ (-), z_{w3} (-)$]_{obj_1}$ = [4.5, 7.7, 5.7, 0], $[t_{R,den}$ (s), $t_{R,ext}$ (s), $t_{R,ann}$ (-), z_{w3} (-)$]_{obj_2}$ = [1.5, 4.7, 2.7, 1], $[t_{R,den}$ (s), $t_{R,ext}$ (s), $t_{R,ann}$ (-), z_{w3} (-)$]_{obj_3}$ = [1.5, 4.7, 2.7, 1] and $[t_{R,den}$ (s), $t_{R,ext}$ (s), $t_{R,ann}$ (-), z_{w3} (-)$]_{obj_4}$ = [1.5, 4.7, 2.7, 1] respectively. These designs are then tested including the Joule Heating model. Details of these designs and the values of the objectives can be found in Tables 3.40 and 3.41 respectively. The optimum designs of obj_1, obj_2, obj_3 and obj_4 are presented in Figures 3.46a, 3.47b, 3.48b and 3.49b respectively.

Design 4 (see Table 3.40) offers a 16.42% increase in the value of $log_2\frac{[DNA]}{[DNA]_o}$ (or $\sim$ 5.7% increase in [DNA]) and 50.54% and 5.62% decrease in the values of pressure drop and total substrate volume respectively, from the corresponding values obtained for the $[W_2$ (μm), H_{Fluid} $(\mu m)]$=[200, 50] design of Papadopoulos et al. (2015). In order to examine the significance of the $\sim$ 5.7% increase in [DNA] for a single unitcell, ten consecutive PCR cycles are simulated for Designs 2 and 4 (see Table H.1, Appendix H), using the Joule Heating model for the function of the copper wire heaters. The results are presented in Figure 3.50. According to the data obtained for Design 4, this $\sim$ 5.7% increase in [DNA] in the first PCR cycle, is expected to increase the concentration of DNA approximately by $\sim$ 32% in ten cycles (compared to Design 2). Furthermore, by offering a $\sim$ 51% reduction in the pressure drop requirements, the operating cost of such a device is expected to be reduced significantly. However, this design also leads to an increase of 58.7% in the total residence time.

TABLE 3.40: Details of the designs appearing in Figure 3.50 and Table 3.41.

Design	Reference	Objective to opt	W_2 (μm)	W_3 (μm)	H_{Fluid} (μm)	$t_{R,den}$ (s)	$t_{R,ext}$ (s)	$t_{R,ann}$ (s)
1	P	-	200	400	50	3.0	6.2	4.2
2	CW	-	200	400	50	3.0	6.2	4.2
3	Z	obj_1	**400**	800	**50**	3.0	6.2	4.2
4	CW	obj_1	400	**400**	50	**4.5**	**7.7**	**5.7**
5	Z	obj_2	**400**	800	**80**	3.0	6.2	4.2
6	CW	obj_2, obj_3, obj_4	400	**800**	50	**1.5**	**4.7**	**2.7**

CW: Current Work, Z: Zagklavara et al. (2021), P: Papadopoulos et al. (2015). The design variables in each study are presented in **bold**.

On the other hand, Design 6 (see Table 3.40) leads to a 80.50%, 17.80% and 43.23% decrease in the values of pressure drop, total residence time and total substrate volume respectively. However, this design also comes with a 13.43 % decrease in

TABLE 3.41: Optimum solutions obtained with e05jbc NAG routine for $log_2\frac{[DNA]}{[DNA]_o}$, ΔP, $t_{R,tot}$ and $V_{S,tot}$. Details of Designs 1-6 can be found in Table 3.40.

Design	$log_2(\frac{[DNA]}{[DNA]_o})^*$		ΔP^*		$t^*_{R,tot}$		$V^*_{S,tot}$	
	$(-)$	(%)	(Pa)	(%)	(s)	(%)	(m^3)	(%)
1	0.67	-	-	-	-	-	-	-
2	0.67	0.00	284.29	-	18.47	-	$1.22 \cdot 10^{-8}$	-
3	0.70	4.48	74.88	-73.66	-	-	$8.12 \cdot 10^{-9}$	-33.45
4	0.78	16.42	140.62	-50.54	29.31	58.71	$1.15 \cdot 10^{-8}$	-5.62
5	0.62	-7.46	13.74	-95.17	-	-	$7.62 \cdot 10^{-9}$	-37.51
6	0.58	-13.43	55.44	-80.50	15.18	-17.80	$6.92 \cdot 10^{-9}$	-43.23

* All the values are calculated using the Joule Heating module. The deviations are calculated based on Design 2.

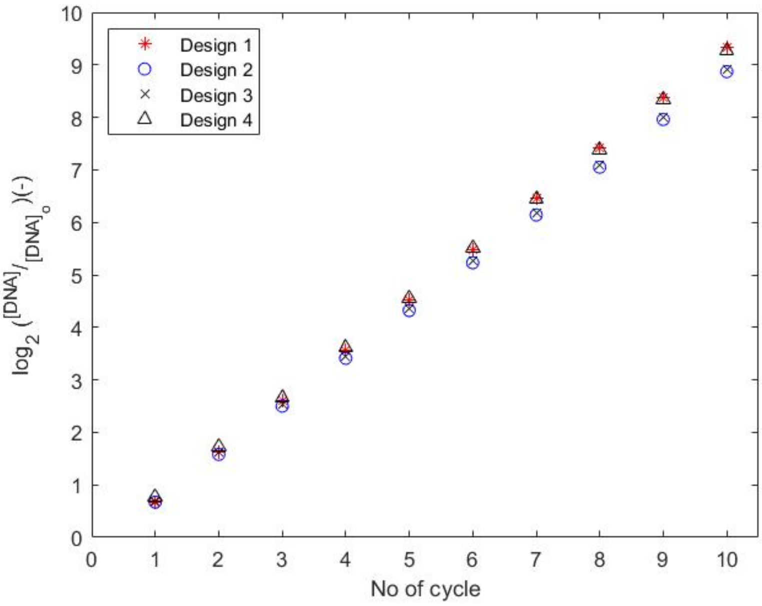

FIGURE 3.50: Values of $log_2(\frac{[DNA]}{[DNA]_o})(-)$ for 10 PCR cycles. The details of the four designs are presented in Table 3.40. Designs 1 and 2 present the designs by Papadopoulos et al. (2015) and its validation (current work). Designs 3 (Zagklavara et al., 2021) and 4 (current work) present the designs offering maximum DNA amplification.

$log_2\frac{[DNA]}{[DNA]_o}$ (or a 6.6% decrease in the [DNA]) compared to the one presented by Papadopoulos et al. (2015). Figure 3.51 presents a comparison between the different unitcell designs, together with their temperature profiles. Figure 3.52 shows the DNA concentration profiles at the middle plane in the fluid domain for the two designs optimising the four objectives.

Multi-Objective study The single-objective optimisation studies indicate that conflicts between the objectives result in a complex multi-objective optimisation design problem. For the purposes of visualisation, three out of the four objectives

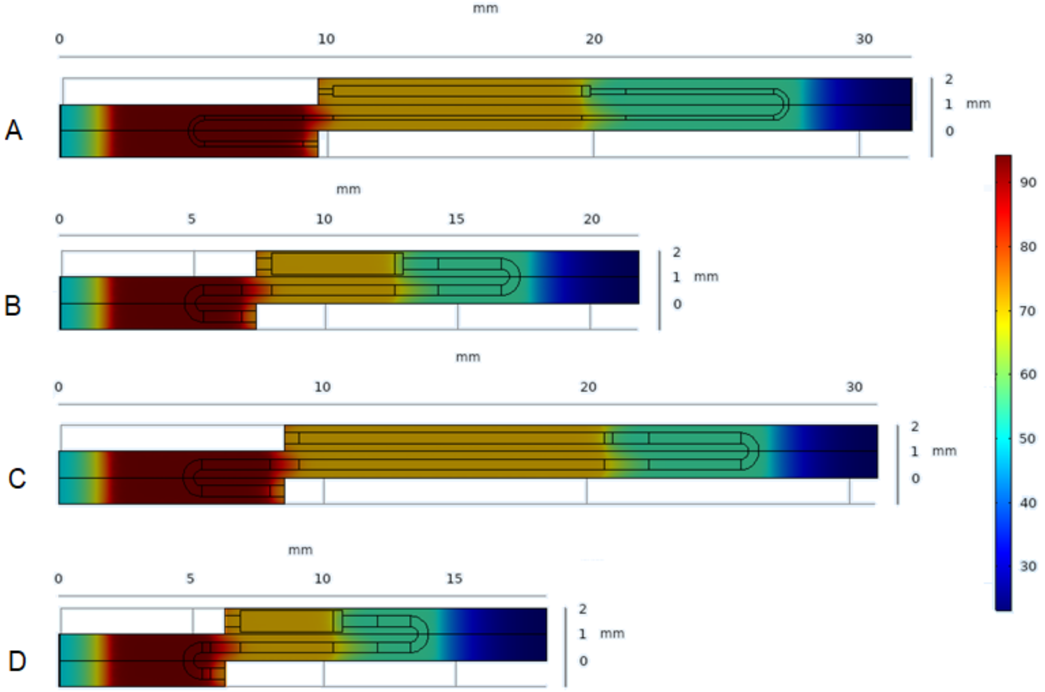

FIGURE 3.51: Temperature profiles of the different unitcell designs presented in Tables 3.40 and 3.41: A) Design 2, B) Design 3, C) Design 4, D) Design 6.

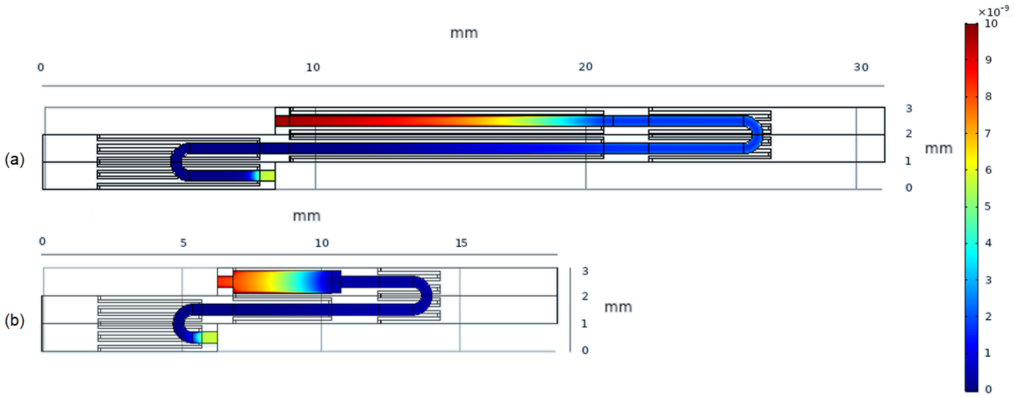

FIGURE 3.52: DNA concentration profiles at the centreline along the length of the microchannel of a) Design 4 and b) Design 6 of the unitcell, presented in Tables 3.40 and 3.41.

($log_2\frac{[DNA]}{[DNA]_o}$, $t_{R,tot}$, $V_{S,tot}$) are selected to generate a Pareto front (Figure 3.53). The Pareto front is hence a 3D plot, that is developed using the *gamultiobj* function (MathWorks, 2020), in order to demonstrate the available compromises between the three objectives. The values of obj_1, obj_3 and obj_4 are dimensionless and scaled between 0 and 1, to aid the visualisation of the multi-objective results. The values of *FunctionTolerance* and *MaxGenerations* are adjusted to $1 \cdot 10^{-6}$ and $N_{DVARS} \cdot 200$, where

N_{DVARS} is the number of design variables (N_{DVARS}=4). Three of the optimal solutions in the Pareto front plot are validated using the simulation model (Tables 3.42 and 3.43), deviating less than $\sim$ 0.15% for all three cases. The Pareto front offers the ability to significantly ameliorate the performance of the device depending on the requirements of the designer/engineer. For example, the design of Point 2 appearing in Tables 3.42 and 3.43, illustrates the ability to improve $t_{R,tot}$ and $V_{S,tot}$ by 24.64% and 25.75% respectively when compromising on $log_2 \frac{[DNA]}{[DNA]_o}$ by only 2.22%.

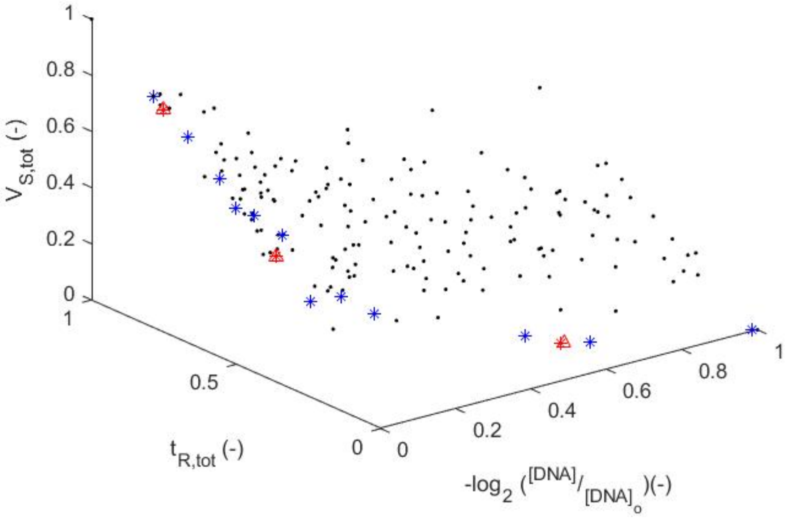

FIGURE 3.53: Pareto front (star points) generated with *gamultiobj* (MathWorks, 2020) of MATLAB®, for the $-log_2(\frac{[DNA]}{[DNA]_o})$ (obj_1), the $t_{R,tot}$ (obj_3) and the $V_{S,tot}$ (obj_4). Three points of the Pareto front (red star points) are validated (red triangle points) (see Tables 3.42 and 3.43). The black dots and red triangles represent high-fidelity data obtained using COMSOL Multiphysics.

TABLE 3.42: Validation of three points appearing in the Pareto-front plot (Figure 3.53).

Point	$t_{R,den}$		$t_{R,ext}$		$t_{R,ann}$		z_{w3}	W_3
	$(-)$	(s)	$(-)$	(s)	$(-)$	(s)	(-)	(μm)
1	0.0747	1.72	0.9974	7.69	0.9611	5.58	0.0544	421.76
2	0.0259	1.58	0.9817	7.65	0.621	4.56	0.7257	690.28
3	0.0037	1.51	0.3211	5.66	0.0121	2.74	0.9923	796.92

The results of this study indicate that doubling the width of the microchannel in the extension zone, together with the residence time in denaturation and annealing zones does have a significant effect on DNA amplification. The residence time in extension zone however has been found to be strongly related to DNA amplification. From consideration of the Pareto front, several designs are presented, and depending on design priorities, different design solutions can be used to improve

TABLE 3.43: Validation of three points appearing in Figure 3.53.

	Pareto Optimum			Model			Deviation		
Point	O1 (-)	O3 (s)	O4 (m^3)	O1 (-)	O3 (s)	O4 (m^3)	O1 (%)	O3 (%)	O4 (%)
1	0.770	26.014	$1.050 \cdot 10^{-8}$	0.770	26.014	$1.050 \cdot 10^{-8}$	0.00	0.00	0.01
2	0.755	22.083	$8.546 \cdot 10^{-9}$	0.755	22.084	$8.546 \cdot 10^{-9}$	0.00	0.00	0.00
3	0.674	16.680	$7.187 \cdot 10^{-9}$	0.673	16.681	$7.187 \cdot 10^{-9}$	0.15	-0.01	0.00

O1: $log_2 \frac{[DNA]}{[DNA]_o}$, O3: $t_{R,tot}$, O4: $V_{S,tot}$.

the designs of Papadopoulos et al. (2015) and Zagklavara et al. (2021). The Pareto front includes designs ranging from those with low DNA amplification, low total device volume and operation time to high values of DNA amplification, high total device volume and operation time or design compromises between the three objectives.

The first type of design offers the ability to reduce the total material volume, operation time and pressure drop requirements by up to $\sim$ 43.2%, $\sim$ 17.8% and $\sim$ 80.5% respectively. However, such design modifications can lead up to $\sim$ 6.6% reduction in the [DNA] in a unitcell. Single objective optimisation on the DNAAE, shows that it is possible to increase DNA concentration by up to $\sim$ 5.7% in the first PCR cycle, which simulations show results in an increase of $\sim$ 32% over ten PCR cycles. At the same time, this design offers a reduction in the total pressure drop ($\sim$ 50.5%) together with a small reduction in the material volume ($\sim$ 5.6%), having however a $\sim$ 58.7% increase in the total operating time. According to the results obtained, all designs have the potential to minimise pumping requirements for such devices; with reductions in pressure drop allowing for smaller pumps to be used (particularly when building integrated lab-on-chip devices). The smaller size and reduced pumping requirements also minimise power requirements, which is an important consideration when these are used within handheld devices containing their own power sources. This supports the ongoing efforts to develop field-ready microfluidic systems.

3.4.9 Summary

As part of this work, a number of optimisation studies have been completed, addressing single- and multi- objective optimisation problems of interest, while examining different design variables in SP-CF-PCR devices. These studies present the effect that different geometries/designs have on a number of competing objectives. More specifically, this work demonstrates that the optimisation of PCR systems presents complex, multi-objective design optimisation problems with several competing objectives; the DNA amplification, pressure drop, total operating time and volume. The reduction of pressure drop is highly important, since it leads to lower pumping and power requirements, allowing for smaller pumps to be used. This becomes significant when building integrated lab-on-chip devices, supporting the ongoing efforts to develop field-ready microfuidic systems. The reduction in the volume of a device leads to lower production cost, hence reducing the price of such devices, while lower operating times lead to the development of faster devices.

According to one of the first optimisation studies performed considering only two design variables, it appears that the output DNA concentration can be increased by 2.1% from the original design when increasing the channel width. In the designs studied, the channel length in each temperature region was modified in order to account for the changes in the cross-sectional area, ensuring a constant fluid volume per region. For the purposes of observing the effect that this particular design modification is expected to have after several consecutive PCR cycles are performed, the study is extended to ten PCR cycles, demonstrating the ability to improve the output DNA concentration by up to 3.2%. Furthermore, a strong link between temperature uniformity and the optimum DNA amplification is observed as recorded in the literature, that however requires further investigation.

According to other studies conducted on optimising the geometrical channel characteristics between the heaters, increasing the spacing between heaters and the channel width is expected to increase the DNA amplification. At the same time, the pressure drop is minimised for designs with the lowest heater spacing and greatest channel width. Varying the spacing between the heaters appears to have a bigger impact on both objectives compared to varying the channel width between the heaters, especially for the smaller values of heater spacing (for the ranges of values of the design variables considered). The effect of varying the channel width between the heaters appears to become more significant for the higher values of heater spacing in terms of both pressure drop and DNA amplification. In terms of the latter, this is due to the fact that the higher values of heater spacing, the higher the amount of time the fluid spends in the device outside the temperature zones of interest, a residence time that is increased even further by higher values of channel width between the heaters. Furthermore, due to the competing behaviour of the two objectives, the Pareto-front generated offers a variety of designs that can be used to enhance the performance of the microfluidic CFPCR device.

In the latest optimisation study focusing on optimising both the channel width in the extension zone and the PCR protocol, the longer total residence time in the device is found to lead to higher DNA amplification, while the DNA amplification appears to be highly correlated with the time the sample spends in the extension zone (residence time in the extension zone). The output DNA concentration is found to be able to improve by up to 7.9% compared to the initial one, for the higher values of residence time. In the same study, a different design indicated that the pressure drop, total volume and total residence time can be improved by up to 80.5%, 43.2% and 17.8% respectively in a single PCR cycle compared to the initial one, for the smallest residence times. As a result, future designs are expected to be characterised by higher residence times in the extension zone and higher values of channel width.

Due to the different optimum designs for the objectives of interest, designs generated by a Pareto Front can be used to assist further the improvement of microfluidic CFPCR devices.

The results of the current investigation indicate that there is significant room for improvement in terms of microfluidic CFPCR devices, allowing significant cost reduction and performance improvement while providing useful examples of the optimal trade-off between the various objectives. This is expected to facilitate the designing process of such devices by providing a useful guide. At the same time, surrogate-enabled optimisation methods are becoming increasingly popular and have proven effective when applied in microfluidic PCR optimisation. Increasing the channel width (from the starting design) offers significant benefits in terms of DNA amplification, pressure drop and substrate volume; hence designs with higher values of channel width are expected to lead to significant performance improvement and cost reduction (both in terms of operating and material cost). Furthermore, for designs with higher channel width values (of the design domain examined), the lower the channel height the higher and lower the DNA amplification and pressure drop respectively. As far as the PCR protocol is concerned, increasing the residence time in the extension zone is expected to improve the DNA amplification.

As part of all these studies, different algorithms/methods were used and compared to develop the response surfaces and generate the optimum designs. Both Neural Network and Polyharmonic Spline successfully generated the response surfaces for all optimisation studies considered, while the former is expected to provide greater flexibility in more complicated problems. For the response surfaces produced, both genetic algorithm (*ga* MATLAB® function) and Multi-level Coordinate Search method (*e*05*jbc* of the NAG optimisation library in MATLAB®) successfully obtained the global optimum solutions with minor differences amongst each other. Even though both optimisation algorithms perform similarly in the set of optimisation problems examined in this work, it is expected that the *e*05*jbc* function might potentially struggle in larger optimisation problems (NAG, 2020).

The Pareto fronts developed in the individual studies provide a guide on how to obtain the optimal trade-off between the competing objectives. Depending on the engineer/designer's approach, improvements in certain objectives can be achieved with a compromise on others, enabling the best possible designs to be generated.

Chapter 4

Development of an experimental setup for droplet-based microfluidic applications

This Chapter presents the combined computational and experimental work conducted for the development of a droplet-based microfluidic device. This device is expected to perform a particular stage of the PCR process, as part of the Melting Curve Analysis (MCA) technique (Matsuda, 2017). The development of this device aims to provide a better understanding of the heat transfer phenomena that take place in droplet-laden flows in microfluidic devices. More specifically, the effect of the presence of droplets (and their packing) on the temperature profiles of the stream on the microfluidic channel is expected to be investigated and compared to the one of single-phase flows. COMSOL ® 5.4 is used to optimise the design of the microfluidic device, before the onset of the experimental work. The Margaret Steel Award and funding was obtained for the design and principal idea behind the development of this device.

At the same time, a collaboration is made with a group of biologists from the University of Leeds (group of Joan Boyes), in order to facilitate their work by using this device to perform MCA. MCA is based on a PCR stage, where while the conversion of double-stranded DNA into single-stranded DNA takes place due to heat denaturation, the change in fluorescence of dsDNA-binding dye is monitored during the shift in temperature (Matsuda, 2017). Some of their work in this area has focused on v(D)j recombination; more specifically, part of their current work involves the study of the kinetics of v(D)j recombination, and that includes the quantification of the different DNA molecules existing in the collected samples.

As a result, a DNA MCA device is designed and developed, aiming to facilitate the work of this team, while at the same time obtaining a better understanding of the heat transfer phenomena in droplet-laden flows. Contrary to other existing MCA experimental devices, this experimental setup offers the advantage of easily replacing the microfluidic channels (capillaries) after use, avoiding the need for any further treatment of the channels, while at the same time it is easier and cheaper to develop.

Furthermore, the required experimental setup can be easily disassembled, the various experimental parts can be replaced in case the system's requirements change per application and equipment already present in a lab can be used to perform parts of the experimental process.

4.1 Literature Review

4.1.1 Heat transfer in droplet-laden flows

This chapter presents a brief review of the experimental and computational studies on the heat transfer phenomena taking place in droplet-laden flows over the last few years (Ganguli and Pandit, 2021).

The publications of Asthana et al. (2011), Eain, Egan, and Punch (2015), Dai et al. (2015) and Ma et al. (2021) are some examples where heat transfer has been experimentally studied in microchannels, involving liquid-liquid two-phase flow. Their studies involve water-light mineral, silicon oil water, water-hexadecane and aqueous glycerol-toluene systems respectively, studying the heat transfer in slug flows (Figure 4.1). Asthana et al. (2011) have observed a significant increase in the heat transfer due to liquid-liquid two-phase flow compared to single-phase flow, together with an increase in the pressure drop. According to the results of Eain, Egan, and Punch (2015), the heat transfer appears to increase when decreasing the slug lengths. Furthermore, according to Ma et al. (2021), two important parameters that affect the mass/heat transfer are the thickness and distribution of the liquid film between the droplet and channel wall.

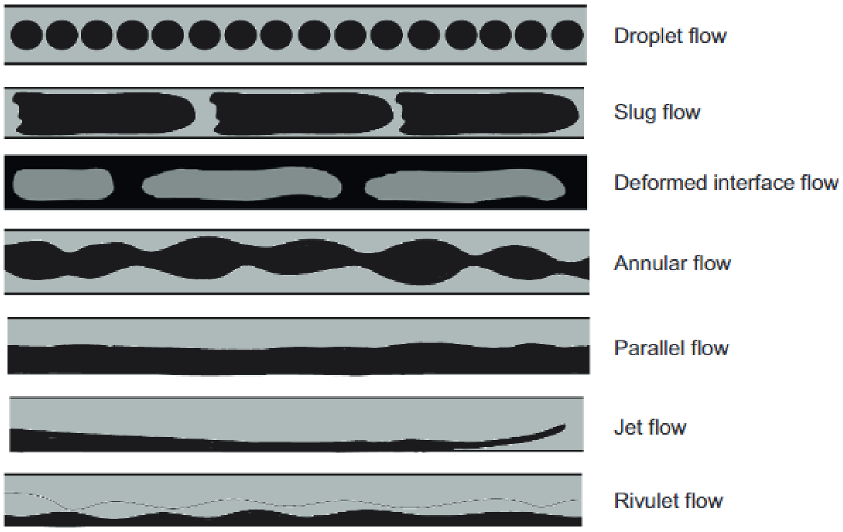

FIGURE 4.1: Common flow patterns in liquid-liquid flow (Figure obtained from Verma and Ghosh (2019)).

The publications of Urbant, Leshansky, and Halupovich (2008), Vivekanand and Raju (2018), Wang (2017), Fischer, Juric, and Poulikakos (2010), Che, Wong, and Nguyen (2012), Che, Wong, and Nguyen (2013) and Li et al. (2021) are some of the numerical publications that can be found in this area. Vivekanand and Raju (2018) used the Volume of Fluid (VOF) method in 100 μm channels, for both constant wall heat flux and constant wall boundary conditions. Their results present an increase in Nusselt number (Nu) compared to ones obtained from single-phase studies. According to Urbant, Leshansky, and Halupovich (2008) that also used VOF, the forced heat transfer in a droplet-laden flow was found to have significantly improved (compared to the forced heat transfer in a single-phase Poiseuille flow), with the fluid reaching wall temperature faster. This is considered to be due to: i) the disturbance of the unidirectional Poiseuille flow, caused by the translation of droplets (Urbant, Leshansky, and Halupovich, 2008) and ii) the presence of internal circulation inside the droplets (Urbant, Leshansky, and Halupovich, 2008; Abdollahi, Sharma, and Vatani, 2017). According to Wang (2017) and Urbant, Leshansky, and Halupovich (2008), when "slender" droplets are present instead of spherical ones, the heat transfer is expected to be better, due to the circulation present between the droplets. The droplet size and distance between consecutive droplets are two parameters that after optimisation can lead to better heat transfer (Wang, 2017). Furthermore, according to the numerical investigation of Urbant, Leshansky, and Halupovich (2008), increasing the droplet size has been found to improve the Nu number. Fischer, Juric, and Poulikakos (2010) studied the heat transfer of liquid-liquid flows in a 2D axisymmetric geometry of 0.1–1 mm diameter microcapillaries. They also reported an increase in the heat transfer rates for the water-silicon oil system studied, compared to single-phase fluids. Che, Wong, and Nguyen (2012) performed simulations in 2D, concluding that heat transfer appears to increase when decreasing the slug lengths, due to the higher transverse velocity within the slugs. Che, Wong, and Nguyen (2013) performed 3D large eddy simulations (LES) for a water-mineral oil system. They concluded that the recirculation appearing in the continuous and dispersed phases results in the increase of the Nu number. Li et al. (2021) also utilised the VOF method, to study the heat transfer improvement achieved when droplets are included in a cylindrical microchannel. They included the average vorticity magnitude in the droplets in their simulations. They concluded that the heat transfer does not enhance monotonously with the increase in droplet size or flow rate. More specifically, increasing the flowrate is found to increase the vorticity inside the droplet, enhancing the mixing while at the same time increasing the thickness of the film formed between the droplets and the walls. Furthermore, the Nu number is found to increase at first, and then decrease with the droplet size. For small droplet diameters, the presence of a droplet appears to have no significant effect on the improvement of heat transfer, since the average Nu in the entrance and fully developed regions of droplet liquid-liquid flow is similar to the one of a single-phase flow (Li et al., 2021).

According to Abdollahi, Sharma, and Vatani (2017), there is a need for further investigation on the flow patterns, heat transfer characteristics and pressure drop calculation of liquid-liquid two-phase flows. Urbant, Leshansky, and Halupovich

(2008) also pointed out the need for further theoretical research on droplet motion and manipulation for microfluidic applications. Furthermore, the study of this type of droplet-laden flows and heat transfer is of particular interest when applied in rectangular and square microchannels (Urbant, Leshansky, and Halupovich, 2008; Abdollahi, Norris, and Sharma, 2020). Moreover, there is the need to further investigate the effect that the characteristics of the film (thickness, distribution) formed between the droplets and the wall have on the heat transfer in liquid-liquid systems, especially for square/rectangular channels (Ma et al., 2021). In addition, there exists no previous study on the effect that dense packing of small droplets might have on heat transfer in liquid-liquid systems.

4.1.2 Melting Temperature

The melting temperature (T_m) is defined as the temperature where 50 % of a double-stranded DNA melts or changes into single-stranded DNA. This temperature depends on the number and type of non-covalent bonds in the folded state, the pH and other solution conditions (Haynie, 2001). Further information related to the nucleic acid structure and properties of DNA can be found in the work of Bhagavan (2002).

Many researchers have developed empirical correlations for T_m as a function of the DNA's GC content, size and concentration of ions (Haynie, 2001), such as Owen, Hill, and Lapage (1969) and Frank-Kamenetskii (1971), who developed the empirical Equations 4.1 and 4.2 respectively, that predict the T_m of DNA as a function of its GC content and concentration of Na^+ ions in solution:

$$\theta_{GC} = [tan(70.077 + 3.32M_g)](T_m - 175.95) + 260.34 \tag{4.1}$$

$$T_m = 176.0 - (2.60 - x_o)(36.0 - 7.04log[Na^+]) \tag{4.2}$$

where θ_{GC}: the fraction of GC pairs in the DNA (%), T_m: the melting temperature (^{o}C) and M_g: the log[Na^+], [Na^+] being the total concentration of Na^+ (mol/L). At the same time, a number of software programs are available that offer the ability to use different methods for the theoretical estimation of T_m (Panjkovich and Melo, 2005).

4.1.3 Melting Curve Analysis

According to Haynie (2001), measuring and recording different T_m can be a way of identifying the genetic material of genomes. T_m can be identified by plotting the negative derivative of the fluorescence signal over temperature (-dF/dT) versus temperature (*Melting Curve*), with peaks appearing at the T_m of the molecules present

(Meuer, Wittwer, and Nakagawara, 2012). Examples of such figures can be found in the work of Palais and Wittwer (2009) (Figure 4.2).

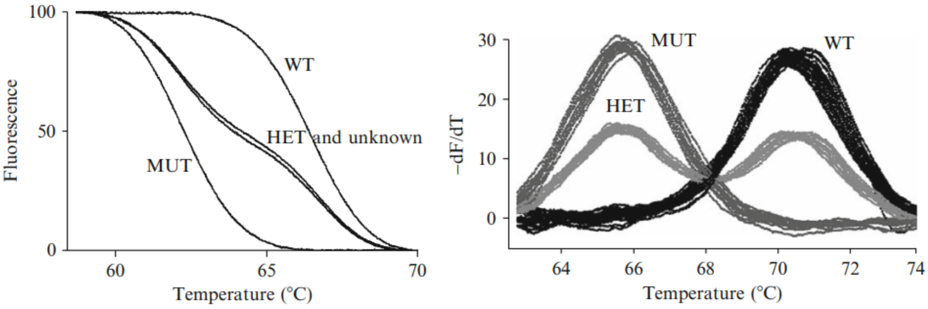

FIGURE 4.2: Fluorescence and -dF/dT figures obtained from Palais and Wittwer (2009).

MCA is often used to provide insight into the specificity of the qPCR products by recording the different T_m, indicating the presence of different double-stranded (ds) DNA products within a sample. The specificity of DNA amplification becomes important when it comes to intercalating dye assays since they are not sequence-specific and bind to any dsDNA product contrary to the probe-based assays that are target-specific (see Chapter 2.1.5.2). When using DNA binding dyes, the formation of single-stranded molecules can be observed as the temperature increases. While the temperature increase takes place and the dissociation of the dsDNA molecules begins, the dye molecules release into the sample. As the dye molecules start releasing into the sample, their fluorescence is reduced, as observed in the dissociation graphs (Fluidigm Corporation, 2015).

Several publications can be found in this area, such as the one of Wittwer et al. (1997), who used Fluorescent MCA for continuous monitoring of the performance of PCR. Another example of Fluorescent MCA used to detect and quantify the different PCR products using the dsDNA dye SYBR Green I is described in the work of Ririe, Rasmussen, and Wittwer (1997). Queipo-Ortuño et al. (2005) performed MCA to verify the specificity of the PCR products in serum samples. In many cases, when using Fluorescent MCA, further analysis by electrophoresis is no longer required (Farrar and Wittwer, 2017). The works of Nicolas, Milon, and Prina (2002), Pham et al. (2005) and Pietilä et al. (2000) are only some of the examples where MCA can be used in the identification of species in diagnostic or epidemiological studies of leishmaniasis or asymptomatic parasitism, the detection and differentiation of Newcastle disease virus (NDV) isolates and the B. burgdorferi sensu lato genospecies, respectively.

The common temperatures range that MCA is performed is 40 - 90 ^oC (for the denaturation of DNA to take place). Two main approaches exist for MCA; a time-based and a spatial-based. Details of the time-based method can be found in Li et al. (2014), while quantitative Polymerase Chain Reaction (qPCR) and High-Resolution Melt (HRM) techniques fall under this category. In the spatial-based approach, a

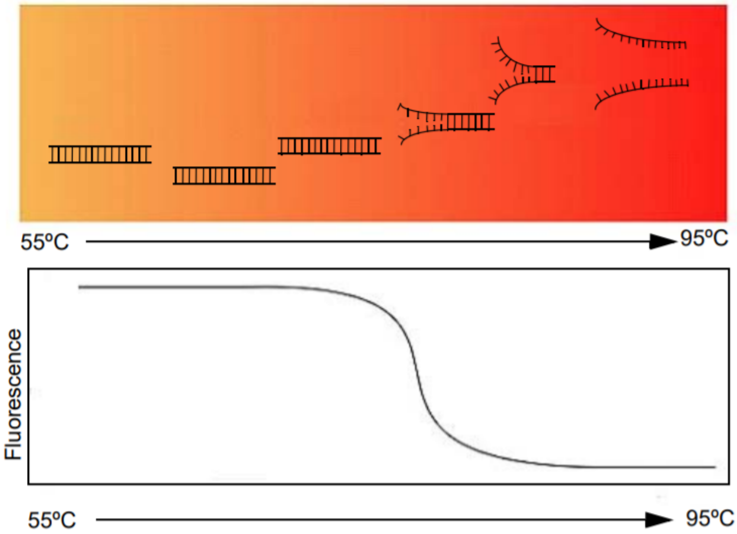

FIGURE 4.3: Melting or Dissociation Curve (Figure obtained from Fluidigm Corporation (2015)).

temperature gradient is implemented and fluorescence measurements are collected (Li et al., 2014).

4.1.4 Melting Curve Analysis and droplet-based technology

This Chapter presents publications examining experimental designs of droplet-based DNA MCA devices, in order to obtain an understanding of the relevant technological designs.

When compared to temperature-dependent reactions conventionally performed in tubes (such as PCR), reactions performed in droplets are characterised by better heat transfer efficiency, leading to better performance (Liu and Zhu, 2020). In particular, droplets are considered to act as small reactors where DNA MCA can be performed, while no immobilization of reagents is needed (Liu et al., 2018; Liu et al., 2017). Bio-Rad Laboratories and RainDance Technologies provide commercial platforms for emulsion dPCR, generating monodisperse droplets. The droplets can be collected to perform PCR thermocycling. The reinjection of the droplets into a microfluidic channel might be needed in order to obtain the fluorescence signals, for the detection of the PCR products (Zec, Shin, and Wang, 2014).

One of the first publications of experimental work in this area is the publication of Dalton, Kinahan, and Davies (2005), who developed a device that performs MCA that successfully differentiates between two samples with different T_m. They concluded that such a device can be used for quality control and for multiplex analysis. Their rig consists of a copper block, with a slot created in the middle to account for a channel that can fit a glass capillary. Plugs are introduced containing the DNA samples, and are heated along the length of the capillary. Fan-cooled thermo-electric modules and thick film heaters are attached at the opposite ends of the rig. A temperature difference of 11 ^oC is implemented between the opposite ends (95^oC and

84^oC) of the device. A schematic of the rig developed can be found in Figure 1 of Dalton, Kinahan, and Davies (2005).

Kinahan, Dalton, and Davies (2008) later developed a microfluidic device that utilises the same principle as the one presented by Dalton, Kinahan, and Davies (2005), suitable for performing droplet-based Fluorescent MCA within a microchannel. Using a similar setup, they introduced a series of plugs of 45 nL containing the PCR samples in the microfluidic channel, producing melting curves in order to distinguish homozygous PCR samples based on the different T_m. According to Kinahan, Dalton, and Davies (2008), the volume of the plugs and the recirculation which may occur in them appear to have no effect on the observed denaturation temperature (within the observed accuracy of the rig) and the thermal development of the flow respectively. Furthermore, the experimental rig is found to be capable of performing homozygous T_m measurements but unable to perform multiplex PCR analysis or heterozygous melting curve analysis, since these techniques require accurate measurements of the shape of the melt curve and not only the measurement of T_m.

Several publications exist that use a different technique, soft lithography (Zhao, Xia, and Whitesides, 1997), to perform MCA. Further details on this method can be found in the publication of Zhao, Xia, and Whitesides (1997). Soft lithography is often used for biological applications, since its resolution can reach the micro- or even nano-scale found in biology. It is also suitable for microfluidic devices that require a nontoxic, transparent, and hydrophobic environment, due to the use of PDMS. However, this technique is considered resource-consuming and expensive, hence often limiting its commercial potential. Furthermore, clean room facilities and specialized training is often required (Walsh III et al., 2017).

Liu et al. (2017) developed a microchip using soft lithography techniques for Single Nucleotide Polymorphism (SNP) genotyping (more information on SNP can be found in Kim and Misra, (2007)) applications. They introduced a train of droplets containing genomic DNA into the fluidic channels of the microchip, leading them through a detection zone with a constant temperature gradient. By gradually increasing the temperature from 60 ^{o}C to 85 ^{o}C, denaturation of the DNA strains took place, and the melting curves were obtained. They also used a droplet detection and tracking software system, that performed droplet identification, tracking, interactive annotation and data acquisition, after the user's selection of the target droplet. Their device was successfully tested, by performing SNP discrimination from homozygotes and heterozygotes, producing results similar to the ones from a commercial qPCR device. Furthermore, they also concluded that :

- the larger droplets present higher values of T_m compared to the smaller ones, due to the larger temperature variation between the opposite sides of the larger droplets.

These results contradict the ones presented in the work of Kinahan, Dalton, and Davies (2008), who concluded that the length or volume of the sample plugs has no effect on the observed denaturation temperatures T_m. This can be attributed to the difference i) in the accuracy of the two test rigs, and ii) the sizes of the droplets/plugs studied.

- the size of the droplet affects the fluorescent intensity.

  The shrinking of the droplets as the temperature increased, resulted to an increase of the fluorescent dye concentration and in the fluorescent intensity. More specifically, increasing the concentration of the fluorescent dye was found to linearly increase the fluorescent intensity, while an inverse proportional relation was recorded between the fluorescent intensity and the volume of the droplet.

- the high heating rate applied during the melting process is found to cause the sifting of T_m to higher values, due to the small heating capacity of the droplets.

Liu et al. (2018) also used soft lithography techniques for the detection and quantification of the methylation status. More specifically, they used their experimental setup to discriminate between the different T_m for samples of different percentages of methylated DNA. The unmethylated DNA (0%) had a lower T_m (73.1 ^{o}C) compared to the methylated DNA (100%), which has a T_m of 74.9 ^{o}C. The T_m values for unmethylated and methylated DNA mixtures are at different methylation levels (between 73.1 and 74.9 ^{o}C). Their setup was tested against commercial qPCR equipment, and it was proven to: i) offer lower volume consumption and ii) perform better in discriminating the methylation levels in different DNA samples.

Using droplet technology but in a static setup, Liu, Zhu, and Fang (2017) developed a static droplet array as part of a microfluidic droplet-based thermal shift assay system (dTSA). More specifically, their system consists of three main parts; a nanoliter droplet array chip, a microfluidic droplet robot, and a real-time fluorescence detection system. Figure 4.4 presents the schematic diagram of the workflow of their dTSA system.

4.1.5 Dyes

With the continuous expansion of PCR technology, a big development in probe-based systems has been made, including Taqman probes (Heid et al., 1996), molecular beacons (Piatek et al., 1998), FRET1 probes (Chen and Kwok, 1999), Scorpions (Solinas et al., 2001), and iFRET (Howell, Jobs, and Brookes, 2002). Probe-based technology can be replaced with fluorescent double-stranded DNA (dsDNA)-specific intercalating dyes, such as the YO-PRO-1 (Ishiguro et al., 1995), SYBR Green I (Wittwer et al., 1997; Ririe, Rasmussen, and Wittwer, 1997), BEBO (Bengtsson et al., 2003), and LC Green (Wittwer et al., 2003) that have been evaluated for use in real-time PCR applications.

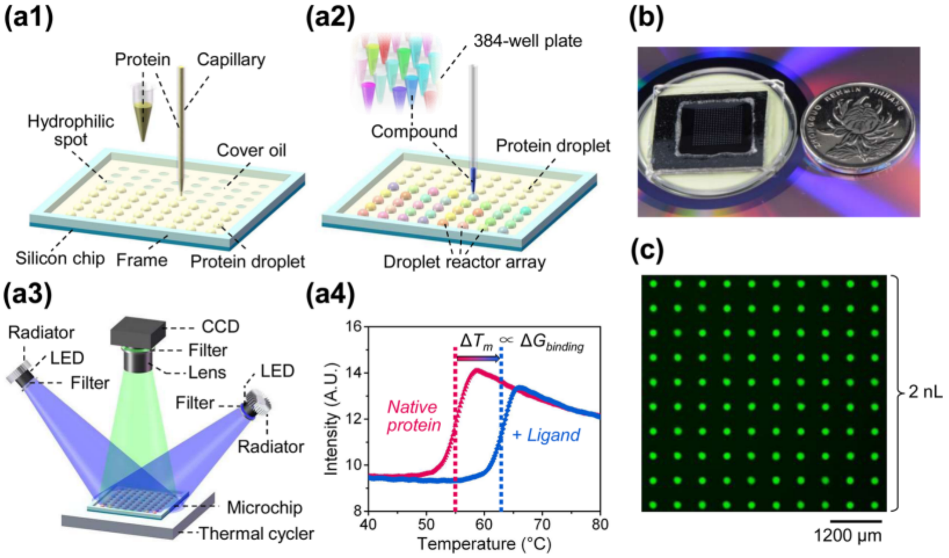

FIGURE 4.4: (a) Schematic diagrams showing the workflow of the dTSA system. (b) Photograph of the microchip with an 18 x 18 droplet array. (c) Fluorescent image of a 10 × 10 array of 2-nL droplet (Figure obtained from Liu, Zhu, and Fang(2017)).

According to Wittwer et al. (1997) and Ririe, Rasmussen, and Wittwer (1997), SYBR Green I is considered to be more cost-effective compared to probe-based systems. Despite its advantages, the use of SYBR Green I is limited by the (i) optimisation of the conditions and the addition of extra reagents required, aiming to improve the efficiency of the reaction, (ii) concentration (Wittwer et al., 1997; Nath et al., 2000) and the degradation products of the dye (Karsai et al., 2002) which have been found to inhibit PCR, depending on the conditions of the reaction.

As far as the DNA MCA is concerned, the melting temperature measurement is affected by the concentrations of the dye (Ririe, Rasmussen, and Wittwer, 1997) and DNA (Xu et al., 2000). Such an example is presented in the work of Ririe, Rasmussen, and Wittwer (1997), where a difference of more than 1 ^{o}C in T_m is observed for the case of a 3 log-fold difference in the number of starting copies of target DNA (Monis, Giglio, and Saint, 2005). The publications of Woo et al. (1998), Pietilä et al. (2000), Mommert et al. (2001), Rantakokko-Jalava and Jalava (2001) and Tanrıverdi et al. (2002) are only some of the examples where SYBR Green I has been used for the identification of a variety of organisms.

Two different dyes are considered in this research: SYBR Green ((Sigma-Aldrich, 2020)) and Alexa Fluor 488^{R}-dUTP (ThermoFisher, 2020; Bioscience, 2006). The maximum excitation wavelength of SYBR Green I is 497 nm (λ_{exc}), with a secondary excitation peak near 254 nm. The fluorescence emission of SYBR Green I stained DNA is centred at 520 nm (λ_{emm}) (Sigma-Aldrich, 2020). As far as the spectroscopic properties of the AF488 dye are concerned, the excitation (λ_{exc}) and emission (λ_{emm}) wavelengths are at 494 and 515 nm respectively (Bioscience, 2006).

4.1.6 Optics

In this Chapter, the basic principles of optics commonly appearing in microfluidic systems are presented.

4.1.6.1 Optical Fluorescence

Fluorescence is widely used in biology, biotechnology, biomedicine, and other analytical fields due to its high sensitivity and specificity, simplicity, and low cost compared to most other analytical techniques (Erdogan, 2011).

The phenomenon of optical fluorescence (Figure 4.5) describes the absorption of light by a fluorescent molecule, known as a fluorophore, that takes place at a range of lengths (absorption band). More specifically, when a photon is absorbed by the fluorophore, its excitation takes place from the electronic ground state to the excited state. This lasts approximately from 1 ns to 100 ns (characteristic time), after which a rapid emission of light (photon) takes place at greater wavelengths (emission band). The emitted photon in this case is characterised by lower energy or a longer wavelength compared to the excitation photon.

Fluorescence emission is significantly weaker compared to the excitation light, which is why it is important to eliminate any scattered excitation and ambient light received by the detectors used. As a result, optical filters are required on the excitation and emission sides of the system (Erdogan, 2011).

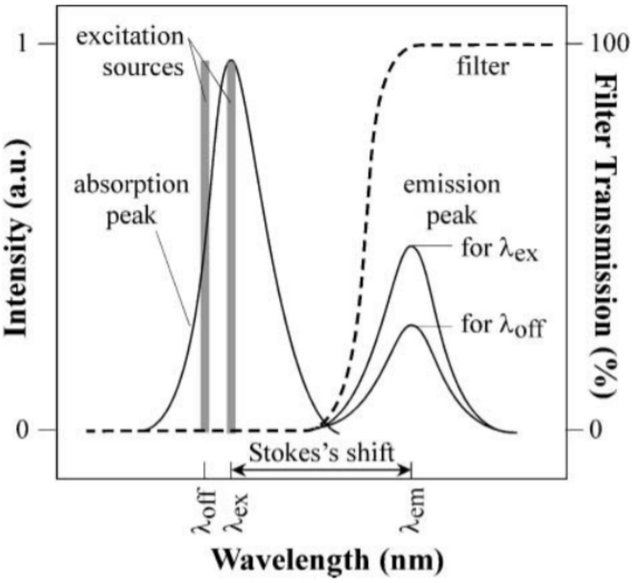

FIGURE 4.5: Typical peaks in the excitation and emission spectra. The wavelength filter (dashed line) must reject the excitation light and transmit the emitted fluorescent light. Excitation with off-peak (λ_{off}) wavelengths lowers the emission intensity (Figure obtained by Dandin, Abshire, and Smela, 2007).

4.1.6.2 Optical filters

Several publications exist that describe the experimental setups for MCA where fluorescence is measured using a CCD camera, such as Pješčić et al. (2010), Hayes and Dalton (2015), Liu, Zhu, and Fang (2017), Liu et al. (2017) and Liu et al. (2018). Other authors have used fluorescence microscopes to collect their data, such as Kinahan, Dalton, and Davies (2008) and Zhu et al. (2020). In the experimental setups where CCD cameras are used, filters are required in order to obtain the fluorescence signals. Light-emitted diodes (LEDs) are often used as excitation sources, emitting at the wavelength required to excite the fluorochrome used (Hayes and Dalton, 2015).

Filters permit only the desired light to pass within the absorption and emission bands. The use of filters is required in order to be able to discriminate the desired fluorescence signals from scattered excitation light and auto-fluorescence from the sample, substrate, and other optics in the system (Erdogan, 2011).

There are many types of filters to be considered, such as coloured glass, thin-film interference filters, diffraction gratings, dispersive prisms, liquid-crystal and acousto-optic tunable filters, and interferometers. The three most common types of filters used are an excitation filter, a dichroic beamsplitter and an emission filter (Figure 4.8). A bandpass filter is usually used as an excitation filter, allowing only the wavelengths absorbed by the fluorophore to pass. The dichroic filter is usually a long-wave-pass (LWP) edge filter, reflecting light within the excitation band and transmitting light within the emission band. The emission filter is usually a bandpass filter as well, passing only the wavelengths emitted by the fluorophore while blocking the unwanted light outside the emission band (Erdogan, 2011). Details about the different basic types of filters (Figure 4.6) together with basic configurations for optical filters in the most popular fluorescence instruments (Figure 4.7) can be found in the work of Erdogan (2011).

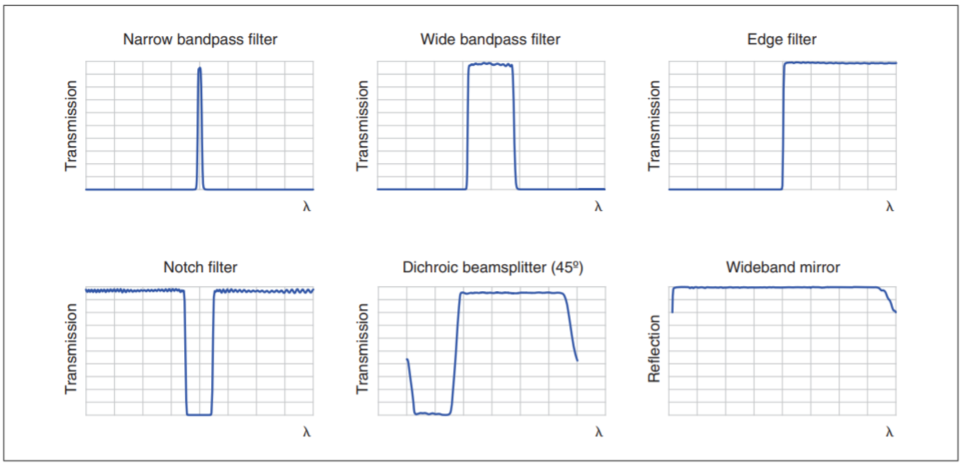

FIGURE 4.6: Basic types of thin-film interference filters used in fluorescence instrumentation (Figure obtained from Erdogan (2011)).

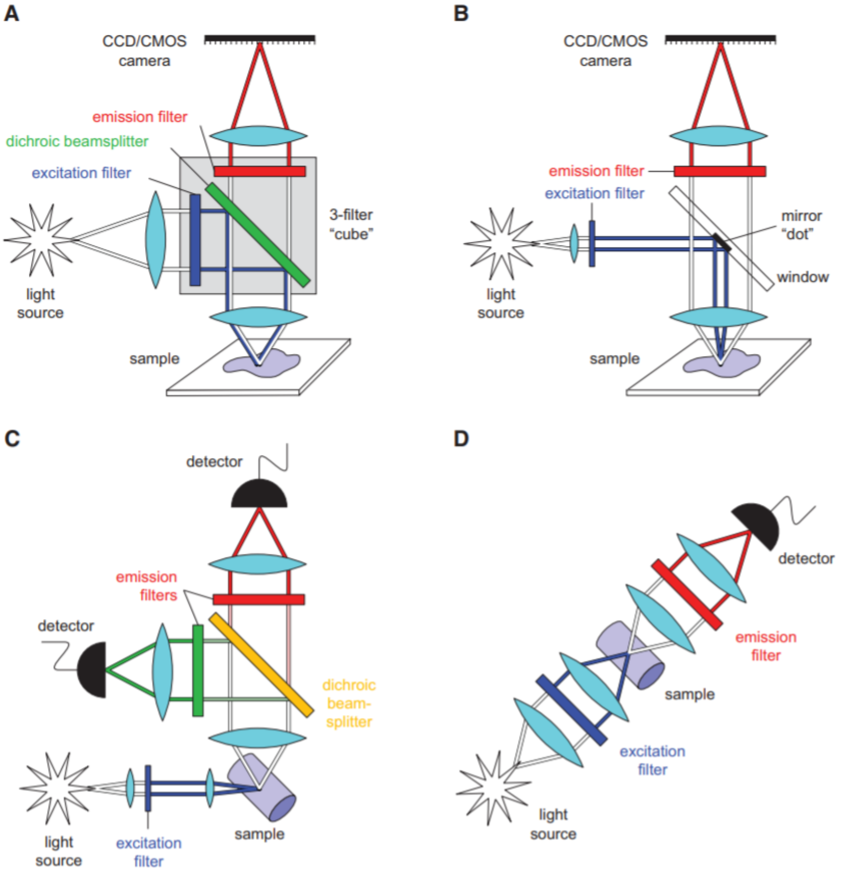

FIGURE 4.7: Basic setups for optical filters (Figure obtained from Erdogan (2011)).

4.1.7 Temperature Control

4.1.7.1 Linear temperature gradient along a microfluidic device.

This Chapter focuses on presenting some publications related to experimental microfluidic devices where a constant temperature gradient along the microfluidic devices has been created.

Liu et al. (2019) designed a microfluidic setup, which creates a stable temperature gradient for microtube (MT) polymerization. The setup consists of a heating chip, a thermometer and a microcontroller for monitoring and controlling the temperature conditions. A linear temperature gradient is achieved. For generating a temperature gradient using a heater, Liu et al. (2019) controlled the power output (P) through Equation 4.3:

$$P = \frac{I^2 \rho L}{hd} \tag{4.3}$$

,where P is the power, I is the current, ρ is the resistivity, L is the length of resistance, h is the height of the ITO layer and d is the width of the ITO layer. They validated the linear temperature gradient successfully at ten positions.

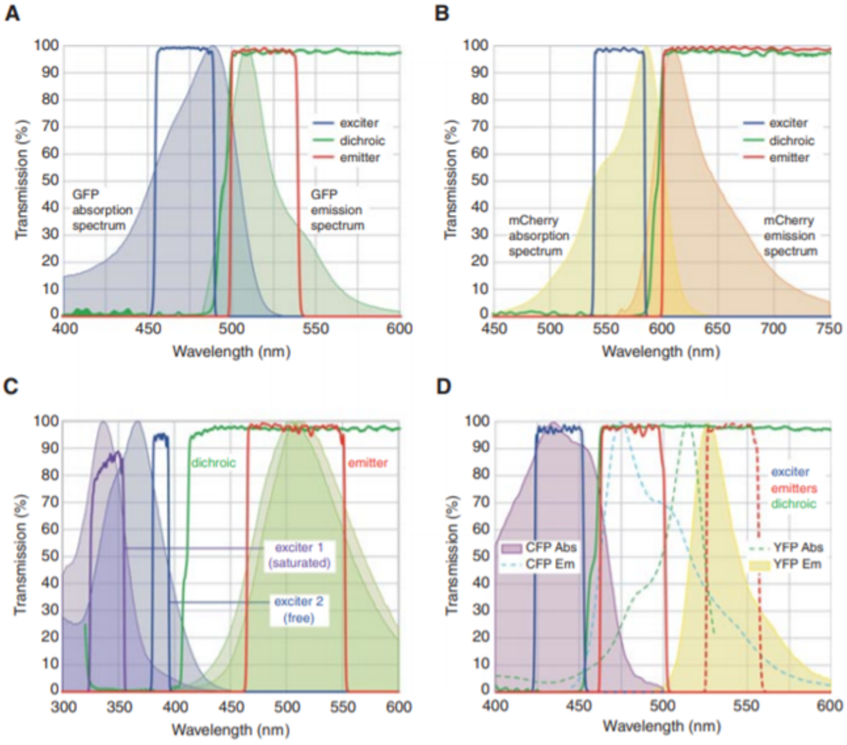

FIGURE 4.8: Examples of filter spectra for single-color fluorescence imaging and detection (Figure obtained from Erdogan (2011)).

Other authors that have developed experimental devices that produce a linear temperature gradient are Kinahan, Dalton, and Davies (2008), Liu et al. (2017) and Liu et al. (2018), with the latter implementing a temperature PID control system that adjusts the voltage of the heater to maintain the temperature gradient in the microchannel.

4.1.7.2 PID Control

PID control stands for Proportional, Integral and Derivative control, and is the most commonly used control method in the industry.

Obtaining the required response from a process often requires an open-loop or a closed-loop control system to be implemented. As far as the open-loop systems are concerned, the controller implements the input signal to the process with regard to the reference signal only. In closed-loop systems, on the other hand, the controller implements the input signal by also taking into consideration the values of the output. The latter type of control allows the system to adjust the process variable close to the setpoint value despite any disturbances and changes in the process dynamics (Visioli, 2006).

4.1.7.2.1 Feedback Control A typical feedback control system is presented in Figure 4.9. **P** describes the process, **C** is the controller, **F** is a feedforward filter, **r** is the reference signal, **e** = r - y is the control error, **u** is the manipulated (control) variable, **y** is the process (controlled) variable, **d** is a load disturbance signal and **n** is a measurement noise signal.

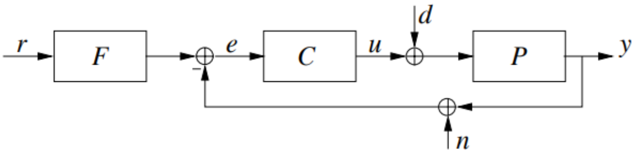

FIGURE 4.9: A block diagram describing a typical feedback control loop (Figure obtained by Visioli, 2006).

Proportional - Integral - Derivative (PID) control systems are three-term controllers that have been used for automatic control of various processes since the start of the last century (Bennett, 2000). According to Visioli (2006), the use of all three types of controls is not required for projects. More specifically, the aim of the control system is to offer the best cost/benefit ratio in the simplest way.

4.1.7.2.2 The three parts of PID control

Proportional The proportional control action is proportional to the current control error, according to the following Equation 4.4 (Visioli, 2006):

$$u(t) = K_p e(t) = K_p(r(t) - y(t)) \tag{4.4}$$

where K_p is the proportional gain and e is the error, given by Equation 4.5:

$$e(t) = r(t) - y(t) \tag{4.5}$$

The control variable is increased when the control error increases, while K_p reduces but does not eliminate the steady-state error (Matlab & Simulink, 2021). Furthermore, the transfer function of a proportional controller can be described by Equation 4.6 (Visioli, 2006):

$$C(s) = K_p \tag{4.6}$$

According to Visioli (2006), the main disadvantage of this type of controller is the non-zero steady-state error. For tasks where this is not an issue, the proportional type controller can be the best choice due to its simple design (for a process with low-order dynamics, K_P can be set to a high value in order to provide a fast response and a low steady-state error).

Integral The integral action is proportional to the integral of the control error (Equation 4.7) and hence takes into account the former values of the control error. The transfer function takes the form of Equation 4.8 (Visioli, 2006).

Furthermore, adding an integral term to the controller tends to help reduce steady-state error to zero. More specifically, this is due to the pole at the origin of the complex plane (Visioli, 2006). For the cases of persistent errors, the integrator continues to build up, increasing the control signal and hence reducing the error. However, the integrator might result in a slower response of the system, since when the error signal changes sign, it may take a while for the integrator to "unwind" (Matlab & Simulink, 2021). When both proportional and integral control are implemented, the resulting transfer function takes the form of Equation 4.9 (Visioli, 2006).

$$u(t) = K_i \int_0^t e(\tau)\, d\tau \tag{4.7}$$

$$C(s) = K_i/s \tag{4.8}$$

$$C(s) = K_p(1 + \frac{1}{T_i s}) \tag{4.9}$$

where K_i is the integral gain and T_i is the integral time constant.

Derivative The derivative control action provides a prediction of the future values of the control error (Equation 4.10). The corresponding controller transfer function is presented in Equation 4.11 (Visioli, 2006):

$$u(t) = K_d \frac{de(t)}{dt} \tag{4.10}$$

$$C(s) = K_d \cdot s \tag{4.11}$$

where K_d is the derivative gain. The anticipation of the system's response adds damping to the system, reducing overshoot. Furthermore, adding a derivative term does not affect the steady-state error (Matlab & Simulink, 2021).

4.1.7.2.3 Structures of PID control The proportional, integral and derivative actions of control can be combined in different ways. Equation 4.13 describes the ideal or non-interacting form, that is derived by taking the Laplace form of the sum of Equations 4.4, 4.7 and 4.10:

$$u(t) = K_p + K_i \int_0^t e(\tau)\, d\tau + K_d \frac{de(t)}{dt} \tag{4.12}$$

$$u(s) = K_p(1 + \frac{1}{T_i s} + T_d s) \tag{4.13}$$

where K_p is the proportional gain, T_i is the integral time constant, and T_d is the derivative time constant. Other forms of implementation of a PID controller are the series of interacting and parallel forms (Visioli, 2006).

4.2 Contribution of the device

4.2.1 Contribution to the work of Joan Boyes at the University of Leeds

This experimental work presents a great interest since it will enable this team of biologists to check for the presence of rare DNA species and possible contaminations in their collected samples in a fast, robust and relatively cheap way. Contrary to other MCA experimental devices, this experimental setup requires simple experimental techniques to be built. More specifically, no particular treatment of the microfluidic channels is required for cleaning between uses, since the glass capillaries can be easily replaced for every experiment. Moreover, there is great potential for optimising such technology and making it an affordable diagnostic tool for specific viruses or genetic abnormalities, thanks to its ability to detect the presence of rare DNA species.

Accurate detection of nucleic acids is central to modern molecular biology research, from the quantification of transcript levels to measuring viral load or gene copy number to determining the levels of immunoprecipitated products. Quantitative PCR (qPCR) revolutionised the ability of scientists to perform such experiments and has been very important in molecular biology, virology and genomics labs for many years. The excellent dynamic range of 6-8 orders of magnitude, coupled with its high accuracy and simplicity means that qPCR will remain integral to the research of numerous labs for many years to come.

Whilst qPCR is extremely powerful, it suffers from a number of drawbacks including the inability to detect low-level transcripts or rare somatic mutations within a high background of other transcripts or DNA. It also lacks the sensitivity to detect small changes in copy number or gene expression and multiplex experiments that examine two or more transcripts simultaneously require extensive optimisation to ensure that there is no interference between the probes (Dorak, 2007).

Digital PCR is a new cutting-edge approach that offers superior accuracy and sensitivity compared to qPCR by giving absolute measurements. Here, the sample is dispersed into thousands of partitions such that there are either 1 or 0 templates per partition. PCRs are performed within the individual partition and data are collected at the PCR endpoint to determine whether a template is, or is not, present within an individual partition. This offers a range of advantages including:

1) It measures the absolute amount of product (i.e. how many individual reactions give a signal) and therefore there is no need to calibrate to a standard curve,

2) It is highly sensitive, detecting very low amounts of transcript or rare mutations in a background of more abundant sequences,

3) It is much more specific and reproducible (standard qPCR varies according to the accuracy of the standard curve),

4) Provided the reaction is in the digital range (i.e. 1 or 0 copies per droplet) it is straightforward to perform multiplex experiments – i.e. to examine two to five PCR products simultaneously, depending on the machine,

5) This means it is possible to examine whether two (to five) transcripts are present concurrently within a single cell,

6) It does not suffer from artefacts due to inhibitors to the same extent as standard qPCR.

There are two main ways to partition the PCR reaction – either via physical chips with partitions etched onto the chips or via droplet PCR. Droplet PCR is preferred since it is possible to get more partitions per experiment and is more cost-effective. The PCR product can be detected via either a Taqman probe or using dyes that intercalate into the DNA such as SYBR Green or Eva Green. The latter is more cost-effective but droplet PCR suffers the drawback that it is not possible to test if the reaction is specific if dyes are used. The proposed device will offer an innovative solution by testing if the DNA product has a unique melting temperature. Given the huge increase in state-of-the-art digital PCR use, such a device has significant commercial potential.

The idea of building this device is driven by the need to provide a fast and robust way of identifying:

- quantitatively and qualitatively the different types of DNA that a biological sample might contain,
- the specificity of the DNA molecules in that sample,

while at the same time maintaining a simple and reusable design. The simplicity of developing the experimental rig will enable the smooth use of the device by the biologists. Furthermore, the fact that the device can be easily reused after each run, simply by replacing the glass capillaries, will facilitate their work even further, avoiding any special treatment/cleaning that might be required. Moreover, the required experimental setup can be easily disassembled, the various experimental parts can be replaced in case the system's requirements change per application (ex. heat resistors) and equipment already present in a lab can be used to perform parts of the experimental process.

This experimental device is expected to be used in investigating the mechanism by which v(D)j recombination is regulated and how mistakes in this reaction can lead to oncogene activation. The examined samples can be products of their research on B-cells, where the specificity of these cells can be tested. This device will use a train of droplets that contain potentially different types of DNAs, introduced together with another immiscible fluid into a microfluidic channel where there is a controlled temperature environment, while fluorescence signal measurements will be taken. Due to the fact that different DNA molecules generate different fluorescence signals under different conditions, and that each droplet only contains one or even no DNA molecule, the position where a signal would be detected would directly indicate the presence of a particular DNA molecule. As part of our discussions, two different temperature ranges where the detection of T_m would take place are suggested: i) 81 and 83.5 ^oC and ii) 82 - 90 ^oC. Both of these temperature ranges are used to develop the final experimental rig. Moreover, the amount of droplets to be processed is expected to be at about 20,000.

4.2.2 General contribution and potential of the device

However, the use of the device is not limited by the assistance it can provide in the understanding of v(D)j recombination kinetics. This device can help scientists in general to identify and quantify the different types of non-specific PCR products that might be present in the samples. As far as PCR is related, the presence of different types of non-specific molecules (by-products) is a common problem, and is usually identified by DNA Gel electrophoresis, after PCR takes place. As a result, scientists often proceed with PCR reaction, not knowing the exact composition of their samples, which sometimes carry by-products that inhibit the reaction.

This robust, and inexpensive platform will be the first to our knowledge to detect the presence of such molecules in such a simple setup. With its cheap and disposable capillaries, it will be easy to use and avoid any contamination issues between samples. Even though more sophisticated devices that use the same principle idea have recently been built (Liu et al., 2017; Liu et al., 2018), they have never been applied for these specific functions. The PCR samples encapsulated into a series of droplets will be transported through a detection region, where a stable temperature gradient is created. As the temperature is elevated, the DNA samples denature and the associated fluorescence signals decay, with the relationship being acquired as the melting curve. The droplets serve as discrete reactors for conducting DNA melting curve analysis in the liquid phase, thereby eliminating the need for immobilization of reagents. This chip will offer an enhanced discrimination ability and lower volume consumption, compared to the commercial qPCR machine.

Furthermore, a better understanding of the role of the droplets in the heat transfer in droplet-laden flows is expected to be obtained from thermal images of the rig and the droplets. More specifically, the presence of droplets and their packing in the stream is expected to lead to an understanding of their effect on the temperature distribution in the stream, and their effect on the enhancement in heat transfer compared to single-phase flows. To our understanding, no previous research exists that studies the effect that the packing of small droplets has on heat transfer and Nu in liquid-liquid flows (see Chapter 4.1.1).

Summarising, this device, will not only enable this specific group of scientists at the University of Leeds to quantify the different DNA molecules in their study of the kinetics while also detecting the presence of molecules that inhibit the progress of PCR reaction. Such a device can offer great assistance to biologists and scientists in general since it will provide a robust and cheap way of quantifying and qualifying their samples.

4.3 CFD Simulations

COMSOL ® 5.4 is used to optimise the design of the microfluidic device, before the onset of the experimental work. Several simulations of different designs are performed, before concluding to the final design. COMSOL ® 5.4 is then used to simulate and help estimate the power requirements and heat losses in this particular design, for the different experimental parts, before proceeding with their purchase.

The simulations conducted during the different stages of designing the experimental setup mainly focus on studying the temperature profiles on a heated channel, using different materials, geometrical designs, number and placement of heaters. Their main goal is to conclude on the appropriate materials and their geometrical features that enable the creation of a linear temperature profile along the microchannel where a train of droplets can be successfully introduced. That is expected to allow the gradual heating of the droplets as they cross the microchannel, while at the same time the temperature of the fluidic stream is measured by using thermocouples. The effect of the droplets' presence and their spacing on the temperature profile of the droplet-laden stream compared to the one predicted by the model using single-phase flow is of particular interest.

For the purposes of utilising this setup to perform MCA, droplets containing different DNA samples can be introduced under an appropriate setup, obtaining the melting temperature of each sample through the measurements of fluorescence signals of the flowing droplets along the channel. This is expected to enable the identification of the different types of DNA molecules existing in the original sample.

4.3.1 Preliminary studies

This set of simulations is designed while considering the first temperature range for the melting temperatures; $T_m(^oC)$ = [81, 83.5]. The preliminary studies aim at performing CHT simulations using different materials; PMMA and copper (Table 4.1).

TABLE 4.1: Thermal properties used in the preliminary studies.

No	Heat capacity (J/kgK)	Thermal Conductivity (W/mK)
PMMA	1420	0.19
Copper	385	400

TABLE 4.2: Parameter values of the two experiments with uniform heat flux rate at the bottom side.

No	U_{in} [mm/s]	L [cm]	W_i [μm]	W_s [mm]	Q[W/m^2]
PMMA	1.5	15	200	1	10
Copper	0.75	15	200	1	125

4.3.1.1 Single substrate simulations using uniformly heated straight channel.

In this set of simulations, two setups are examined using different substrate materials, copper and PMMA, in order to investigate how the different thermal properties of the two materials might affect their ability to generate a linear temperature profile along a channel where liquid flows.

A number of assumptions are made in terms of the boundary conditions and the heating setup. More specifically, a straight channel (Figure 4.10) is heated uniformly through the bottom surface with heat rates of $q''_{PMMA} = 10$ W/m^2 and $q''_{copper} = 130$ W/m^2 for PMMA and copper substrates respectively. Water runs through the channel at the inlet velocity (U_{in}) of 1.5 and 0.75 mm/s for PMMA and copper substrates respectively. The heat fluxes and inlet velocities are selected so that the temperature regimes of interest can be achieved, while it is important to point out that other potential values might also be appropriate. The temperature profiles are compared (Figure 4.12) for the two substrate materials, while an adiabatic boundary condition (zero heat flux, thermally insulated) is applied at all other sides of the channel. The parameters of the simulations are presented in Table 4.2.

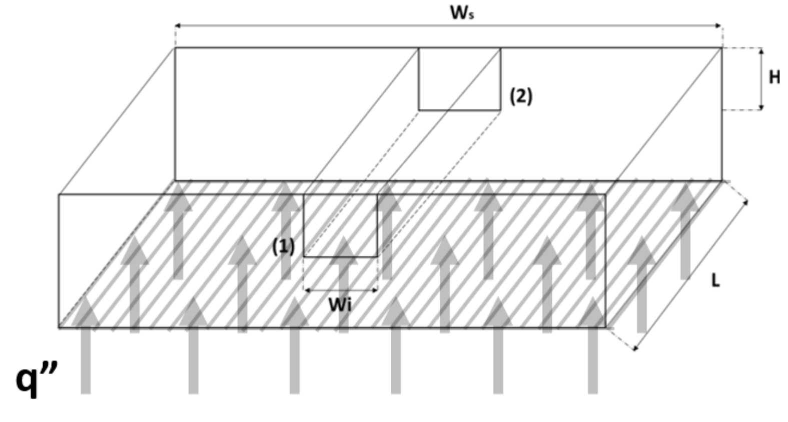

FIGURE 4.10: A rig with a straight channel, heated uniformly at the bottom surface. PMMA/copper are used as substrates.

PMMA and copper are characterised by significantly different thermal properties, resulting in different temperature profiles. Due to the very high thermal conductivity of copper, the heat flux at the solid-water interface is higher at the inlet (Figure 4.11). On the contrary, PMMA has a thermal conductivity that is three orders of magnitude smaller than copper’s. This fact results in a more well-distributed heat flux at the solid-water interface (apart from the start and end of the channel), providing a linear temperature profile along the entire length of the channel. Considering

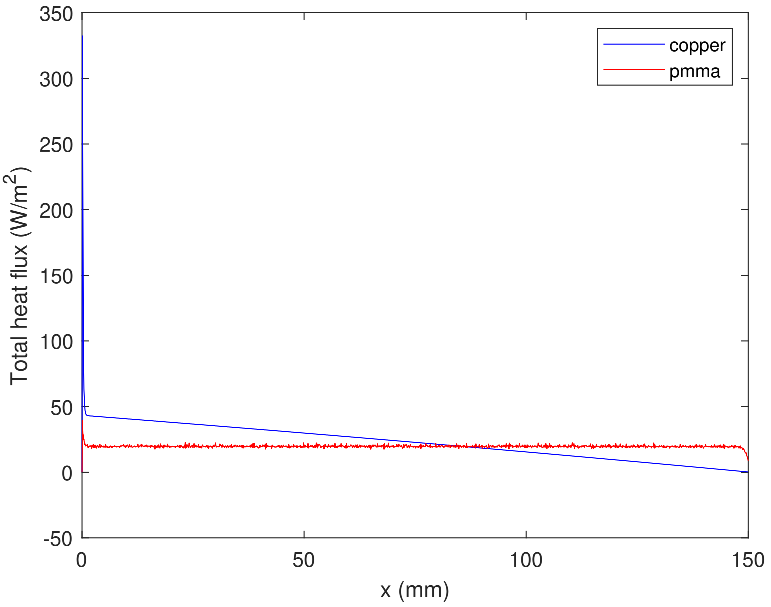

FIGURE 4.11: Total heat flux at the centreline along a microchannel on the solid-fluid interface. PMMA and copper are used as substrate materials. The setup is uniformly heated from the bottom with 10 and 130 W/m^2 respectively. Water runs through a channel with L=15 cm and W=200 μm at 1.5 mm/s.

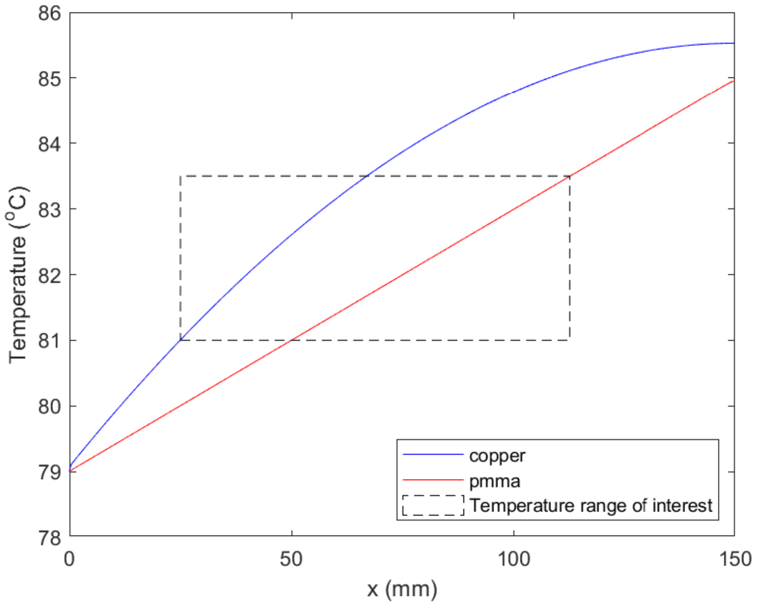

FIGURE 4.12: Temperature profile of the centreline along a microchannel, with PMMA and copper as the substrate materials. The setup is uniformly heated from the bottom with 10 and 130 W/m^2 respectively. Water runs through a channel with L=15 cm and W=200 μm at 1.5 mm/s.

that both designs appear to generate successfully acceptable temperature profiles in the region of interest (Figure 4.12), further investigation needs to take place in order to decide the most appropriate material.

4.3.1.2 Single substrate simulations using multiple heaters.

After conducting the first set of simulations (Chapter 4.3.1.1), the next step is to start introducing boundary conditions that can be achieved experimentally.

Instead of the constant heat flux boundary condition at the bottom of the substrate material, ten small heaters set in series along the bottom of the channel are placed. These heaters resemble the copper wire heaters that are often used in experimental devices (Moschou et al., 2014). When using these heaters, a series of constant temperature boundary conditions are implemented at the bottom of the channel, one for each (copper wire) heater, assuming a uniform temperature distribution at the heater-substrate interface. Each of the heaters has a different temperature, starting from 76 ^{o}C and increasing to 85 ^{o}C with a step of 1 ^{o}C (T_{h1}-T_{h10}). The sides and top surface of the experimental setup are thermally insulated.

The length and width of the substrate are set at L = 15 cm and W_S = 1 mm respectively (Figure 4.13). Water runs through a channel with L = 15 cm and W_I = 200 μm at 1.5 mm/s. The inlet temperature (T_{in}) and the height of the substrate (H) are set at 76 ^{o}C and 6.5 mm respectively, while the length of each heater (L_S) is set at 1.5 cm.

The temperature profiles at the centreline at the bottom of the substrate, the solid-fluid interface and the middle plane of the channel are presented in Figure 4.14. The total heat flux at the centreline at the solid-fluid interface is presented in Figure 4.15. However, the use of multiple small heaters placed in such a small proximity (thermal cross-talk) is still considered hard to achieve experimentally. As a result, the decision to utilise a few or a single heater is made, while varying the geometrical features of the device in order to achieve a linear temperature profile along the length of the channel.

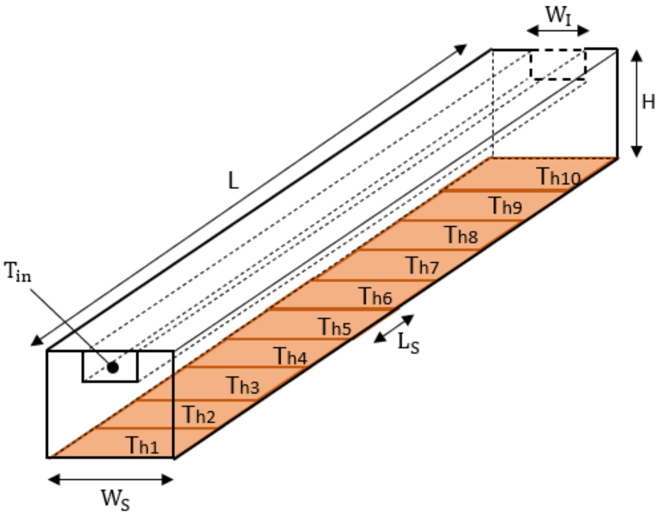

FIGURE 4.13: Schematic graph of the experimental setup using ten heaters placed in series at the bottom of the rig.

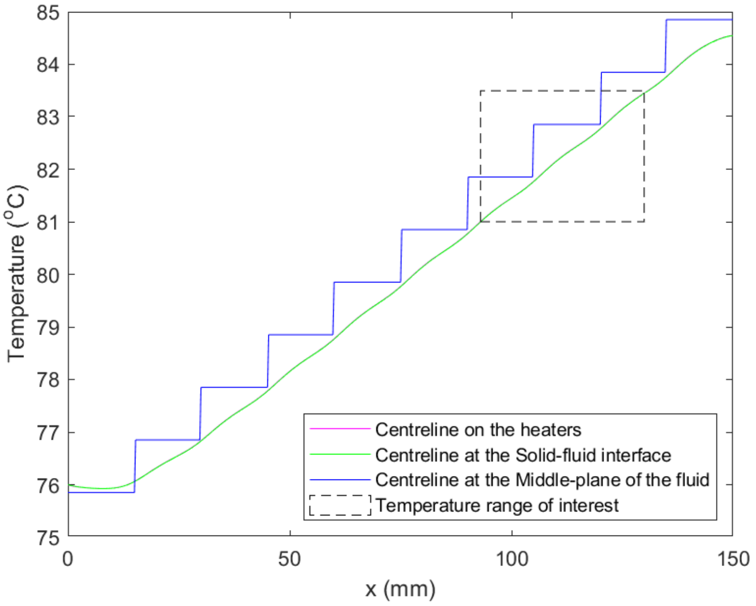

FIGURE 4.14: Temperature profile of the centreline at the bottom of the substrate, the solid-fluid interface and the middle plane of the channel.

4.3.1.3 Double substrate simulations

This set of simulations presents the generation of a linear temperature profile along the centreline of the channel. More specifically, in this attempt, the same two substrate materials are chosen (PMMA and copper), one laying on top of the other, and a constant heat flux is supplied at the bottom of the device.

This design is selected in order to investigate the ability to create a linear temperature profile when more than one material is used, in case there is a need in the final

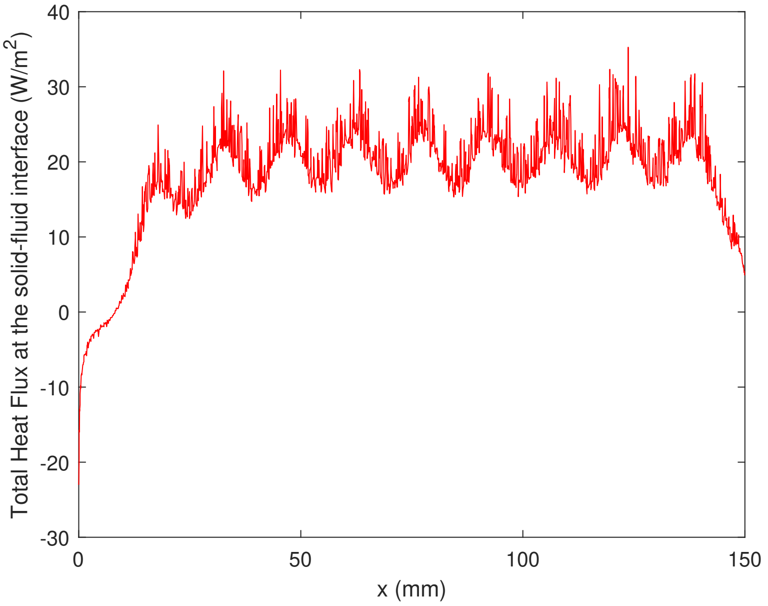

FIGURE 4.15: Total heat flux at the centreline at the solid-fluid interface.

design to place heating/cooling devices on one of the two materials. Furthermore, utilising two materials is expected to allow greater temperature control in terms of the more conductive material. Moreover, the interface between the two substrate materials is designed to be inclined, with the top substrate increasing in volume along the length of the channel in design case 1 and the bottom substrate increasing in volume along the length of the channel in design case 2. The inclined interface between the two substrates is examined in order to test the effect that it will have on the temperature gradient. Also, the order of the two materials is changed, in order to study the effect that the different material properties might have on conjugate heat transfer (Figure 4.16).

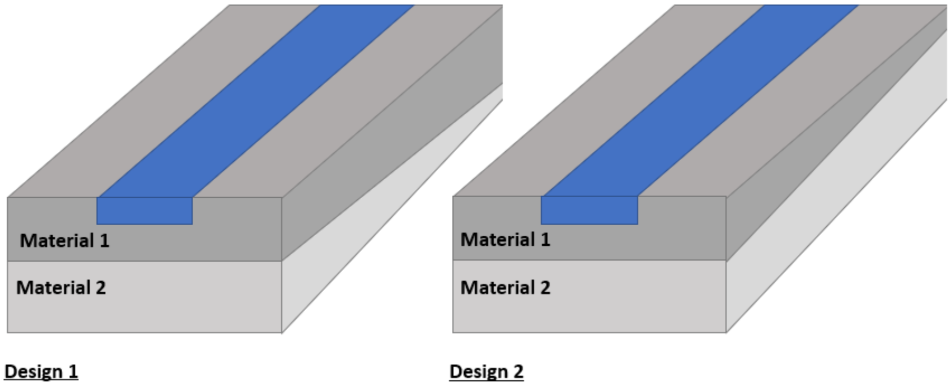

FIGURE 4.16: Schematic graph of the two different types of designs used. Copper and PMMA are used in different order (top and bottom) in designs 1 and 2.

As far as the boundary conditions are concerned: i) a heat flux of Q_{in} (general inward heat flux) is implemented at the bottom face of Material 2 to account for the presence of a heater, ii) a T_{in} inlet temperature is implemented at the inlet of the fluid domain, iii) a thermal insulation boundary condition is implemented at all faces of the solid domains but at the bottom of Material 2, iv) an average fully-developed inlet velocity of $U_{in} = 3mm/s$ is implemented at the inlet of the fluid domain, v) a no-slip boundary condition is implemented at the solid-fluid interface, assuming that at a solid boundary, the fluid has zero velocity relative to the boundary.

TABLE 4.3: Details of the four types of simulations.

No	Design type	Material 1	Material 2	$T_{in}(^oC)$	$Q_{in}(W/m^2)$
1	1	Copper	PMMA	79	50
2	1	PMMA	Copper	79	4
3	2	Copper	PMMA	79	50
4	2	PMMA	Copper	79	4

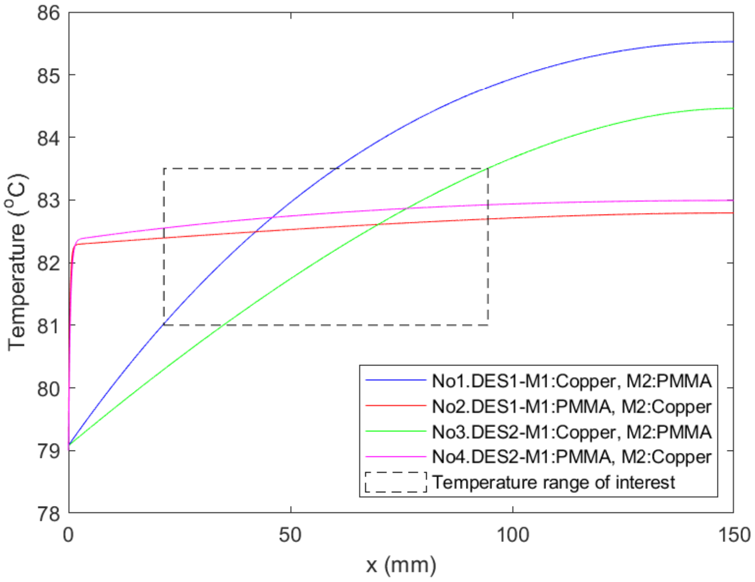

FIGURE 4.17: Temperature profiles of the four design cases.

The four temperature profiles for the different cases (Table 4.3) are presented in Figure 4.17. The inlet temperature (T_{in}) and the values of the uniform heat flux (Q_{in}) at the bottom substrate are presented in Table 4.3. As it can be observed by Figure 4.17, all four temperature profiles fall into the first temperature regime of interest (81-83.5 ^oC). The simulations are conducted with the same initial temperature, and the same uniform heat flux for case numbers No1, No3 and No2, No4 of Table 4.3. That is done in order to understand the difference in the heat transfer phenomena that take place, when the geometry and the substrate materials vary. The No1 and No3 temperature profiles are obtained from the simulations of geometries with copper and PMMA used as Material 1 and 2 respectively. The No2 and No4 temperature profiles are obtained from the simulations of geometries with copper and PMMA used as Material 2 and 1 respectively. The length of the channel is set to 15 cm for all four types of simulations.

It can be observed that when copper is used as Material 2 (No2 and No4), the temperature profile is linear, with a temperature gradient much smaller than the one when used as Material 1 (No1 and No3). However, considering that the aim of this setup is to create a temperature range of 81-83.5 ^oC, both No2 and No4 setups appear to be unsuitable. On the other hand, designs No1 and No3 cover the temperature region of interest, and appear to be more suitable for our purpose. More specifically, design case No3 has a smaller temperature gradient compared to No1, while both designs can be described as relatively linear in the region of interest.

A significant conclusion from this work is that when copper is used as a second substrate at the position on Material 2, most of the heat flux is transferred close to the inlet, due to the higher thermal conductivity of the copper. That results in a rapid temperature increase at the entrance of the channel, and an almost negligible temperature gradient regardless of the type of design selected (Design 1 or 2 (Figure 4.17)). Due to the very small temperature gradient throughout the rest of the device, the selection of copper as Material 2 should not be considered, since it would be hard to cover the desired temperature range, and therefore designs No2 and No4 will not be considered any further.

When comparing the designs No1 and No3, design No3 appears to be more suitable for the purposes of this work, since it presents a smaller temperature gradient and there is a biggest portion of the experimental setup that would lie in the temperature regime of interest. As a result, the geometry described in Design 2 of Figure 4.17 would be more suitable for our application, since it would require a smaller value of uniform Q_{in} in order to create the temperature range of interest.

Summarising, placing the less heat-conductive material under the more conductive one appears to ensure the development of a linear temperature profile at the centreline of a microfluidic channel. When the interface between the two substrates is inclined, control over the temperature gradient can be achieved; reducing the thickness of the most conductive material along the length of the rig is found to decrease the temperature gradient at the centreline of the microfluidic channel without affecting (significantly) the linearity of the temperature profile.

4.3.2 Final design

After the results obtained from the study presented in Chapter 4.3.1.3, a design with two material substrates is studied in this Chapter. It is important to point out that there is no change in the width of both substrates along the length of the rig. This set of simulations is designed while considering the second and final temperature range for the melting temperatures; $T_m(^oC)$ = [80, 90]. The function of the heating (heat resistors) and cooling elements (peltier) is also simulated, in order to obtain a realistic representation of the developing rig. The assumptions and the model are presented in Chapter 4.3.2.1.

4.3.2.1 Model

Considering the previous studies, the next set of simulations describes real experimental conditions. This chapter presents the model developed in COMSOL Multiphysics ®5.4 to describe the heat transfer and fluid flow phenomena that take place in the experimental rig. The schematic graph is presented in Figure 4.18. Perspex and Aluminium Alloy 1060 substrates are used; materials of low and high thermal conductivity respectively.

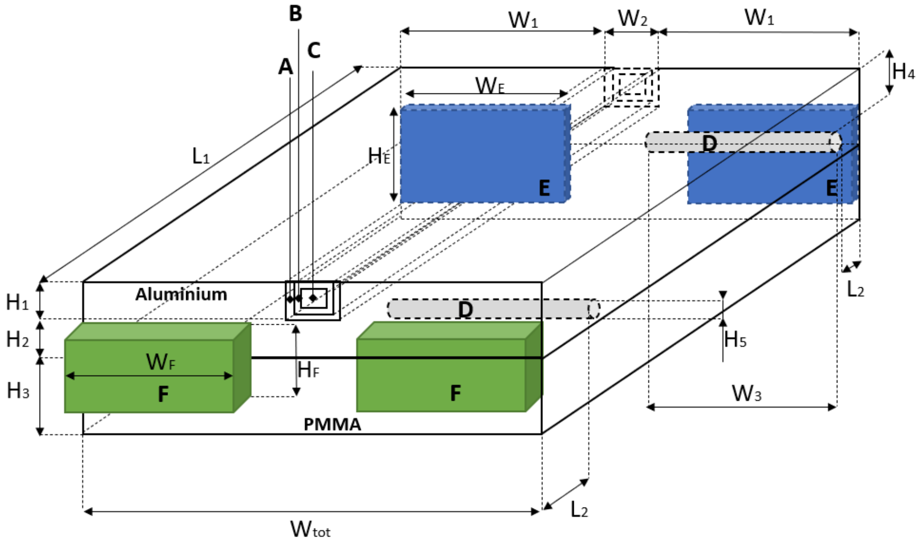

FIGURE 4.18: Schematic of the setup of the finalised simulations using a square capillary, where A: Arctic Silver, B: Borosilicate square glass capillary, C: Silicone oil (Teitel, Schwabe, and Gelfgat, 2008), D: thermocouples, E: Peltier Element and F: Heat Resistor.

A square capillary made of borosilicate glass is used, in order to enable a good fitting within the aluminium substrate (see Figure 4.18 B). The capillary is surrounded by arctic silver (see Figure 4.18 A), in order to stabilise its position while at the same time preventing any scattered light from being recorded and ensuring proper thermal contact. The fluid (see Figure 4.18 C) used in this step of the simulations is the third silicone oil used in the work of Teitel, Schwabe, and Gelfgat (2008).

The experimental equipment and the materials appearing in Figure 4.18 are presented in detail in Chapter 4.4 and Chapter 4.3.2.1.3 respectively. Table 4.4 presents the dimensions of the parameters appearing in Figure 4.18. The temperature profile obtained at the centreline of the square capillary is presented in Figure 4.23, for a stream of silicone oil (Teitel, Schwabe, and Gelfgat, 2008)) with an inlet temperature of 25 ^oC.

4.3.2.1.1 Assumptions As part of generating the model of the experimental device, a number of assumptions are made in order to simplify the model:

- Considering that this model is focusing on simulating and predicting the heat transfer in the experimental rig and its ability to generate a linear temperature profile, the function of the heating and cooling elements is simplified. As a result, the resistors and the peltier elements are simulated as copper blocks.

- Considering that this model is focusing on simulating and predicting the heat transfer in the experimental rig and its ability to generate a linear temperature profile, the function of the heating and cooling elements as well as the thermocouples is simplified. As a result, the resistors and the peltier elements are simulated as copper blocks, while the thermocouples as stainless steel cylinders.

- Natural and/or forced heat convection take place on all sides of the rig. More specifically, natural convection takes place at all sides, except the top plane and the plane where the peltier elements are located. As far as the natural and forced convection heat transfer coefficients are concerned, their values are set at $h_{Nat.Conv.} = 10W/(m^2 \cdot K)$ and $h_{Forced.Conv.} = 70W/(m^2 \cdot K)$ respectively, in accordance to the ranges appearing in Kosky et al. (2013). At this point, it is important to point out that the values of the convection heat transfer coefficients when performing the experiment might be different to the ones assumed here, which might result in a variation in the total amount of power provided and extracted by the heating and cooling elements respectively.

4.3.2.1.2 Geometry Figures 4.18, 4.19 and 4.20 present different views of the experimental rig. More specifically, Figure 4.18 illustrates the arctic silver, the square borosilicate glass, the silicone oil, the two thermocouples, the two peltier elements and the two resistors with the letters A, B, C, D, E and F respectively.

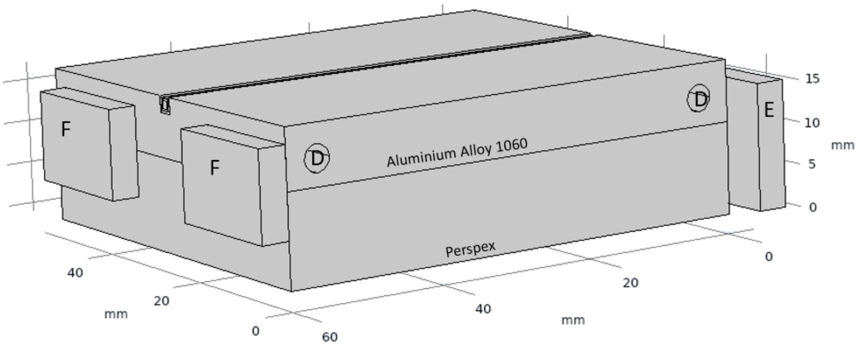

FIGURE 4.19: Back view of the experimental rig, presenting the two resistors (F), as developed in COMSOL Multiphysics ®.

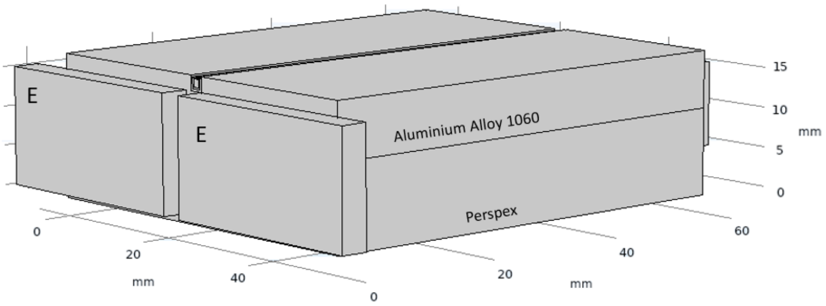

FIGURE 4.20: Front view of the experimental rig, presenting the two peltier elements (E), as developed in COMSOL Multiphysics ®.

TABLE 4.4: Dimensions of the device as appearing in Figure 4.18

Parameters	Unit (mm)
H_1	2
H_2	5.25
H_3	12
H_4	3
H_5	3.19
H_E	15
H_F	10
W_1	25
W_2	2
W_E	30
W_F	16
W_{tot}	52
L_1	60
L_2	3

4.3.2.1.3 Materials The materials used and their properties are presented in Table 4.5. The Aluminium Alloy 1060 is used for the top part of the device, in order to take advantage of its thermal properties. More specifically, its high thermal conductivity allows for the fast thermal response to the temperature variations implemented by the heating and cooling elements of the system. This allows the heat transfer to take place rapidly and hence facilitates the temperature control of the system. As mentioned earlier in Chapter 4.3.2.1.1, the resistors and the peltier elements are simulated as copper blocks, while the thermocouples as stainless steel cylinders.

4.3.2.1.4 Fluid Flow The fluid flow in the square pipe is found to be laminar, according to the indicative Reynolds number calculated (Equation 4.14). As a result, the Laminar Fluid Flow model is used. The incompressible Navier-Stokes equations (Equations 3.18 and 3.19) are implemented in steady state, and the following boundary conditions are applied:

TABLE 4.5: Properties of the materials used in the simulations.

Material	C_p ($\frac{J}{kg \cdot K}$)	ρ ($\frac{kg}{m^3}$)	k ($\frac{W}{m \cdot K}$)	μ ($mPa \cdot s$)	α ($1/K$)
PMMA	1420	1190	0.19	-	$70 \cdot 10^{-6}$
Copper	385	8960	400	-	$17 \cdot 10^{-6}$
Borosilicate glass	800	2230	1.14	-	$3.3 \cdot 10^{-6}$
Aluminium Alloy 1060 (Handbook et al., 1996)	900	2700	234	-	$23.6 \cdot 10^{-6}$
Silicone oil*	1400	910	0.11	4.75	-
Arctic Silver	235	10500	8.9	-	$19 \cdot 10^{-6}$
Stainless Steel (310)	500	8000	14.2 (at 100 ^{o}C)	-	$15.9 \cdot 10^{-6}$

* the 3^{rd} silicone oil presented in Table 1 by Teitel, Schwabe, and Gelfgat, (2008).

$$Re = D_{ID} \cdot U_{in} \cdot \rho / \mu = \frac{1 \cdot 10^{-3} \cdot 6.3 \cdot 10^{-4} \cdot 910}{4.75 \cdot 10^{-3}} = 0.12 \tag{4.14}$$

$$U_{in} = Q_{vol} / A \tag{4.15}$$

$$A = D_{ID}^2 \tag{4.16}$$

where ρ is the fluid density, D_{ID} the internal diameter of the square capillary and μ the viscosity (McDonough, 2009; Gerbeau and Le Bris, 2000). The terms of inlet velocity, volumetric flowrate and internal diameter, U_{in}, Q_{vol} and D_{ID}, appearing in Equations 4.15 and 4.16 take the values of $6.3 \cdot 10^{-4}$ mm/s, 38 μL/min and 1 mm respectively.

Equations 3.18 and 3.19 are solved on the geometry appearing in Figures 4.20 and 4.19, subject to the following boundary conditions: (i) no-slip at the microchannel walls, assuming that at a solid boundary, the fluid has zero velocity relative to the boundary; (ii) fully-developed flow and a value of average inlet velocity, U_{in}, at the inlet of the square channel; (iii) zero (relative) pressure at the exit of the microchannel.

4.3.2.1.5 Heat Transfer The conjugate heat transfer is modelled in steady state, using Equation 4.17:

$$\rho C_p (\mathbf{u} \cdot \nabla T) = \nabla \cdot (k \nabla T) + \Sigma Q_{Resistors} - \Sigma Q_{Peltier} + Q_{Nat.conv} + Q_{Forced.conv} \tag{4.17}$$

$$Q_{Nat.Conv.} = h_{Nat.Conv.} \cdot (T_{amb} - T) \tag{4.18}$$

$$Q_{Forced.Conv.} = h_{Forced.Conv.} \cdot (T_{amb} - T) \tag{4.19}$$

where T_{amb}: the ambient temperature, **u**=**0** everywhere except in the fluid domain. The terms $h_{Nat.Conv.} = 10[W/(m^2 \cdot K)]$ and $h_{Forced.Conv.} = 70[W/(m^2 \cdot K)]$ are the natural and forced convection heat transfer coefficients respectively. Their values are selected according to the ranges appearing in Kosky et al. (2013), but the actual experimental conditions are expected to vary. The terms $\Sigma Q_{Resistors}$ corresponds to the heat provided to the system by the two heating elements (resistors), and is only non-zero at the interface between the resistors and the solid substrates (PMMA, Aluminium Alloy 1060). The term $\Sigma Q_{Peltier}$ corresponds to the heat extracted by the system through the two cooling elements (peltier element), and is only non-zero at the interface between the peltier elements and the solid substrates (PMMA, Aluminium Alloy 1060). The terms $Q_{Nat.conv}$ and $Q_{Forced.conv}$ describe the heat losses of the system due to natural (Equation 4.18) and forced convection (Equation 4.19).

The boundary conditions are applied on the geometry appearing in Figures 4.20 and 4.19 as follows: (i) the heat resistor temperatures at their interface with the solid substrates are set to $T_{STP,Resistors}$ = 90 ^oC; (ii) the peltier element temperatures at their interface with the solid substrates are set to $T_{STP,Peltier}$ = 80 ^oC; (iii) a heat flux of $Q_{Nat.conv}$ (Equation 4.18) is applied at all sides of the rig, apart from those where forced heat convection is applied; (iv) a heat flux of $Q_{Forced.Conv.}$ (Equation 4.19) is applied at the top and the side of the rig where the peltier elements are located. More specifically, this term is used to describe the heat losses caused by the cool air flowing at the top and the side of the rig generated by the two fans used to cool the cooling blocks attached to the hot side of the peltier elements (see Figure 4.32).

4.3.2.2 Mesh Independence Study

A mesh independence study is conducted in order to ensure that the model not only converges but is also independent of the mesh resolution. Seven meshes with a different number of elements are implemented (9,568, 24,501, 67,241, 181,519, 356,836, 922,323, 1,015,444), and the values of Conductive Heat Flux Magnitude are recorded for both the resistors and the peltier elements. The values (Table 4.6) are presented in Figures 4.21 and 4.22 for the resistors and the peltier elements respectively. According to the results obtained, the mesh with the 922,323 elements - mesh is selected to proceed with the simulations since both values of Conductive Heat Flux Magnitude are stabilised.

4.3.2.3 Results

After completing the mesh independence study, the 922,323 elements - mesh is selected to obtain the temperature profile at the centreline of the square capillary, along

TABLE 4.6: Mesh independence study recording the values of conductive heat flux magnitude for seven meshes.

	No of mesh elements	Conductive Heat Flux Magnitude of peltier elements	Conductive Heat Flux Magnitude of the resistors
1	9568	4.3485	8.7576
2	24,501	4.3149	9.0504
3	67,241	4.3139	9.3514
4	181,519	4.3957	9.8164
5	356,836	4.4294	10.141
6	922,323	4.4965	11.009
7	1,015,444	4.4965	11.009

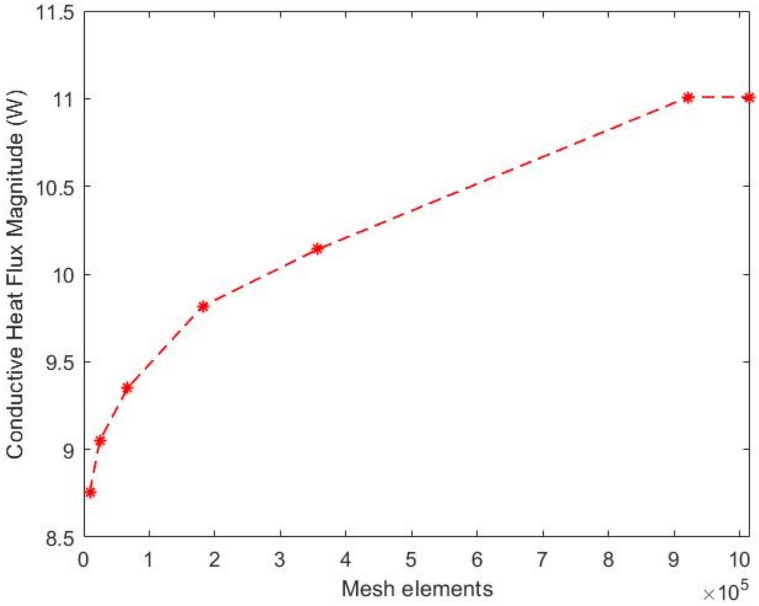

FIGURE 4.21: Magnitude of the conductive heat flux passing through the resistors for the different meshes.

the length of the capillary. Figure 4.23 presents the temperature profile, with the temperature range of interest ($T_m(^oC)$ = [82, 90]) being marked with a dotted line.

This design appears to be able to successfully generate the linear temperature profile at the centreline of the microfluidic channel, within the desired temperature range.

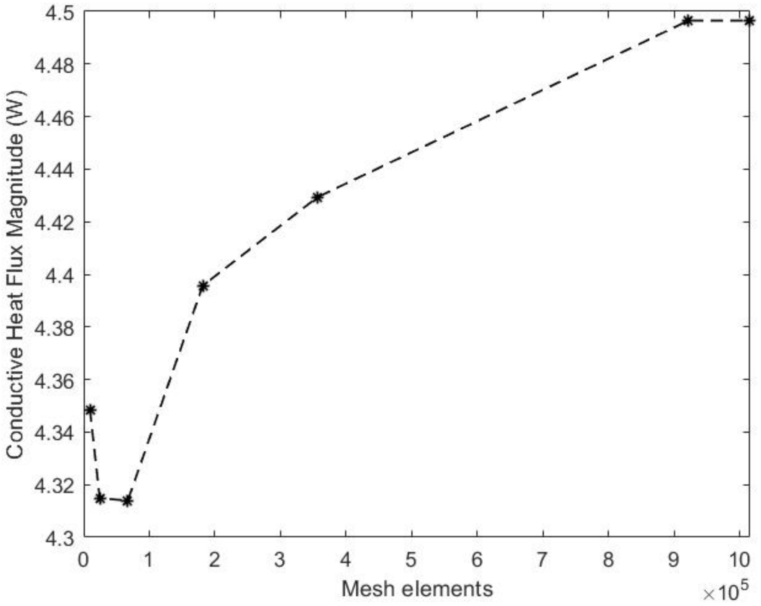

FIGURE 4.22: Magnitude of the conductive heat flux passing through the peltier elements for the different meshes.

4.4 Experimental Equipment

The experimental equipment that is used to develop the design simulated in Chapter 4.3.2 is presented in this Chapter.

4.4.1 QX100 Droplet Generator

The droplet generator QX100 requires the use of Supermix (Code: 1863010), Oil (Code: 1864005) and Buffer control(Code: 1863052) to produce the droplets. The use of the buffer control is to ensure that no wells within the cartridge are left empty when creating droplets. If any wells are left empty, this will stop droplet production early and the number of the produced will be decreased. The buffer control is essentially a diluted version of the supermix (1:1 dilution of the supermix).

4.4.2 Rig

4.4.2.1 Substrate Materials

Perspex and Aluminium Alloy 1060 are used as substrate materials in the simulations of Chapter 4.3.2 and in the rig of the experimental device. The parts are built with the assistance of Samuel Flint (technician at the University of Leeds). Their properties are presented in Table 4.5. The two substrate base parts are presented in Figure 4.24, while the H_1, H_2, H_3, L_2, W_2 and W_{tot} dimensions of the substrates introduced in COMSOL ® are set to 2, 5.25, 12, 60, 2 and 52 mm respectively (Table 4.4).

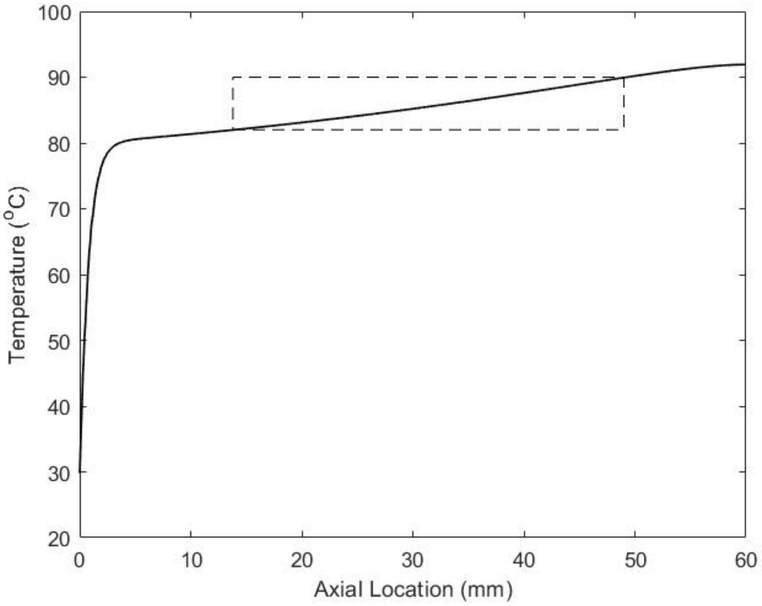

FIGURE 4.23: Temperature profile of the centreline in the middle plane of the silicone oil. The inlet temperature and the velocity are 25 ^oC and 6.3 $\cdot 10^{-4}$ m/s respectively. The setpoint temperatures are set at $T_{STP,Resistor} = 90^oC$ and $T_{STP,Peltier} = 80^oC$.

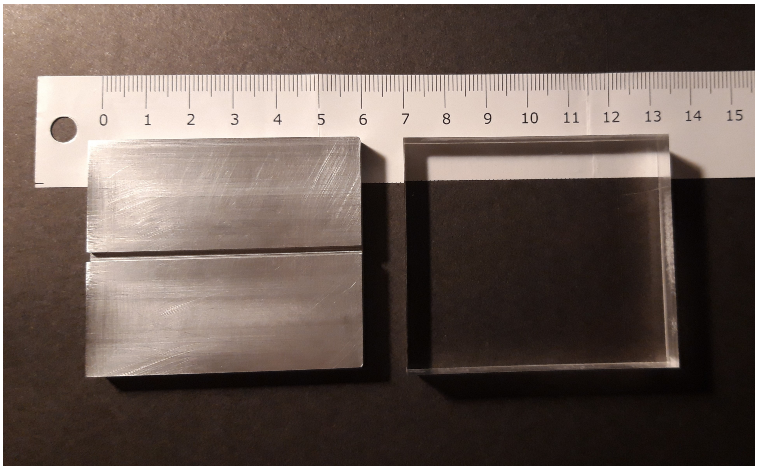

FIGURE 4.24: Perspex and Aluminium Alloy 1060 substrates. The dimensions are presented in mm.

4.4.2.2 Power Resistor

Two AP821 power resistors (ARCOL, 2020) are selected in order to heat the end of the device (see F, Figure 4.18). The dimensions of the resistor are presented in Figure 4.25. The working temperature range is between -65^{o}C and 150^{o}C. Its resistance is at 33 Ohms, while the power rating is at 20 W. The power resistor is simulated as a block of copper wire heater with the same dimensions, placed at the side of the setup (see F in Figure 4.19).

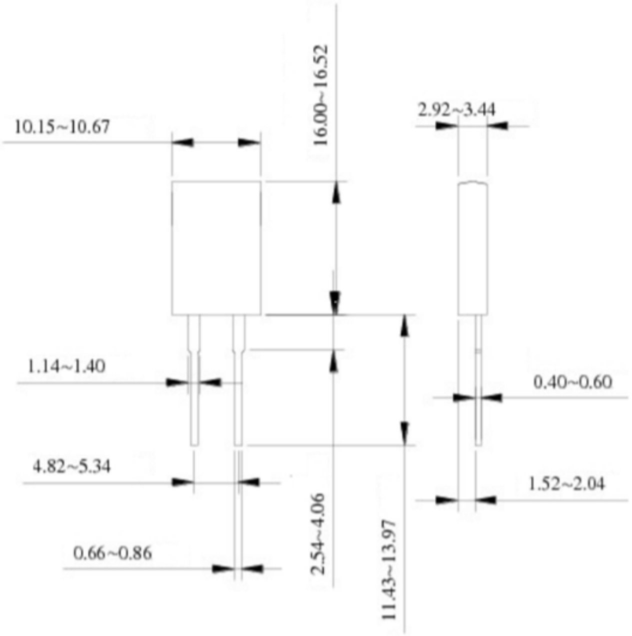

FIGURE 4.25: AP821 power resistor (ARCOL, 2020). The dimensions are presented in mm.

4.4.2.3 Peltier Element

A Peltiér element is a thermoelectric element having two surfaces. If a temperature difference is maintained between the surfaces a current is generated (Seebeck effect). This can be used to generate current or measure the temperature. Inversely one surface is heated and the other is cooled, if a current is conducted through the element (Peltiér effect) (Millgard, 1992).

Two peltier elements are selected as a means of cooling the side of the substrate at the inlet (see E at Figure 4.18). The two peltier elements (CUI Devices, 2019) have hot-plate temperatures of 80 ^oC. Figure 4.26 presents a basic schematic of the geometry of the peltier element. The A and B dimensions for the peltier elements are A_I = 15 mm, B_I = 30 mm (CUI Devices, 2019).

4.4.2.4 Arctic silver

Arctic silver (Innovatek, 2010) is commonly used to conduct heat in modern high-power CPUs and high-performance heatsinks or water-cooling solutions. This product is made of 99.9% pure silver, and in this particular setup is used to keep the capillary and the aluminium substrate in contact (the capillary is fitted into a slot of the aluminium block) when thermal expansion takes place (see A at Figure 4.18, Chapter 4.3.2), while at the same time promote the thermal conductivity between them. The coefficients of thermal expansion of the different materials are presented in Table 4.5.

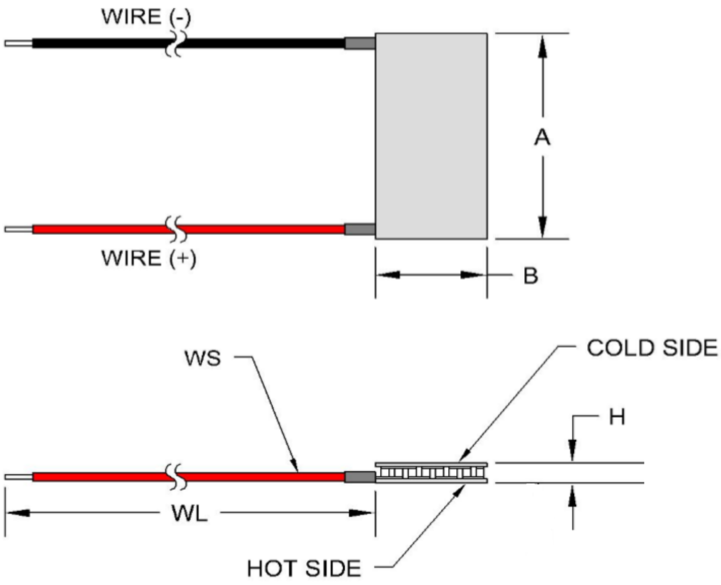

FIGURE 4.26: Schematic graph of a peltier element (TE Technology, 2010).

4.4.2.5 Square Borosilicate Capillary

A square capillary made of borosilicate glass is selected for this design (product name: 8100 (VitroCom, 2020)) (see B at Figure 4.18, Chapter 4.3.2). With a thermal expansion coefficient of at least 3.2 $\cdot 10^{-6}$ 1/K, pure borosilicate glass is significantly more resistant to temperature changes where other types of glass may become warped or deformed. This characteristically low thermal expansion allows the material to maintain its integrity, even when transferred from a cold region to a hot area in seconds (Matmatch, 2020). Figure 4.27 presents the schematic of the capillary, together with the dimensions of interest.

4.4.2.6 Thermocouple

Two K-type thermocouples are used, with a miniature flat pin plug, colour-coded ‘Green’ in accordance IEC. The thermocouple has a 3 mm diameter and 150 mm length. Its temperature range is from -40 - 1100 ^{o}C, while the sheath is made of stainless steel 310 (Farnell, 2020). The properties of stainless steel 310 are described by AZO Materials (2008). The thermocouples are included in the simulations as two round stainless steel cylinders, placed close to the walls of the capillary (see D at Figure 4.18, Chapter 4.3.2).

The first type of thermocouple tried is a K-type grounded thermocouple (item code: 872-2503 (RS, 2021)). Because the thermocouple used is grounded (the junction is welded to the sheath at the tip of the sensor), no measurements could be taken when both thermocouples touched the aluminium rig. Therefore, a set of ungrounded thermocouples of the same size is purchased (SterlingSensors, 2021), where the junction does not touch the sheath.

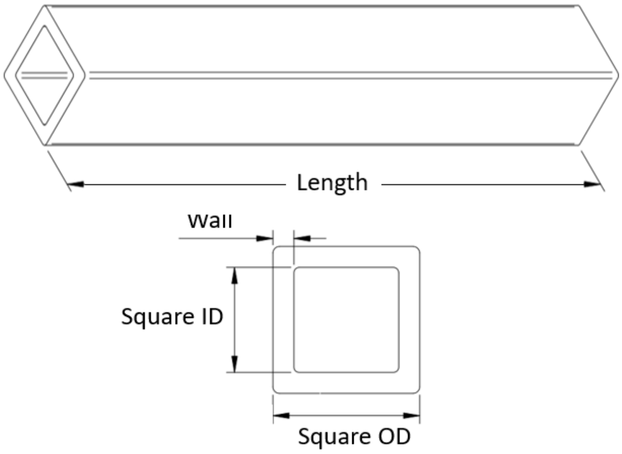

FIGURE 4.27: Square borosilicate glass capillary. For the product name 8100 produced by VitroCom (2020), the square internal (SID) and outer diameter (SOD) are set at 1.000 and 1.400 mm respectively (0.200 mm wall thickness). The length of the capillary is adjusted accordingly.

FIGURE 4.28: Thermocouple.

4.4.2.7 Fluidic part

The following parts are used in order to develop the equipment appearing in Figures 4.34 and 4.35, where the droplet-laden flow takes place:

- Idex P-702-01 Low-Pressure Union, Female Straight, Natural PEEK, 0.020" Bore, 1/4-28 Flat Bottom; 1/EA
- Spex VapLock^{TM} Fitting, Green PP w/ Blue ETFE, Straight, Compression to Threaded Adapter, 1/16" OD x 1/4-28 UNF(M); 10/PK
- Spex VapLock^{TM} Fitting, Yellow PP w/ Orange ETFE, Straight, Compression to Threaded Adapter, 3.0 mm OD x 1/4-28 UNF(M); 10/PK
- ADAPTER 1/4"-28 FEMALE TO FEMALE LUER
- 1/16" tubing

- TE Connectivity Adhesive Lined Heat Shrink Tubing, Black 4mm Sleeve Dia. x 1.2m Length 4:1 Ratio HT.

These parts are connected to the tube by welding the Adhesive Lined Heat Shrink Tubing.

4.4.2.8 Temperature controller (Arduino)

A type of controller is required in order to maintain the temperatures of the cold side of the peltier elements and the resistors at the setpoint values (see Chapter 4.3.2). Given that this device needs to be as easy to use as possible for any end-users, Arduino is considered.

Arduino is an open-source electronics platform based on easy-to-use hardware and software used to build electronics projects, allowing users to design and build devices that can interact with their surroundings. It consists of both a physical programmable circuit board (microcontroller (Figure 4.29)) and a piece of software, or IDE (Integrated Development Environment), used to write and upload computer code to the physical board. Unlike most previous programmable circuit boards, the Arduino does not need a separate piece of hardware (called a programmer) in order to load new code onto the board (a USB cable can be used). Additionally, the Arduino IDE uses a simplified version of C++, making it easier to learn to program (Bista, 2016). More information about Arduino can be found at Arduino (2020).

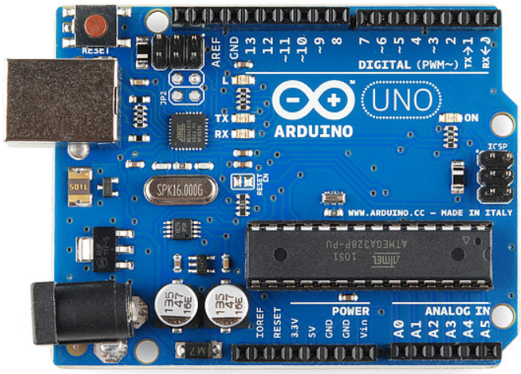

FIGURE 4.29: Arduino Uno.

Several examples of Arduino devices used in microfluidic setups exist in the literature. Lee et al. (2017) developed a temperature-controllable microfluidic device for the accurate measurement of temperature-dependent interfacial tensions between two immiscible liquids. For their temperature controller, a microcontroller board (Arduino, UNO-R3) is used to input a programmed pulse width modulation (PWM) to a MOSFET switch module for fine current control over the heating power of the microheater.

Shih et al. (2015) developed a hybrid droplet-to-digital microfluidic platform that integrates droplet-in-channel microfluidics with digital microfluidics for performing multi-step assays. They used an Arduino microcontroller to control the Peltier cooler, which is used to maintain constant surface temperature on the DMF during cell culture.

Angus et al. (2015) developed a novel PCR device for the identification of the 16S rRNA gene V3 hypervariable region from Escherichia coli genomic DNA, that uses wire-guided droplet manipulation to guide a droplet over three different heating chambers. Fluorescence detection takes place using a smartphone-based fluorescence microscope, after PCR amplification is complete. The Arduino Uno microcontroller is used to control the heaters and the motor through thermocouple feedback. A different Arduino is used by Angus et al. (2015) to control a motor, that transports the droplets to a different chamber.

4.4.2.9 MOSFET

In order to control the current and hence the heating power of the microheater, a MOSFET (Metal Oxide Field Effect Transistor) switch is required in combination with the Arduino. MOSFET is used to switch or amplify voltages in circuits (Figure 4.30). It is a current-controlled device, constructed with 3 terminals; source, gain and drain, with the working principle differing based on the type of MOSFET (Seedstudio, 2020).

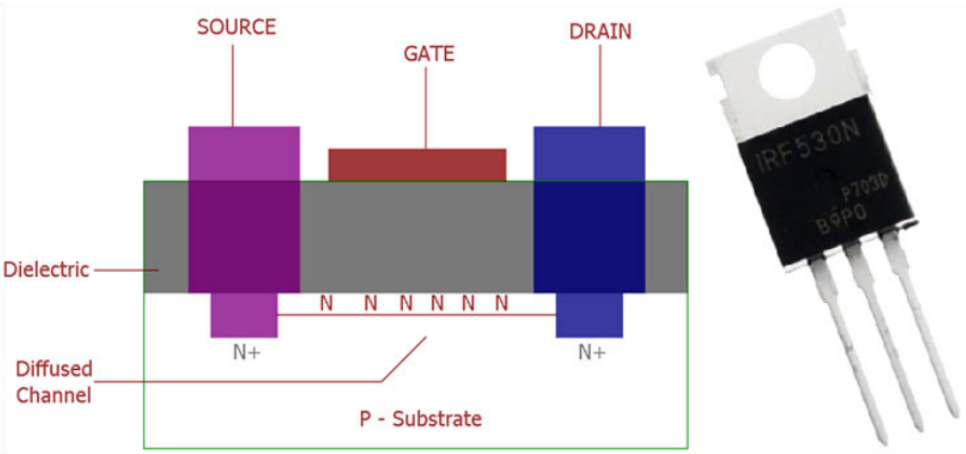

FIGURE 4.30: Schematic view (left) and picture (right) of MOSFETs.

MOSFET act like switches, by varying the voltage at one terminal, the gate, changes the resistance between the other two terminals, source and drain. There are two classes of MOSFETS; Depletion Mode, and enhancement mode. Each class is available as n-channel or p-channel, tallying up to four types of MOSFETs in total.

4.4.3 Optics

Two main plans are mentioned in this Chapter related to the optics of the experimental device; i) using a fluorescence microscope to view and record the fluorescence signals and ii) developing an optical rig, consisting of a light source, appropriate excitation, emission and dichroic filters, a filter cube and an appropriate camera.

Only the first of the two approaches is tested, using the Zeiss LSM880 + Airyscan Upright Confocal Microscope (Leeds, 2021). The microscope is tested and measurements of the fluorescence signals are obtained from the rig without the use of a capillary and droplets as a test run (Figure 4.31). Furthermore, this microscope is also found suitable to obtain measurements for temperatures of $\sim 90^oC$. Further investigation/tests are required for setups including droplets inside a capillary.

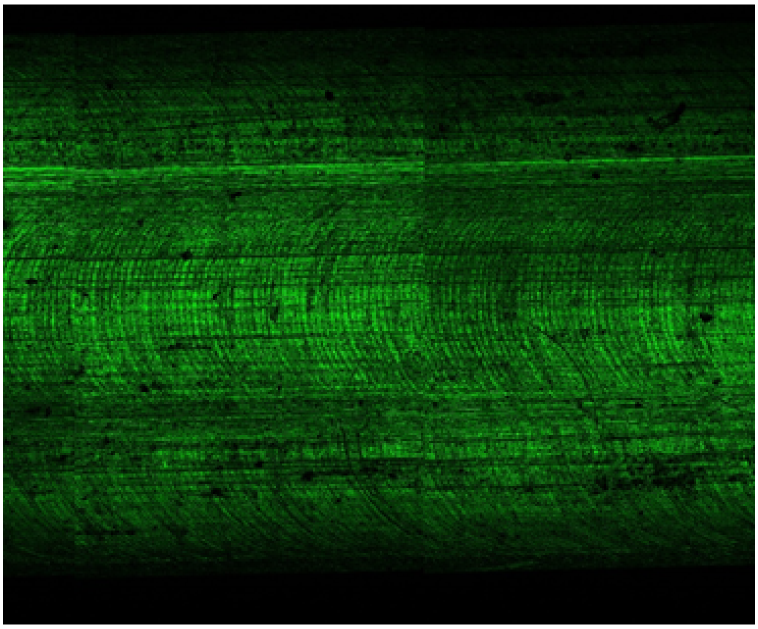

FIGURE 4.31: Fluorescence measurement of the top view of the rig, where the capillary is placed, obtained by the Zeiss LSM880 + Airyscan Upright Confocal Microscope.

4.5 Experimental Methodology

4.5.1 Materials

4.5.1.1 Consumables

The consumables used are the following (BIO-RAD, 2021):

- DG8^{TM} Droplet Generator cartridges (single-use)
- DG8^{TM} gaskets (single-use)
- ddPCR^{TM} Droplet Generation (DG) oil (10 x 6mL)
- 2X PCR Master Mix (5 x 1mL)
- Droplet Reader (DR) oil (2 x 1L)

4.5.1.2 Additional Materials

The additional materials required are the following (BIO-RAD, 2021):

- Pipettes (10, 100, 1000 μL with compatible tips)
- 96-well PCR plates (Eppendorf twin.tec, semi-skirted)
- Heat sealer (Eppendorf)
- Heat sealing PCR foil (Thermo Fisher)
- 96-well plate Thermal Cycler (Eppendorf Mastercycler, Bio-rad C-1000 or ABI 9700)
- 20X Primer and Taqman Probe Mix
  Standard ddPCR final concentrations: 900nM Primers, 250 nM Probe
- Chemical waste container
- Reagent reservoir (Optional, 25 mL divided, Thermo Fisher)

4.5.1.3 Storage Conditions

The storage conditions are the following (BIO-RAD, 2021):

- ddPCR 2X PCR Master Mix: Store at -20 ^oC. Thaw and allow to equilibrate to ambient temperature. Vortex and spin down prior to use. Once thawed, store at 4 ^oC for up to 7 day
- DG and DR Oils: Store at ambient temperature

4.5.2 Workflow

The workflow is described in this section (BIO-RAD, 2021).

4.5.2.1 Sample Preparation

All reagents before sample preparation should be at room temperature before use (BIO-RAD, 2021).

- Reaction mixtures can be assembled in vials or in 96-well plates. If the prepared samples are arranged in a PCR plate, they can be loaded into the DG8 using an 8-channel pipette.
- The concentration of intact human genomic DNA should be <66 ng per 20 μL reaction. Above this concentration, DNA should be pre-digested with a restriction endonuclease that does not cut the target or reference amplicons.
- Prepare PCR reaction mixture by combining 2X PCR Master Mix, 20X Primers and Probe Mix, and DNA sample. Mix by vortexing, and spin down.

TABLE 4.7: Sample Preparation (BIO-RAD, 2021)

1X Master Mix Formulations	1rxn (μL)	48 Reactions
2X PCR Master Mix	10	480
20X Target primers/probe (FAM)	1	48
20X Reference primers/probe (VIC)	1	48
DNA Sample/Water	8	8X48
Final Volume (μL)	20	960

4.5.2.2 Droplet Generation

The Bio-Rad QX100^{TM} Droplet Digital^{TM} PCR system performs digital PCR. The droplet generation takes place as follows, generating approximately 20,000 monodisperse nanoliter droplets for each of the 8 prepared samples.

- Load reagent reservoir trough with DG oil (600 μL per DG8 cartridge)
- Place DG8 cartridge into the holder
- Transfer your 20μL prepared samples from 96-well plate or tubes, to the DG8 cartridge's middle wells. Ground the 20μL pipette tip against the bottom edge of the sample well. Avoid producing air bubbles, especially at the bottom of the well. With the pipette tip at the bottom edge of the well, slowly dispense a small portion of the sample, then slowly lift the tip up the side of the wall while slowly dispensing the remainder of the sample.
- Pipette 70μL of DG oil into each well.
- Secure DG8 gasket over DG8 in holder.
- Press the green button to open the DG door.
- Place assembled DG8 cartridge and holder into the DG. System display indicated when DG8 is in place.
- Push the button to close the door. When the door is closed, a manifold is automatically positioned over the outlet wells, drawing oil and sample through microfluidic channels where droplets are created. Droplets flow to the droplet well where they accumulate. The system display indicates when droplets are being generated and when the process is complete.
- Push the button to open the door and remove the DG8.
- Remove the DG8 gasket and discard.
- Set pipette volume to 40μL. Then carefully aspirate droplets from the wells using an 8-channel pipette.
- Slowly dispense droplets into the column of a 96-well PCR plate.
- Open DG8 holder and discard DG8.

4.5.3 Rig

The experimental rig is presented in Figures 4.32 and 4.33. Figure 4.34 provides a close look at the rig where the droplet-laden flow takes place (as it is developed with the assistance of William Davis Birch). Figure 4.35 presents the connection of the fluidic part to the syringe. Details of the parts used to produce the equipment appearing in Figures 4.34 and 4.35 are presented in Chapter 4.4.2.7. Figure 4.36 presents a schematic graph of the connections made between the different elements appearing in Figure 4.33.

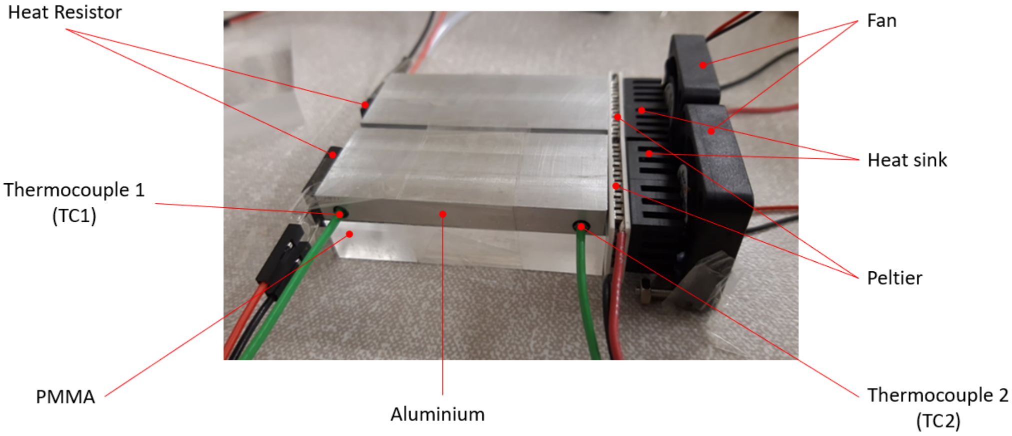

FIGURE 4.32: Main part of the experimental rig.

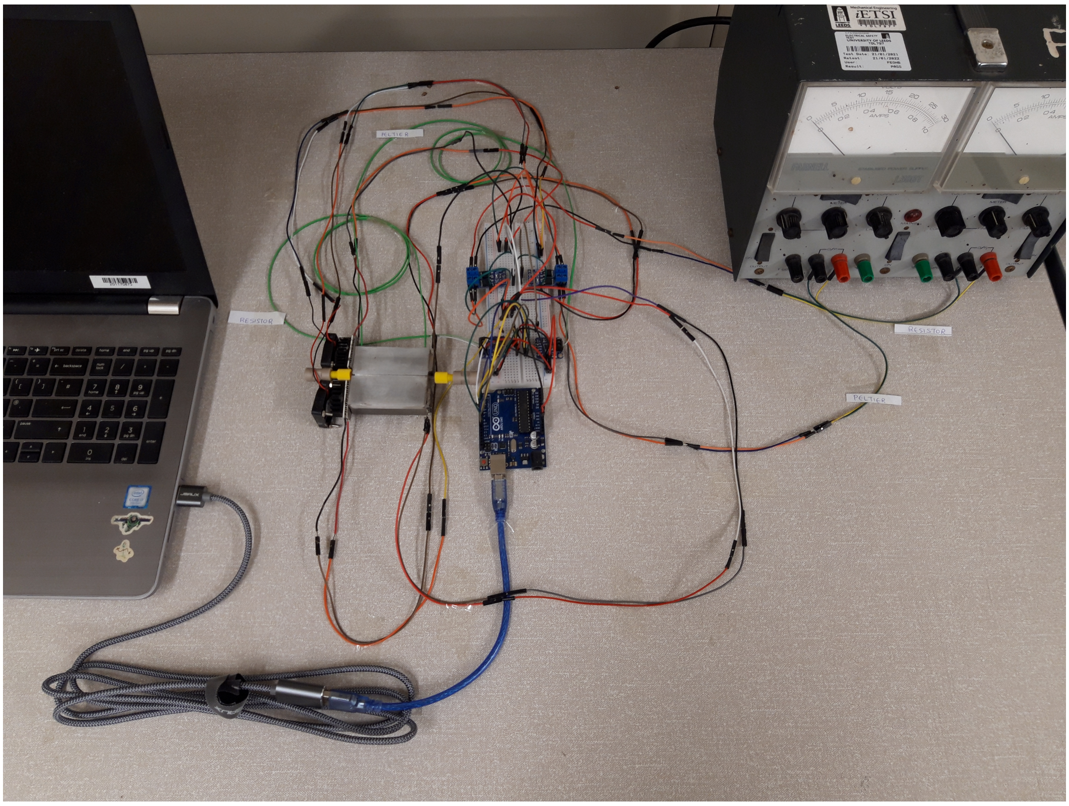

FIGURE 4.33: Top view of the entire experimental setup.

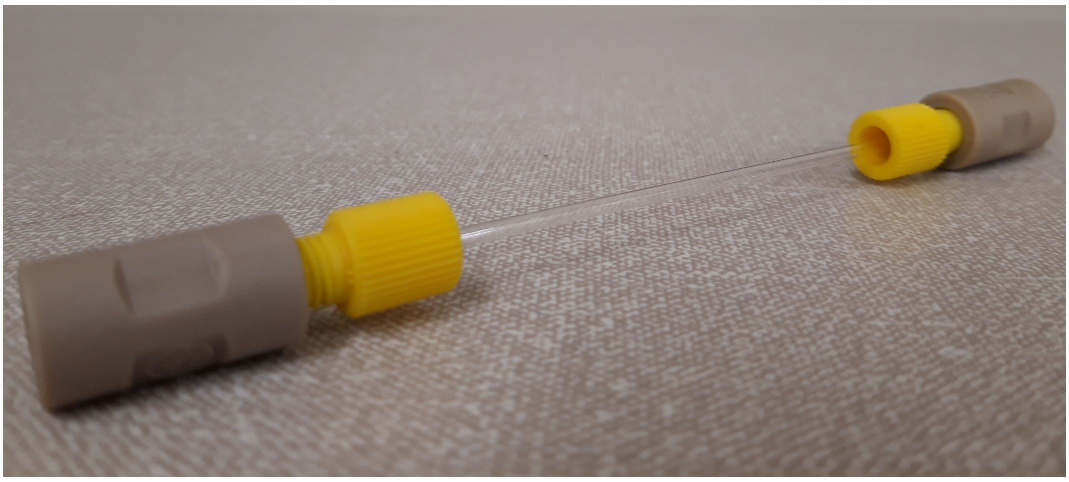

FIGURE 4.34: Close look of the fluidic part of the experimental rig.

FIGURE 4.35: Attachment of the fluidic part to the syringe.

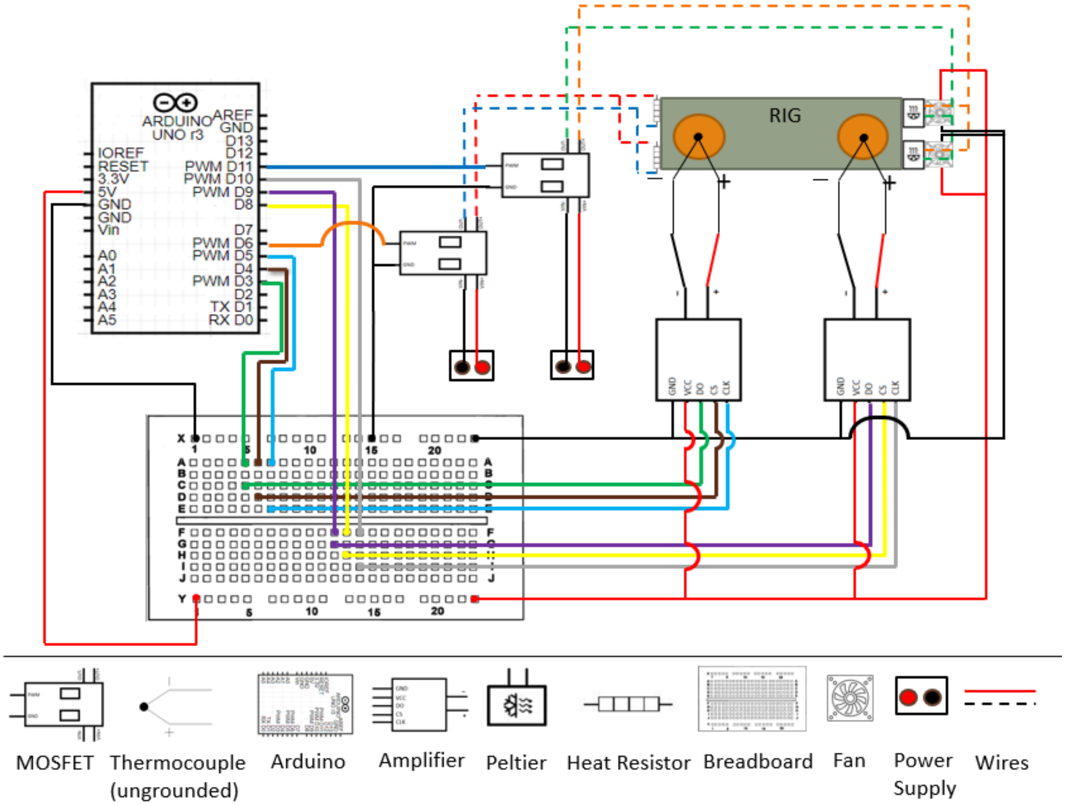

FIGURE 4.36: Schematic of the connections implemented in the rig.

4.5.4 Droplets

The droplets are generated using the methodology described in Chapter 4.5.2.2. Figures 4.37 and 4.38 present the droplets generated using QX100 ddPCR, when they are inserted into the square glass capillary. The droplets are found to be monodisperse when examined under a microscope, quite stable (do not coalesce) and packed in a dense formation. The droplet volume is of nanolitre scale, while the droplet diameter to channel width ratio is found to be approximately 0.13. Extra care is given when extracting them from the wells in order to avoid the formation of air bubbles.

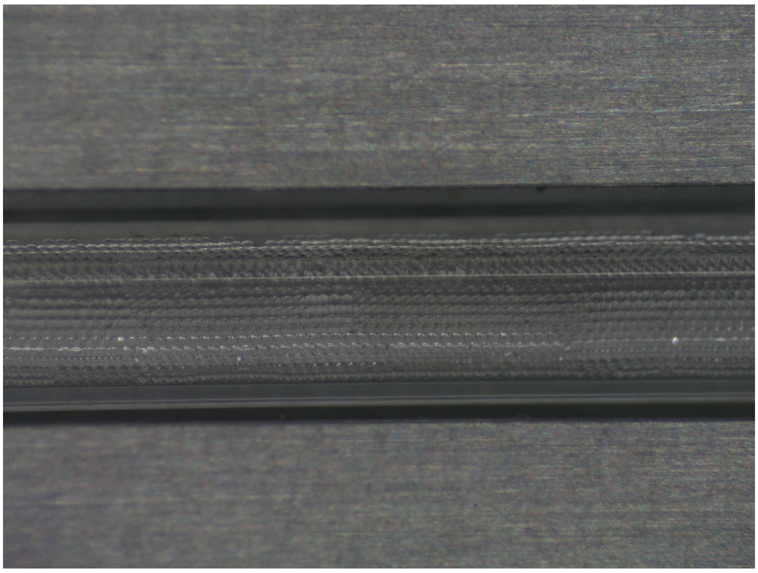

FIGURE 4.37: Droplets generated using the QX100 ddPCR.

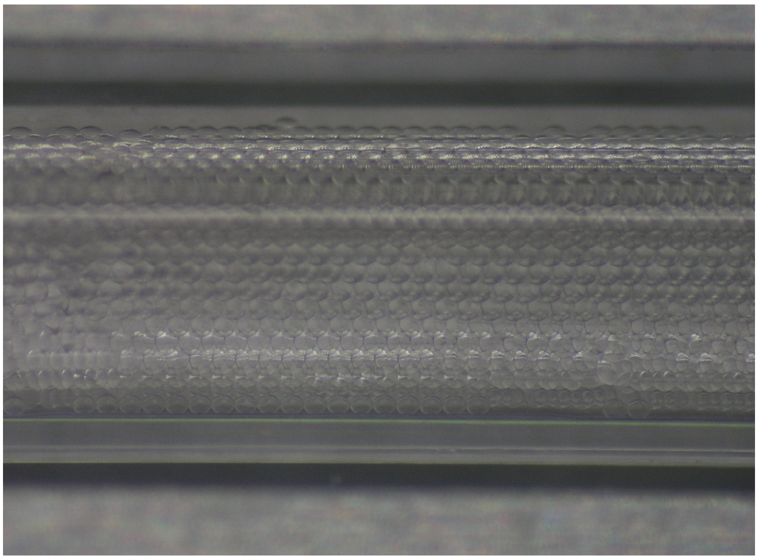

FIGURE 4.38: Image presenting some of the layers of the generated droplets in the square capillary.

4.6 Results

In the experiments presented in this chapter, the decision to implement PI (K_D=0) control is made, considering that PI control (Visioli, 2006):

- is the most commonly used one in industrial applications,
- is the simplest type of control that can offer zero steady-state error,
- avoids any difficulties related to the derivative control action, such as the need to filter the measurement noise and the selection of the appropriate K_D value.

4.6.1 Preliminary experiments and tuning of the parameters.

This chapter presents the results obtained by performing two preliminary sets of experiments at the setpoint temperatures of $T_{STP,Resistor} = 40^oC$ and 60^oC. These temperature setpoints are selected in order to successfully achieve temperature control at safer temperatures (than the 80^oC and 90^oC degrees). The effect of varying the three PID parameters (K_P, K_D, K_I) and the voltage settings for the resistor ($V_{Resistor}$) and the peltier elements ($V_{peltier}$) are also examined, in order to achieve good PID control for the $T_{STP,Resistor} = 90^oC$.

4.6.1.1 First set of experiments at $T_{STP,Resistor} = 40^oC$.

Figure 4.39 presents the temperature profiles generated by the two thermocouples (TC1 and TC2) for the setpoint temperature of $T_{STP,Resistor} = 40^oC$, while the two peltier elements remain turned off ($V_{Peltier} = 0V$). Three experiments are performed with varying K_I parameter values, while the values of the K_P and K_D parameters are kept constant (K_P = 35, K_D = 0). Furthermore, the voltage setting of the two resistors is fixed at $V_{Resistor}$ = 10V. According to the results appearing in Figure 4.39 for K_D = 0 and K_P = 35:

- the higher the K_I parameter, the faster the temperature profile approaches the setpoint temperature of 40 ^oC,
- all three experiments appear to achieve the $T_{STP,Resistor}$,
- the temperature variation between the two thermocouples is reported at 0.25 ^oC,
- no overshoot appears to take place for any of the three experiments studied.

4.6.1.2 Second set of experiments at $T_{STP,Resistor} = 60^oC$.

The next set of experiments examines the behaviour of the system for $T_{STP,Resistor}$ = 60 ^oC and $T_{STP,Peltier}$ = 50 ^oC, while this time the peltier elements are activated.

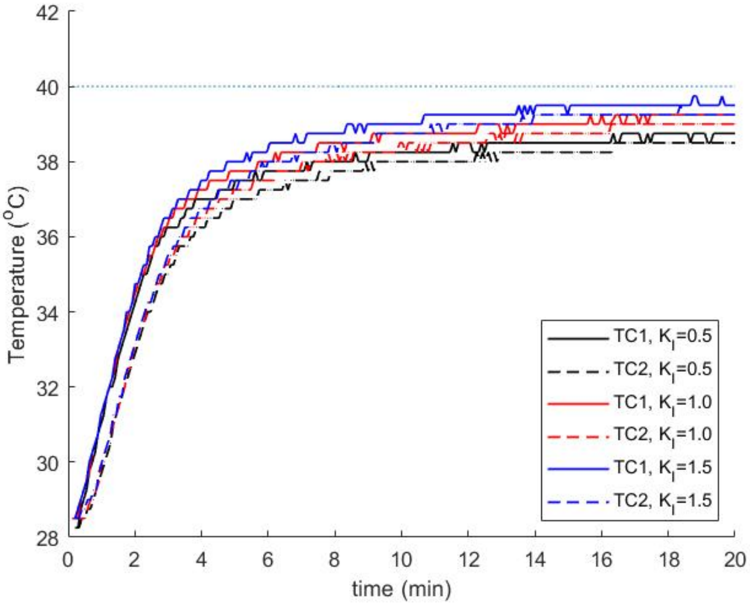

FIGURE 4.39: Investigation of the importance of K_I parameter in the temperature profiles and PID control for T_{STP}= 40 ^oC, $K_P = 35$, $K_D = 0$, $V_{Resistor} = 10V$ and $V_{Peltier} = 0V$.

Figure 4.40 presents the temperature profiles generated by the TC1 and TC2 thermocouples, when utilising varying K_P and K_I parameter values (with K_D = 0). The peltier cooling elements are this time turned on ($V_{Peltier} = 7V$) while the voltage of the resistors take the following values $V_{Resistor}$ = 10, 12, 15V. The experimental parameters are presented in Table 4.8. During this set of experiments, it is observed that:

- the temperature variation along the two thermocouples increases as the $V_{Resistor}$ increases (Experiments 1 and 4, Figure 4.40),
- increasing the value of the K_P (while keeping the same values of K_I and K_D) appears to not significantly reduce the steady-state error from the setpoint temperature (Experiments 1 and 2, Figure 4.40),
- increasing the value of the K_I parameter (while keeping the same values of K_D and K_D) appears to reduce the steady-state error from the setpoint temperature (Experiments 1 and 3, Figure 4.40),
- the experiments with $V_{Resistor}$ = 10, 12V (Experiments 1 - 4, Figure 4.40) appear to be power bound, since they fail to achieve the $T_{STP,Resistor}$ = 60 ^oC. More specifically, the power provided by the power supply to experiments 1-4 does not appear to be enough to heat the experimental rig to the appropriate temperature, while the peltier elements are never activated since the $T_{STP,Peltier}$ is never reached.

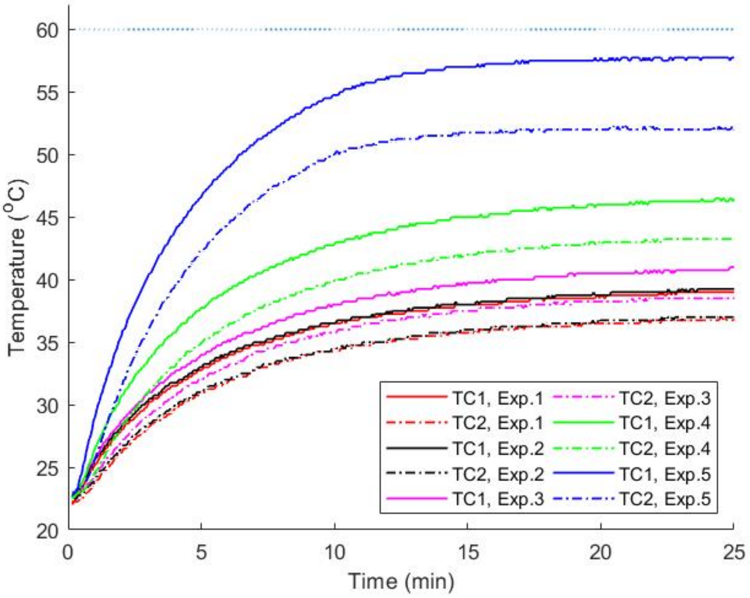

FIGURE 4.40: Investigation of the importance of $V_{Resistor}$ for different cases of K_P and K_I parameters. The details of the experiments are presented in Table 4.8.

TABLE 4.8: Parameters of the experiments appearing in Figure 4.40.

Experiment	TC	K_P	K_I	K_D	$V_{Resistor}$(V)	$V_{Peltier}$(V)	$\Delta T(^oC)$
1	1	30	1	0	10	-	2.25
	2	30	1	0	-	7	
2	1	50	1	0	10	-	2.25
	2	50	1	0	-	7	
3	1	30	1.2	0	10	-	2.25
	2	30	1.2	0	-	7	
4	1	30	1	0	12	-	3.00
	2	30	1	0	-	7	
5	1	30	1	0	15	-	5.75
	2	30	1	0	-	7	

According to the results appearing in Figure 4.40, the higher the K_I parameter, the faster the temperature profile approaches the setpoint temperature of 60 ^oC. Furthermore, increasing the value of K_P while maintaining the same value of K_I appears to only slightly improve the system's performance.

4.6.2 Main experiment and parameters' sensitivity for different experiments

After completing the experiments presented in Chapter 4.6.1, the values of K_P, K_I, K_D, $V_{peltier}$ and $V_{Resistor}$ are selected by trial and error in order to achieve the ΔT = 82-90 ^oC required to perform MCA (peltier elements are active). More specifically, the values presented in Table 4.9 for experiment 3 are selected in order to achieve

TABLE 4.9: Parameters of the experiments appearing in Figure 4.41 for $K_P = 30$, $K_I = 1.2$, $K_D = 0$, $V_{peltier}$ = 7 V and $V_{Resistor}$ = 21.5 V.

Experiment	TC	$T_{STP,Resistor} (^oC)$	$T_{STP,Peltier} (^oC)$	$\Delta T (^oC)$
1	1	95	-	9.50
	2	-	85	
2	1	80	-	10.75
	2	-	70	
3	1	90	-	9.00
	2	-	80	

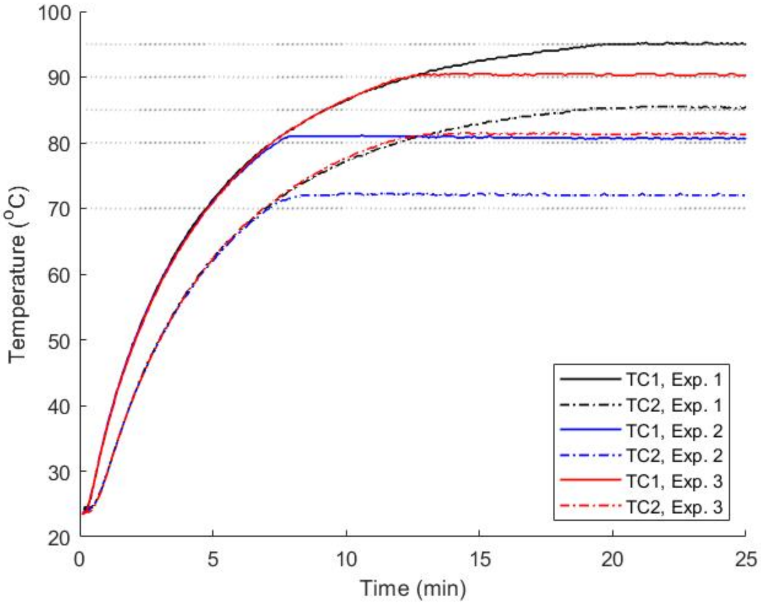

FIGURE 4.41: Temperature PID control using two heating elements (resistors) and two cooling elements (peltier) with $V_{Resistor}$ = 21.5 V, $V_{peltier}$ = 7 V, $K_P = 30, K_I = 1.2, K_D = 0$ and different $T_{STP,Resistor}$ and $T_{STP,Peltier}$.

the temperature variation of ΔT = 82-90 ^oC between the two thermocouples, TC1 and TC2.

Furthermore, experiments 1 and 2 appearing in Table 4.9 present the ability of this system's parameters (K_P, K_I, K_D, $V_{peltier}$ and $V_{Resistor}$) to be used for different $T_{STP,Resistor}$ (TC1) and $T_{STP,Peltier}$ (TC2) than the ones originally designed for (ΔT = 82-90 ^oC), demonstrating the ability of the setup to successfully achieve the other setpoints.

According to the results appearing in Figure 4.41, in case different temperature ranges are required, the adjustment of the PID parameters (K_P = 30, K_I = 1.2, K_D = 0) or the voltage settings of the peltier elements ($V_{peltier}$ = 7 V) and the resistors ($V_{Resistor}$ = 21.5 V) does not appear to be needed. More specifically, in this set of experiments, one can observe that the $V_{Resistor}$ provided in the system is enough to generate the power to achieve the required setpoint temperatures.

4.6.3 Data Reproducibility and Control of the System

This chapter presents the ability to control the system with the developed experimental setup. More specifically, Figure 4.42 presents the temperature profiles obtained through the two thermocouples during three different experiments performed using the same parameters ($T_{STP,Resistor}(TC1) = 90^oC$, $T_{STP,Peltier}(TC2) = 80^oC$, K_P = 30, K_I = 1.2, K_D = 0). The three experiments are performed at different times on different days, in order to test the ability of the system to perform under different environmental conditions. Figures 4.43 and 4.44 present the steady-state temperature measurements obtained from the two thermocouples for the three experiments presented in Figure 4.42. As a result of the data obtained from Figures 4.42-4.44, the developed setup appears to allow good temperature control of the system, without requiring further adjustment of the design parameters. The temperature measurements are subject to the accuracy of type Class 1, according to the Sterling Sensors specifications (SterlingSensors, 2021).

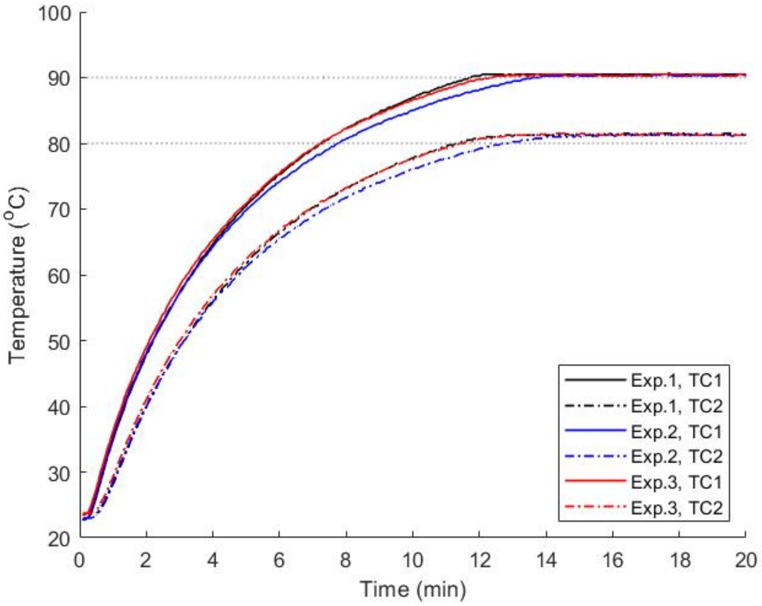

FIGURE 4.42: Reproducibility of the experiment $T_{STP,Resistor}$ $(TC1) = 90^oC$ and $T_{STP,Peltier}$ $(TC2) = 80^oC$ with three experiments. K_P, K_I and K_D are set at the values of 30, 1.2 and 0 respectively.

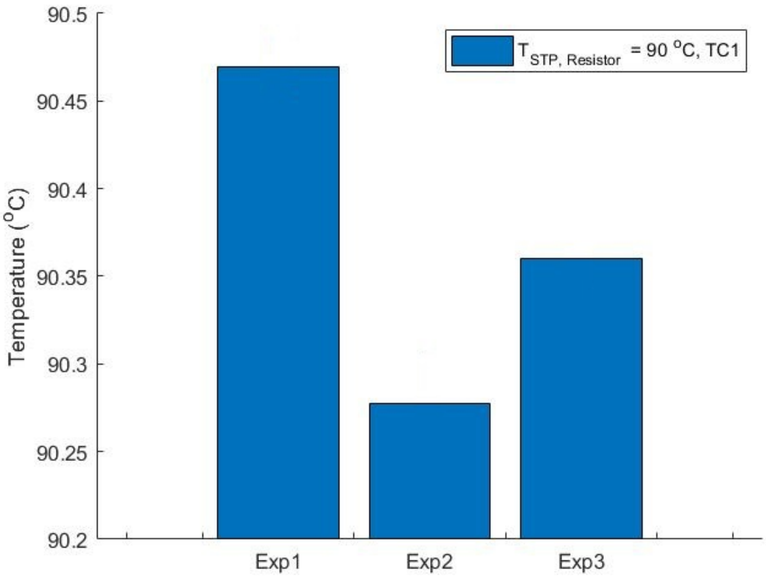

FIGURE 4.43: Steady-state temperature measurements obtained during the three experiments appearing in Figure 4.42 ($T_{STP,Resistor}(TC1) = 90^oC$).

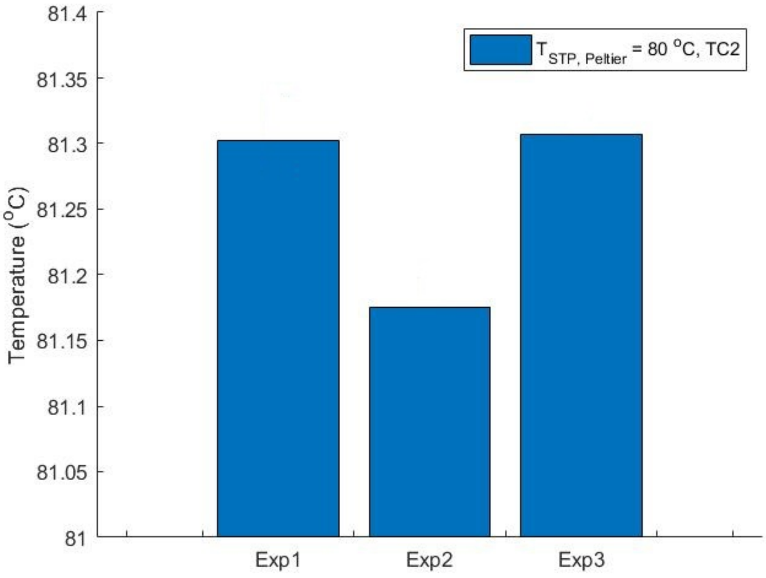

FIGURE 4.44: Steady-state temperature measurements obtained during the three experiments appearing in Figure 4.42 ($T_{STP,Peltier}(TC2) = 80^oC$).

4.6.4 Data Accuracy

In order to test the accuracy of the data obtained, the accuracy of the thermocouples is considered and tested. The manufacturing accuracy of the thermocouples used is Class 1, which accounts for $\mp 2^oC$. In order to test their accuracy further, data are obtained by measuring the temperature of boiling water (100^oC at $1atm$). The data obtained by the two thermocouples present mean values of 100.191 ^oC and 100.400 ^oC respectively, with standard deviations of 0.527 ^oC and 0.558 ^oC respectively (3 measurements per thermocouple), falling between the expected range.

4.7 Summary

The development of the experimental rig was completed using affordable materials, that can be easily replaced, making this rig suitable for the execution of multiple experiments. Monodisperse droplets were successfully generated using the QX100 ddPCR, and were found to be stable to be collected and introduced into the square glass capillary.

The PID temperature control has successfully been implemented in the developed experimental rig, generating successfully a temperature difference of 10 ^oC. The system's parameters (K_P, K_I, K_D, $V_{peltier}$ and $V_{Resistor}$) were also used/tested for different $T_{STP,Resistor}$ (TC1) and $T_{STP,Peltier}$ (TC2) than the ones originally designed for (ΔT = 82-90 ^oC), demonstrating the ability of the setup to successfully achieve stable temperature control at different setpoints.

4.8 Discussion & Future Work

As far as future work is concerned, the follow points need to be considered:

- The model developed using COMSOL ® 5.4 is made under the assumptions presented in Chapter 4.3.2.1.1. Depending on the final setup (under the microscope), the heat losses are expected to vary. As a result, the values of $h_{Nat.Conv.}$ and $h_{Forced.Conv.}$ might need to be modified. Furthermore, in that case, the values presented in Table 4.6 are expected to also change.

- The experimental system appeared to be power bound in some cases (see Experiments 1 - 4 in Chapter 4.6.1.2). This needs to be taken into account when attempting to perform the experiments under the microscope, since the voltage of the heating elements, $V_{Resistor}$, might need to be modified in order to provide enough power to the system.

- According to the simulations performed, the presence of the thermocouples does not appear to affect the temperature profiles at the centre of the microchannel. As a result, more thermocouples can be added equally spaced along the rig's centreline in order to obtain more data.

- Comparison of the temperature profiles obtained when densely-packed small droplets (droplet diameter to channel width ratio of 0.13) are introduced in the microchanels to single-phase flows are of particular interest. Other experimental runs with an increase in the spacing between consecutive droplets can also be performed and compared to the results obtained from single-phase flows. Simulations using COMSOL ® 5.4 including the droplets can be included in future work, in order to optimise/study the spacing between samples if needed.

- The optical setup used for the fluorescence measurements can be potentially updated/modified with a setup that includes an appropriate combination of filters and a camera, depending on the needs of the end user and the nature of the experiments.

4.8.1 Completion of the experimental idea

This chapter presents the main steps for the completion of this experimental idea. As part of this project, the design of the experimental rig has and is expected to be optimised using CFD, in order to: i) obtain a better understanding of the role that the presence (and potentially the concentration) of droplets plays in CHT phenomena in droplet-laden flows, ii) create a reusable, cheap and easy-to-fabricate device that can perform MCA. In order for these to be achieved, more steps need to take place (see Figure 4.45).

In terms of the following future steps:

- STEPS 4C and 5C (Figure 4.45):
  As illustrated in Figures 4.37 and 4.38, the droplets produced by QX100 ddPCR appear to be spaced quite densely, while the droplet diameter to channel width ratio is found to be approximately at ∼0.13. The study of heat transfer when densely packed droplets are introduced in a microfluidic channel is of interest. After this study is completed, the droplets need to be separated and then introduced individually into a stream of a surrounding fluid in order to record the T_m of every single droplet. This can be achieved using T-junction chips, such as the ones developed by Dolomite technology (dolomite, 2021). Figures 4.46 and 4.47 present examples of T-junction setups that result in increasing the spacing between the droplets, as they appear in the publications of Holtze et al. (2008) and Lee et al. (2014) respectively. Simulations using COMSOL ® 5.4 of the droplet-laden flow can be used to optimise the spacing between samples, depending on the effect that the droplet's presence has on the flow and heat transfer.

- STEPS 4E and 5E (Figure 4.45):
  After discussion with biologists and technicians from the Faculty of Biological Sciences, the Zeiss LSM880 + Airyscan Upright Confocal Microscope (Leeds, 2021) is considered to be suitable equipment to proceed with the fluorescence

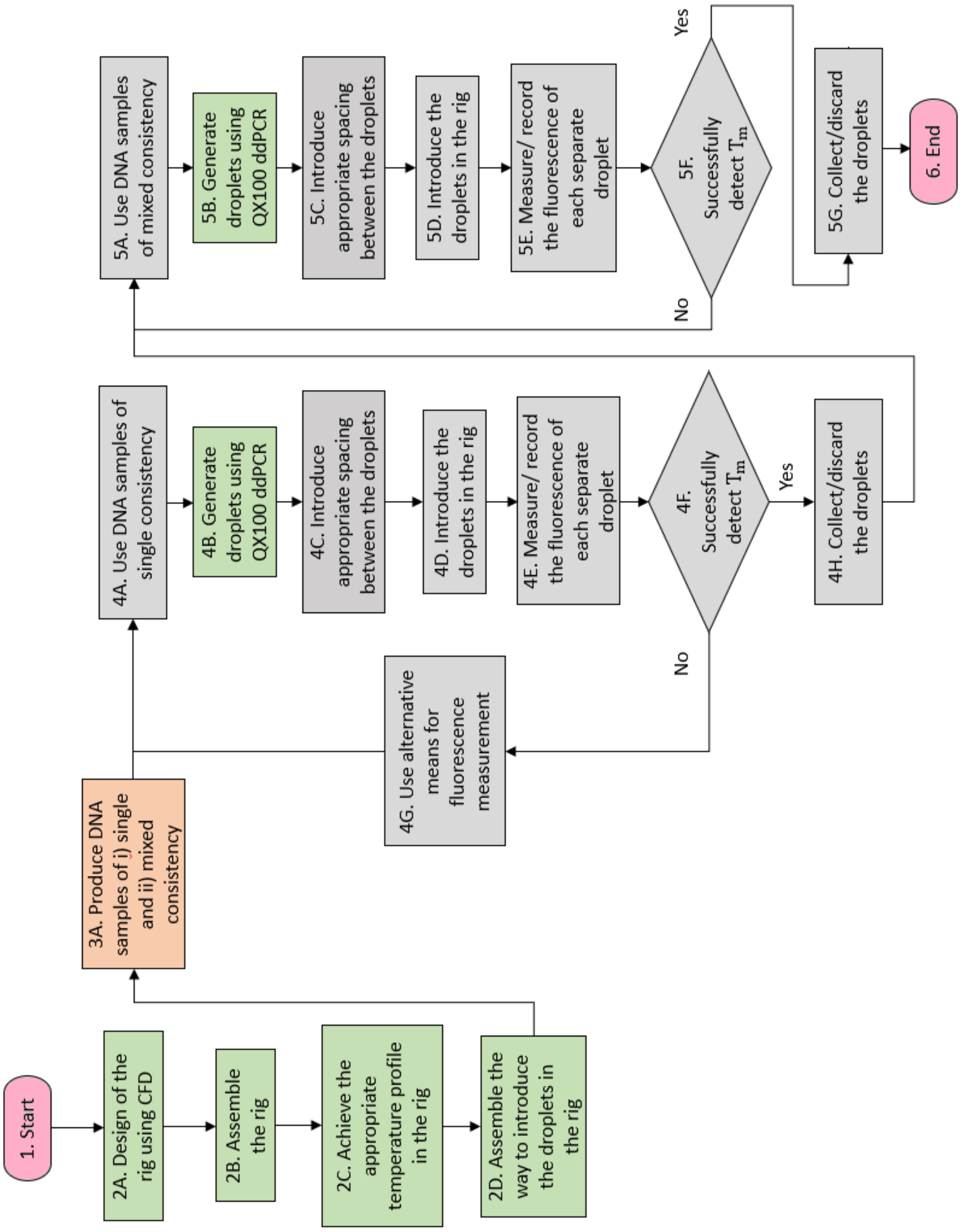

FIGURE 4.45: Flowchart of the experimental process. The elements in green and orange represent the parts of the experimental process that have already been completed and are performed by the biologists in collaboration respectively.

measurements required for MCA to take place. Due to the high temperatures that the experiments have to take place, the ability of this particular equipment to obtain measurements was confirmed. At this step, the tracking of every single droplet is important, to automate this process.

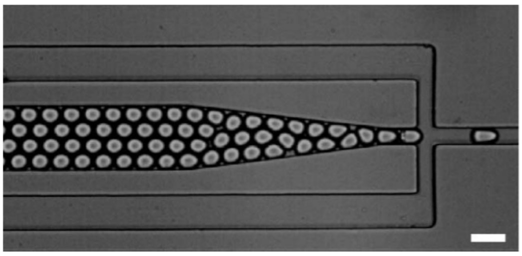

FIGURE 4.46: Technology used for increasing the spacing between the droplets (Figure obtained by Holtze et al., 2008).

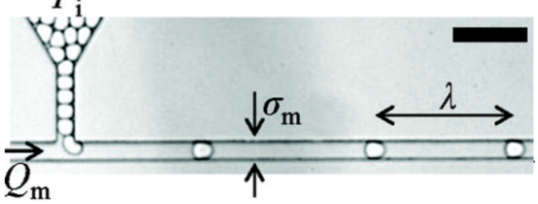

FIGURE 4.47: Setup used for increasing the spacing between the droplets (Figure obtained by Lee et al., 2014).

Chapter 5

Conclusions and Future Work

This thesis is concerned with precision thermal control in microfluidic systems used for Continuous Flow Polymerase Chain Reaction (CFPCR) and Melting Curve Analysis (MCA), while the same conclusions/techniques can be applied to a number of related application areas, such as heat sinks. Both single-phase and droplet-based microfluidic systems have been explored.

A Surrogate-enabled Optimisation methodology has been applied on a microfluidic CFPCR system found in literature (Papadopoulos et al., 2015). The main conclusions of this work include the following:

- the highest and smallest values of channel width and height respectively in this microfluidic CFPCR system are found to lead to the maximum increase of the output DNA concentration (Chapter 3.4.5),
- the optimum pressure drop is obtained for the highest values of channel width and height (Chapter 3.4.5),
- increasing the spacing between the heaters and the channel width is found to increase the DNA amplification (Chapters 3.4.6 and 3.4.7),
- designs with the lowest heater spacing and greatest channel width are found to minimise the pressure drop (Chapters 3.4.6 and 3.4.7),
- varying the spacing between the heaters appears to have a bigger impact on both objectives compared to varying the channel width between the heaters for the design variables' values considered, especially for the smaller values of heater spacing (Chapters 3.4.6 and 3.4.7),
- the effect of varying the channel width between the heaters appears to become more significant for the higher values of heater spacing in terms of both pressure drop and DNA amplification for the ranges of the design variables considered (Chapters 3.4.6 and 3.4.7). This is due to the fact that the higher values of heater spacing, the higher the amount of time the fluid spends in the device outside the temperature zones of interest, a residence time that is increased even further by higher values of channel width between the heaters.

- the longer the total residence time in the device and the smaller the channel width in the extension zone are found to lead to the highest DNA amplification (Chapter 3.4.8),
- the DNA amplification appears to be highly correlated with the time the sample spends in the extension zone (residence time in the extension zone) (Chapter 3.4.8),
- the output DNA concentration is found to be able to improve by up to 7.9% compared to the initial one, for the higher values of residence time (Chapter 3.4.8),
- the design with the smallest residence times in the device together with the largest channel width in the extension zone indicated that the pressure drop, total volume and total residence time can be improved by up to 80.5%, 43.2% and 17.8% respectively in a single PCR cycle compared to the initial one (Chapter 3.4.8).
- all of the above strongly indicate that there is significant room for improvement in terms of microfluidic CFPCR devices, allowing significant cost reduction and performance improvement.
- as part of all the studies presented in Chapters 3.4.5-3.4.8, both Neural Network and Polyharmonic Spline successfully generated the response surfaces for all optimisation studies considered. The results obtained with the two different methods present great similarities.
- as part of all the studies presented in Chapters 3.4.5-3.4.8, both genetic algorithm (*ga* MATLAB® function) and Multi-level Coordinate Search method (*e*05*jbc* of the NAG optimisation library in MATLAB®) successfully obtained the global optimum solutions with minor differences amongst each other.

Driven by the need to improve microfluidic systems in terms of temperature uniformity and pressure drop further, the use of diverging microchannels has also been explored. This study has been applied to heat sinks which present many similarities to CFPCR systems. The findings of this work include the following:

- increasing the diverging angle and the hydraulic diameter is found to reduce the temperature uniformity at the solid-fluid interface, while at the same time decreasing the pressure drop (Chapter 3.3.4.1).

  Hence, when developing/testing such channel geometries, developing the Pareto Front is expected to be beneficial in the designing process.
- when maintaining a constant volume of fluid in such channel geometries while varying the diverging angles (and at the same time adjusting the hydraulic diameter), the higher the diverging angles, the better the temperature uniformity and smaller pressure drop (Chapter 3.3.4.2).

- all three of the algorithms/methods presented in Chapters 3.3.4.1 - 3.3.4.2 (inverse multi-quadric, the multi-quadric and the Gaussian Radial Basis Functions (RBF)) successfully developed the response surfaces.

- as part of all these studies presented in Chapters 3.3.4.1 - 3.3.4.2, both genetic algorithm (*ga* MATLAB® function) and Particle Swarm Optimisation (PSO) method (*particleswarm* MATLAB® function) successfully managed to obtain the global optimum solutions.

In an effort to examine droplet-based PCR and droplet-laden flows in general, the study, design and optimisation of microfluidic systems continued in the field of biological research under a different application, this time focusing on improving the understanding of heat transfer in droplet-laden flows in microfluidic systems while at the same time performing MCA.

Several microfluidic setups have been developed that can facilitate this particular work but are often quite complicated or expensive to fabricate, not easy to use for multiple experiments and/or do not take place in real-time. These difficulties lead to the design and optimisation of an in-house experimental setup, combining both computational (COMSOL 5.4) and experimental work. Prior to the experimental work, computational work was conducted in order to simulate the single-phase flow that takes place in a microfluidic channel using COMSOL 5.4. Different designs and materials were tested as part of the optimisation of the experimental design, while the heating and cooling requirements of the device were estimated as part of simulating the final design. The results of these computational studies indicate:

- the ability to successfully generate linear temperature profiles at the centreline of a microfluidic channel, when two substrate materials are used.

- that the use of two material substrates enables better temperature control, allowing to benefit from the different thermal properties of the two materials.

  Placing the least heat-conductive material under the more conductive one (where the channel can be placed) ensures the development of a linear temperature profile at the centreline of a microfluidic channel. When the interface between the two substrates is inclined, control over the temperature gradient can be achieved; reducing the thickness of the most conductive material along the length of the rig is found to decrease the temperature gradient at the centreline of the microfluidic channel without affecting (significantly) the linearity of the temperature profile.

The latest results of this work present an experimental rig that:

- consists of affordable materials and is easy to assemble/disassemble in order to customise the device based on the requirements of each experiment.

- exhibits successful robust temperature PID control with the use of an Arduino, creating a stable temperature difference of 10^{o}C across the two ends of the device.
- can be used for different temperature ranges with the same PID parameters, indicating the robustness of the system and its applicability for different experiments.

  More specifically, the PID temperature control has successfully been tested and reproduced in two different temperature ranges using the same values of the PID parameters.
- can successfully load droplets generated using the $QX100ddPCR$ as part of an in-house experimental setup that can be easily replaced/adjusted if needed per experimental run. The droplets were stable during their collection and introduction in the microfluidic channel.

As far as future work is concerned, the next steps required to finalise the experimental droplet MCA device include:

- the increase in spacing between the produced droplets,
- the introduction of droplets containing DNA in the microfluidic channels,
- obtaining the fluorescence measurements using the Zeiss LSM880 + Airyscan Upright Confocal Microscope,
- recording and tracking the fluorescence measurements for every single droplet.

  The device is expected to assist researchers in performing MCA on a variety of applications, while at the same time utilising a cheap, easy-to-modify and -fix device, consisting of easily replaceable parts. At the same time, the device will enable the study of fluid flow and heat transfer of droplet-laden flows, comparing it with simulations of both single- and multiphase flow.
- obtaining experimentally and comparing the temperature profiles of droplet-laden flows of different droplet packing
- comparing the obtained temperature profiles with the ones of single-phase flows (experimental and numerical results)

  As a result of the above, the effect of the droplet distribution/spacing on the heat transfer can be studied.

When it comes to the multi-objective optimisation of the microfluidic CFPCR device, the next steps would be to:

- further investigate the effect of temperature uniformity on DNA amplification.

  This can be achieved by incorporating the Joule Heating model in the computational model, using an optimisation setting of COMSOL Multiphysics.

- experimentally validate the outcome of the computational work, by building a microfluidic chip with the appropriate geometry depending on the objective(s) where the focus of the engineers/scientists lies.

  The geometrical characteristics of the microfluidic chips can be chosen from the designs obtained from the Pareto Front.

- apply the same multi-objective surrogate-enabled optimisation methodology in microfluidic CFPCR chips where fins or other geometries are present, in order to promote temperature uniformity and mixing.

Appendix A

Important Figures

A.1 Neural Networks

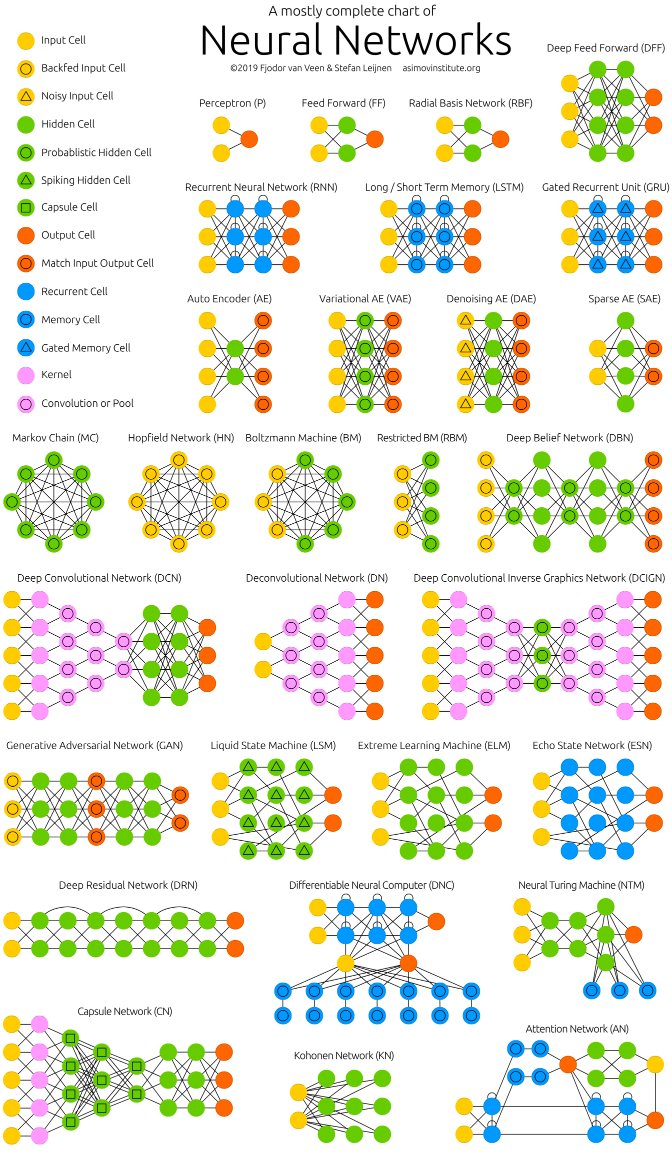

FIGURE A.1: Types of NN (Leijnen and Veen, 2020).

Appendix B

DoE Points and Values of Objective Functions

B.1 DoE points of the optimisation problem in Chapter 3.3.4.1

TABLE B.1: DoE Points in Chapter 3.3.4.1

No	X1 ($\theta(^\circ)$)	X2 ($W_i(\mu m)$)	Obj_1	Obj_2
1	2.00	210.0	0.961613715	102675.06410
2	10.00	210.0	3.16488015	55373.45173
3	2.00	330.0	1.226983747	74055.68711
4	10.00	330.0	2.992417345	42119.73038
5	2.00	262.8	1.067233549	86997.36304
6	2.32	234.0	1.144939044	89356.85703
7	2.64	286.8	1.385267983	74605.07431
8	2.96	310.8	1.573935051	67953.53740
9	3.28	253.2	1.653857948	73810.96995
10	3.60	219.6	1.726970662	79205.53111
11	3.92	272.4	1.964176475	66103.99042
12	4.24	325.2	2.158338243	57448.37075
13	4.56	301.2	2.233792795	59596.31721
14	4.88	238.8	2.316428291	66652.36749
15	5.20	214.8	2.417498792	70937.31089
16	5.52	320.4	2.594655704	53029.15083
17	5.84	282.0	2.68359436	56604.49682
18	6.16	258.0	2.77625105	59346.65967
19	6.48	229.2	2.832989356	61463.47502
20	6.80	306.0	2.896130954	51184.49291
21	7.12	277.2	2.960690772	52666.6838
22	7.44	210.0	3.033677712	62587.6733
23	7.76	330.0	3.038638075	45695.90697
24	8.08	248.4	3.074183939	54220.98140
25	8.40	291.6	3.074051116	48658.78570
26	8.72	224.4	3.154937644	56765.60042
27	9.04	315.6	3.054397849	45540.42154
28	9.36	267.6	3.097478322	49166.53560
29	9.68	243.6	3.114017902	51834.20074
30	10.00	296.4	3.010923718	45838.28162

B.2 DoE points of the optimisation problem in Chapter 3.3.4.2

TABLE B.2: DoE Points in Chapter 3.3.4.2

No	X1 ($\theta(^\circ)$)	X2 ($\theta(^\circ)$)	Obj_1	Obj_2
1	0.653061224	0.081632653	5.374500E-01	11874.54
2	0.755102041	0.714285714	4.490200E-01	12898.00
3	0.326530612	0.408163265	5.410300E-01	11852.20
4	0.469387755	0.959183673	4.577700E-01	12926.20
5	0.510204082	0.12244898	5.529400E-01	11774.40
6	0.918367347	0.020408163	5.069100E-01	12116.70
7	0.714285714	1.000000000	4.265100E-01	13465.46
8	0.183673469	0.857142857	5.059900E-01	12289.00
9	0.795918367	0.510204082	4.633200E-01	12602.70
10	0.265306122	0.93877551	4.850000E-01	12542.20
11	0.591836735	0.673469388	4.729600E-01	12586.00
12	0.020408163	0.571428571	5.684500E-01	11782.20
13	0.367346939	0.632653061	5.054600E-01	12174.00
14	0.530612245	0.816326531	4.649580E-01	12759.00
15	0.12244898	0.612244898	5.459424E-01	11894.50
16	0.693877551	0.591836735	4.675100E-01	12602.70
17	0.551020408	0.428571429	5.058790E-01	12125.40
18	0.632653061	0.326530612	5.069400E-01	12125.00
19	0.87755102	0.306122449	4.768010E-01	12376.00
20	0.775510204	0.040816327	5.245900E-01	11986.60
21	0.408163265	0.775510204	4.844000E-01	12468.00
22	0.244897959	0.551020408	5.356900E-01	11928.50
23	0.06122449	0.000000000	6.551200E-01	11512.50
24	0.224489796	0.755102041	5.115400E-01	12184.00
25	0.571428571	0.244897959	5.262400E-01	11940.00
26	0.734693878	0.265306122	5.005000E-01	12182.00
27	0.673469388	0.795918367	4.503200E-01	12950.20
28	0.816326531	0.836734694	4.318600E-01	13110.30
29	0.346938776	0.87755102	4.803600E-01	12567.00
30	0.306122449	0.06122449	5.952200E-01	11594.00
31	0.000000000	0.387755102	5.998900E-01	11622.70
32	0.387755102	0.102040816	5.752900E-01	11657.40
33	0.163265306	0.489795918	5.552400E-01	11787.00
34	0.428571429	0.469387755	5.170400E-01	12033.00
35	0.836734694	0.142857143	5.027400E-01	12165.00
36	0.142857143	0.346938776	5.805700E-01	11665.00
37	0.448979592	0.285714286	5.387200E-01	11858.00
38	1.000000000	0.367346939	4.565500E-01	12325.60
39	0.285714286	0.224489796	5.741500E-01	11659.50
40	0.93877551	0.448979592	4.563300E-01	12496.00
41	0.897959184	0.693877551	4.388100E-01	12769.00
42	0.959183673	0.183673469	4.821800E-01	12254.00
43	0.081632653	0.204081633	6.132400E-01	11558.00

Table B.2. (continued)

No	X1 ($\theta(^\circ)$)	X2 ($W_i(\mu m)$)	Obj_1	Obj_2
44	0.979591837	0.918367347	4.163700E-01	11028.40
45	0.857142857	0.979591837	4.172900E-01	13041.40
46	0.040816327	0.897959184	5.222630E-01	12211.00
47	0.102040816	0.734693878	5.324500E-01	12041.00
48	0.204081633	0.163265306	5.981200E-01	11581.30
49	0.612244898	0.530612245	4.864500E-01	12375.50
50	0.489795918	0.653061224	4.877500E-01	12376.00
51	0.000000000	0.000000000	6.682800E-01	11523.40
52	0.000000000	1.000000000	5.183800E-01	123230
53	1.000000000	0.000000000	4.992500E-01	12124.70
54	1.000000000	1.000000000	4.136300E-01	8716.00

B.3 DoE Points for the 2-design variable optimisation problem presented in Chapter 3.4.5.

TABLE B.3: DoE Points for the 2-design variable optimisation problem presented in Chapter 3.4.5.

No	W_2 (μm)	H_{Fluid} (μm)	$log_2\frac{[DNA]}{[DNA]_o}$ ($-$)	ΔP (Pa)	$T.U._{den}$ (%)	$T.U._{ext}$ (%)	$T.U._{ann}$ (%)
1	100.0	50.0	0.68610	1325.60	94.89	97.51	99.98
2	100.0	80.0	0.66773	272.62	90.44	95.79	100.00
3	400.0	80.0	0.68672	13.74	69.5	88.48	100.00
4	400.0	50.0	0.70438	74.72	84.09	93.86	100.00
5	100.0	60.8	0.68095	670.57	93.47	96.91	100.00
6	196.0	76.0	0.68345	66.10	84.82	93.61	100.00
7	376.0	79.2	0.68786	15.93	71.56	89.36	100.00
8	352.0	53.6	0.70148	73.47	84.53	93.85	100.00
9	276.0	55.6	0.69836	102.35	86.8	94.49	100.00
10	200.0	56.8	0.69324	180.08	89.52	95.45	100.00
11	296.0	68.8	0.69272	41.18	81.38	92.46	100.00
12	184.0	65.2	0.68715	130.31	88.25	94.97	100.00
13	400.0	52.8	0.70323	61.21	82.86	93.42	100.00
14	248.0	51.2	0.69971	171.30	89.18	95.35	100.00
15	300.0	61.2	0.69632	61.29	83.98	93.48	100.00
16	384.0	74.8	0.69060	18.76	73.44	89.98	100.00
17	160.0	64.4	0.68555	183.35	89.65	95.44	100.00
18	344.0	72.8	0.69150	25.32	76.95	91.08	100.00
19	132.0	64.0	0.68210	288.46	91.14	96.05	100.00
20	236.0	72.0	0.68827	54.62	83.61	93.16	100.00
21	144.0	55.2	0.69037	403.09	92.29	96.48	100.00
22	188.0	79.6	0.68094	61.41	84.33	93.45	100.00
23	336.0	57.2	0.69976	63.17	83.77	93.54	100.00
24	136.0	78.8	0.67513	131.93	88.1	94.87	100.00
25	396.0	64.8	0.69684	29.63	77.48	91.39	100.00
26	152.0	76.4	0.67933	113.00	87.46	94.63	100.00
27	168.0	77.6	0.68015	85.75	86.18	94.10	100.00
28	316.0	59.2	0.69782	62.69	83.79	93.50	100.00
29	124.0	62.0	0.68180	371.86	91.98	96.34	100.00
30	148.0	52.4	0.69227	458.91	92.65	96.59	100.00
31	208.0	50.4	0.69858	258.37	90.69	95.92	100.00
32	140.0	60.4	0.68477	309.84	91.38	96.15	100.00
33	380.0	66.0	0.69595	29.92	77.97	91.53	100.00
34	108.0	51.6	0.68761	992.03	94.34	97.26	100.00
35	224.0	56.0	0.69476	150.65	88.80	95.15	100.00
36	176.0	73.2	0.68277	95.00	86.85	94.34	100.00
37	340.0	69.6	0.69304	30.39	78.53	91.62	100.00
38	308.0	54.4	0.69994	89.71	85.86	94.29	100.00
39	348.0	58.8	0.69899	53.55	82.66	93.15	100.00
40	280.0	77.2	0.68823	30.40	79.22	91.62	100.00

Table B.3. (continued)

No	W_2 (μm)	H_{Fluid} (μm)	$log_2\frac{[DNA]}{[DNA]_o}$ $(-)$	ΔP (Pa)	$T.U._{den}$ (%)	$T.U._{ext}$ (%)	$T.U._{ann}$ (%)
41	156.0	67.6	0.68347	163.13	89.13	95.28	100.00
42	292.0	74.4	0.68970	31.94	79.53	91.71	100.00
43	164.0	71.6	0.68260	119.62	87.89	94.76	100.00
44	128.0	76.8	0.67454	166.24	89.01	95.21	100.00
45	232.0	62.8	0.69212	92.47	86.49	94.32	100.00
46	244.0	68.0	0.69065	62.74	84.41	93.47	100.00
47	180.0	53.2	0.69392	284.82	91.21	96.08	100.00
48	264.0	60.0	0.69597	84.40	86.01	94.18	100.00
49	204.0	54.0	0.69714	208.22	89.98	95.63	100.00
50	368.0	73.6	0.69120	21.48	74.85	90.45	100.00
51	328.0	74.0	0.69066	26.11	77.32	91.13	100.00
52	260.0	71.2	0.68968	46.86	82.52	92.82	100.00
53	320.0	70.0	0.69281	33.37	79.40	91.91	100.00
54	104.0	75.6	0.67071	295.14	90.84	95.93	100.00
55	388.0	61.6	0.69831	36.94	79.59	92.11	100.00
56	192.0	70.8	0.68537	88.62	86.50	94.23	100.00
57	228.0	59.6	0.69352	115.76	87.62	94.75	100.00
58	324.0	50.0	0.70437	111.01	86.74	94.68	100.00
59	256.0	63.6	0.69326	72.65	85.2	93.83	100.00
60	284.0	72.4	0.69067	37.16	80.74	92.15	100.00
61	120.0	58.0	0.68636	507.14	92.73	96.70	100.00
62	332.0	78.4	0.68831	20.79	75.19	90.34	100.00
63	356.0	67.2	0.69460	31.63	78.84	91.72	100.00
64	220.0	68.4	0.68890	75.61	85.47	93.90	100.00
65	216.0	65.6	0.68965	91.23	86.51	94.27	100.00
66	304.0	50.8	0.70304	117.98	87.29	94.79	100.00
67	212.0	78.0	0.68406	51.19	83.12	92.95	100.00
68	288.0	58.4	0.69774	78.67	85.45	93.99	100.00
69	268.0	75.2	0.68842	36.36	80.68	92.11	100.00
70	240.0	57.6	0.69542	118.31	87.72	94.75	100.00
71	364.0	52.0	0.70257	77.11	84.71	93.91	100.00
72	116.0	66.4	0.67736	343.05	91.58	96.24	100.00
73	392.0	70.4	0.69325	22.42	75.06	90.57	100.00
74	252.0	54.8	0.69717	128.99	88.02	94.93	100.00
75	112.0	69.2	0.67619	328.30	91.41	96.16	100.00
76	172.0	62.4	0.68852	175.88	89.50	95.42	100.00
77	312.0	80.0	0.68736	21.78	75.72	90.52	100.00
78	272.0	66.8	0.69275	53.99	83.41	93.13	100.00
79	360.0	56.4	0.70067	58.49	83.09	93.35	100.00
80	372.0	63.2	0.69713	36.38	79.76	92.11	100.00

B.4 DoE Points for 2-design variable optimisation problem presented in Chapter 3.4.6.

TABLE B.4: DoE Points for 2-design variable optimisation problem presented in Chapter 3.4.6.

No	L_5 (μm)	L_7 (μm)	$log_2 \frac{[DNA]}{[DNA]_o}$ ($-$)	ΔP (Pa)	$T.U._{den}$ (%)	$T.U._{ext}$ (%)	$T.U._{ann}$ (%)
1	500.0	500.0	0.68640	260.25	88.82	95.15	97.18
2	500.0	2500.0	0.70831	288.15	89.07	95.88	97.20
3	2500.0	2500.0	0.71153	325.29	89.03	95.99	100.00
4	2500.0	500.0	0.68952	295.00	88.87	95.24	100.00
5	500.0	1220.0	0.69749	269.54	89.22	96.03	97.19
6	1140.0	2233.3	0.70917	294.57	89.11	96.68	98.68
7	2340.0	2446.7	0.71272	321.39	89.06	96.08	100.00
8	2180.0	740.0	0.69248	291.97	89.14	95.55	100.00
9	1673.3	873.3	0.69531	284.60	89.17	95.80	100.00
10	1166.7	953.3	0.69552	276.89	89.18	95.91	98.76
11	1806.7	1753.3	0.70705	298.92	89.21	96.83	100.00
12	1060.0	1513.3	0.70334	282.71	89.22	96.81	98.48
13	2500.0	686.7	0.69314	297.38	89.11	95.44	100.00
14	1486.7	580.0	0.69051	277.55	88.94	95.46	99.77
15	1833.3	1246.7	0.70124	292.41	89.26	96.28	100.00
16	2393.3	2153.3	0.70991	317.54	89.07	96.73	100.00
17	900.0	1460.0	0.70223	279.24	89.20	96.69	98.07
18	2126.7	2020.0	0.70848	309.22	89.16	96.77	100.00
19	713.3	1433.3	0.70096	275.95	89.16	96.58	97.63
20	1406.7	1966.7	0.70710	295.08	89.07	96.84	99.50
21	793.3	846.7	0.69234	269.42	89.12	95.75	97.82
22	1086.7	2473.3	0.71002	297.41	89.07	96.18	98.54
23	2073.3	980.0	0.69693	293.18	89.21	95.86	100.00
24	740.0	2420.0	0.70917	290.83	89.04	96.18	97.70
25	2473.3	1486.7	0.70450	307.49	89.17	96.62	100.00
26	846.7	2260.0	0.70765	290.04	89.06	96.59	97.97
27	953.3	2340.0	0.70894	293.05	89.09	96.43	98.21
28	1940.0	1113.3	0.69885	292.46	89.25	96.04	100.00
29	660.0	1300.0	0.69890	273.22	89.20	96.27	97.52
30	820.0	660.0	0.69032	267.42	89.03	95.51	97.88
31	1220.0	526.7	0.68870	272.39	88.93	95.43	98.93
32	766.7	1193.3	0.69911	273.52	89.18	96.17	97.75
33	2366.7	1566.7	0.70534	306.64	89.15	96.71	100.00
34	553.3	606.7	0.68848	262.55	89.00	95.31	97.30
35	1326.7	900.0	0.69508	278.89	89.19	95.84	99.25
36	1006.7	2046.7	0.70813	289.60	89.11	96.84	98.34
37	2100.0	1806.7	0.70738	305.18	89.18	96.79	100.00
38	1886.7	793.3	0.69359	287.26	89.14	95.67	100.00
39	2153.3	1086.7	0.69890	296.06	89.23	96.01	100.00
40	1700.0	2313.3	0.71031	306.24	89.05	96.47	100.00
41	873.3	1673.3	0.70488	281.92	89.13	96.82	98.01

Table B.4. (continued)

No	L_5 (μm)	L_7 (μm)	$log_2\frac{[DNA]}{[DNA]_o}$ ($-$)	ΔP (Pa)	$T.U._{den}$ (%)	$T.U._{ext}$ (%)	$T.U._{ann}$ (%)
42	1780.0	2126.7	0.70913	303.98	89.05	96.83	100.00
43	926.7	1940.0	0.70741	286.70	89.14	96.84	98.14
44	686.7	2286.7	0.70821	287.84	89.12	96.46	97.59
45	1380.0	1353.3	0.70217	285.84	89.19	96.53	99.41
46	1460.0	1700.0	0.70631	292.15	89.17	96.86	99.68
47	1033.3	713.3	0.69113	271.68	89.08	95.62	98.40
48	1593.3	1166.7	0.69872	287.16	89.18	96.20	100.00
49	1193.3	766.7	0.69242	274.89	89.11	95.70	98.83
50	2286.7	2073.3	0.70872	314.17	89.04	96.75	100.00
51	2020.0	2100.0	0.70895	308.70	89.10	96.81	100.00
52	1566.7	1913.3	0.70736	297.01	89.18	96.86	100.00
53	1966.7	1833.3	0.70872	303.00	89.15	96.79	100.00
54	526.7	2206.7	0.70699	284.10	89.15	96.56	97.25
55	2420.0	1273.3	0.70278	303.57	89.23	96.24	100.00
56	1113.3	1886.7	0.70735	288.98	89.18	96.85	98.63
57	1353.3	1140.0	0.69846	282.53	89.25	96.16	99.33
58	1993.3	500.0	0.68973	285.71	88.85	95.34	100.00
59	1540.0	1406.7	0.70327	289.39	89.20	96.60	99.94
60	1726.7	1993.3	0.70778	301.11	89.08	96.82	100.00
61	633.3	1033.3	0.69490	269.27	89.16	95.86	97.46
62	2046.7	2393.3	0.71026	314.88	89.00	96.25	100.00
63	2206.7	1646.7	0.70606	304.94	89.24	96.75	100.00
64	1300.0	1726.7	0.70613	289.68	89.16	96.87	99.16
65	1273.3	1540.0	0.70390	286.61	89.18	96.84	99.08
66	1860.0	553.3	0.69018	283.96	88.93	95.39	100.00
67	1246.7	2366.7	0.70936	298.34	89.09	96.39	99.01
68	1753.3	1060.0	0.69758	288.42	89.18	96.02	100.00
69	1620.0	2180.0	0.70874	301.97	89.10	96.82	100.00
70	1433.3	1006.7	0.69796	282.10	89.24	95.97	99.59
71	2260.0	633.3	0.69061	292.12	89.07	95.43	100.00
72	606.7	1593.3	0.70221	276.46	89.22	96.70	97.42
73	2446.7	1860.0	0.70766	313.74	89.12	96.70	100.00
74	1513.3	820.0	0.69420	281.18	89.17	95.74	99.86
75	580.0	1780.0	0.70447	278.72	89.18	96.69	97.38
76	980.0	1326.7	0.70071	278.79	89.25	96.45	98.25
77	1913.3	2500.0	0.71061	314.02	89.04	96.07	100.00
78	1646.7	1620.0	0.70497	294.13	89.25	96.85	100.00
79	2233.3	926.7	0.69599	295.43	89.21	95.74	100.00
80	2313.3	1380.0	0.70283	303.02	89.26	96.46	100.00

B.5 DoE Points for 2-design variable optimisation problem presented in Chapter 3.4.7.

TABLE B.5: DoE Points for 2-design variable optimisation problem presented in Chapter 3.4.7.

No	W_{gap} (μm)	L_{gap} (μm)	$log_2 \frac{[DNA]}{[DNA]_o}$ ($-$)	ΔP (Pa)	$T.U._{den}$ (%)	$T.U._{ext}$ (%)	$T.U._{ann}$ (%)
1	100	500	0.68462	279.24	90.229	95.051	97.067
2	100	2500	0.69831	435.54	90.356	96.041	100
3	200	2500	0.71079	324.96	90.623	96.019	100
4	200	500	0.68364	260.12	90.526	95.105	97.183
5	100	1220	0.69212	331.33	90.94	96.119	98.704
6	132	2233.33	0.70269	360.45	90.302	96.675	100
7	192	2446.67	0.71079	326.58	89.905	95.97	100
8	184	740	0.68947	269.39	90.207	95.466	97.576
9	158.67	873.33	0.69277	278.76	90.481	95.668	97.88
10	133.33	953.33	0.69115	290.65	90.723	95.76	98.045
11	165.33	1753.33	0.70314	311	90.459	96.824	100
12	128	1513.33	0.69908	322.6	90.665	96.671	99.673
13	200	686.67	0.68886	265.27	90.836	95.464	97.583
14	149.33	580	0.68592	269.73	90.308	95.223	97.256
15	166.67	1246.67	0.69804	290.75	90.625	96.215	98.863
16	194.67	2153.33	0.70744	316.59	90.803	96.835	100
17	120	1460	0.69659	325.99	90.767	96.526	99.474
18	181.33	2020	0.70766	314.5	90.274	96.782	100
19	110.67	1433.33	0.69575	334.17	90.79	96.475	99.357
20	145.33	1966.67	0.70377	332.98	90.504	96.773	100
21	114.67	846.67	0.68901	293.53	90.785	95.619	97.787
22	129.33	2473.33	0.70381	377.71	90.225	96.023	100
23	178.67	980	0.69374	277.92	90.491	95.817	98.13
24	112	2420	0.70129	400.77	90.388	96.213	100
25	126.67	713.33	0.68834	281.17	90.595	95.431	97.526
26	117.33	2260	0.70007	380.59	90.393	96.633	100
27	122.67	2340	0.70257	378.44	90.48	96.378	100
28	172	1113.33	0.69564	284.05	90.531	96.011	98.486
29	108	1300	0.69543	327.04	90.834	96.249	98.93
30	116	660	0.68761	282.36	90.53	95.349	97.395
31	136	526.67	0.68622	269.29	90.211	95.117	97.12
32	113.33	1193.33	0.69321	316.03	90.8	96.09	98.633
33	193.33	1566.67	0.70226	297.12	90.897	96.916	99.93
34	102.67	606.67	0.68477	287.89	91.256	95.411	97.348
35	141.33	900	0.69129	284.94	90.592	95.694	97.952
36	125.33	2046.67	0.70233	355.66	90.703	96.781	100
37	180	1806.67	0.70634	307.4	90.329	96.795	100
38	169.33	793.33	0.68961	273.7	90.47	95.558	97.695
39	182.67	1086.67	0.69596	281.12	90.438	95.99	98.425
40	160	2313.33	0.70611	339.47	90.217	96.373	100
41	118.67	1673.33	0.69936	340.03	90.685	96.819	100

Table B.5. (continued)

No	W_{gap} (μm)	L_{gap} (μm)	$log_2 \frac{[DNA]}{[DNA]_o}$ ($-$)	ΔP (Pa)	$T.U._{den}$ (%)	$T.U._{ext}$ (%)	$T.U._{ann}$ (%)
42	164	2126.67	0.70573	328.01	90.291	96.743	100
43	121.33	1940	0.70051	353.78	90.627	96.797	100
44	109.33	2286.67	0.69956	395.77	90.464	96.59	100
45	144	1353.33	0.69792	304.75	90.706	96.374	99.16
46	148	1700	0.70233	318.4	90.546	96.828	100
47	126.67	713.33	0.68834	281.17	90.595	95.431	97.526
48	154.67	1166.67	0.69727	292.05	90.647	96.077	98.619
49	134.67	766.67	0.68901	280.68	90.561	95.511	97.631
50	189.33	2073.33	0.70838	314.11	90.153	96.747	100
51	176	2100	0.70545	322.93	91.069	96.901	100
52	153.33	1913.33	0.70396	325.32	90.499	96.784	100
53	173.33	1833.33	0.70571	311.02	90.381	96.814	100
54	101.33	2206.67	0.6964	409.66	91.286	96.747	100
55	196	1273.33	0.69793	286.89	91.075	96.363	98.954
56	130.67	1886.67	0.70046	340.61	90.53	96.793	100
57	142.67	1140	0.69558	295.08	90.735	96.042	98.532
58	174.67	500	0.68451	262.59	89.945	95.056	97.063
59	152	1406.67	0.70039	302.92	90.605	96.488	99.345
60	161.33	1993.33	0.70442	322.94	90.387	96.778	100
61	106.67	1033.33	0.69273	310.71	90.821	95.863	98.227
62	177.33	2393.33	0.70938	332.21	90.163	96.15	100
63	185.33	1646.67	0.70537	299.04	90.393	96.819	100
64	140	1726.67	0.7022	324.98	90.654	96.812	100
65	138.67	1540	0.6993	316.56	90.657	96.71	99.782
66	168	553.33	0.68459	265.06	90.084	95.184	97.162
67	137.33	2366.67	0.7034	362.2	90.279	96.296	100
68	162.67	1060	0.69458	284.8	90.524	95.939	98.329
69	156	2180	0.70558	335.57	90.435	96.763	100
70	146.67	1006.67	0.69313	288.38	90.681	95.863	98.2
71	188	633.33	0.68703	265.54	90.109	95.283	97.331
72	105.33	1593.33	0.69594	351.51	90.751	96.75	99.86
73	106.67	1033.33	0.69273	310.71	90.821	95.863	98.227
74	150.67	820	0.69042	278.85	90.583	95.596	97.771
75	104	1780	0.69577	367.61	90.679	96.793	100
76	124	1326.67	0.69573	315.73	90.813	96.316	99.047
77	170.67	2500	0.7079	339.98	90.062	95.921	100
78	157.33	1620	0.70204	309.11	90.621	96.834	99.997
79	186.67	926.67	0.69315	274.91	90.439	95.742	98.004
80	190.67	1380	0.70202	288.25	90.41	96.462	99.321

B.6 DoE Points for optimisation problem presented in Chapter 3.4.8.

TABLE B.6: DoE Points for optimisation problem presented in Chapter 3.4.8.

No	$t_{R,den}$	$t_{R,ext}$	$t_{R,ann}$	z_{w3}	$log_2(-)$	$\Delta P(-)$	$t_{R,tot}$(-)	$V_{s,tot}$(-)
1	0.0000	0.0000	0.0000	0.0000	0.8894	0.3287	0.1506	0.2935
2	0.0000	0.0000	0.0000	1.0000	1.0000	0.0000	0.0000	0.0000
3	0.0000	0.0000	1.0000	0.0000	0.8541	0.5363	0.3630	0.4701
4	0.0000	0.0000	1.0000	1.0000	0.9782	0.2082	0.2124	0.1766
5	0.0000	1.0000	0.0000	0.0000	0.0194	0.6623	0.5753	0.6468
6	0.0000	1.0000	0.0000	1.0000	0.1183	0.1214	0.3186	0.1668
7	0.0000	1.0000	1.0000	0.0000	0.0004	0.8726	0.7877	0.8234
8	0.0000	1.0000	1.0000	1.0000	0.0956	0.3295	0.5309	0.3434
9	1.0000	0.0000	0.0000	0.0000	0.8766	0.4513	0.3630	0.4701
10	1.0000	0.0000	0.0000	1.0000	0.9993	0.1233	0.2124	0.1766
11	1.0000	0.0000	1.0000	0.0000	0.8633	0.6655	0.5753	0.6468
12	1.0000	0.0000	1.0000	1.0000	0.9658	0.3314	0.4247	0.3532
13	1.0000	1.0000	0.0000	0.0000	0.0190	0.7869	0.7877	0.8234
14	1.0000	1.0000	0.0000	1.0000	0.1141	0.2445	0.5309	0.3434
15	1.0000	1.0000	1.0000	0.0000	0.0000	1.0000	1.0000	1.0000
16	1.0000	1.0000	1.0000	1.0000	0.1030	0.4553	0.7432	0.5200
17	0.8741	0.3706	0.1399	0.2378	0.4546	0.4094	0.4480	0.4644
18	0.4895	0.2308	0.9860	0.9301	0.6458	0.3043	0.3927	0.3113
19	0.1259	0.5315	0.5524	0.6434	0.3441	0.2734	0.3561	0.2939
20	0.6224	0.9301	0.1189	0.2797	0.0875	0.4832	0.5916	0.5491
21	0.9580	0.7622	0.3147	0.0280	0.1191	0.7380	0.7315	0.7639
22	0.6853	0.2028	0.5734	0.5175	0.6548	0.3278	0.3840	0.3617
23	0.6503	0.0000	0.4056	0.4476	0.9374	0.2719	0.2790	0.2987
24	0.5524	0.6643	0.9650	0.6783	0.2520	0.4231	0.5742	0.4590
25	0.9650	0.6573	0.5664	0.3357	0.2274	0.5269	0.6416	0.5873
26	0.5105	0.8671	0.6224	0.8112	0.1431	0.3400	0.5407	0.3923
27	0.8951	0.6154	0.8392	0.7413	0.2840	0.4146	0.5947	0.4698
28	0.9441	0.1399	0.1678	0.1329	0.6936	0.4269	0.4057	0.4645
29	0.8811	0.1049	0.8741	0.7832	0.7930	0.3372	0.4243	0.3657
30	0.5594	0.9510	0.8252	0.8462	0.1118	0.3912	0.6168	0.4425
31	0.3916	0.8112	0.1329	0.9021	0.1917	0.1947	0.3812	0.2509
32	0.5664	0.7832	0.1538	0.7972	0.2003	0.2411	0.4274	0.3076
33	0.0070	0.4126	0.7552	0.8811	0.4535	0.2289	0.3047	0.2269
34	0.9371	0.1748	0.4476	0.5664	0.6867	0.3142	0.3941	0.3642
35	0.1888	0.5245	0.9580	0.2308	0.3065	0.5384	0.5372	0.5348
36	0.2517	0.6853	0.3846	0.5105	0.2305	0.3233	0.4232	0.3635
37	0.4336	0.2797	0.0000	1.0000	0.6165	0.0875	0.1812	0.1232
38	0.9510	0.2517	0.2378	0.7902	0.6245	0.2330	0.3520	0.2920
39	0.0350	0.2937	0.9231	0.0070	0.4811	0.6285	0.4762	0.5617
40	0.1678	0.2448	0.4965	0.3427	0.5768	0.3173	0.3029	0.3244
41	0.1329	0.9371	0.7762	0.8252	0.1198	0.3322	0.5143	0.3618

Table B.6 (continued)

No	$t_{R,den}$	$t_{R,ext}$	$t_{R,ann}$	z_{w3}	$log_2(-)$	$\Delta P(-)$	$t_{R,tot}$(-)	$V_{s,tot}$(-)
42	0.6434	0.9650	0.5594	0.8951	0.1138	0.3361	0.5760	0.3997
43	0.9790	0.7692	0.8951	0.9161	0.2014	0.4180	0.6525	0.4785
44	0.0000	0.5594	0.3357	0.9720	0.3453	0.1428	0.2523	0.1583
45	0.7063	0.0629	0.0140	0.4336	0.8533	0.2138	0.2324	0.2586
46	0.4196	0.9021	0.2587	0.1049	0.0675	0.6213	0.6296	0.6444
47	0.8112	0.8322	0.6364	0.6643	0.1577	0.4167	0.6186	0.4852
48	0.9720	0.0839	0.0909	0.2937	0.8009	0.3178	0.3370	0.3707
49	0.1538	0.8531	0.1958	0.7343	0.1596	0.2261	0.3812	0.2735
50	0.3007	0.4196	0.3566	0.6853	0.4422	0.2259	0.3077	0.2557
51	0.7902	0.0559	0.1818	0.3497	0.8316	0.2864	0.2970	0.3277
52	0.7622	0.3357	0.5245	0.1888	0.4679	0.5000	0.5052	0.5264
53	0.6713	0.0420	0.8881	0.6503	0.8876	0.3315	0.3752	0.3465
54	0.6993	0.3497	0.4266	0.7483	0.5088	0.2638	0.3758	0.3090
55	0.0490	0.0070	0.6713	0.9510	0.9634	0.1534	0.1587	0.1358
56	0.2727	0.0909	0.5804	0.0839	0.7392	0.4481	0.3444	0.4283
57	0.6364	0.9091	0.3427	0.1748	0.0763	0.6048	0.6691	0.6500
58	0.8042	0.4336	0.6573	0.1399	0.3706	0.5917	0.5952	0.6131
59	0.2028	0.3636	0.3007	0.3846	0.4714	0.2885	0.3041	0.3104
60	0.7832	0.1469	0.9720	0.7133	0.7407	0.3661	0.4455	0.3884
61	0.7692	0.3427	0.8531	0.9930	0.5196	0.3154	0.4543	0.3449
62	0.9231	0.5524	0.2238	0.1818	0.2879	0.5163	0.5624	0.5694
63	0.1748	0.5385	0.3986	0.8392	0.3528	0.2006	0.3103	0.2256
64	0.8252	0.4476	0.8112	0.8601	0.4235	0.3501	0.5040	0.3921
65	0.3846	0.7552	0.1259	0.5524	0.1978	0.2826	0.4130	0.3416
66	0.7552	0.5664	0.9161	0.5944	0.3098	0.4470	0.5866	0.4914
67	0.3636	0.9580	0.6783	0.0350	0.0233	0.7935	0.7612	0.7841
68	0.0769	0.5035	0.6294	0.8042	0.3748	0.2392	0.3311	0.2509
69	0.4825	0.4266	0.7832	0.1469	0.3731	0.5711	0.5487	0.5724
70	0.0839	0.2378	0.2937	0.4755	0.6129	0.2149	0.2158	0.2267
71	0.1049	0.7133	0.0350	0.8741	0.2500	0.1323	0.2712	0.1724
72	0.6573	0.3776	0.3217	0.2028	0.4269	0.4424	0.4524	0.4773
73	0.6084	0.6364	0.0979	0.5035	0.2655	0.3019	0.4221	0.3673
74	0.6294	0.2587	0.6503	0.3287	0.5706	0.4161	0.4415	0.4421
75	0.1958	0.0210	0.4615	0.7692	0.9302	0.1575	0.1647	0.1585
76	0.2937	0.8042	0.8601	0.0210	0.0885	0.7907	0.7271	0.7632
77	0.8392	0.6084	0.7692	0.3706	0.2584	0.5266	0.6315	0.5727
78	0.5385	0.0699	0.4685	0.3147	0.8093	0.3312	0.3159	0.3495
79	0.5245	0.9441	0.5455	0.4965	0.0954	0.4429	0.6097	0.5047
80	0.6643	0.1678	0.9510	0.2168	0.6529	0.5150	0.5027	0.5226
81	0.6014	0.6783	0.8671	0.9231	0.2530	0.3521	0.5362	0.3894
82	0.5734	0.8182	0.2517	0.3217	0.1412	0.4506	0.5551	0.5114
83	0.6923	0.8741	0.1049	0.0699	0.0814	0.6497	0.6584	0.6835
84	0.6154	0.4755	0.2727	0.7552	0.3952	0.2382	0.3665	0.2896
85	0.8322	0.8462	0.8182	0.1189	0.0889	0.7608	0.8079	0.7882
86	0.2308	0.2238	0.0769	0.2098	0.6106	0.2971	0.2484	0.3108
87	0.8182	0.1888	0.3636	0.9650	0.6972	0.2048	0.3139	0.2461
88	0.0699	0.9231	0.1748	0.0979	0.0597	0.5727	0.5490	0.5799
89	0.3077	0.8881	0.0629	0.8182	0.1549	0.2001	0.3848	0.2596

Table B.6 (continued)

No	$t_{R,den}$	$t_{R,ext}$	$t_{R,ann}$	z_{w3}	$log_2(-)$	$\Delta P(-)$	$t_{R,tot}$(-)	$V_{s,tot}$(-)
90	0.5455	0.4615	0.1888	0.4825	0.3877	0.2883	0.3700	0.3394
91	0.5315	0.3566	0.0490	0.5594	0.4944	0.2142	0.2876	0.2640
92	0.9091	0.1958	0.7972	0.0140	0.5904	0.6647	0.5911	0.6550
93	0.4476	0.8601	0.3776	0.5804	0.1340	0.3504	0.5110	0.4099
94	0.3706	0.9860	0.0420	0.3916	0.0745	0.3778	0.5106	0.4463
95	0.0140	1.0000	0.4755	0.2517	0.0470	0.5191	0.5736	0.5404
96	0.0559	0.5874	0.2797	0.4615	0.2900	0.2784	0.3342	0.3060
97	0.4266	0.0979	0.2098	0.0420	0.7303	0.4338	0.3137	0.4154
98	0.4965	0.7413	0.4196	0.8322	0.2186	0.2744	0.4505	0.3251
99	0.8601	0.4406	0.4895	0.8531	0.4329	0.2881	0.4415	0.3417
100	0.3217	0.0769	0.9441	0.9860	0.8537	0.2477	0.2944	0.2386
101	1.0000	0.1119	0.3077	0.9441	0.8062	0.2088	0.3176	0.2587
102	0.0210	0.5105	0.9021	0.5734	0.3433	0.3504	0.4117	0.3538
103	0.1608	0.8392	0.4545	0.0559	0.0862	0.6613	0.6115	0.6511
104	0.4685	0.9790	0.2448	0.4685	0.0815	0.3924	0.5528	0.4618
105	0.0979	0.6503	0.9091	0.1678	0.2057	0.5948	0.5756	0.5821
106	0.3986	0.4895	0.1119	0.7622	0.3952	0.1787	0.2901	0.2239
107	0.5175	0.3287	0.6084	0.6154	0.5222	0.3085	0.3857	0.3384
108	0.2448	0.5804	0.0839	0.0909	0.2505	0.4773	0.4303	0.4898
109	0.2587	0.6713	0.7133	0.9371	0.2604	0.2741	0.4270	0.2973
110	0.1119	0.1818	0.0070	0.6713	0.7117	0.0963	0.1145	0.1159
111	0.7133	0.7483	0.7413	0.4406	0.1788	0.4984	0.6339	0.5501
112	0.4126	0.1538	0.7622	0.1119	0.6666	0.5035	0.4304	0.4906
113	0.4406	0.1329	0.6643	0.4266	0.7373	0.3321	0.3405	0.3455
114	0.9930	0.2657	0.0699	0.4196	0.5858	0.3051	0.3808	0.3726
115	0.3357	0.3217	0.8462	0.0769	0.4540	0.5876	0.5108	0.5655
116	0.8462	0.6014	0.2867	0.6084	0.2832	0.3282	0.4820	0.3994
117	0.0909	0.9720	0.2657	0.2657	0.0655	0.4628	0.5302	0.5008
118	0.4615	0.4545	0.2168	0.2867	0.3721	0.3675	0.3966	0.4055
119	0.2657	0.6224	1.0000	0.9580	0.2893	0.3242	0.4714	0.3362
120	0.7343	0.4965	0.6923	0.3986	0.3365	0.4569	0.5458	0.5011
121	0.9021	0.3916	0.8322	0.5455	0.4484	0.4332	0.5470	0.4797
122	0.8531	0.2727	0.7203	0.7203	0.5888	0.3391	0.4483	0.3795
123	0.5944	0.4056	0.6853	0.0000	0.3682	0.6839	0.5946	0.6628
124	0.3566	0.1189	0.0280	0.4056	0.7661	0.1937	0.1859	0.2215
125	0.3497	0.2098	0.5315	0.5874	0.6534	0.2598	0.2965	0.2773
126	0.0629	0.2867	0.6154	0.7273	0.5708	0.2203	0.2622	0.2226
127	0.2867	0.4685	0.6993	0.3776	0.3576	0.4066	0.4464	0.4246
128	0.5804	0.5175	0.3497	0.9091	0.3725	0.2235	0.3715	0.2692
129	0.4056	0.7762	0.5944	0.1958	0.1377	0.5775	0.6142	0.6010
130	0.7413	0.0140	0.9371	0.8671	0.9471	0.3067	0.3707	0.3199
131	0.8881	0.8811	0.1608	0.3077	0.1092	0.4968	0.6301	0.5748
132	0.7273	0.5944	0.0559	0.1538	0.2471	0.4843	0.5106	0.5342
133	0.4545	0.1608	0.1469	0.4895	0.7130	0.2115	0.2338	0.2442
134	0.7762	0.3007	0.5175	0.6224	0.5547	0.3151	0.4107	0.3602
135	0.1818	0.6923	0.7343	0.1259	0.1709	0.6123	0.5875	0.6055
136	0.9161	0.3846	0.3916	0.6364	0.4716	0.3161	0.4405	0.3765
137	0.4755	0.2168	0.4126	0.6923	0.6533	0.2261	0.2872	0.2539

Table B.6 (continued)

No	$t_{R,den}$	$t_{R,ext}$	$t_{R,ann}$	z_{w3}	$log_2(-)$	$\Delta P(-)$	$t_{R,tot}$(-)	$V_{s,tot}$(-)
138	0.8671	0.8252	0.4406	0.5315	0.1506	0.4277	0.6109	0.5057
139	0.7483	0.9930	0.7063	0.1608	0.0353	0.7281	0.8085	0.7688
140	0.3776	0.7063	0.5385	0.9790	0.2366	0.2481	0.4218	0.2841
141	0.3427	0.7902	0.8811	0.5245	0.1650	0.4514	0.5821	0.4857
142	0.7203	0.6993	0.9790	0.2727	0.1930	0.6278	0.7096	0.6592
143	0.6783	0.5455	0.6434	0.6993	0.3343	0.3479	0.4894	0.3945
144	0.3287	0.0350	0.5874	0.8881	0.9165	0.1829	0.2141	0.1855
145	0.2238	0.7972	0.9301	0.3566	0.1475	0.5280	0.6079	0.5467
146	0.0420	0.5734	0.9930	0.3636	0.2871	0.4658	0.4985	0.4656
147	0.9860	0.7343	0.7902	0.4545	0.1902	0.5357	0.6941	0.5979
148	0.5874	0.3147	0.8042	0.4126	0.5094	0.4198	0.4696	0.4450
149	0.2378	0.1259	0.7273	0.3007	0.7266	0.3667	0.3307	0.3621
150	0.1469	0.8951	0.3706	0.5385	0.1235	0.3338	0.4662	0.3790
151	0.9301	0.7273	0.4825	0.7762	0.2206	0.3522	0.5588	0.4250
152	0.3147	0.6294	0.5105	0.2238	0.2272	0.4882	0.5114	0.5115
153	0.2168	0.7203	0.3287	0.7063	0.2234	0.2493	0.3825	0.2903
154	0.2797	0.9161	0.6014	0.6294	0.1183	0.3684	0.3825	0.2903
155	0.1189	0.3077	0.5035	0.0629	0.4726	0.4934	0.3825	0.2903
156	0.7972	0.0280	0.7483	0.2587	0.8697	0.4360	0.3825	0.2903
157	0.0280	0.6434	0.0210	0.0490	0.2105	0.4958	0.3825	0.2903
158	0.1399	0.3986	0.2028	0.6014	0.4594	0.1927	0.2454	0.2188
159	0.2098	0.0490	0.2308	0.6573	0.8836	0.1370	0.1393	0.1488
160	0.5035	0.4825	0.4336	0.2448	0.3431	0.4481	0.4728	0.4789

Appendix C

Arduino Code

The code is developed for the PID temperature control

```
/*
 This code is implemented to perform PID control on 2 peltier and 2 heat resistor elements as part of my PhD with title : " Optimisation of microfluidic flow systems".
*/
// ---------------------------------------------------------------------
// ----------------------- LOAD LIBRARIES
// ---------------------------------------------------------------------
#include <PID_v1.h>
#include <Wire.h>
#include <SPI.h>
#include "Adafruit_MAX31855.h"

// FIRST TC - RESISTOR
#define MAXDO1   3
#define MAXCS1   4
#define MAXCLK1  5
// SECOND TC - PELTIER
#define MAXDO2   9
#define MAXCS2   8
#define MAXCLK2  10

// ---------------------------------------------------------------------
// -------------------------- THERMOCOUPLES
// ---------------------------------------------------------------------
// FIRST TC - RESISTOR
Adafruit_MAX31855 thermocouple1(MAXCLK1, MAXCS1, MAXDO1);

// SECOND TC - PELTIER
Adafruit_MAX31855 thermocouple2(MAXCLK2, MAXCS2, MAXDO2);

// ---------------------------------------------------------------------
// -------------------- PID PARAMETERS & PRIAMBLE
// ---------------------------------------------------------------------
// FIRST TC - RESISTOR
double Setpoint1 ;
double Input1;
double Output1 ;
```

```
//PID parameters
double Kp1= 30, Ki1=1.2, Kd1= 0;
//create PID instance
PID myPID1(&Input1, &Output1, &Setpoint1, Kp1, Ki1, Kd1, DIRECT);
//set time interval that measurement takes place
const int resistor_Interval = 2000;

//  SECOND TC - PELTIER
double Setpoint2 ;
double Input2;
double Output2 ;
//PID parameters
double Kp2= 30, Ki2=1.2, Kd2= 0;
//create PID instance
PID myPID2(&Input2, &Output2, &Setpoint2, Kp2, Ki2, Kd2, REVERSE);
//see here: https://forum.arduino.cc/t/peltier-temperature-control
    /538025/42
//set time interval that measurement takes place
const int peltier_Interval =  2000;


void setup() {
  // FIRST TC - RESISTOR
  pinMode(MAXCS1, OUTPUT);
  pinMode(MAXCLK1, OUTPUT);
  pinMode(MAXDO1, INPUT);
  Serial.begin(9600);
  while (!Serial) delay(1);
  Serial.println("MAX31855 test");
  // wait for MAX chip to stabilize
  delay(1000);
  //Setpoint temperature value for the resistors
  Setpoint1 =90 ;// In degrees Celsius
  //Turn the PID on
  myPID1.SetMode(AUTOMATIC);
  //Adjust PID values
  myPID1.SetTunings(Kp1, Ki1, Kd1);
  delay(1000);

  // SECOND TC - PELTIER
  pinMode(MAXCS2, OUTPUT);
  pinMode(MAXCLK2, OUTPUT);
  pinMode(MAXDO2, INPUT);
  Serial.begin(9600);
  while (!Serial) delay(1);
  Serial.println("MAX31855 test");
  // wait for MAX chip to stabilize
  delay(1000);
  //Setpoint temperature value for the peltier elements
  Setpoint2 = 80;// In degrees Celsius
  //Turn the PID on
  myPID2.SetMode(AUTOMATIC);
```

```
  //Adjust PID values
  myPID2.SetTunings(Kp2, Ki2, Kd2);
  delay(1000);
  }


// --------------------------------------------------------------------
// -------------------- MAIN SCRIPT
// --------------------------------------------------------------------
void loop() {
    // READ TEMPERATURE AND PLOT TC1
    plot_TC1_fn();
    //CHECK if it's time to run AND RUN PID on resistors
    resistor_fn();
    // READ TEMPERATURE AND PLOT TC2
    plot_TC2_fn();
    //CHECK if it's time to run AND RUN PID on peltier elements
    peltier_fn();
  }

// --------------------------------------------------------------------
// -------------------- FUNCTIONS USED
// --------------------------------------------------------------------
void plot_TC1_fn() {
//see here: https://arduino.stackexchange.com/questions/37684/can-i-make-multiple-void-loops-with-arduino-uno/37703
       // FIRST TC - RESISTOR
       delay(500);
       double c1 = thermocouple1.readCelsius();
       if (isnan(c1)) {
         Serial.println("Something wrong with thermocouple1!");
       } else {
         Serial.print("TC1 temperature = ");
         Serial.print(millis());
         Serial.print(",");
         Serial.print(c1);
         //Serial.print("\t");
       }
       delay(500);
}


void resistor_fn() {
  static unsigned long lastTime = 0;
  const long interval = resistor_Interval;
  unsigned long now = millis();
  double c1 = thermocouple1.readCelsius();
  if (now - lastTime > interval) {
      lastTime = now;
      // FIRST TC - RESISTOR
      //Read the value from the TC1
      Input1 = c1;
```

```
      //PID calculation
      delay(150);
      myPID1.Compute();
      //Write the output as calculated by the PID function
      analogWrite(6,Output1);
      //Send data by serial for plotting
      delay(500);
  }
}

void plot_TC2_fn(){
        // SECOND TC - PELTIER
        delay(500);
        double c2 = thermocouple2.readCelsius();
        if (isnan(c2)) {
           Serial.println("Something wrong with thermocouple2!");
         } else {
           Serial.print("TC2 temperature = ");
           Serial.print(millis());
           Serial.print(",");
           Serial.println(c2);
         }
         delay(500);
}


void peltier_fn() {

  static unsigned long lastTime = 0;
  const long interval = peltier_Interval;
  unsigned long now = millis();
  double c2 = thermocouple2.readCelsius();
  if (now - lastTime > interval) {
    lastTime = now;
        // SECOND TC - PELTIER
        Input2 = c2;
        //PID calculation
        delay(150);
        myPID2.Compute();
        //Write the output as calculated by the PID function
        analogWrite(11,Output2);
        delay(500);
  }
}
```

LISTING C.1: Arduino PID code

Appendix D

Power Consumption Calculations

Using the Joule Heating model, the power consumption for the heater in the denaturation regime for the design case presented in the work of Papadopoulos et al. (2015) is calculated as follows:

$$A_{heater} = W_{heater} \cdot H_{heater} = 2 \cdot 10^{-9} m^2 \tag{D.1}$$

$$J_{normal} = I_{den} / A_{heater} = \frac{0.2345[A]}{2 \cdot 10^{-9}[m^2]} = 1.17 \cdot 10^{8} [A/m^2] \tag{D.2}$$

$$\varrho(T)_{den} = \varrho_{293K}[1 + \alpha(T_{den} - T_{ref})] = 2.16636 \cdot 10^{-8}[\Omega m] \tag{D.3}$$

$$L_{den,heater} = 8 \cdot 0.0071[m] + 9 \cdot 200 \cdot 10^{-6}[m] = 0.0586[m] \tag{D.4}$$

$$\mathcal{R}_{den} = \varrho_{DEN,293K} \frac{L_{den,heater}}{A_{heater}} = 2.16636 \cdot 10^{-8}[\Omega m] \frac{0.0586[m]}{2 \cdot 10^{-9}[m^2]} = 0.63474[\Omega] \tag{D.5}$$

$$P_{den} = \mathcal{R}_{den} I_{den}^2 = 0.63474[\Omega] \cdot (0.2345[A])^2 = 0.03490[W] \tag{D.6}$$

where α : the coefficient of thermal expansion of copper (0.0386 K^{-1}), ϱ_{293K} : the reference resistivity of copper at 293 K (1.68 $\cdot 10^{-8}$ Ωm), $\varrho(T)_{den}$: the resistivity of the copper-wire heater at denaturation zone, T_{ref} : $293.15K$, T_{den} : $368.15K$, $\mathcal{R}$: the resistance (Ω) and P the power consumption (W). The width (W_{heater}), height (H_{heater}) and length ($L_{den,heater}$) of the copper wires used in the simulations is 10^{-4} m, $2 \cdot 10^{-5}$ m and 0.0586 m respectively, while the value of I_{den} is found to be equal to 0.2345 A by trial and error. The copper wire is bent nine times, resulting to eight straight parts ($L_{den,straight}$ = 0.0071 m) covering the bottom of the heater in a serpentine shape (see Figure 3.23). The power consumption of the heaters at the other zones are calculated in the same way, and are equal to 0.02367 and 0.01201 W respectively.

Appendix E

PCR Kinetics

The temperature dependence of the various rate constants mentioned earlier, k_D^+, k_D^-, k_E, k_A^+ and k_A^-, are given by Equations E.1 - E.5, as demonstrated also in the work of Papadopoulos et al. (2015):

$$k_D^+(T) = 0.5 \cdot k_o^+ \cdot \left(1 + tanh\left(\frac{T - 361.15}{5}\right)\right) \tag{E.1}$$

$$k_D^-(T) = 0.5 \cdot k_o^- \cdot \left(1 + tanh\left(\frac{348.15 - T}{5}\right)\right) \tag{E.2}$$

$$k_A^+(T) = 0.5 \cdot k_1^+ \cdot \left(1 + tanh\left(\frac{335.65 - T}{5}\right)\right) \tag{E.3}$$

$$k_A^-(T) = 0.5 \cdot k_1^- \cdot \left(1 + tanh\left(\frac{T - 339.15}{5}\right)\right) \tag{E.4}$$

$$k_E(T) = k_2 \cdot exp\left(-\left(\frac{T - 345.15}{5}\right)^2\right) \tag{E.5}$$

where T is the temperature in K, and the $k_o^+, k_o^-, k_1^+, k_1^-$ and k_2 constants are presented in Table E.1. The reaction rates are given by Equations E.6 - E.12.

$$R_1 = -k_D^+ C_1 + k_D^- C_2 C_3 + k_E C_6 C_7 \tag{E.6}$$

$$R_2 = k_D^+ C_1 - k_D^- C_2 C_3 - k_A^+ C_2 C_5 + k_A^- C_7 \tag{E.7}$$

$$R_3 = k_D^+ C_1 - k_D^- C_2 C_3 - k_A^+ C_3 C_4 + k_A^- C_6 \tag{E.8}$$

$$R_4 = -k_A^+ C_3 C_4 + k_A^- C_6 \tag{E.9}$$

$$R_5 = -k_A^+ C_5 C_2 + k_A^- C_7 \tag{E.10}$$

$$R_6 = k_A^+ C_4 C_3 - (k_A^- + k_E) C_6 \tag{E.11}$$

$$R_7 = k_A^+ C_2 C_5 - (k_A^- + k_E) C_7 \tag{E.12}$$

TABLE E.1: Values of constants in reaction rate constants (Papadopoulos et al., 2015)

Parameter	Values	Description
k_o^+	$12.5[1/s]$	Constant parameter in reaction rate constant k_D^+
k_o^-	$10^3[m^3/(mol \cdot s)]$	Constant parameter in reaction rate constant k_D^-
k_1^+	$5 \cdot 10^3[m^3/(mol \cdot s)]$	Constant parameter in reaction rate constant k_A^+
k_1^-	$10^{-4}[1/s]$	Constant parameter in reaction rate constant k_A^-
k_2	$0.32[1/s]$	Constant parameter in reaction rate constant k_E

Appendix F

Meta-models of the four objectives

F.1 Visual representation of the $log_2 \frac{[DNA]}{[DNA]_o}$ (-) objective.

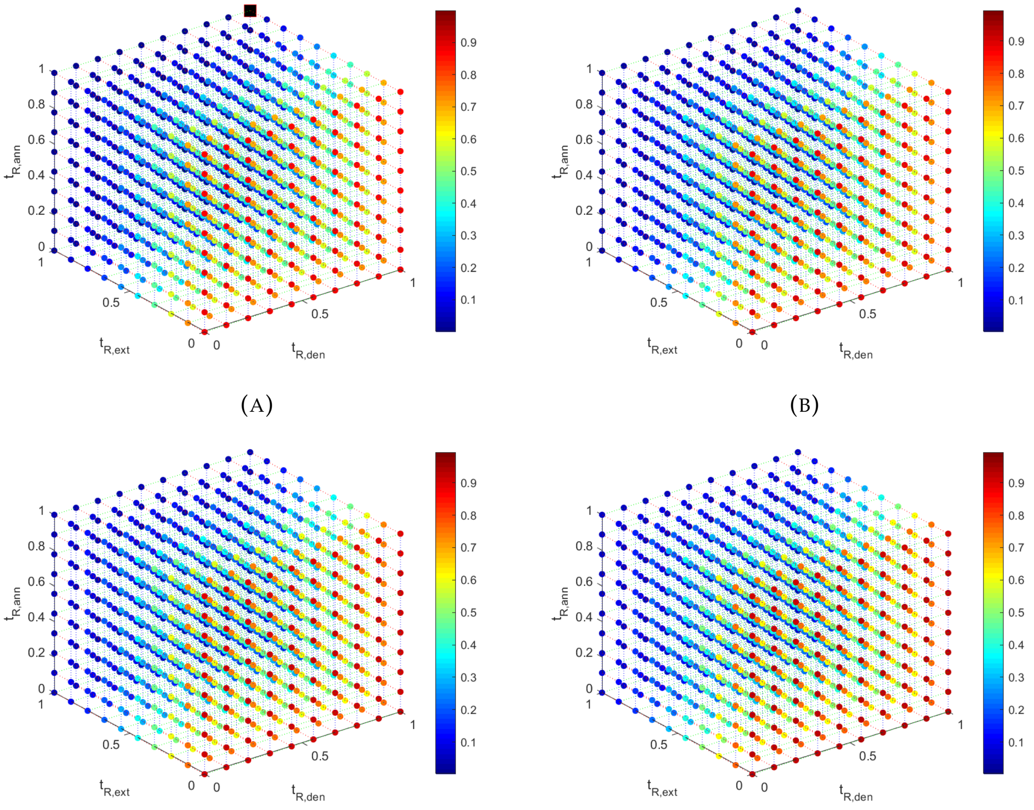

(A)

(B)

(C)

(D)

FIGURE F.1: Visual representation of the $log_2 \frac{[DNA]}{[DNA]_o}$ (-) data (colorbar) for (a) $z_{w3} = 0$, (b) $z_{w3} = 0.\bar{1}$, (c) $z_{w3} = 0.\bar{2}$, (d) $z_{w3} = 0.\bar{3}$.

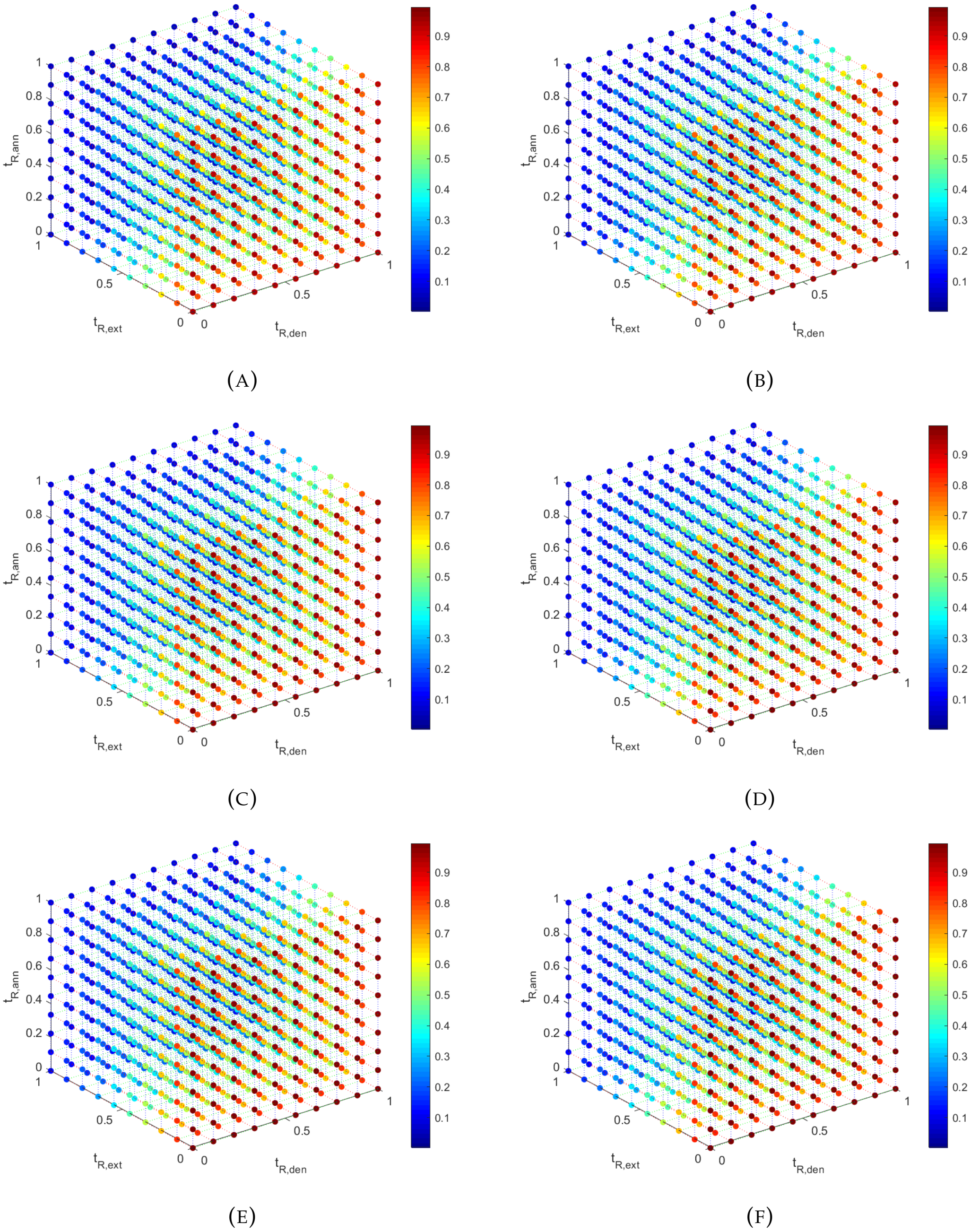

(A) (B) (C) (D) (E) (F)

FIGURE F.2: Visual representation of the $log_2 \frac{[DNA]}{[DNA]_o}$ (-) data (colorbar) for (a) $z_{w3} = 0.\bar{4}$, (b) $0.\bar{5}$, (c) $z_{w3} = 0.\bar{6}$, (d) $z_{w3} = 0.\bar{7}$, (e) $z_{w3} = 0.\bar{8}$, (f) z_{w3} = 1.

F.2 Visual representation of the Δp (-) objective.

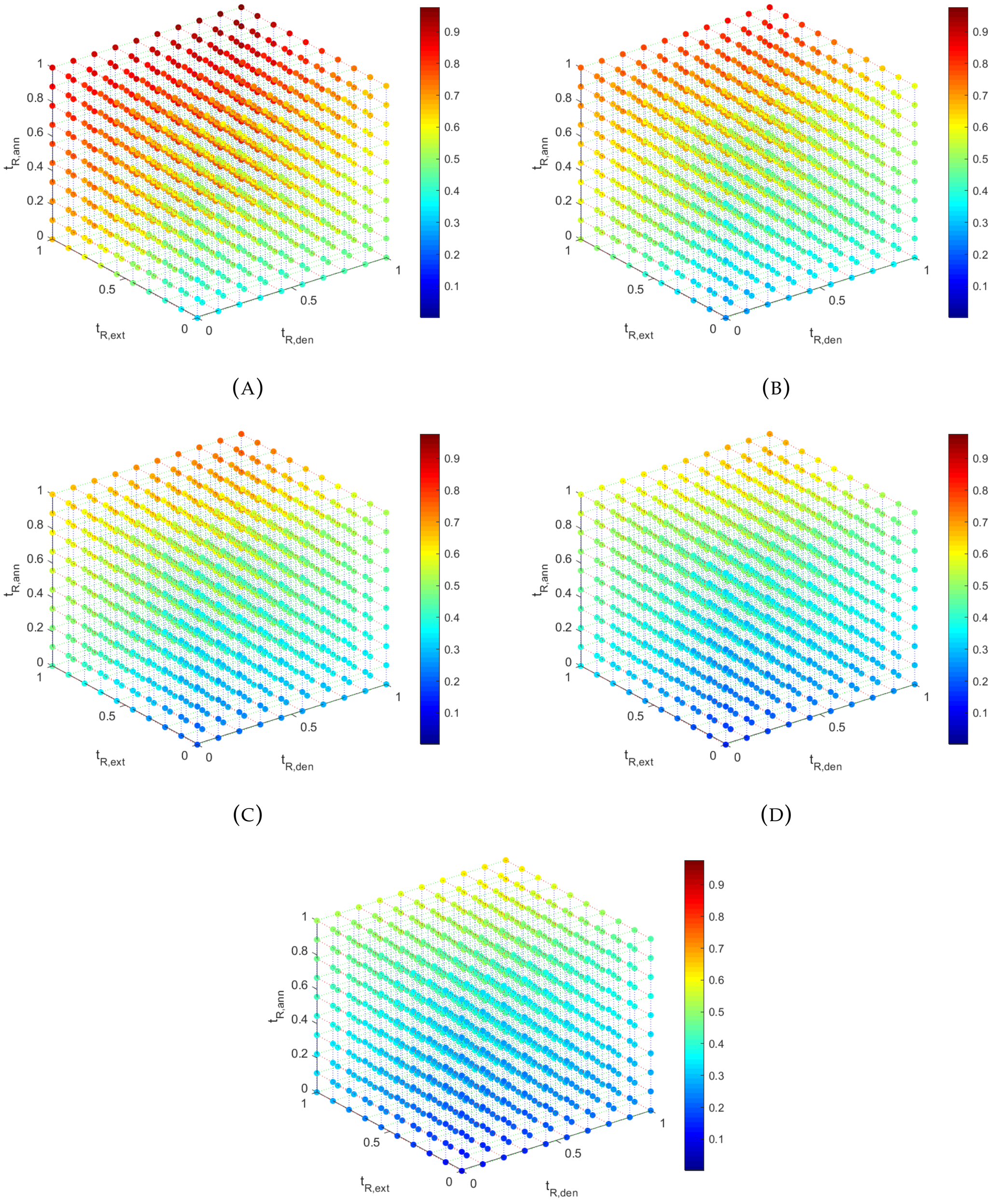

(A) (B) (C) (D) (E)

FIGURE F.3: Visual representation of the Δp(-) data (colorbar) for (a) $z_{w3} = 0$, (b) $z_{w3} = 0.\bar{1}$, (c) $z_{w3} = 0.\bar{2}$, (d) $z_{w3} = 0.\bar{3}$, (e) $z_{w3} = 0.\bar{4}$.

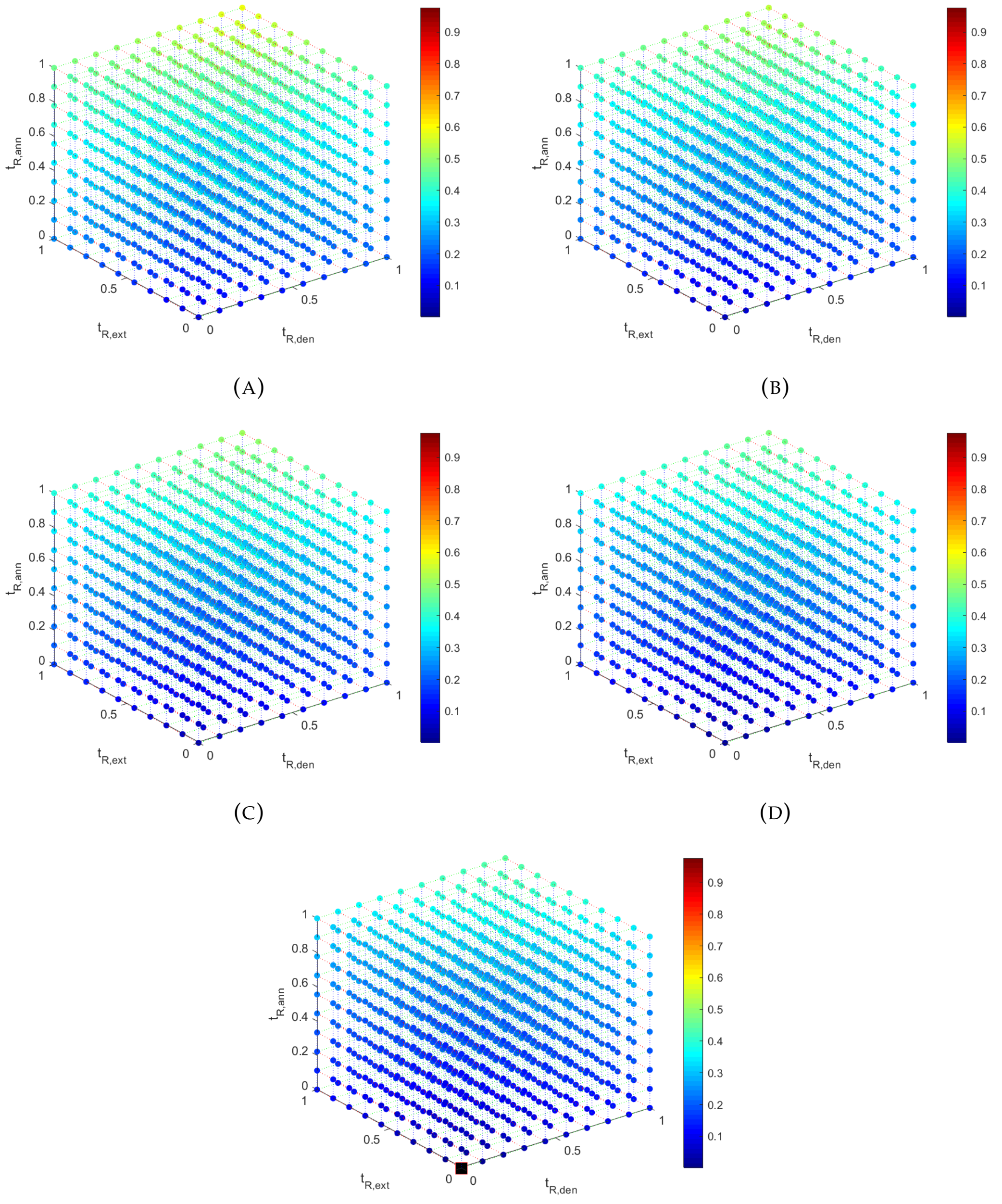

(A) (B)

(C) (D)

(E)

FIGURE F.4: Visual representation of the Δp (-) data (colorbar) for (a) $0.\bar{5}$, (b) $z_{w3} = 0.\bar{6}$, (c) $z_{w3} = 0.\bar{7}$, (d) $z_{w3} = 0.\bar{8}$, (e) $z_{w3} = 1$.

F.3 Visual representation of the $t_{R,tot}$ (-) objective.

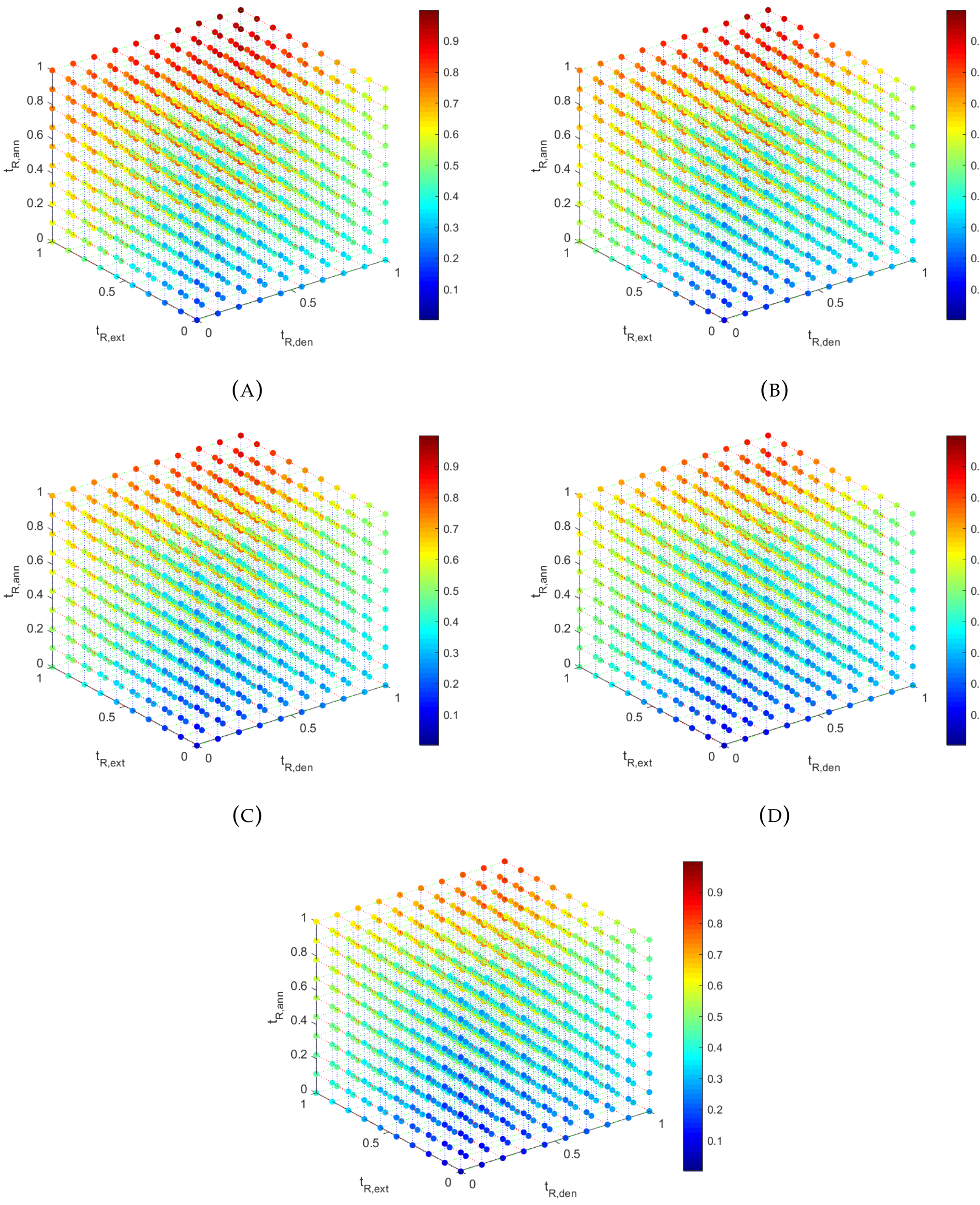

(A) (B)

(C) (D)

(E)

FIGURE F.5: Visual representation of the $t_{R,tot}$ (-) data (colorbar) for (a) $z_{w3} = 0$, (b) $z_{w3} = 0.\bar{1}$, (c) $z_{w3} = 0.\bar{2}$, (d) $z_{w3} = 0.\bar{3}$, (e) $z_{w3} = 0.\bar{4}$.

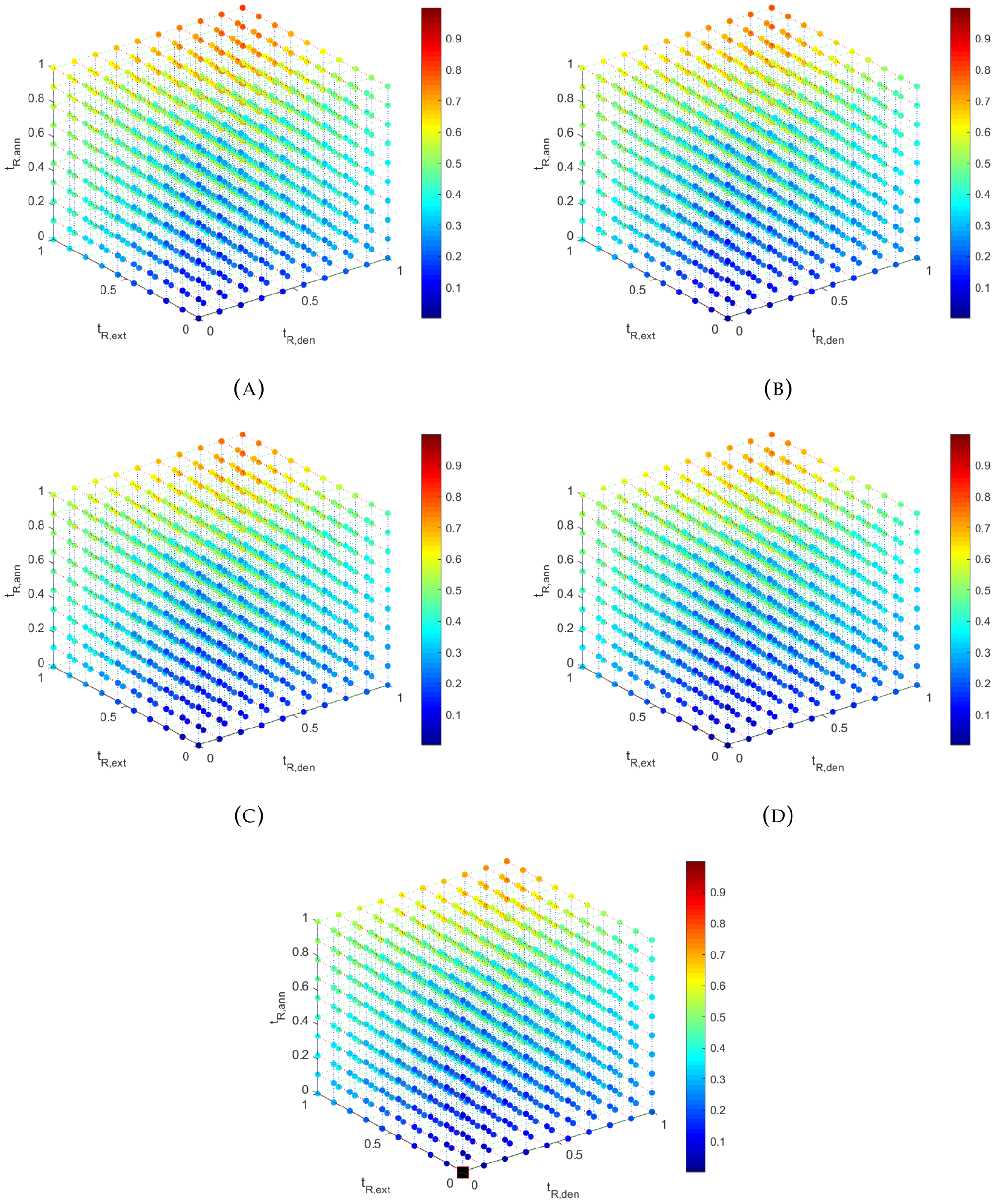

(A)

(B)

(C)

(D)

(E)

FIGURE F.6: Visual representation of the $t_{R,tot}$ (-) data (colorbar) for (a) $0.\bar{5}$, (b) $z_{w3} = 0.\bar{6}$, (c) $z_{w3} = 0.\bar{7}$, (d) $z_{w3} = 0.\bar{8}$, (e) $z_{w3} = 1$.

F.4 Visual representation of the $V_{S,tot}$ (-) objective.

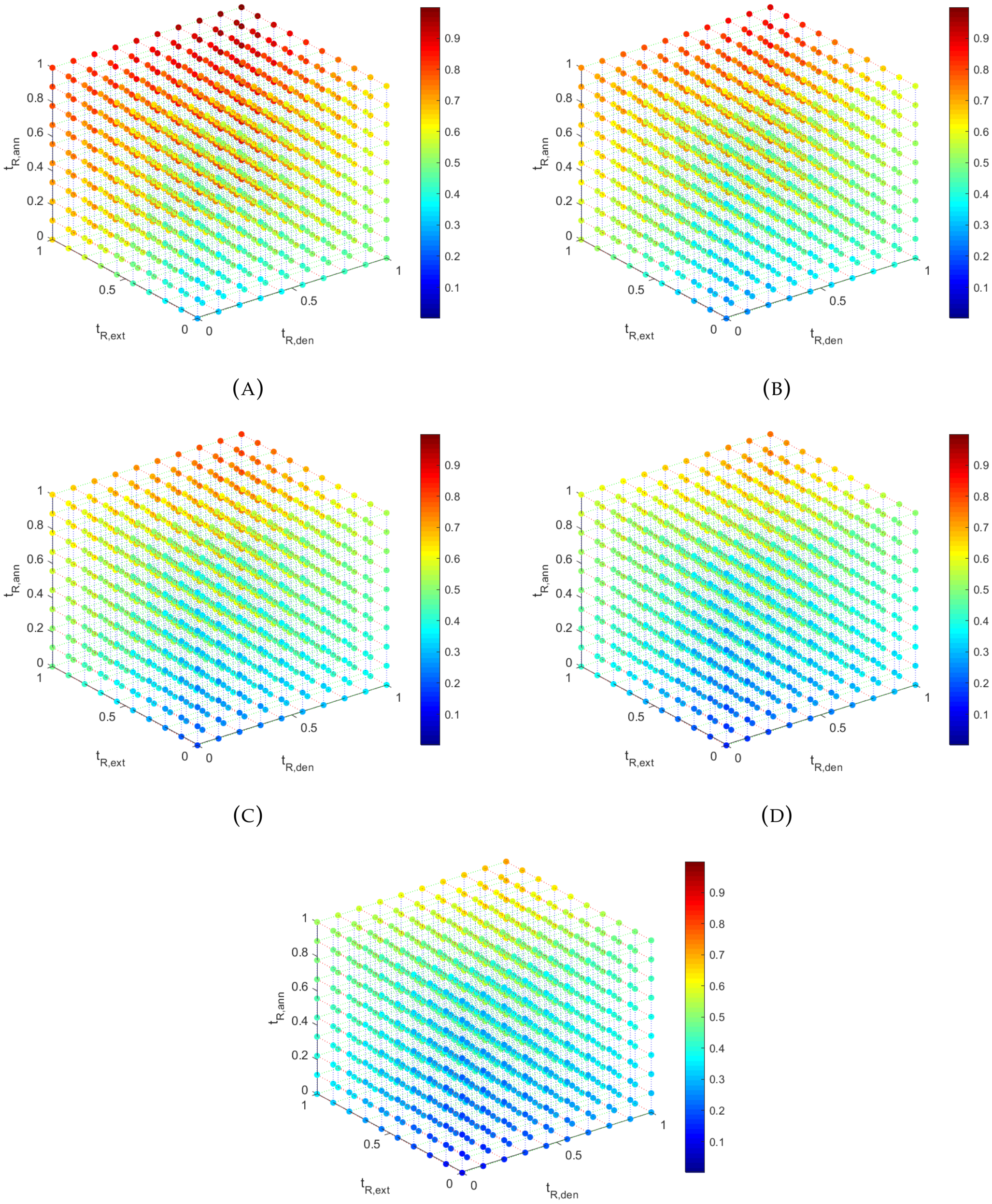

(A)

(B)

(C)

(D)

(E)

FIGURE F.7: Visual representation of the $V_{S,tot}$ (-) data (colorbar) for (a) $z_{w3} = 0$, (b) $z_{w3} = 0.\bar{1}$, (c) $z_{w3} = 0.\bar{2}$, (d) $z_{w3} = 0.\bar{3}$, (e) $z_{w3} = 0.\bar{4}$.

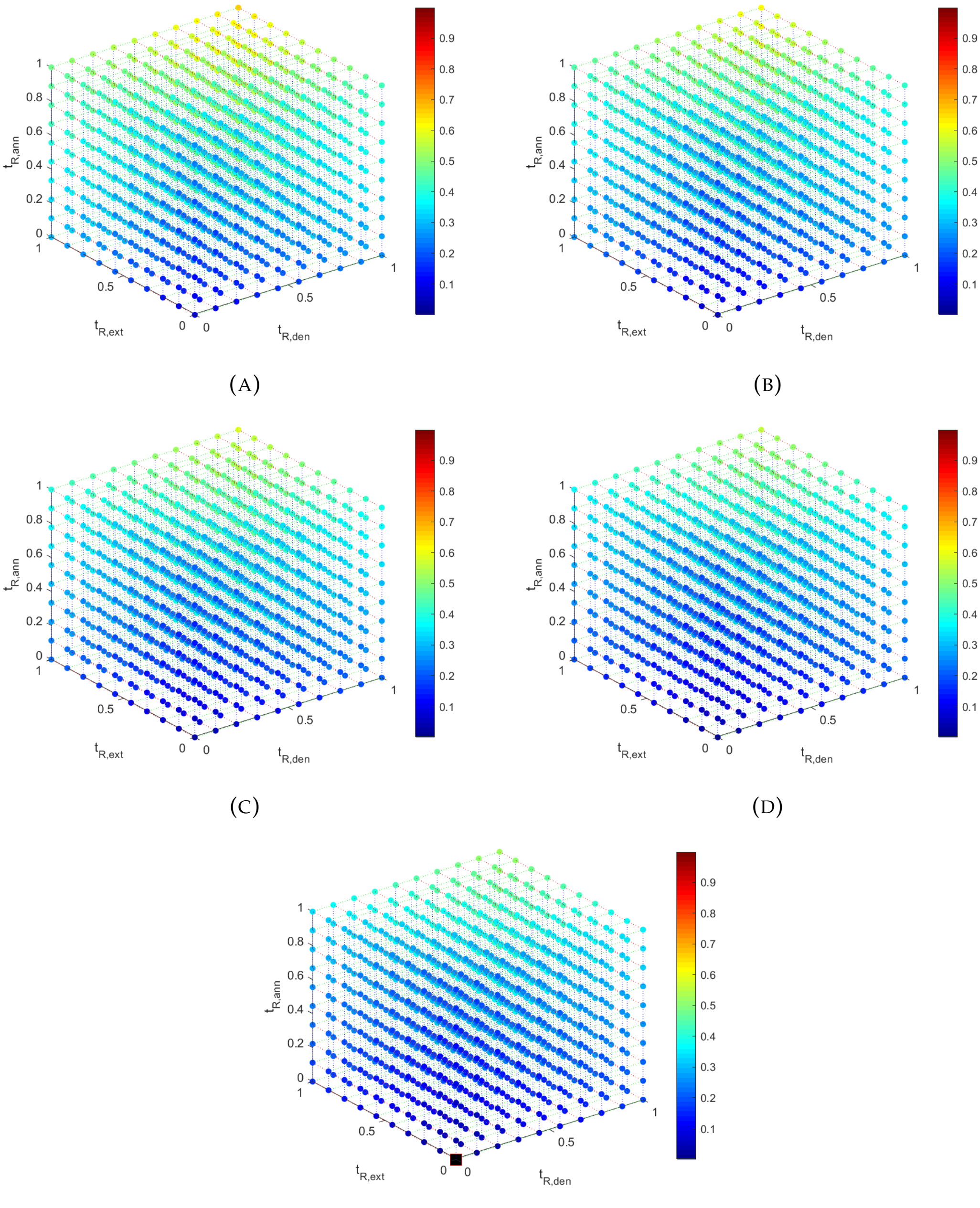

(A) (B)

(C) (D)

(E)

FIGURE F.8: Visual representation of the $V_{S,tot}$ (-) data (colorbar) for (a) $0.\bar{5}$, (b) $z_{w3} = 0.\bar{6}$, (c) $z_{w3} = 0.\bar{7}$, (d) $z_{w3} = 0.\bar{8}$, (e) $z_{w3} = 1$.

Appendix G

Scaling of values

All values of the objective functions are scaled between 0-1 for the purposes of multi-objective optimisation. Furthermore, just for the first objective, the values of $-log_2\frac{[DNA]}{[DNA]_o}$ are scaled between 0-1, in order for all optimisation studies to be minimisation problems. Equation G.1 is used to scale all values, while Table G.1 presents two cases of scaling values of objectives.

TABLE G.1: Calculations for scaling the values of objective functions.

Example	Objective	Starting Value, V_1	max(V_1), V_2	min(V_1), V_3	Scaled value, V_4
1	$-log_2\frac{[DNA]}{[DNA]_o}$	-0.617 (-)	-0.597 (-)	-0.772 (-)	0.889 (-)
2	Δp	88.437 (Pa)	140.622 (Pa)	55.436 (Pa)	0.329 (-)

$$V_4 = \frac{V_1 - V_3}{V_2 - V_3} = \begin{cases} \frac{(-0.617)-(-0.772)}{(-0.597)-(-0.772)}, & \text{Example 1} \\ \frac{(88.437)-(55.436)}{(140.622)-(55.436)}, & \text{Example 2} \end{cases} \tag{G.1}$$

Appendix H

Concentrations for 10 cycles.

This Chapter presents data of ten consecutive PCR runs of two μPCR setups (Designs 4 and 2 of Table 3.40), presented in Chapter 3.4.8.4.2. The concentration of all species present in the reactions are presented. The data are also presented in Figure 3.50.

TABLE H.1: Concentrations of all PCR products for 10 cycles for Design 4 (see Table 3.40).

Design 4 (see Table 3.40)	C_1 (mol/m^3)	C_2 (mol/m^3)	C_3 (mol/m^3)	C_4 (mol/m^3)	C_5 (mol/m^3)	C_6 (mol/m^3)	C_7 (mol/m^3)
Start	$5.7100 \cdot 10^{-9}$	0.0000	0.0000	$3.0000 \cdot 10^{-4}$	$3.0000 \cdot 10^{-4}$	0.0000	0.0000
Cycle 1	$9.7358 \cdot 10^{-9}$	$5.0622 \cdot 10^{-10}$	$5.0622 \cdot 10^{-10}$	$2.9999 \cdot 10^{-4}$	$2.9999 \cdot 10^{-4}$	$6.7201 \cdot 10^{-10}$	$6.7201 \cdot 10^{-10}$
Cycle 2	$1.8816 \cdot 10^{-8}$	$9.8893 \cdot 10^{-10}$	$9.8893 \cdot 10^{-10}$	$2.9998 \cdot 10^{-4}$	$2.9998 \cdot 10^{-4}$	$1.2395 \cdot 10^{-9}$	$1.2395 \cdot 10^{-9}$
Cycle 3	$3.6261 \cdot 10^{-8}$	$1.9046 \cdot 10^{-9}$	$1.9046 \cdot 10^{-9}$	$2.9996 \cdot 10^{-4}$	$2.9996 \cdot 10^{-4}$	$2.3936 \cdot 10^{-9}$	$2.3936 \cdot 10^{-9}$
Cycle 4	$6.9871 \cdot 10^{-8}$	$3.6683 \cdot 10^{-9}$	$3.6683 \cdot 10^{-9}$	$2.9992 \cdot 10^{-4}$	$2.9992 \cdot 10^{-4}$	$4.6117 \cdot 10^{-9}$	$4.6117 \cdot 10^{-9}$
Cycle 5	$1.3455 \cdot 10^{-7}$	$7.0563 \cdot 10^{-9}$	$7.0563 \cdot 10^{-9}$	$2.9984 \cdot 10^{-4}$	$2.9984 \cdot 10^{-4}$	$8.8753 \cdot 10^{-9}$	$8.8753 \cdot 10^{-9}$
Cycle 6	$2.5892 \cdot 10^{-7}$	$1.3545 \cdot 10^{-8}$	$1.3545 \cdot 10^{-8}$	$2.9969 \cdot 10^{-4}$	$2.9969 \cdot 10^{-4}$	$1.7037 \cdot 10^{-8}$	$1.7037 \cdot 10^{-8}$
Cycle 7	$4.9806 \cdot 10^{-7}$	$2.5982 \cdot 10^{-8}$	$2.5982 \cdot 10^{-8}$	$2.9941 \cdot 10^{-4}$	$2.9941 \cdot 10^{-4}$	$3.2591 \cdot 10^{-8}$	$3.2591 \cdot 10^{-8}$
Cycle 8	$9.5834 \cdot 10^{-7}$	$4.9859 \cdot 10^{-8}$	$4.9859 \cdot 10^{-8}$	$2.9887 \cdot 10^{-4}$	$2.9887 \cdot 10^{-4}$	$6.2271 \cdot 10^{-8}$	$6.2271 \cdot 10^{-8}$
Cycle 9	$1.8427 \cdot 10^{-6}$	$9.5281 \cdot 10^{-8}$	$9.5281 \cdot 10^{-8}$	$2.9783 \cdot 10^{-4}$	$2.9783 \cdot 10^{-4}$	$1.1961 \cdot 10^{-7}$	$1.1961 \cdot 10^{-7}$
Cycle 10	$3.5361 \cdot 10^{-6}$	$1.8177 \cdot 10^{-7}$	$1.8177 \cdot 10^{-7}$	$2.9583 \cdot 10^{-4}$	$2.9583 \cdot 10^{-4}$	$2.2951 \cdot 10^{-7}$	$2.2951 \cdot 10^{-7}$

TABLE H.2: Concentrations of all PCR products for 10 cycles for Design 2 (see Table 3.40).

Design 2 (see Table 3.40)	C_1 (mol/m^3)	C_2 (mol/m^3)	C_3 (mol/m^3)	C_4 (mol/m^3)	C_5 (mol/m^3)	C_6 (mol/m^3)	C_7 (mol/m^3)
Start	$5.71{\cdot}10^{-9}$	0	0	$3.0000\cdot10^{-4}$	$3.0000\cdot10^{-4}$	0	0
Cycle 1	$9.066{\cdot}10^{-9}$	$8.0298{\cdot}10^{-10}$	$8.0298{\cdot}10^{-10}$	$2.9998\cdot10^{-4}$	$2.9998\cdot10^{-4}$	$8.1024{\cdot}10^{-10}$	$8.1024{\cdot}10^{-10}$
Cycle 2	$1.7119{\cdot}10^{-8}$	$1.5355{\cdot}10^{-9}$	$1.5355{\cdot}10^{-9}$	$2.9998\cdot10^{-4}$	$2.9998\cdot10^{-4}$	$1.4611{\cdot}10^{-9}$	$1.4611{\cdot}10^{-9}$
Cycle 3	$3.2232{\cdot}10^{-8}$	$2.8895{\cdot}10^{-9}$	$2.8895{\cdot}10^{-9}$	$2.9997\cdot10^{-4}$	$2.9997\cdot10^{-4}$	$2.7564{\cdot}10^{-9}$	$2.7564{\cdot}10^{-9}$
Cycle 4	$6.0689{\cdot}10^{-8}$	$5.4356{\cdot}10^{-9}$	$5.4356{\cdot}10^{-9}$	$2.9995\cdot10^{-4}$	$2.9995\cdot10^{-4}$	$5.1896{\cdot}10^{-9}$	$5.1896{\cdot}10^{-9}$
Cycle 5	$1.1422{\cdot}10^{-7}$	$1.0193{\cdot}10^{-8}$	$1.0193{\cdot}10^{-8}$	$2.9992\cdot10^{-4}$	$2.9992\cdot10^{-4}$	$9.7721{\cdot}10^{-9}$	$9.7721{\cdot}10^{-9}$
Cycle 6	$2.1476{\cdot}10^{-7}$	$1.9007{\cdot}10^{-8}$	$1.9007{\cdot}10^{-8}$	$2.9986\cdot10^{-4}$	$2.9986\cdot10^{-4}$	$1.8402{\cdot}10^{-8}$	$1.8402{\cdot}10^{-8}$
Cycle 7	$4.0357{\cdot}10^{-7}$	$3.534{\cdot}10^{-8}$	$3.534{\cdot}10^{-8}$	$2.9975\cdot10^{-4}$	$2.9975\cdot10^{-4}$	$3.4602{\cdot}10^{-8}$	$3.4602{\cdot}10^{-8}$
Cycle 8	$7.5864{\cdot}10^{-7}$	$6.5717{\cdot}10^{-8}$	$6.5717{\cdot}10^{-8}$	$2.9935\cdot10^{-4}$	$2.9935\cdot10^{-4}$	$6.5075{\cdot}10^{-8}$	$6.5075{\cdot}10^{-8}$
Cycle 9	$1.4256{\cdot}10^{-6}$	$1.2203{\cdot}10^{-7}$	$1.2203{\cdot}10^{-7}$	$2.9856\cdot10^{-4}$	$2.9856{\cdot}10^{-4}$	$1.2279{\cdot}10^{-7}$	$1.2279{\cdot}10^{-7}$
Cycle 10	$2.6751{\cdot}10^{-6}$	$2.2813{\cdot}10^{-7}$	$2.2813{\cdot}10^{-7}$	$2.9703\cdot10^{-4}$	$2.9703\cdot10^{-4}$	$2.3102{\cdot}10^{-7}$	$2.3102{\cdot}10^{-7}$

Appendix I

Calculation of the threshold cycle

This Appendix presents the ability of the optimised geometry of $[W_2(\mu m),\ H_{Fluid}$ $(\mu m)]_{obj_1}$ = [400, 50] to reduce the number of PCR cycles required to achieve the threshold cycle (C_t) or crossing point (C_p) (Schmittgen and Livak, 2008).

Considering that no value of C_t is provided in the work of Papadopoulos et al. (2015) for the suggested design, an estimate needs to be made. To do so, the performance of this device is tested with the case studied presented in the work of Biosystems (2004). Biosystems (2004) produce different initial DNA concentrations in order to calculate the PCR efficiency of a given sample, after the experimental measurement of C_t takes place. More specifically, the values of C_t are collected for a variety of different initial DNA concentrations. These values are described by a linear graph, that follows the general form of Equation I.3 (Biosystems, 2004). The slope of the line graph is then used to obtain the value of the PCR efficiency (Equation I.2) (Biosystems, 2004).

According to Biosystems (2004), the equations that predict C_t for efficiencies of 1 and 5.95 are given by Equations I.4 and I.5 respectively. After taking Equations I.4 and I.5 into account, we extrapolate the values of the β constants for λ= 0.8496 and 0.8555 as presented in Equations I.6 and I.7 respectively. Then, both β values are introduced in Equation I.3 for λ= 0.8496 and 0.8555, resulting to the values of C_t = 36 and C_t = 35 respectively. The $log([DNA]_o)$ is calculated, after converting the initial convent $[DNA]_o$ from mol/m^3 to μg (Equation I.1) for $\mathcal{N}$= 90 bp DNA molecules. The values of C_t, λ, slopes and DNA concentrations of interest are presented in Table I.1.

$$DNA[pmol] = DNA[\mu g] \cdot \frac{[pmol]}{660[pg]} \cdot \frac{10^6[pg]}{1[\mu g]} \cdot \frac{1}{\mathcal{N}} \tag{I.1}$$

$$slope = \frac{-1}{log_{10}(\lambda + 1)} \tag{I.2}$$

$$C_t = slope \cdot log[[DNA]_o(\mu g)] + \beta \tag{I.3}$$

TABLE I.1: Calculations

Efficiency Scenarios	[DNA]$_o$ (mol/m^3)	[DNA]$_o$ $(ng/\mu L)$	$log([DNA]_o)^*$ (μg)
Papadopoulos et al. (2015)	$5.71 \cdot 10^{-9}$	$4.15 \cdot 10^{-4}$	-4.201
$[W_2(\mu m), H_{Fluid}(\mu m)]$ =[200, 50]	$5.71 \cdot 10^{-9}$	$4.15 \cdot 10^{-4}$	-4.201
$[W_2(\mu m), H_{Fluid}(\mu m)]$ =[400, 50]	$5.71 \cdot 10^{-9}$	$4.15 \cdot 10^{-4}$	-4.201
Biosystems	-	-	-
(2004)	-	-	-

*The volume used is $35 \cdot V_{unitcell} = 35 \cdot 5.3\ \mu$L = 185.5 μL

TABLE I.2: Parameters used in the calculations

Efficiency Scenarios	λ (-)	slope (-)	β (-)	C_t (-)
Papadopoulos et al. (2015)	0.909	-3.5612	19.889	35
$[W_2(\mu m), H_{Fluid}(\mu m)]$ =[200, 50]	0.8496	-3.744	19.817	36
$[W_2(\mu m), H_{Fluid}(\mu m)]$ =[400, 50]	0.8555	-3.523	19.820	35
Biosystems	1	-3.3300	20	34
(2004)	5.95	-1.1905	26	31

*The volume used is $35 \cdot V_{unitcell} = 35 \cdot 5.3\ \mu$L = 185.5 μL

$$C_{t,\lambda=1} = -3.3300 \cdot log[[DNA]_o(\mu g)] + 20 \tag{I.4}$$

$$C_{t,\lambda=5.95} = -1.1905 \cdot log[[DNA]_o(\mu g)] + 26 \tag{I.5}$$

$$C_{t,\lambda=0.849} = -3.744 \cdot log[[DNA]_o(\mu g)] + 19.817 \tag{I.6}$$

$$C_{t,\lambda=0.8555} = -3.523 \cdot log[[DNA]_o(\mu g)] + 19.820 \tag{I.7}$$

where the value of $[DNA]_o$ is given in μg, $\mathcal{N}$ is the number of base pairs in a DNA molecule and β is a dimensionless constant.

Appendix J

Matlab code that executes DOE

```matlab
clear all
clc
% ---------------------------------------------------------
% -------- LOAD the DOE points from the txt file ----------
% ---------------------------------------------------------
delimiterOut=' ';
datafile ='DOE_input.txt';
[A,delimiterOut]=importdata(datafile);
[numRows,numCols] = size(A);
% ---------------------------------------------------------
% --- Set the run for all the numRows DoE points ----------
% ---------------------------------------------------------
% Create the matrices for collecting the values of all the OBJ functions
Log2_table(numRows,1)=zeros;
pressure_drop_table(numRows,1)=zeros;
Re_table(numRows,1)=zeros;
den_TU_table(numRows,1)=zeros;
ext_both_TU_table(numRows,1)=zeros;
ann_TU_table(numRows,1)=zeros;
DEN_Watt_table(numRows,1)=zeros;
EXT_Watt_table(numRows,1)=zeros;
ANN_Watt_table(numRows,1)=zeros;
fluid_vol_table(numRows,1)=zeros;
substr_vol_table(numRows,1)=zeros;
% Create the character for units
sec=' [s]';
no_unit='';
for i=[1,160]%numRows
   % -----------------------------------------------------
   % -- Call the BB_COMSOL for all the DOE points --------
   % -----------------------------------------------------
```

```
    % ---------VAR1
    tR_den=A(i,1);
    a=num2str(tR_den) ;
    tR_den=strcat(a,sec);
    % ---------VAR2
    tR_ext=A(i,2);
    b=num2str(tR_ext) ;
    tR_ext=strcat(b,sec);
    % ---------VAR3
    tR_ann=A(i,3);
    c=num2str(tR_ann) ;
    tR_ann=strcat(c,sec);
    % ---------VAR4
    ratio=A(i,4);
    d=num2str(ratio) ;
    ratio=strcat(d,no_unit);
    [Log2, pressure_drop, Re, den_TU,ext_both_TU,ann_TU,
    fluid_vol,substr_vol]=example_for_thesis_fn(tR_den,
    tR_ext,tR_ann,ratio);
    % ---------------------------------------------------
    % ----- Save the values of the OBJ in the tables -----
    % ---------------------------------------------------
    Log2_table(i,1)=Log2;
    pressure_drop_table(i,1)=pressure_drop;
    Re_table(i,1)=Re;
    den_TU_table(i,1)=den_TU;
    ext_both_TU_table(i,1)=ext_both_TU;
    ann_TU_table(i,1)=ann_TU;
    fluid_vol_table(i,1)=fluid_vol;
    substr_vol_table(i,1)=substr_vol;
    % ---------------------------------------------------
    % ---- Save the values of the OBJ in results.txt -----
    % ---------------------------------------------------
    T = table(Log2_table, pressure_drop_table, Re_table,
    den_TU_table, ext_both_TU_table, ann_TU_table,
    fluid_vol_table,substr_vol_table,'VariableNames', { '
    Log2', 'Pressure_Drop','Re','den_TU','ext_both_TU','
    ann_TU','Fluid_vol','Substr_Vol'})
    % Write data to text file
    writetable(T, 'results_DOE.txt')
end
```

example_for_thesis.m

```matlab
function [Log2, pressure_drop, Re, den_TU,ext_both_TU,
    ann_TU, fluid_vol,substr_vol]= example_for_thesis_fn(
    tR_den,tR_ext,tR_ann,ratio)
  cmd = sprintf('comsol batch -inputfile COMSOL_input_file.
    mph -outputfile COMSOL_output_file.mph -job b1 -pname
    tR_den,tR_ext,tR_ann,ratio -plist "%s,%s,%s,%s"', tR_den
    ,tR_ext,tR_ann,ratio);
  system(cmd);
  % -----------------------------------------------------
  filename = 'PROPERTIES.txt';
  delimiterIn = ' ';
  headerlinesIn = 5;
  C = importdata(filename,delimiterIn,headerlinesIn)
  pressure_drop=C.data(1,6)
  Re=C.data(1,7)
  % -----------------------------------------------------
  filename = 'LOG2.txt';
  delimiterIn = ' ';
  headerlinesIn = 5;
  C = importdata(filename,delimiterIn,headerlinesIn) ;
  Log2=C.data(1,6)
  % -----------------------------------------------------
  filename = 'DEN.txt';
  delimiterIn = ' ';
  headerlinesIn = 5;
  C = importdata(filename,delimiterIn,headerlinesIn) ;
  den_TU=C.data(1,6)/C.data(1,7)*100
  % -----------------------------------------------------
  filename = 'ANN.txt';
  delimiterIn = ' ';
  headerlinesIn = 5;
  C = importdata(filename,delimiterIn,headerlinesIn);
  ann_TU=C.data(1,6)/C.data(1,7)*100
  % -----------------------------------------------------
  filename = 'EXT_both.txt';
  delimiterIn = ' ';
  headerlinesIn = 5;
  A = importdata(filename,delimiterIn,headerlinesIn);
  ext_both_TU=A.data(1,6)/A.data(1,7)*100;
  % -----------------------------------------------------
  filename = 'fluidvol.txt';
```

```
  delimiterIn = ' ';
  headerlinesIn = 5;
  A = importdata(filename,delimiterIn,headerlinesIn);
  fluid_vol=A.data(1,6);
  % -------------------------------------------------------
  filename = 'substrate_vol.txt';
  delimiterIn = ' ';
  headerlinesIn = 5;
  A = importdata(filename,delimiterIn,headerlinesIn);
  substr_vol=A.data(1,6);
end
```

example_for_thesis_fn.m

Bibliography

Aach, John and George M Church (2004). "Mathematical models of diffusion - constrained polymerase chain reactions: basis of high-throughput nucleic acid assays and simple self-organizing systems". In: *Journal of theoretical biology* 228.1, pp. 31–46.

Abdollahi, Ayoub, Stuart E Norris, and Rajnish N Sharma (2020). "Fluid flow and heat transfer of liquid-liquid Taylor flow in square microchannels". In: *Applied Thermal Engineering* 172, p. 115123.

Abdollahi, Ayoub, Rajnish N Sharma, and Ashkan Vatani (2017). "Fluid flow and heat transfer of liquid-liquid two phase flow in microchannels: A review". In: *International Communications in Heat and Mass Transfer* 84, pp. 66–74.

Abouali, O and N Baghernezhad (2010). "Numerical investigation of heat transfer enhancement in a microchannel with grooved surfaces". In: *Journal of heat transfer* 132.4.

Aggarwal, Aman and Hari Singh (2005). "Optimization of machining techniques—a retrospective and literature review". In: *Sadhana* 30.6, pp. 699–711.

Agrawal, Basant and Gopal Nath Tiwari (2010). *Building integrated photovoltaic thermal systems: for sustainable developments*. Royal Society of Chemistry.

Ahmed, Hamdi E et al. (2018). "Optimization of thermal design of heat sinks: A review". In: *International Journal of Heat and Mass Transfer* 118, pp. 129–153.

Ahn, Chong H et al. (2004). "Disposable smart lab on a chip for point-of-care clinical diagnostics". In: *Proceedings of the IEEE* 92.1, pp. 154–173.

Ahrberg, Christian D, Andreas Manz, and Bong Geun Chung (2016). "Polymerase chain reaction in microfluidic devices". In: *Lab on a Chip* 16.20, pp. 3866–3884.

Al-Farhany, Khaled and Ammar Abdulkadhim (2018). "Numerical investigation of conjugate natural convection heat transfer in a square porous cavity heated partially from left sidewall". In: *International journal of heat and technology* 36.1, pp. 237–44.

Alkasmoul, Fahad S et al. (2018). "A practical evaluation of the performance of Al2O3-water, TiO2-water and CuO-water nanofluids for convective cooling". In: *International Journal of Heat and Mass Transfer* 126, pp. 639–651.

Amanifard, N et al. (2008). "Modelling and Pareto optimization of heat transfer and flow coefficients in microchannels using GMDH type neural networks and genetic algorithms". In: *Energy Conversion and Management* 49.2, pp. 311–325.

Angus, Scott V et al. (2015). "A portable, shock-proof, surface-heated droplet PCR system for Escherichia coli detection". In: *Biosensors and Bioelectronics* 74, pp. 360–368.

ARCOL (2020). *AP821 20 Watts TO-220 High Power Resistors*. https://www.mouser.co.uk/ datasheet/2/303/AP821-5-14.392-1287906.pdf. Accessed: 2020-07-12.

Arduino (2020). *Arduino*. https://www.arduino.cc/. Accessed: 2020-07-12.

Asthana, Ashish et al. (2011). "Significant Nusselt number increase in microchannels with a segmented flow of two immiscible liquids: An experimental study". In: *International Journal of Heat and Mass Transfer* 54.7-8, pp. 1456–1464.

Athavale, M et al. (2001). "Coupled multiphysics and chemistry simulations of PCR microreactors with active control". In: *Modeling & Simulation Microsystems*.

Audze, Peteris (1977). "New approach to planning out of experiments". In: *Problems of dynamics and strengths* 35, pp. 104–107.

Aziz, Mahdi and Mohammad-H Tayarani-N (2014). "An adaptive memetic Particle Swarm Optimization algorithm for finding large-scale Latin hypercube designs". In: *Engineering Applications of Artificial Intelligence* 36, pp. 222–237.

AZO Materials (2008). *Stainless Steel - Properties and Applications of Grades 310/310s Stainless Steel*. https://www.azom.com/article.aspx?ArticleID=4392. Accessed: 2020-07-12.

Baker, Monya (2012). "Digital PCR hits its stride". In: *nature methods* 9.6, pp. 541–544.

Balakrishnan, Vivekananthan et al. (2018). "A generalized analytical model for Joule heating of segmented wires". In: *Journal of Heat Transfer* 140.7.

Balayssac, Jean-Paul and Vincent Garnier (2017). *Non-destructive testing and evaluation of civil engineering structures*. Elsevier.

Bansal, Vineet et al. (2011). "3-D design, electro-thermal simulation and geometrical optimization of spiral platinum micro-heaters for low power gas sensing applications using COMSOL". In: *Excerpt from the proceeding of the COMSOL Conference Bangalore*.

Barnett, Gregory A, Natasha Flyer, and Louis J Wicker (2015). "An RBF-FD polynomial method based on polyharmonic splines for the Navier-Stokes equations: Comparisons on different node layouts". In: *arXiv preprint arXiv:1509.02615*.

Bates, Stuart, Johann Sienz, and Vassili Toropov (2004). "Formulation of the optimal Latin hypercube design of experiments using a permutation genetic algorithm". In: *45th AIAA/ASME/ASCE/AHS/ASC Structures, Structural Dynamics & Materials Conference*, p. 2011.

Beatson, RK, Michael James David Powell, and AM Tan (2007). "Fast evaluation of polyharmonic splines in three dimensions". In: *IMA Journal of Numerical Analysis* 27.3, pp. 427–450.

Bejan, Adrian and Allan D Kraus (2003). *Heat transfer handbook*. Vol. 1. John Wiley & Sons.

Bengtsson, Martin et al. (2003). "A new minor groove binding asymmetric cyanine reporter dye for real-time PCR". In: *Nucleic acids research* 31.8, e45–e45.

Bennett, Stuart (2000). "The past of PID controllers". In: *IFAC Proceedings Volumes* 33.4, pp. 1–11.

Bhagavan, N.V. (2002). "CHAPTER 23 - Nucleic Acid Structure and Properties of DNA". In: *Medical Biochemistry (Fourth Edition)*. Ed. by N.V. Bhagavan. Fourth Edition. San Diego: Academic Press, pp. 521–543. ISBN: 978-0-12-095440-7. DOI: `https://doi.org/10.1016/B978-012095440-7/50025-1`. URL: `https://www.sciencedirect.com/science/article/pii/B9780120954407500251`.

Bhaskaran, Rajesh and Lance Collins (2002). "Introduction to CFD basics". In: *Cornell University-Sibley School of Mechanical and Aerospace Engineering*, pp. 1–21.

BIO-RAD (2021). *QX100 Droplet Generator*. URL: `https://www.bio-rad.com/webroot/web/pdf/lsr/literature/bulletin_10026322.pdf`. (accessed: 10.03.2021).

Biolabs, New England (2019). *Guidelines for PCR Optimization with Taq DNA Polymerase*. URL: `https://international.neb.com/tools-and-resources/usage-guidelines/guidelines-for-pcr-optimization-with-taq-dna-polymerase`.

Bioscience, Jena (2006). *Aminoallyl-dUTP-XX-AF488*. https://www.jenabioscience.com/nucleotides-nucleosides/nucleotides-by-structure/fluorescent-nucleotides/uridines-dye- labeled/aminoallyl-dutp/nu-803-xx-af488-aminoallyl-dutp-xx-af488. Accessed: 2020-07-12.

Biosystems, Apllied (2004). "Guide to performing relative quantitation of gene expression using real-time quantitative PCR". In: *Applied Biosystems*.

Bista, Dinesh (2016). "Understanding and Design of an Arduino-based PID Controller". In.

Bodey, Isaac T, Rao V Arimilli, and James D Freels (2011). "Complex Geometry Creation and Turbulent Conjugate Heat Transfer Modeling". In: *COMSOL Conference CD, COMSOL Conference Boston*.

Booth, Christine S et al. (2010). "Efficiency of the polymerase chain reaction". In: *Chemical engineering science* 65.17, pp. 4996–5006.

Brisset, S. and F. Gillon (2015). "4 - Approaches for multi-objective optimization in the ecodesign of electric systems". In: *Eco-Friendly Innovation in Electricity Transmission and Distribution Networks*. Ed. by Jean-Luc Bessède. Oxford: Woodhead Publishing, pp. 83–97. ISBN: 978-1-78242-010-1. DOI: `https://doi.org/10.1016/B978-1-78242-010-1.00004-5`. URL: `https://www.sciencedirect.com/science/article/pii/B9781782420101000045`.

Brouzes, Eric et al. (2009). "Droplet microfluidic technology for single-cell high-throughput screening". In: *Proceedings of the National Academy of Sciences* 106.34, pp. 14195–14200.

Bucci, Alessio et al. (2003). "Water single-phase fluid flow and heat transfer in capillary tubes". In: *ASME 2003 1st International Conference on Microchannels and Minichannels*. American Society of Mechanical Engineers, pp. 319–326.

Bustin, Stephen A and Tania Nolan (2004). "Pitfalls of quantitative real-time reverse-transcription polymerase chain reaction". In: *Journal of biomolecular techniques: JBT* 15.3, p. 155.

Caccavale, Paolo, Maria Valeria De Bonis, and Gianpaolo Ruocco (2016). “Conjugate heat and mass transfer in drying: A modeling review”. In: *Journal of Food Engineering* 176, pp. 28–35.

Cao, QingQing, Min-Cheol Kim, and Catherine Klapperich (2011). “Plastic microfluidic chip for continuous-flow polymerase chain reaction: Simulations and experiments”. In: *Biotechnology journal* 6.2, pp. 177–184.

Cavazzuti, Marco (2013). *Optimization Methods: From Theory to Design Scientific and Technological Aspects in Mechanics*. Springer.

Celata, Gian Piero et al. (2002). “Experimental investigation of hydraulic and single-phase heat transfer in 0.130-mm capillary tube”. In: *Microscale Thermophysical Engineering* 6.2, pp. 85–97.

Celata, Gian Piero et al. (2004). *Heat transfer and fluid flow in microchannels*. Begell House New York.

Celata, GP et al. (2006). “Microtube liquid single-phase heat transfer in laminar flow”. In: *International Journal of Heat and Mass Transfer* 49.19-20, pp. 3538–3546.

Chapman, William L et al. (1994). “Arctic sea ice variability: Model sensitivities and a multidecadal simulation”. In: *Journal of Geophysical Research: Oceans* 99.C1, pp. 919–935.

Che, Zhizhao, Teck Neng Wong, and Nam-Trung Nguyen (2012). “Heat transfer enhancement by recirculating flow within liquid plugs in microchannels”. In: *International Journal of Heat and Mass Transfer* 55.7-8, pp. 1947–1956.

— (2013). “Heat transfer in plug flow in cylindrical microcapillaries with constant surface heat flux”. In: *International journal of thermal sciences* 64, pp. 204–212.

Chen, Jyh Jian and Kun Tze Li (2018). “Analysis of PCR Kinetics inside a Microfluidic DNA Amplification System”. In: *Micromachines* 9.2, p. 48.

Chen, Ray-Bing et al. (2013). “Optimizing Latin hypercube designs by particle swarm”. In: *Statistics and computing* 23.5, pp. 663–676.

Chen, Xiangning and Pui-Yan Kwok (1999). “Homogeneous genotyping assays for single nucleotide polymorphisms with fluorescence resonance energy transfer detection”. In: *Genetic analysis: biomolecular engineering* 14.5-6, pp. 157–163.

Cheng, Suzanne et al. (1994). “Effective amplification of long targets from cloned inserts and human genomic DNA”. In: *Proceedings of the National Academy of Sciences* 91.12, pp. 5695–5699.

Choi, KK, Byeng D Youn, and Ren-Jye Yang (2001). “Moving least square method for reliability-based design optimization”. In: *Proc. 4th World Cong. Structural & Multidisciplinary Optimization*.

COMSOL (2014). *Conjugate Heat Transfer*. URL: `https://www.comsol.com/blogs/conjugate-heat-transfer/`. (accessed: 02.05.2022).

— (2018a). *Fluid Flow: Conservation of Momentum, Mass, and Energy*. URL: `https://www.comsol.com/multiphysics/fluid-flow-conservation-of-momentum-mass-and-energy\#1`.

— (2018b). *Heat Transfer: Conservation of Energy*. URL: `https://www.comsol.com/multiphysics/heat-transfer-conservation-of-energy`. (accessed: 23.05.2019).

— (2022). *COMSOL Multiphysics Simulation Software*. `https://www.comsol.com/comsol-multiphysics`. Accessed: 2022-01-09.

CUI Devices (2019). *Peltier module: CP85*. https://www.cuidevices.com/product/resource/cp85.pdf. Accessed: 2020-07-12.

Dai, Zhenhui et al. (2015). "Taylor flow heat transfer in microchannels—Unification of liquid–liquid and gas–liquid results". In: *Chemical Engineering Science* 138, pp. 140–152.

Dalton, Tara M, David J Kinahan, and Mark R Davies (2005). "Fluorescent melting curve analysis compatible with a flowing polymerase chain reactor". In: *ASME International Mechanical Engineering Congress and Exposition*. Vol. 42134, pp. 31–36.

Damblin, Guillaume, Mathieu Couplet, and Bertrand Iooss (2013). "Numerical studies of space-filling designs: optimization of Latin Hypercube Samples and subprojection properties". In: *Journal of Simulation* 7.4, pp. 276–289.

Dandin, Marc, Pamela Abshire, and Elisabeth Smela (2007). "Optical filtering technologies for integrated fluorescence sensors". In: *Lab on a Chip* 7.8, pp. 955–977.

D'Auria, Francesco (2017). *Thermal-hydraulics of water cooled nuclear reactors*. woodhead publishing.

Dede, Ercan M, Shailesh N Joshi, and Feng Zhou (2015). "Topology optimization, additive layer manufacturing, and experimental testing of an air-cooled heat sink". In: *Journal of Mechanical Design* 137.11.

Dinca, Mihai P et al. (2009). "Fast and accurate temperature control of a PCR microsystem with a disposable reactor". In: *Journal of Micromechanics and Microengineering* 19.6, p. 065009.

Ding, J and RM Manglik (1996). "Analytical solutions for laminar fully developed flows in double-sine shaped ducts". In: *Heat and Mass Transfer* 31.4, pp. 269–277.

dolomite (2021). *T-Junction Chip*. URL: `https://www.dolomite-microfluidics.com/product/t-junction-chip/`. (accessed: 02.11.2021).

Dong, Xiaobin et al. (2021). "Rapid PCR powered by microfluidics: A quick review under the background of COVID-19 pandemic". In: *TrAC Trends in Analytical Chemistry*, p. 116377.

Dorak, M Tevfik (2007). *Real-time PCR*. Taylor & Francis.

Duan, Zhipeng and MM Yovanovich (2009). "Pressure drop for laminar flow in microchannels of arbitrary cross-sections". In: *2009 25th Annual IEEE Semiconductor Thermal Measurement and Management Symposium*. IEEE, pp. 111–120.

Duryodhan, VS, Shiv Govind Singh, and Amit Agrawal (2013). "Liquid flow through a diverging microchannel". In: *Microfluidics and nanofluidics* 14, pp. 53–67.

Duryodhan, VS et al. (2016). "A simple and novel way of maintaining constant wall temperature in microdevices". In: *Scientific reports* 6, p. 18230.

Eain, Marc Mac Giolla, Vanessa Egan, and Jeff Punch (2015). "Local Nusselt number enhancements in liquid–liquid Taylor flows". In: *International Journal of Heat and Mass Transfer* 80, pp. 85–97.

Eckert, Ernst Rudolf Georg and Robert M Drake Jr (1987). "Analysis of heat and mass transfer". In.

Emmert-Streib, Frank et al. (2020). "An introductory review of deep learning for prediction models with big data". In: *Frontiers in Artificial Intelligence* 3, p. 4.

Erdogan, Turan (2011). "Optical filters for wavelength selection in fluorescence instrumentation". In: *Current protocols in cytometry* 56.1, pp. 2–4.

Faghri, Amir, Yuwen Zhang, and John R Howell (2010). *Advanced heat and mass transfer*. Global Digital Press.

Fajrial, Apresio Kefin et al. (2021). "A frugal microfluidic pump". In: *Lab on a Chip*.

Fang, Kai-Tai, Chang-Xing Ma, and Peter Winker (2002). "Centered L_2-discrepancy of random sampling and Latin hypercube design, and construction of uniform designs". In: *Mathematics of Computation* 71.237, pp. 275–296.

Farnaghi, Sepehr (2017). "Optimization of Polymerase Chain Reaction Machine". PhD thesis.

Farnell (2020). *IEC Mineral Insulated Thermocouple with Miniature Plug*. http://www.farnell.com/datasheets/1918886.pdf?_ga=2.265245263.1570869930.158455572 8 - 846861914.158443 8197. Accessed: 2020-07-12.

Farrar, Jared S and CT Wittwer (2017). "High-resolution melting curve analysis for molecular diagnostics". In: *Molecular diagnostics*. Elsevier, pp. 79–102.

Firouzi, M and SH Hashemabadi (2009). "Analytical solution for Newtonian laminar flow through the concave and convex ducts". In: *Journal of Fluids Engineering* 131.9, p. 094501.

Fischer, Magnus, Damir Juric, and Dimos Poulikakos (2010). "Large convective heat transfer enhancement in microchannels with a train of coflowing immiscible or colloidal droplets". In: *Journal of Heat Transfer* 132.11, p. 112402.

Fisher, Timothy S and Kenneth E Torrance (2001). "Optimal shapes of fully embedded channels for conjugate cooling". In: *IEEE Transactions on advanced packaging* 24.4, pp. 555–562.

Fluidigm Corporation (2015). *Melting Curve Analysis*. https://www.fluidigm.com/binaries/content/documents/ fluidigm/resources/melting-curve-analysis-ug - 68000118/melting-curve-analysis-ug - 68000118/fluidigm%3Afile. Accessed: 2020-06-24.

Frank-Kamenetskii, MD (1971). "Simplification of the empirical relationship between melting temperature of DNA, its GC content and concentration of sodium ions in solution". In: *Biopolymers: Original Research on Biomolecules* 10.12, pp. 2623–2624.

Gad, Ahmed Fawzy, Ahmed Fawzy Gad, and Suresh John (2018). *Practical computer vision applications using deep learning with CNNs*. Springer.

Ganguli, Arijit A and Aniruddha B Pandit (2021). “Hydrodynamics of Liquid-Liquid Flows in Micro Channels and Its Influence on Transport Properties: A Review”. In: *Energies* 14.19, p. 6066.

Garud, Sushant S, Iftekhar A Karimi, and Markus Kraft (2017). “Design of computer experiments: A review”. In: *Computers & Chemical Engineering* 106, pp. 71–95.

Gerbeau, J-F and Claude Le Bris (2000). “A basic remark on some Navier-Stokes equations with body forces”. In: *Applied Mathematics Letters* 13.3, pp. 107–112.

Giunta, Anthony, Steven Wojtkiewicz, and Michael Eldred (2003). “Overview of modern design of experiments methods for computational simulations”. In: *41st Aerospace Sciences Meeting and Exhibit*, p. 649.

Goldberg, Norman (1984). “Narrow channel forced air heat sink”. In: *IEEE transactions on components, hybrids, and manufacturing technology* 7.1, pp. 154–159.

Grosso, Andrea, ARMJU Jamali, and Marco Locatelli (2009). “Finding maximin latin hypercube designs by iterated local search heuristics”. In: *European Journal of Operational Research* 197.2, pp. 541–547.

Hadzhiev, Ivan, Ivan Yatchev, and Emil Mechkov (2018). “Conjugate Heat Transfer Analysis Using 3D FEM Model of an Oil-immersed Distribution Transformer”. In: *2018 International Conference on High Technology for Sustainable Development (HiTech)*. IEEE, pp. 1–4.

Haertel, Jan Hendrik Klaas et al. (2015). “Topology optimization of thermal heat sinks”. In: *Proceedings of COMSOL conference*. Vol. 2015.

Hajmohammadi, MR, P Alipour, and H Parsa (2018). “Microfluidic effects on the heat transfer enhancement and optimal design of microchannels heat sinks”. In: *International Journal of Heat and Mass Transfer* 126, pp. 808–815.

Hamad, Hazim S et al. (2021a). “CFD-Enabled Optimization of Polymerase Chain Reaction Thermal Flow Systems”. In: *Advances in Heat Transfer and Thermal Engineering*. Springer, pp. 409–416.

Hamad, Hazim S et al. (2021b). “Computational fluid dynamics analysis and optimisation of polymerase chain reaction thermal flow systems”. In: *Applied Thermal Engineering* 183, p. 116122.

Handbook, Structural Alloys et al. (1996). “CINDAS/Purdue University”. In: *West Lafayette, Ind, USA*.

Harvey, Richard A, Denise R Ferrier, et al. (2011). “Lippincott’s illustrated reviews: Biochemistry”. In.

Hatch, Andrew C et al. (2014). “Continuous flow real-time PCR device using multichannel fluorescence excitation and detection”. In: *Lab on a Chip* 14.3, pp. 562–568.

Hauser, Julia S et al. (2016). “Controlled electromigration and oxidation of freestanding copper wires”. In: *Applied Physics A* 122.12, p. 1068.

Hayes, Christopher J and Tara M Dalton (2015). “Microfluidic droplet-based PCR instrumentation for high-throughput gene expression profiling and biomarker discovery”. In: *Biomolecular detection and quantification* 4, pp. 22–32.

Haynie, Donald T (2001). *Biological thermodynamics*. Cambridge University Press.

He, Ziqiang, Yunfei Yan, and Zhien Zhang (2020). "Thermal management and temperature uniformity enhancement of electronic devices by micro heat sinks: A review". In: *Energy*, p. 119223.

— (2021). "Thermal management and temperature uniformity enhancement of electronic devices by micro heat sinks: A review". In: *Energy* 216, p. 119223.

Heid, Christian A et al. (1996). "Real time quantitative PCR." In: *Genome research* 6.10, pp. 986–994.

Herwig, H and O Hausner (2003). "Critical view on "new results in micro-fluid mechanics": an example". In: *International Journal of Heat and Mass Transfer* 46.5, pp. 935–937.

Hetsroni, G et al. (2005a). "Fluid flow in micro-channels". In: *International Journal of Heat and Mass Transfer* 48.10, pp. 1982–1998.

— (2005b). "Heat transfer in micro-channels: Comparison of experiments with theory and numerical results". In: *International Journal of Heat and Mass Transfer* 48.25-26, pp. 5580–5601.

Hindson, Benjamin J et al. (2011). "High-throughput droplet digital PCR system for absolute quantitation of DNA copy number". In: *Analytical chemistry* 83.22, pp. 8604–8610.

Holmes, DB and JR Vermeulen (1968). "Velocity profiles in ducts with rectangular cross sections". In: *Chemical Engineering Science* 23.7, pp. 717–722.

Holtze, C et al. (2008). "Biocompatible surfactants for water-in-fluorocarbon emulsions". In: *Lab on a Chip* 8.10, pp. 1632–1639.

Howell, W Mathias, Magnus Jobs, and Anthony J Brookes (2002). "iFRET: an improved fluorescence system for DNA-melting analysis". In: *Genome research* 12.9, pp. 1401–1407.

Hsieh, Tsung-Min et al. (2008). "Enhancement of thermal uniformity for a microthermal cycler and its application for polymerase chain reaction". In: *Sensors and Actuators B: Chemical* 130.2, pp. 848–856. ISSN: 0925-4005. DOI: `https://doi.org/10.1016/j.snb.2007.10.063`. URL: `https://www.sciencedirect.com/science/article/pii/S0925400507008842`.

Hunicke-Smith, Scott P (1998). "PCR and cycle sequencing reactions: A new device and engineering model." In.

Husain, Afzal and Kwang-Yong Kim (2007). "Design Optimization of Micro-Channel for Micro Electronic Cooling". In: *ASME 2007 5th International Conference on Nanochannels, Microchannels, and Minichannels*. American Society of Mechanical Engineers, pp. 201–207.

— (2008a). "Multiobjective optimization of a microchannel heat sink using evolutionary algorithm". In: *Journal of Heat Transfer* 130.11, p. 114505.

— (2008b). "Optimization of a microchannel heat sink with temperature dependent fluid properties". In: *Applied thermal engineering* 28.8-9, pp. 1101–1107.

— (2008c). “Shape optimization of micro-channel heat sink for micro-electronic cooling”. In: *IEEE Transactions on Components and Packaging Technologies* 31.2, pp. 322–330.

— (2010). “Enhanced multi-objective optimization of a microchannel heat sink through evolutionary algorithm coupled with multiple surrogate models”. In: *Applied Thermal Engineering* 30.13, pp. 1683–1691.

Husslage, Bart GM et al. (2011). “Space-filling Latin hypercube designs for computer experiments”. In: *Optimization and Engineering* 12.4, pp. 611–630.

Huyer, Waltraud and Arnold Neumaier (1999). “Global optimization by multilevel coordinate search”. In: *Journal of Global Optimization* 14.4, pp. 331–355.

Innis, Michael A et al. (2012). *PCR protocols: a guide to methods and applications*. Academic press.

Innovatek (2010). *Arctic Silver 5*. https://asset.conrad.com/media10/add/160267/c1/-/en/000150352DS02/datasheet-150352-arctic-silver-arctic-silver-5-thermally-conductive-paste-89-wmk-35-g-max-temperature-130-c.pdf. Accessed: 2020-07-12.

Ishiguro, Takahiko et al. (1995). “Homogeneous quantitative assay of hepatitis C virus RNA by polymerase chain reaction in the presence of a fluorescent intercalater”. In: *Analytical biochemistry* 229.2, pp. 207–213.

Jin, Ruichen, Wei Chen, and Agus Sudjianto (2003). “An efficient algorithm for constructing optimal design of computer experiments”. In: *International Design Engineering Technical Conferences and Computers and Information in Engineering Conference*. Vol. 37009, pp. 545–554.

Jones, Donald R, Matthias Schonlau, and William J Welch (1998). “Efficient global optimization of expensive black-box functions”. In: *Journal of Global optimization* 13.4, pp. 455–492.

Joo, Younghwan, Ikjin Lee, and Sung Jin Kim (2017). “Topology optimization of heat sinks in natural convection considering the effect of shape-dependent heat transfer coefficient”. In: *International Journal of Heat and Mass Transfer* 109, pp. 123–133.

Julie (2012). *Surrogate Model Optimization Toolbox, MATLAB Central File Exchange*. URL: `https://www.mathworks.com/matlabcentral/fileexchange/38530-surrogate-model-optimization-toolbox`. (accessed: 14.05.2020).

Kainz, Peter (2000). “The PCR plateau phase–towards an understanding of its limitations”. In: *Biochimica et Biophysica Acta (BBA)-Gene Structure and Expression* 1494.1-2, pp. 23–27.

Kang, J et al. (2006). “Simulation and optimization of a flow-through micro PCR chip”. In: *Nanotech (ed) NSTI Nanotech. Nanotech, Boston, Massachusetts*, pp. 585–588.

Kaprou, Georgia D et al. (2019). “Ultrafast, low-power, PCB manufacturable, continuous-flow microdevice for DNA amplification”. In: *Analytical and bioanalytical chemistry* 411.20, pp. 5297–5307.

Karsai, Albert et al. (2002). "Evaluation of a homemade SYBR® Green I reaction mixture for real-time PCR quantification of gene expression". In: *Biotechniques* 32.4, pp. 790–796.

Kawano, K et al. (1998). "Application of Heat Transfer in Equipment Systems, and Education". In: *Development of microchannels heat exchanging, RA Nelson Jr., LW Swanson, MVA Bianchi, and C. Camci, Eds. New York: ASME* 361, p. 3.

Keane, Andy and Prasanth Nair (2005). *Computational approaches for aerospace design: the pursuit of excellence*. John Wiley & Sons.

Kenny, Q Ye, William Li, and Agus Sudjianto (2000). "Algorithmic construction of optimal symmetric Latin hypercube designs". In: *Journal of statistical planning and inference* 90.1, pp. 145–159.

Keohavong, Phouthone and William G Thilly (1989). "Fidelity of DNA polymerases in DNA amplification". In: *Proceedings of the National Academy of Sciences* 86.23, pp. 9253–9257.

Kim, Sobin and Ashish Misra (2007). "SNP genotyping: technologies and biomedical applications". In: *Annu. Rev. Biomed. Eng.* 9, pp. 289–320.

Kim, Sung Jin (2004). "Methods for thermal optimization of microchannel heat sinks". In: *Heat transfer engineering* 25.1, pp. 37–49.

Kinahan, David J, Tara M Dalton, and Mark R Davies (2008). "Microchannel Fluorescent Melting Curve Analysis". In: *ASME 2008 6th International Conference on Nanochannels, Microchannels, and Minichannels*. American Society of Mechanical Engineers Digital Collection, pp. 1579–1585.

Kleijnen, Jack PC (2017). "Regression and Kriging metamodels with their experimental designs in simulation: a review". In: *European Journal of Operational Research* 256.1, pp. 1–16.

Knight, Roy W et al. (1992). "Heat sink optimization with application to microchannels". In: *IEEE Transactions on Components, Hybrids, and Manufacturing Technology* 15.5, pp. 832–842.

Knight, RW, JS Goodling, and DJ Hall (1991). "Optimal thermal design of forced convection heat sinks-analytical". In: *Journal of Electronic Packaging* 113.3, pp. 313–321.

Koehn, Philipp (1994). "Combining genetic algorithms and neural networks: The encoding problem". In.

Koo, J and C Kleinstreuer (2004). "Viscous dissipation effects in microtubes and microchannels". In: *International Journal of Heat and Mass Transfer* 47.14-16, pp. 3159–3169.

Kopp, Martin U, H John Crabtree, and Andreas Manz (1997). "Developments in technology and applications of microsystems". In: *Current Opinion in Chemical Biology* 1.3, pp. 410–419. ISSN: 1367-5931. DOI: `https://doi.org/10.1016/S1367-5931(97)80081-6`. URL: `https://www.sciencedirect.com/science/article/pii/S1367593197800816`.

Kopp, Martin U, Andrew J De Mello, and Andreas Manz (1998). “Chemical amplification: continuous-flow PCR on a chip”. In: *Science* 280.5366, pp. 1046–1048.

Kosky, Philip et al. (2013). “Chapter 12 - Mechanical Engineering”. In: *Exploring Engineering (Third Edition)*. Ed. by Philip Kosky et al. Third Edition. Boston: Academic Press, pp. 259–281. ISBN: 978-0-12-415891-7. DOI: `https://doi.org/10.1016/B978-0-12-415891-7.00012-1`. URL: `https://www.sciencedirect.com/science/article/pii/B9780124158917000121`.

Kulkarni, Madhusudan B, Mary Salve, and Sanket Goel (2021). “Miniaturized Thermal Monitoring Module With CO_2 Laser Ablated Microfluidic Device for Electrochemically Validated DNA Amplification”. In: *IEEE Transactions on Instrumentation and Measurement* 70, pp. 1–8.

Kulkarni, Madhusudan B et al. (2021). “Miniaturized and IoT enabled continuous-flow based microfluidic PCR device for DNA amplification”. In: *IEEE Transactions on NanoBioscience*.

Kumar, Sunil et al. (2018). “A review of flow and heat transfer behaviour of nanofluids in micro channel heat sinks”. In: *Thermal Science and Engineering Progress* 8, pp. 477–493.

Lee, Doojin et al. (2017). “Temperature controlled tensiometry using droplet microfluidics”. In: *Lab on a Chip* 17.4, pp. 717–726.

Lee, Manhee et al. (2014). “Synchronized reinjection and coalescence of droplets in microfluidics”. In: *Lab on a Chip* 14.3, pp. 509–513.

Leeds, University of (2021). *Bio-imaging equipment: Zeiss LSM880 + Airyscan Upright Confocal Microscope*. URL: `https://biologicalsciences.leeds.ac.uk/facilities/doc/bio-imaging-equipment/page/6/`. (accessed: 02.11.2021).

Leijnen, Stefan and Fjodor van Veen (2020). “The Neural Network Zoo”. In: *Multidisciplinary Digital Publishing Institute Proceedings*. Vol. 47. 1, p. 9.

Lelea, Dorin, Shigefumi Nishio, and Kiyoshi Takano (2004). “The experimental research on microtube heat transfer and fluid flow of distilled water”. In: *International Journal of Heat and Mass Transfer* 47.12-13, pp. 2817–2830.

Levy, Sigal and David M Steinberg (2010). “Computer experiments: a review”. In: *AStA Advances in Statistical Analysis* 94.4, pp. 311–324.

Li, Hao et al. (2019a). “Experimental and numerical investigation of liquid-cooled heat sinks designed by topology optimization”. In: *International Journal of Thermal Sciences* 146, p. 106065.

Li, Honghua et al. (1988). “Amplification and analysis of DNA sequences in single human sperm and diploid cells”. In: *Nature* 335.6189, p. 414.

Li, Hung-Yi and Shung-Ming Chao (2009). “Measurement of performance of plate-fin heat sinks with cross flow cooling”. In: *International Journal of Heat and Mass Transfer* 52.13-14, pp. 2949–2955.

Li, Hung-Yi et al. (2010). “Thermal performance of plate-fin vapor chamber heat sinks”. In: *International Communications in Heat and Mass Transfer* 37.7, pp. 731–738.

Li, Kan-Chien et al. (2014). "Melting analysis on microbeads in rapid temperature-gradient inside microchannels for single nucleotide polymorphisms detection". In: *Biomicrofluidics* 8.6, p. 064109.

Li, Xinlong et al. (2021). "Heat transfer enhancement of droplet two-phase flow in cylindrical microchannel". In: *Applied Thermal Engineering* 186, p. 116474.

Li, Yaping et al. (2019b). "An artificial neural network assisted optimization system for analog design space exploration". In: *IEEE Transactions on Computer-Aided Design of Integrated Circuits and Systems* 39.10, pp. 2640–2653.

Liefvendahl, Mattias and Rafał Stocki (2006). "A study on algorithms for optimization of Latin hypercubes". In: *Journal of statistical planning and inference* 136.9, pp. 3231–3247.

Liu, Dong and Suresh V Garimella (2004). "Investigation of liquid flow in microchannels". In: *Journal of Thermophysics and heat transfer* 18.1, pp. 65–72.

Liu, F-W et al. (2017). "Automated melting curve analysis in droplet microfluidics for single nucleotide polymorphisms (SNP) genotyping". In: *RSC advances* 7.8, pp. 4646–4655.

Liu, F-W et al. (2018). "DNA methylation assay using droplet-based DNA melting curve analysis". In: *Lab on a Chip* 18.3, pp. 514–521.

Liu, Jia-Hong et al. (2019). "Microtubule polymerization in alignment by an on-chip temperature gradient platform". In: *Sensors and Actuators B: Chemical* 298, p. 126813.

Liu, Songsong and Lazaros G Papageorgiou (2013). "Multiobjective optimisation of production, distribution and capacity planning of global supply chains in the process industry". In: *Omega* 41.2, pp. 369–382.

Liu, Weihong and David A Saint (2002). "Validation of a quantitative method for real time PCR kinetics". In: *Biochemical and biophysical research communications* 294.2, pp. 347–353.

Liu, Wen wen and Ying Zhu (2020). ""Development and application of analytical detection techniques for droplet-based microfluidics"-A review". In: *Analytica Chimica Acta* 1113, pp. 66–84. ISSN: 0003-2670. DOI: `https://doi.org/10.1016/j.aca.2020.03.011`. URL: `https://www.sciencedirect.com/science/article/pii/S0003267020303184`.

Liu, Wen-Wen, Ying Zhu, and Qun Fang (2017). "Femtomole-scale high-throughput screening of protein ligands with droplet-based thermal shift assay". In: *Analytical chemistry* 89.12, pp. 6678–6685.

Loeppky, Jason L, Jerome Sacks, and William J Welch (2009). "Choosing the sample size of a computer experiment: A practical guide". In: *Technometrics* 51.4, pp. 366–376.

Logan, Julie et al. (2009). *Real-time PCR: current technology and applications*. Horizon Scientific Press.

Long, Teng et al. (2016). "A deterministic sequential maximin Latin hypercube design method using successive local enumeration for metamodel-based optimization". In: *Engineering Optimization* 48.6, pp. 1019–1036.

Ma, Haiyun et al. (2021). "Effect of fluid viscosities on the liquid-liquid slug flow and pressure drop in a rectangular microreactor". In: *Chemical Engineering Science* 241, p. 116697.

Manriquez-Sandoval, Edgar (2021). *K-Fold Cross Validation with & without Random Shuffle Data*. URL: `https://www.mathworks.com/matlabcentral/fileexchange/68274-k-fold-cross-validation-with-without-random-shuffle-data`. (accessed: 32.01.2021).

Mathworks (2019). *MATLAB Optimization Toolbox*. URL: `https://uk.mathworks.com/matlabcentral/fileexchange/38530-surrogate-model-optimization-toolbox`.

MathWorks (2020a). *Feedforward neural network*. https://uk.mathworks.com/help/deep learning/ref/feedforwardnet.html. Accessed: 2020-07-12.

— (2020b). *Find Pareto front of multiple fitness functions using genetic algorithm*. https://uk.mathworks.com/help/gads/gamultiobj.html. Accessed: 2020-07-12.

— (2020c). *Function fitting neural network*. https://uk.mathworks.com/help/deeple arning /ref/fitnet.html. Accessed: 2020-07-12.

— (2021). *Genetic Algorithm*. URL: `https://uk.mathworks.com/help/gads/ga.html`. (accessed: 06.01.2021).

Matlab & Simulink, Control Tutorials for (2021). *Introduction: PID Controller Design*. URL: `https://ctms.engin.umich.edu/CTMS/index.php?example=Introduction\&section=ControlPID`.

Matmatch (2020). *Borosilicate Glass: Properties, Production and Applications*. https://matmatch.com/learn/material/borosilicate-glass. Accessed: 2020-07-12.

Matsuda, Kazuyuki (2017). "Chapter Two - PCR-Based Detection Methods for Single-Nucleotide Polymorphism or Mutation: Real-Time PCR and Its Substantial Contribution Toward Technological Refinement". In: ed. by Gregory S. Makowski. Vol. 80. Advances in Clinical Chemistry. Elsevier, pp. 45–72. DOI: `https://doi.org/10.1016/bs.acc.2016.11.002`. URL: `https://www.sciencedirect.com/science/article/pii/S0065242316300981`.

McDonough, JM (2009). "Lectures in elementary fluid dynamics". In: *University of Kentucky, Lexington, KY*, pp. 40506–0503.

Mehra, Sarika and Wei-Shou Hu (2005). "A kinetic model of quantitative real-time polymerase chain reaction". In: *Biotechnology and bioengineering* 91.7, pp. 848–860.

Meseguer, José, Isabel Pérez-Grande, and Angel Sanz-Andrés (2012). *Spacecraft thermal control*. Elsevier.

Meuer, Stefan, Carl Wittwer, and Kan-Ichi Nakagawara (2012). *Rapid cycle real-time PCR: methods and applications*. Springer Science & Business Media.

Millgard, Lars OA (1992). *Method to measure a temperature with a peltier element*. US Patent 5,143,451.

Mishra, Rajesh, Jiri Militky, and Mohanapriya Venkataraman (2019). "7 - Nanoporous materials". In: *Nanotechnology in Textiles*. Ed. by Rajesh Mishra and Jiri Militky. The Textile Institute Book Series. Woodhead Publishing, pp. 311–353. ISBN: 978-0-08-102609-0. DOI: `https://doi.org/10.1016/B978-0-08-102609-0.00007-9`. URL: `https://www.sciencedirect.com/science/article/pii/B9780081026090000079`.

Mohammed Adham, Ahmed, Normah Mohd-Ghazali, and Robiah Ahmad (2013). "Thermal and hydrodynamic analysis of microchannel heat sinks: A review". In: *Renewable and Sustainable Energy Reviews* 21, pp. 614–622. ISSN: 1364-0321. DOI: `https://doi.org/10.1016/j.rser.2013.01.022`. URL: `https://www.sciencedirect.com/science/article/pii/S1364032113000531`.

Moharana, Manoj Kumar, Piyush Kumar Singh, and Sameer Khandekar (2012). "Optimum Nusselt number for simultaneously developing internal flow under conjugate conditions in a square microchannel". In: *Journal of Heat Transfer* 134.7, p. 071703.

Mohr, S et al. (2006). "Optimal design and operation for a droplet-based PCR chip". In: *ASME 4th International Conference on Nanochannels, Microchannels, and Minichannels*. American Society of Mechanical Engineers, pp. 649–656.

Mollajan, Mina, Ali Abouei Mehrizi, and Sajad Razavi Bazaz (2016). "A novel microfluidic two-level droplet PCR for DNA amplification". In: *2016 23rd Iranian Conference on Biomedical Engineering and 2016 1st International Iranian Conference on Biomedical Engineering (ICBME)*. IEEE, pp. 276–280.

Mommert, Susanne et al. (2001). "Sensitive Detection of Borrelia burgdorferi Sensu Lato DNA and Differentiation ofBorrelia Species by LightCycler PCR". In: *Journal of clinical microbiology* 39.7, pp. 2663–2667.

Monis, Paul T, Steven Giglio, and Christopher P Saint (2005). "Comparison of SYTO9 and SYBR Green I for real-time polymerase chain reaction and investigation of the effect of dye concentration on amplification and DNA melting curve analysis". In: *Analytical biochemistry* 340.1, pp. 24–34.

Monjezi, Saman et al. (2017). "Computational studies of DNA separations in microfabricated devices: Review of general approaches and recent applications". In: *Advances in Chemical Engineering and Science* 7.04, p. 362.

Morini, Gian Luca (2004). "Single-phase convective heat transfer in microchannels: a review of experimental results". In: *International journal of thermal sciences* 43.7, pp. 631–651.

Morris, Max D and Toby J Mitchell (1995). "Exploratory designs for computational experiments". In: *Journal of statistical planning and inference* 43.3, pp. 381–402.

Moschou, Despina et al. (2014). "All-plastic, low-power, disposable, continuous-flow PCR chip with integrated microheaters for rapid DNA amplification". In: *Sensors and Actuators B: Chemical* 199, pp. 470–478.

Mour, Meenakshi, Debarun Das, and Amar N Mullick (2010). “Characteristics of Fluid Flow through Microchannels”. In: *AIP Conference Proceedings*. Vol. 1298. 1. AIP, pp. 71–79.

Mullis, Kary B and Fred A Faloona (1989). “Specific synthesis of DNA in vitro via a polymerase-catalyzed chain reaction”. In: *Recombinant DNA Methodology*. Elsevier, pp. 189–204.

Myers, Raymond H, Douglas C Montgomery, and Christine M Anderson-Cook (2016). *Response surface methodology: process and product optimization using designed experiments*. John Wiley & Sons.

NAG (2020). *NAG Library Function Document: nag_glopt_bnd_mcs_solve (e05jbc)*. https://www.nag.co.uk/numeric/cl/nagdoc_cl26/pdf/e05/e05jbc.pdf. Accessed: 2020-07-12.

Nath, Kamalendu et al. (2000). “Effects of ethidium bromide and SYBR® Green I on different polymerase chain reaction systems”. In: *Journal of biochemical and biophysical methods* 42.1-2, pp. 15–29.

Newton, Clive R, Alex Graham, and Jane S Ellison (1997). *PcR*. BIOS Scientific Publishers Oxford, UK.

Nguyen, Nam-Trung, Steven T Wereley, and Seyed Ali Mousavi Shaegh (2019). *Fundamentals and applications of microfluidics*. Artech house.

Nicolas, Luc, Geneviève Milon, and Eric Prina (2002). “Rapid differentiation of Old World Leishmania species by LightCycler polymerase chain reaction and melting curve analysis”. In: *Journal of microbiological methods* 51.3, pp. 295–299.

Northrup, MA et al. (1993). “A memsbased miniature DNA analysis system, in transducers 93”. In: *seventh international conference on solid state sensors and actuators*, pp. 924–926.

Obot, NT (2002). “Toward a better understanding of friction and heat/mass transfer in microchannels–a literature review”. In: *Microscale Thermophysical Engineering* 6.3, pp. 155–173.

Ortega, Alfonso, U Wirth, and SungJin Kim (1994). “Conjugate Forced Convection from a Discrete Heat Source on a Plane Conducting Surface, A Benchmark Experiment”. In: *International Mechanical Engineering Congress and exposition*, pp. 25–36.

Owen, RJ, LR Hill, and SP Lapage (1969). “Determination of DNA base compositions from melting profiles in dilute buffers”. In: *Biopolymers: Original Research on Biomolecules* 7.4, pp. 503–516.

Palais, Robert and Carl T Wittwer (2009). “Mathematical algorithms for high-resolution DNA melting analysis”. In: *Methods in enzymology* 454, pp. 323–343.

Palm, B and XF Peng (2004). “Single-phase convective heat transfer”. In: *Heat Transfer and Fluid Flow in Microchannels*.

Palm, Björn (2001). “Heat transfer in microchannels”. In: *Microscale Thermophysical Engineering* 5.3, pp. 155–175.

Pan, Guang, Pengcheng Ye, and Peng Wang (2014). “A novel Latin hypercube algorithm via translational propagation”. In: *The Scientific World Journal* 2014.

Panjkovich, Alejandro and Francisco Melo (2005). “Comparison of different melting temperature calculation methods for short DNA sequences”. In: *Bioinformatics* 21.6, pp. 711–722.

Papadopoulos, Vasileios E et al. (2015). “Comparison of continuous-flow and static-chamber μPCR devices through a computational study: the potential of flexible polymeric substrates”. In: *Microfluidics and Nanofluidics* 19.4, pp. 867–882.

Park, Jaehyun and Heesung Park (2017). “Thermal cycling characteristics of a 3D-printed serpentine microchannel for DNA amplification by polymerase chain reaction”. In: *Sensors and Actuators A: Physical* 268, pp. 183–187.

Park, Jeong-Soo (1994). “Optimal Latin-hypercube designs for computer experiments”. In: *Journal of statistical planning and inference* 39.1, pp. 95–111.

Patrinos, George P and Wilhelm J Ansorge (2010). “Molecular Diagnostics: Past, Present, and Future”. In: *Molecular Diagnostics*. Elsevier, pp. 1–11.

Perwez, Usama et al. (2019). “Numerical Investigation of Design and Operating Parameters of Thermal Gradient Continuous-Flow PCR Microreactor Using One Heater”. In: *Processes* 7.12, p. 919.

Pfaffl, Michael W et al. (2004). “Quantification strategies in real-time PCR”. In: *AZ of quantitative PCR* 1, pp. 89–113.

Pham, HM et al. (2005). “Rapid detection and differentiation of Newcastle disease virus by real-time PCR with melting-curve analysis”. In: *Archives of virology* 150.12, pp. 2429–2438.

Pholdee, Nantiwat and Sujin Bureerat (2015). “An efficient optimum Latin hypercube sampling technique based on sequencing optimisation using simulated annealing”. In: *International Journal of Systems Science* 46.10, pp. 1780–1789.

Piatek, Amy S et al. (1998). “Molecular beacon sequence analysis for detecting drug resistance in Mycobacterium tuberculosis”. In: *Nature biotechnology* 16.4, pp. 359–363.

Pierreval, Henri (1996). “A metamodeling approach based on neural networks”. In: *Int. Journal in Computer Simulation* 6.3, p. 365.

Pietilä, Johanna et al. (2000). “Rapid differentiation of Borrelia garinii from Borrelia afzelii and Borrelia burgdorferi sensu stricto by LightCycler fluorescence melting curve analysis of a PCR product of the recA gene”. In: *Journal of clinical microbiology* 38.7, pp. 2756–2759.

Pinheiro, Leonardo B et al. (2012). “Evaluation of a droplet digital polymerase chain reaction format for DNA copy number quantification”. In: *Analytical chemistry* 84.2, pp. 1003–1011.

Pješčić, Ilija et al. (2010). “Glass-composite prototyping for flow PCR with in situ DNA analysis”. In: *Biomedical microdevices* 12.2, pp. 333–343.

Platts, Adrian E et al. (2008). “Real-time PCR quantification using a variable reaction efficiency model”. In: *Analytical Biochemistry* 380.2, pp. 315–322.

Priye, Aashish, Yassin A Hassan, and Victor M Ugaz (2013). "Microscale chaotic advection enables robust convective DNA replication". In: *Analytical chemistry* 85.21, pp. 10536–10541.

Queipo-Ortuño, MI et al. (2005). "Rapid diagnosis of human brucellosis by SYBR Green I-based real-time PCR assay and melting curve analysis in serum samples". In: *Clinical microbiology and infection* 11.9, pp. 713–718.

Radadia, Adarsh D. (2008). "Microfluidics for Biochemical and Chemical Reactions". In: *Encyclopedia of Microfluidics and Nanofluidics*. Ed. by Dongqing Li. Boston, MA: Springer US, pp. 1195–1207. ISBN: 978-0-387-48998-8. DOI: `10.1007/978-0-387-48998-8_948`. URL: `https://doi.org/10.1007/978-0-387-48998-8_948`.

Rantakokko-Jalava, Kaisu and Jari Jalava (2001). "Development of conventional and real-time PCR assays for detection of Legionella DNA in respiratory specimens". In: *Journal of Clinical Microbiology* 39.8, pp. 2904–2910.

Ririe, Kirk M, Randy P Rasmussen, and Carl T Wittwer (1997). "Product differentiation by analysis of DNA melting curves during the polymerase chain reaction". In: *Analytical biochemistry* 245.2, pp. 154–160.

Rosa, P, TG Karayiannis, and MW Collins (2009). "Single-phase heat transfer in microchannels: The importance of scaling effects". In: *Applied Thermal Engineering* 29.17-18, pp. 3447–3468.

RS (2021). *RS PRO Type K Thermocouple 25mm Length, 3.18mm Diameter*. https://uk.rs-online.com/web/p/thermocouples/8722503/. Accessed: 2021-02-25.

Saiki, Randall K et al. (1985). "Enzymatic amplification of beta-globin genomic sequences and restriction site analysis for diagnosis of sickle cell anemia". In: *Science* 230.4732, pp. 1350–1354.

Schmittgen, Thomas D and Kenneth J Livak (2008). "Analyzing real-time PCR data by the comparative C T method". In: *Nature protocols* 3.6, p. 1101.

Schnell, S and C Mendoza (1997a). "Theoretical description of the polymerase chain reaction". In: *Journal of theoretical biology* 188.3, pp. 313–318.

Schnell, S and Claudio Mendoza (1997b). "Enzymological considerations for the theoretical description of the quantitative competitive polymerase chain reaction (QC-PCR)". In: *Journal of theoretical biology* 184.4, pp. 433–440.

Seedstudio (2020). *What is MOSFET Transistor and How to use with Arduino?* https://www.seeedstudio.com/blog/2020/01/15/what-is-mosfet-transistor-basics-uses-arduino-tutorial/. Accessed: 2020-07-12.

Shah, R.K. and A.L. London (1978). "Chapter VII - Rectangular Ducts". In: *Laminar Flow Forced Convection in Ducts*. Ed. by R.K. Shah and A.L. London. Academic Press, pp. 196 –222. ISBN: 978-0-12-020051-1. DOI: `https://doi.org/10.1016/B978-0-12-020051-1.50012-7`. URL: `http://www.sciencedirect.com/science/article/pii/B9780120200511500127`.

Sharp, Kendra V et al. (2019). "Liquid flows in microchannels". In: *The MEMS Handbook-3 Volume Set*. CRC press, pp. 215–267.

Sheng, James J (2013). *Enhanced oil recovery field case studies*. Gulf Professional Publishing.

Shih, Steve CC et al. (2015). "A droplet-to-digital (D2D) microfluidic device for single cell assays". In: *Lab on a Chip* 15.1, pp. 225–236.

Shojaeefard, Mohammad Hasan et al. (2013). "Modelling and Pareto optimization of mechanical properties of friction stir welded AA7075/AA5083 butt joints using neural network and particle swarm algorithm". In: *Materials & Design* 44, pp. 190–198.

Sigma-Aldrich (2019). *Standard PCR Protocol*. URL: `https://www.sigmaaldrich.com/technical-documents/protocols/biology/standard-pcr.html`.

— (2020). *SYBR products for Real Time PCR & Nucleic Acid Staining*. URL: `https://www.sigmaaldrich.com/content/dam/sigma-aldrich/docs/Sigma-Aldrich/Datasheet/s9430dat.pdf`.

Simpson, Timothy W, Dennis KJ Lin, and Wei Chen (2001). "Sampling strategies for computer experiments: design and analysis". In: *International Journal of Reliability and Applications* 2.3, pp. 209–240.

Solinas, Antonio et al. (2001). "Duplex Scorpion primers in SNP analysis and FRET applications". In: *Nucleic Acids Research* 29.20, e96–e96.

Spiga, M and GL Morino (1994). "A symmetric solution for velocity profile in laminar flow through rectangular ducts". In: *International communications in heat and mass transfer* 21.4, pp. 469–475.

Srinivas, VSS and GK Ananthasuresh (2006). "Analysis and topology optimization of heat sinks with a phase-change material on COMSOL multiphysics™ platform". In: *COMSOL Users Conference*. Vol. 1.

Steinke, Mark E and Satish G Kandlikar (2004). "Review of single-phase heat transfer enhancement techniques for application in microchannels, minichannels and microdevices". In: *International Journal of Heat and Technology* 22.2, pp. 3–11.

SterlingSensors (2021). *Fabricated Thermocouple with Crimp Seal*. https://www.sterlingsensors.co.uk/pdfs/TFCSE.pdf. Accessed: 2021-02-25.

Stolovitzky, Gustavo and Guillermo Cecchi (1996). "Efficiency of DNA replication in the polymerase chain reaction". In: *Proceedings of the National Academy of Sciences* 93.23, pp. 12947–12952.

Sujatha, L et al. (2012). "Design and Analysis of Micro-Heaters using COMSOL Multiphysics For MEMS Based Gas Sensor". In: *Excerpt from the Proceedings of the 2012 COMSOL Conference in Bangalore*.

Syberfeldt, Anna, Henrik Grimm, and Amos Ng (2008). "Design of Experiments for training metamodels in simulation-based optimisation of manufacturing systems". In: *The 18th International Conference on Flexible Automation and Intelligent Manufacturing (FAIM'08) Skövde, Sweden, June 30-July 2, 2008*. University of Skövde.

Sykes, PJ et al. (1992). "Quantitation of targets for PCR by use of limiting dilution". In: *Biotechniques* 13.3, pp. 444–449.

Tamayol, Ali and M Bahrami (2009). "Analytical solutions for laminar fully-developed flow in microchannels with non-circular cross-section". In: *ASME 2009 Fluids Engineering Division Summer Meeting*. American Society of Mechanical Engineers, pp. 1323–1333.

Tanrıverdi, Sultan et al. (2002). "Detection and genotyping of oocysts of Cryptosporidium parvum by real-time PCR and melting curve analysis". In: *Journal of Clinical Microbiology* 40.9, pp. 3237–3244.

Teitel, Maxim, Dietrich Schwabe, and Alexander Yu Gelfgat (2008). "Experimental and computational study of flow instabilities in a model of Czochralski growth". In: *Journal of crystal growth* 310.7-9, pp. 1343–1348.

TE Technology (2010). *Thermoelectric Module:TE-23-1.0-1.3*. https://tetech.com/wp-content/uploads/2018/09/TE-23-1.0-1.3.pdf. Accessed: 2020-07-12.

ThermoFisher (2020). *Alexa Fluor 488 Dye*. https://www.thermofisher.com/uk/en/home/life-science/cell-analysis/fluorophores/alexa-fluor-488.html. Accessed: 2020 - 07 - 12.

Thomas, Susan, Ryan Luis Orozco, and Tim Ameel (2014). "Thermal gradient continuous - flow PCR: a guide to design". In: *Microfluidics and nanofluidics* 17.6, pp. 1039–1051.

Toh, KC, XY Chen, and JC Chai (2002). "Numerical computation of fluid flow and heat transfer in microchannels". In: *International Journal of Heat and Mass Transfer* 45.26, pp. 5133–5141.

Toropov, Vassili V et al. (2005). "Design optimization and stochastic analysis based on the moving least squares method". In: *6th World Congresses of Structural and Multidisciplinary Optimization*.

Tuckerman, Davic B (1984). *Heat-transfer microstructures for integrated circuits*. Tech. rep. Lawrence Livermore National Lab CA.

Tuckerman, David B and Roger Fabian W Pease (1981). "High-performance heat sinking for VLSI". In: *IEEE Electron device letters* 2.5, pp. 126–129.

Tullius, Jami F, Robert Vajtai, and Yildiz Bayazitoglu (2011). "A review of cooling in microchannels". In: *Heat Transfer Engineering* 32.7-8, pp. 527–541.

Urbant, Polina, Alexander Leshansky, and Yulia Halupovich (2008). "On the forced convective heat transport in a droplet-laden flow in microchannels". In: *Microfluidics and Nanofluidics* 4.6, pp. 533–542.

Van Dam, Edwin R et al. (2007). "Maximin Latin hypercube designs in two dimensions". In: *Operations Research* 55.1, pp. 158–169.

Van Den Bergh, Frans (2001). "An Analysis of Particle Swarm Optimizers (PSO)". In: *Pretoria, University of Pretoria*, pp. 78–85.

Verma, Raj Kumar and Sumana Ghosh (2019). "Two-Phase Flow in Miniature Geometries: Comparison of Gas-Liquid and Liquid-Liquid Flows". In: *ChemBioEng Reviews* 6.1, pp. 5–16.

Viana, Felipe AC, Gerhard Venter, and Vladimir Balabanov (2010). “An algorithm for fast optimal Latin hypercube design of experiments”. In: *International journal for numerical methods in engineering* 82.2, pp. 135–156.

Visioli, Antonio (2006). *Practical PID control*. Springer Science & Business Media.

VitroCom (2020). *Square - Miniature Hollow Glass Tubing*. https://www.vitrocom.com/products/view/8100. Accessed: 2020-07-12.

Vivekanand, SVB and VRK Raju (2018). “Numerical study of the hydrodynamics and heat transfer characteristics of liquid–liquid Taylor flow in microchannel”. In: *Heat Transfer—Asian Research* 47.6, pp. 794–805.

Walsh III, David I et al. (2017). “Enabling microfluidics: from clean rooms to makerspaces”. In: *Trends in biotechnology* 35.5, pp. 383–392.

Wang, Dongshu, Dapei Tan, and Lei Liu (2018). “Particle swarm optimization algorithm: an overview”. In: *Soft Computing* 22.2, pp. 387–408.

Wang, Rui-jin (2017). “Numerical investigation on the heat transfer of a droplet-laden flow in a microfluidic system”. In: *International Journal of Numerical Methods for Heat & Fluid Flow*.

Wang, ShiYing and Wei Wang (2010). “Kinetic characteristics of continuous flow polymerase chain reaction chip: A numerical investigation”. In: *Science China Technological Sciences* 53.7, pp. 1967–1972.

Wang, Wei et al. (2005). “Droplet-based micro oscillating-flow PCR chip”. In: *Journal of Micromechanics and Microengineering* 15.8, p. 1369.

Wang, Y et al. (2007). “Multi-physics simulational analysis of a novel PCR microdevice”. In: *Nanotech* 3, pp. 456–459.

Waterfall, Christy M, Robert Eisenthal, and Benjamin D Cobb (2002). “Kinetic characterisation of primer mismatches in allele-specific PCR: a quantitative assessment”. In: *Biochemical and biophysical research communications* 299.5, pp. 715–722.

Wei, Xiaojin and Yogendra Joshi (2003). “Optimization study of stacked microchannel heat sinks for micro-electronic cooling”. In: *IEEE transactions on components and packaging technologies* 26.1, pp. 55–61.

Wiens, Travis (2014). *Radial Basis Function Network*. URL: `https://www.mathworks.com/matlabcentral/fileexchange/22173-radial-basis-function-network`. (accessed: 14.05.2020).

Wilkin, Douglas (2018). *The Polymerase Chain Reaction - Advanced*. `https://www.ck12.org/biology/pcr/lesson/The-Polymerase-Chain-Reaction-Advanced-BIO-ADV/`. Accessed: 2019-01-03.

Williams, Christopher K and Carl Edward Rasmussen (2006). *Gaussian processes for machine learning*. Vol. 2. 3. MIT press Cambridge, MA.

Wittwer, Carl T and David J Garling (1991). “Rapid cycle DNA amplification: time and temperature optimization.” In: *Biotechniques* 10.1, pp. 76–83.

Wittwer, Carl T et al. (1997). “Continuous fluorescence monitoring of rapid cycle DNA amplification”. In: *Biotechniques* 22.1, pp. 130–138.

Wittwer, Carl T et al. (2003). “High-resolution genotyping by amplicon melting analysis using LCGreen”. In: *Clinical chemistry* 49.6, pp. 853–860.

Woo, Tony HS et al. (1998). “Identification of Leptospira inadai by continuous monitoring of fluorescence during rapid cycle PCR”. In: *Systematic and Applied Microbiology* 21.1, pp. 89–96.

Wu, Jian-Kang (1994). *Neural networks and simulation methods*. Marcel Dekker, Inc.

Xiong, F et al. (2009). “Optimizing Latin hypercube design for sequential sampling of computer experiments”. In: *Engineering Optimization* 41.8, pp. 793–810.

Xu, B et al. (2002). “Evaluation of viscous dissipation in liquid flow in microchannels”. In: *Journal of Micromechanics and Microengineering* 13.1, p. 53.

Xu, Hua-Xi et al. (2000). “A rapid method for determining the G+ C content of bacterial chromosomes by monitoring fluorescence intensity during DNA denaturation in a capillary tube.” In: *International journal of systematic and evolutionary microbiology* 50.4, pp. 1463–1469.

Yan, Suna et al. (2019). “Topology optimization of microchannel heat sinks using a two-layer model”. In: *International Journal of Heat and Mass Transfer* 143, p. 118462.

Yang, Kai-Shing et al. (2010). “An experimental investigation of air cooling thermal module using various enhancements at low Reynolds number region”. In: *International journal of heat and mass transfer* 53.25-26, pp. 5675–5681.

Zagklavara, Foteini et al. (2021a). “Numerical Modelling and Analysis of a Microfluidic PCR Device”. In: *6th World Congress on Momentum, Heat and Mass Transfer (MHMT’21)*.

— (2021b). “Optimisation of microfluidic polymerase chain reaction devices”. In: *E3S Web of Conferences*. Vol. 321. EDP Sciences, pp. 01007–01007.

— (2022a). “CFD INVESTIGATION OF THE EFFECT OF HEATER SPACING ON DNA AMPLIFICATION AND PRESSURE DROP IN A MICROFLUIDIC PCR DEVICE”. In.

— (2022b). “Multi-objective optimisation of polymerase chain reaction continuous flow systems”. In: *Biomedical Microdevices* 24.2, pp. 1–31.

Zec, Helena, Dong Jin Shin, and Tza-Huei Wang (2014). “Novel droplet platforms for the detection of disease biomarkers”. In: *Expert review of molecular diagnostics* 14.7, pp. 787–801.

Zhang, Hengyun et al. (2019). *Modeling, Analysis, Design, and Tests for Electronics Packaging beyond Moore*. Woodhead Publishing.

Zhang, Yonghao and Hui-Rong Jiang (2016). “A review on continuous-flow microfluidic PCR in droplets: Advances, challenges and future”. In: *Analytica chimica acta* 914, pp. 7–16.

Zhang, Yonghao and Pinar Ozdemir (2009). “Microfluidic DNA amplification—a review”. In: *Analytica chimica acta* 638.2, pp. 115–125.

Zhao, Xiao-Mei, Younan Xia, and George M Whitesides (1997). “Soft lithographic methods for nano-fabrication”. In: *Journal of Materials Chemistry* 7.7, pp. 1069–1074.

Zhivomirov, Hristo (2021). *5D Data Visualization with Matlab*. https://www.mathworks.com/matlabcentral/fileexchange/41086-5d-data-visualization-with-matlab. Accessed: 2021-01-12.

Zhu, Hanliang et al. (2020). "Heat transfer time determination based on DNA melting curve analysis". In: *Microfluidics and Nanofluidics* 24.1, pp. 1–8.

Zhu, Huaguang et al. (2012). "A novel algorithm of maximin Latin hypercube design using successive local enumeration". In: *Engineering Optimization* 44.5, pp. 551–564.